University of Bath

PHD

Electrochemical Behaviour of Microporous Materials for Water Purification

Putra, Budi Riza Putra

Award date:
2020

Awarding institution:
University of Bath

Link to publication

Alternative formats
If you require this document in an alternative format, please contact:
openaccess@bath.ac.uk

Copyright of this thesis rests with the author. Access is subject to the above licence, if given. If no licence is specified above, original content in this thesis is licensed under the terms of the Creative Commons Attribution-NonCommercial 4.0 International (CC BY-NC-ND 4.0) Licence (https://creativecommons.org/licenses/by-nc-nd/4.0/). Any third-party copyright material present remains the property of its respective owner(s) and is licensed under its existing terms.

Take down policy
If you consider content within Bath's Research Portal to be in breach of UK law, please contact: openaccess@bath.ac.uk with the details. Your claim will be investigated and, where appropriate, the item will be removed from public view as soon as possible.

Download date: 16. May. 2022

Electrochemical Behaviour of Microporous Materials for Water Purification

Budi Riza Putra

A thesis submitted for the degree by

Doctor of Philosophy

University of Bath

Department of Chemistry

April 2020

COPYRIGHT

Attention is drawn to the fact that copyright of this thesis rests with the author. A copy of this thesis has been supplied on condition that anyone who consults it is understood to recognise that its copyright rests with the author and they must not copy it or use material from it except as permitted by law or with the consent of the author.

This thesis may be made available for consultation within the University Library and may be photocopied or lent to other libraries for the purposes of consultation.

Access to this thesis in print or electronically is restricted until …… (date)

Signed on behalf of the Doctoral College …… (print name)

Abstract

Ionic current rectification describes the unique electrochemical behaviour for devices based on microporous materials to conduct ions only in one direction under applied potential bias. The mechanism of ionic current rectification for all types of microporous materials are similar and based on electrolyte accumulation (open diode) and depletion (closed diode) within the region of a microhole in the substrate. The ionic current rectification phenomenon has been investigated for different types of ion conducting microporous materials with applications linked to future water desalination technology. In general, there are three types of microporous materials studied in the thesis that have been investigated based on (i) one-dimensional, (ii) two-dimensional, and (iii) three-dimensional pore systems. All of these microporous materials show good performance as long as semi-permeability can be achieved and maintained.

In this thesis, ionic current rectification phenomena have been studied and investigated for different types of microporous materials such as, bacteriophage M13 (one-dimensional), graphene oxide and titanate nanosheets (two-dimensional), and Nafion and PIM-EA-TB “heterojunction” (three-dimensional). Each of these microporous materials gives unique electrochemical characteristics (ionic current rectification phenomena) when deposited as a film onto a poly-ethylene-terephthalate (PET) susbtrate with 20 μm diameter microhole. In the final chapter of this thesis, it is demonstrated a water desalination prototype based on ionic current rectification in microporous materials. It can be concluded that ionic diode devices based on different types of microporous materials provide a new avenue of fundamental electrochemical study with effects based on materials, device geometry, and electrolyte media. In the future, there is a possibility to develop ionic circuits and a wider range of ionic devices to provide new types of interfaces between artificial electronic systems and biological ionic systems.

Acknowledgements

All praise is due to God Almighty, Allah SWT, who has been giving me the strength and blessing throughout my life and research so that I am able to complete my PhD at Bath. I am very thankful to my parents, brothers and sisters for their endless support and prayers all the time. I would like to thank to my wife Wulan T. Wahyuni who always supports, encourages me to continue my study. I would like to acknowledge the Indonesian Endowment Fund (Ministry of Finance Republic of Indonesia LPDP RI) for full financial support. It would not have been possible to continue my PhD at University of Bath without their funding.

I would like to express my sincere appreciation to my supervisor, Professor Frank Marken, for his invaluable guidance and support. He leads me to the field of electrochemistry, especially ionic diode studies, and gives me a lot of advice on my research work. He supports me to take part in various research activities which provides me with the chance to present my work and also collaborate with many researchers. This thesis would not have been possible without his help.

I would like to thank all co-authors and contributors who provided all the materials, advice, and suggestions. I would like to thank all lab members of the Marken group for their kind help and discussion. I would like to thank my previous supervisor Prof. Latifah K. Darusman† who gave me recommendations and reference letters to study further in the UK your memory will be eternal and all of the staff members of the Analytical Division of the Chemistry Department of Bogor Agricultural University for their continuous support. Thanks to all Indonesian people who have been accompanying and supporting my life in the last 3 years and a half in the UK. I also use this opportunity to express my gratitude to everyone who contributed to my research, and life in Bath over last three and a half years.

Contents

Abbreviations

AC alternating current

CE counter electrode

CNF carbon nanofiber

DLP diffusion limited patterning

$\boldsymbol{E_F}$ Fermi level

EIS electrochemical impedance spectroscopy

DLS Dynamic Light Scattering

DMSO dimethyl sulfoxide

EDL electrical double layer

GO graphene oxide

HOMO highest occupied molecular orbital

IUPAC International Union of Pure of Applied Chemistry

LUMO lowest unoccupied molecular orbital

MOF Metal Organic Framework

PAH poly(allylamine)

PET poly(ethylene-terephthalate)

PIM Polymer of Intrinsic Microporosity

PIM-EA-TB Polymer of Intrinsic Microporosity-Ethanoanthracene-Tröger Base

RE reference electrode

SAXS small angle X-ray scattering

SCE saturated calomel electrode

SE sense electrode

STEM Scanning Transition Electron Microscopy

TEM Transmission Electron Microscopy

WE working electrode

ZIF zeolitic imidazolate framework

List of Symbols

Subscripts

a	anodic reaction at electrode
c	cathodic reaction at electrode
eq	equilibrium
F	Fermi level
Ox	pertaining species Ox in $\mathrm{Ox} + ne^- \rightleftharpoons \mathrm{Red}$
ox	oxidation reaction for $\mathrm{Ox} + ne^- \rightleftharpoons \mathrm{Red}$
Red	pertaining species Red in $\mathrm{Ox} + ne^- \rightleftharpoons \mathrm{Red}$
red	reduction reaction for $\mathrm{Ox} + ne^- \rightleftharpoons \mathrm{Red}$
x	species x
0	zero distance (at electrode surface)

Greek Symbols

Symbol	Description	Typical Units
α	charge transfer coefficient	no units
δ	diffusion layer thickness	V decade^{-1}
γ	activity coefficient	no units
η	overpotential $(E - E_{eq})$	V
ν	scan rate	mV s^{-1}
ϕ	(i) electrode diameter	μm
	(ii) electrostatic potential	V
	phase angle	no units
ω	angular frequency	radian s^{-1}

Roman Symbols

Symbol	Description	Typical Units
a	chemical activity	no units
A	(i) electrode area	cm^2
	(ii) area of the cross-section of the microhole	cm^2
c	concentration of the cation in the microhole	mol dm^{-3}
c_m	concentration of the cation in the adjacent cationic exchange membrane	mol dm^{-3}
c_s	concentration of the cation in the adjacent bulk	mol dm^{-3}
C	concentration	mol dm^{-3}
$C_i(x,t)$	concentration of species i at time t and distance x	mol dm^{-3}
D	diffusion coefficient	cm^2 s^{-1}
D_i	diffusion coefficient of species I	cm^2 s^{-1}
E	potential	V
E^0	standard potential	V
$E^{0'}$	formal standard potential	V
E_a	activation energy	J mol^{-1}
E_{final}	final potential	V

E_{init}	initial potential	V
E_{mid}	redox potential $\left(\frac{1}{2}\left(E_p^a + Ep^c\right)\right)$	V
E_{V1}	first vertex potential	V
E_{V2}	second vertex potential	V
ΔE	potential change	V
f	(i) frequency	Hz
	(ii) flux of the cation in the *x*-direction	no units
F	Faraday constant	C mol^{-1}
G	Gibbs free energy	J mol^{-1}
$G^{\ddagger}$	Gibbs free energy of activation	J mol^{-1}
G^0	standard Gibbs free energy	J mol^{-1}
ΔG	Gibbs free energy change	J mol^{-1}
$\Delta G^{\ddagger}$	change in Gibbs free energy in activation	J mol^{-1}
I	current	A
I_0	exchange current	A
I_{total}	total current from electrolysis	A
k	rate constant	depends on order
	i) homogeneous first order rate constant	s^{-1}
	ii) heterogenous rate constant	m s^{-1}
K_{SP}	solubility product	depends on stoichiometry
L	thickness of the film through which the microhole is made	cm
n	number of transferred electrons	no units
p	pressure	atm
Q	charge	C
R	gas constant	J K^{-1} mol^{-1}
R_h	resistance in the hole	Ω
T	absolute temperature	K
u	dimensionless potential	V
v	velocity	m s^{-2}
V	voltage between the two cells	V
x	distance	m
Z	impedance	Ω

List of Figures

List of Tables

Chapter 1

Introduction to Microporous Materials in Ionics

Contents

1.1. Background and Motivation

Porous materials are widely used and have received considerable attention in many practical fields including those with chemical, environmental/energy, optics, electronics, medical, and biotechnological applications.[1] This is due to properties that are linked to regular pore structures, pore size distribution, shapes and crystallinity. According to an IUPAC definition, these porous materials are divided into three major categories depending on their pore sizes: **macroporous materials** with pore sizes above 50 nm, **mesoporous materials** with pore sizes between 2 and 50 nm, and **microporous materials** with pore sizes below 2 nm. Microporous materials contain interconnected pores of dimensions below 2 nm are important in a wide of applications including gas separation, storage, and purification. The availability of new types of microporous materials for example based on metal-organic frameworks (MOFs)[2], or based on polymer of intrinsic microporosity (PIMs)[3], has resulted in many new developments in particular in gas phase applications. However, also in contact with aqueous electrolyte new phenomena are observed. For example, during ion transport through micropores new effects have been observed consistent with ionic "rectification" phenomena. The term of "ionics" (as compared to electronics) has been coined to describe the transport, behaviour, and application of ionic system in solution or in solid phase.

Ionic rectification or ionic "diode" phenomena describe the unique ability of devices based on microporous materials to conduct ions in one direction with applied potential bias. For one polarity the ion flow is inhibited and with reverse bias the opposite ion flow direction is enhanced. In order to explain this, a simplified analogy can be used based on water flow in tubes with valves (or blood flow in veins). Figure 1A illustrates how the water/blood can flow only in one direction with the pressure gradient driving force. The "open" state occurs when the water is flowing due to the pressure force (open valve), while the "closed" state occurs when water flow is restricted (closed valve). The similar analogy also applies to the ion flow but with the potential gradient as the driving force as shown in Figure 1.1B. The phenomena described by the ion flow only in one direction are called "ionic rectification" or "ionic diode". Interest in ionic diode phenomena originates from

the attempts to mimic nanopores[4] in natural cell membranes and for the development of single channel nanofluidics[5] with potential for desalination[6], energy harvesting[7], sensing[8], and "iontronics"[9] applications.

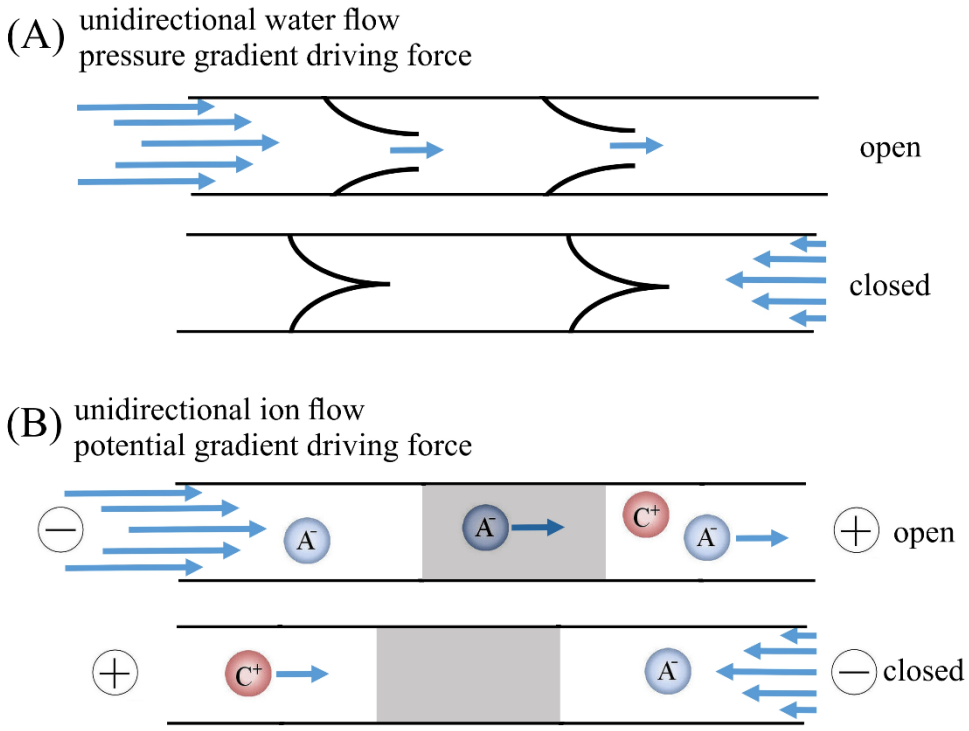

Figure 1.1. Schematic illustration about open and closed states in unidirectional water flow (A) with applied pressure. (B) Unidirectional ion flow with applied potential.

Many efforts have been made to achieve fabrication of ionic diode devices for example based on biological membrane pores[10], in nanofluidic devices[11], and at bipolar membranes.[12] The ionic rectification devices were firstly found using a conical quartz nano-pipet electrode.[13] Then, ionic diode devices were investigated in asymmetrically shaped "track-etch" polycarbonate nanochannels. Until now, the fabrication of ionic diode devices requires a combination of hydrogel materials and/or complex nanofabrication processes with the use of nano-scale composite materials. The devices and processes are not always fully understood. Therefore, there is a need (pursued in this thesis) to prepare ionic diode devices using simple fabrication techniques using a single well-defined microporous material.

In contrast to the nanofluidic ionic rectifiers (which requires expensive nanofabrication), simple microporous materials-cast devices can be made in a conventional laboratory environment. It has recently been shown that ionic diode fabrication can be achieved by solution-casting of a thin microporous material coating, for example, based on Polymer of Intrinsic Microporosity (PIM) materials onto a 6 μm thick poly(ethylene-terephthalate) (PET) film, through which a single 20 μm hole (Figure 2B) was drilled by laser irradiation.[14] The PET film in contact with different electrolyte solutions on each face of the film and was placed into two-compartment voltammetry cell (Figure 2A). A potential was applied across the PIM membrane to measure ion flow. This type of experiment is possible with different dimensional microporous materials and therefore there is a new opportunity for "ionic diode materials" to be developed and investigated (in contrast to ionic diode devices in nanofluidic channels). The new devices offer higher currents, better rectification and chemical control, also provide more opportunities for applications.

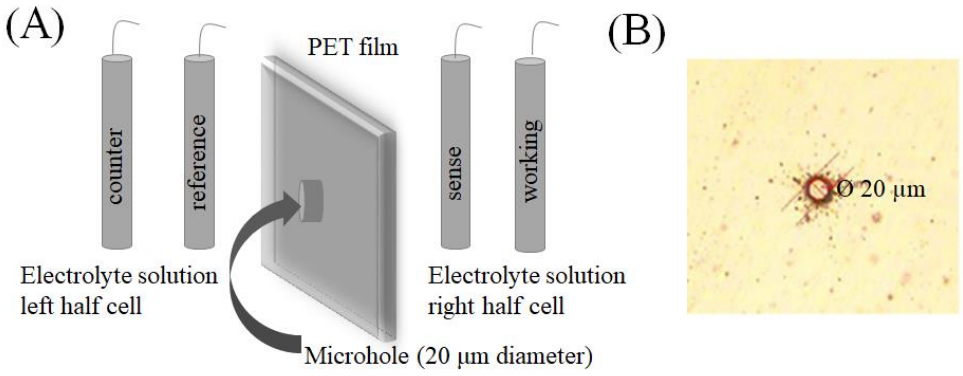

Figure 1.2. (A) Schematic drawing of the electrochemical cell for membrane measurements with left and right half-cells filled with electrolyte and (B) Optical microscopy image of the 20 μm pore in a PET film.

In order to allow ion conduction, usually classical ionomer (materials with covalently attached charges) materials based on Nafion or other commercial ion conductors are considered. However, there is a much wider range of microporous materials (including biological porous materials) that can be employed in thin free-standing films. These films can be prepared for example by solvent-casting on polyethylene-terephthalate (PET) substrate holders. So far, ionic diode devices

using microporous materials on PET substrates have been reported based on polymers of intrinsic microporosity (PIMs)[15], Nafion[16], cellulose derivatives[17], metal-organic frameworks (MOFs)[18], commercial cation-conducting membrane (Fumasep FKS-30)[19], and negatively charged carbon nanofibers (CNFs).[20] The key to the ionic rectification process is in the microhole geometry, which is similar to micro-electrode geometries as it allows spherical diffusion. The study is performed with four electrodes (to apply a potential across the membrane, see Figure 1A) in a cell composed of two half-cells separated by the membrane. The ionic rectification effect is observed when a microhole is asymmetrically covered (e.g. ionomer deposited from only one side) in contact with aqueous electrolyte solution on both sides. When employing macroscopic membrane samples or symmetrically covered microholes only resistive behaviour is observed without ionic diode effects.

Ionic diode phenomena observed from microporous materials potentially can be used for water purification. These phenomena occur at interfaces between asymmetric ionomer material | aqueous electrolyte in microhole devices. Depending on the applied potential, either an "open" or a "closed" diode state is observed switching between a high ion flow rate and a low ion flow rate. Physically, the "open" state is associated mainly with conductivity towards the microhole within the ionomer layer and the "closed" state is dominated by restricted diffusion-migration access to the microhole interface opposite to the ionomer. Therefore, the open state of ionic diode could be useful for water purification because it can remove specific ions from the salt water. The underlying mechanism of ionic diode for water purification is studied in more detail in this report.

Overall, the processes in these ionic diode systems are complex and based on ion diffusion-migration as well as on other effects such as concentration polarisation and the charging of interfaces. In a first approximation, the depletion and accumulation of electrolyte in the cylindrical microhole can be considered crucial. However, for each type of material studied, new types of experiments need to be developed and especially the competing transport of different ions needs to be measured (the current only gives the sum of all contributions). This report

contributes to both, the study of the mechanism and the search for materials and architectures.

This work will focus on investigation of ionic diode phenomena in different types of microporous structures: **one dimensional materials** (bacteriophage M13), **two dimensional materials** (graphene oxide and titanate nanosheets), and **three dimensional materials** (Nafion or Polymers of Intrinsic Microporosity). In the final part of this work, a proof-of-concept device is developed for desalination based on Nafion as cationic diode material and commercial anion exchange membrane (Fumasep FKS-130) as anionic resistor material. The prototype configuration for water desalination are demonstrated combining desalination and salination process for an aqueous 250 mM NaCl solution.

1.2. Project Aims

The project is focused on exploring ionic diode phenomena of various dimensional microporous materials and studying the ionic rectification mechanism. The understanding of the ionic diode mechanism from each microporous material is crucial to improve the ionic current rectification and in order to be used for application purposes. The most suitable microporous material will be developed for proof-of-concept for water desalination. Therefore, this project pursued the following objectives:

(1) Finding new types of one, two, and three-dimensional microporous materials for ionic diodes and developing new methods for the characterisation of ionic diodes
(2) Understanding the ionic current rectification mechanism for different dimensional microporous materials based on physical parameters such as ionic conductivity and semi-permeability
(3) Improving ionic diodes performance based on ionomer film thickness, geometry parameters, and combination of materials in “heterojunctions”
(4) Exploratory development of applications in particular in analytical ionic diodes sensors using PIM-EA-TB | Nafion “heterojunctions”.

(5) Development of a water desalination prototype based on Nafion cationic diode and commercial anion exchange membrane as ionic resistor.

1.3. Thesis Outline

The thesis is divided into Chapter 1 for introduction, Chapter 2 for literature review, Chapter 3 for techniques, Chapter 4 until 9 for the result and discussion, and Chapter 10 for summary, overall conclusions and future works. Chapter 1 explains about the background and motivation for doing this research and also discusses about the aims of the study. Chapter 2 consists of a thorough literature review of introduction of ionic rectification, materials for ionic rectifiers, mechanisms and architectures for ionic rectification and application for ionic rectification. In Chapter 3, electrochemical techniques are introduced and reviewed. In Chapter 4 the discussion is about ionic rectification of one-dimensional nanomaterial based on bacteriophage M13. The discussion of ionic rectification from two dimensional nanomaterials based graphene oxide and its fundamental theory are shown in Chapter 5. In Chapter 6, the discussion of inorganic two dimensional nanomaterials based on titanate nanosheets is provided as well as discussion of its switching diode behaviour. The characteristics of three dimensional nanomaterials as diode based on Polymer of Intrinsic Microporosity | Nafion which is described in Chapter 7. The application of PIM-EA-TB | Nafion heterojunction for potassium sensing has been discussed in Chapter 8. The application of ionic rectification for water desalination based on Nafion diode is also presented in Chapter 9. The studies are summarized and concluded in Chapter 10. Suggestions for further work are given in outline.

1.4. References

1 Ariga, K., Vinu, A., Yamauchi, Y., Ji, Q., Hill. J.P. *Bull. Chem. Soc. Jpn.* **2012**. *85*, 1, 1-32.

2 Madrid, E., Buckingham, M.A., Stone, J.M., Rogers, A.T., Gee, W.J., Burrows, A.D., Raithby, P.R., Celorrio, V., Fermin, D.J., Marken, F. *Chem. Comm*. **2016**. *52*, 2792-2794.

3 Rong, Y., Song, Q., Mathwig, K., Madrid, E., He, D., Niemann, R.G., Cameron, P.J., Dale, S.E.C., Bending, S., Carta, M., Malpass-Evans, R., McKeown, N.B., Marken, F. *Electrochem. Comm*. **2016**. *69*, 41-45.

4 Guo, W., Tiang, Y., Jiang, L. *Acc. Chem. Res*. **2013**. *46*, 12, 2834-2846.

5 Cervera, J., Ramirez, P., Mafe, S., Stroeve, P. *Electrochim. Acta*. **2011**. *56*, 4504-4511.

6 Madrid, E., Cottis, P., Rong, Y.Y., Rogers, A.T., Stone, J.M., Malpass-Evans, R., Carta, M., McKeown, N.B., Marken, F. *J. Mater. Chem. A.* **2015**, 3, 15849-15853.

7 Rankin, D.J., Huang, D.M. *Langmuir*. **2016**. *32*, 12, 3420-3432.

8 Siwy, Z., Trofin, L., Kohli, P., Baker, L.A., Trautmann, C., Martin, C.R. *J. Am. Chem. Soc.* **2005**. *127*, 5000-5001.

9 Chun, H.G., Chung, T.D. *Ann. Rev. Anal. Chem*. **2015**. 8, 441-462.

10 Queralt-Martin, M., Garcia-Giménez, E., Aguilella, V.M., Ramirez, P., Mafe, S., Alcaraz, A. *App. Phys. Lett*. **2013**. *103*, 043707.

11 Siwy, Z., Fuliński, A. *Phys. Rev. Lett*. **2002**. 89, 19, 198103

12 Lovreček, B., Despic, A., Bockris, J. *J. Phys. Chem*. **1959**. *63*, 750-751.

13 Wei, C., Bard, A.J., Feldberg, S.W. *Anal. Chem*. **1997**. *69*, 22, 4627-4633.

14 Madrid, E., Rong, Y., Carta, M., McKeown, N.B., Malpass-Evans, R., Attard, G.A., Clarke, T.J., Taylor, S.H., Long, Y.T., Marken, F. *Angew. Chem. Int. Ed.* **2014**, *53*, 10751-10754.

15 Madrid, E., Cottis, P., Rong Y., Rogers A.T., Stone, J.M., Malpass-Evans, R., Carta, M., McKeown, N.B., Marken, F. *J. Mater. Chem. A.* **2015**. *3*, 15849-15853.

16 He, D., Madrid, E., Aaronson, B., Fan, L., Doughty, J., Mathwig, K., Bond, A.M., McKeown, N.B., Marken, F. *ACS Appl. Mater. Interfaces.* **2017**, *9*, 11272-11278.

17 Aaronson, B.D.B., Wigmore, D., Johns, M.A., Scott, J.L. Polikarpov, I., Marken, F. *Analyst*. **2017**. *142*, 3707-3714.

18 Madrid, E., Buckingham, M.A., Stone, J.M., Rogers, A.T., Gee, W.J., Burrows, A.D., Raithby, P.R., Celorrio, V., Fermin, D.J., Marken, F. *Chem. Comm*. **2016**. *52*, 2792-2794.

19 Tshwenya, L., Arotiba, O., Putra, B.R., Madrid, E., Mathwig, K., Marken, F. *J. Electroanal. Chem*. **2018**. *815*, 114-122.

20 Tshwenya, L., Marken, F., Arotiba, O. *ChemElectroChem*. **2019**. *6*, 12, 3145-3153.

Chapter 2

Introduction to Ionic Rectification

Contents

Chapter Abstract

Ionic current rectification can be considered to be a phenomenon equivalent to electronic rectification, essentially an asymmetric potential-dependent ion flux in electrolyte solution leading to asymmetric current-voltage characteristics. The reason for this asymmetry can be diverse: (i) asymmetry in microscopic double layer structure, (ii) asymmetry in macroscopic potential dependent fields, (iii) potential dependent interfacial reactions, or (iv) potential dependent compositional changes. All cases of rectification are linked to asymmetry and potential-dependent compositional changes.

Since the discovery of ionic current rectification at poly-electrolyte interfaces, the observation and application of ionic current rectification has progressed only very slowly. In this chapter, a general overview is provided about the classification of mechanisms, the link of mechanism to morphology and structure, and the various architectures of ionic current rectification systems from nanoscale and microscale. The ionic current rectification effects at microhole devices based on different types of microporous materials are also introduced. Finally, the potential applications of ionic current rectification in the future are briefly presented.

2.1. Introduction to Ionic Rectification: Bipolar Membrane

Ionic diodes or rectifiers and electrolytic diodes are based on the ability of a membrane to allow the movement of ions preferentially in one direction and inhibit conduction of ions into the opposite directions. Ionic rectification effects have been studied since second half of 20th century. The early studies of rectification effects were mainly concerned with biological samples in nerves and muscles.[1] The analogy in the description between semiconductors and electrolyte solutions by Reis[2] and Fuller[3] had inspired Lovreček et al.[4] to demonstrate current rectification in aqueous solvents using poly-electrolytic or ion-exchange membranes (IEMs) in Figure 2.1A.

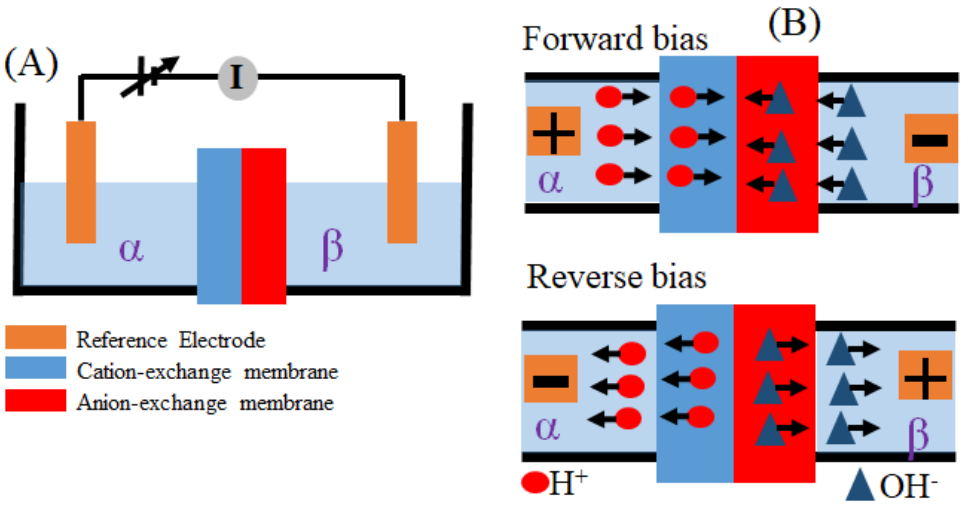

Figure 2.1. (A) The first ionic diode experiments. (B) Schematic of an ion diode fabricated by attaching cation- and anion-exchange membrane.

Lovreček et al. showed in their work that the cation and anion-exchange membrane of a bipolar membrane (that is a membrane combining an anion conductor and a cation conductor) served as equivalents to *p*- and *n*-type semiconductors. They used 2 different electrolytic solutions, the first solution (α) containing an excess of highly mobile protons with corresponding immobile anions in contact with the second solution (β) containing an excess of highly mobile hydroxide anions with corresponding immobile cations. Figure 2.1B shows that during the forward bias when α is positive and β is negative, the current carrying H^+ and OH^- ions will react with each other to form water. This creates an ion

depletion zone (leading to high resistance). In the reversed bias, the mobile current carriers flowing slowly to the opposite direction to the first case (leading to low resistance), and consequently a rectification effect was produced. Since this pioneering work, various structures and materials have been reported to exhibit similar nonlinear or rectifying current-voltage (*I*-*V*) characteristics and the underlying mechanisms have been also theoretically investigated.[5]

2.2. Classification, Mechanism and Architecture for Ionic Rectification

There are many different ways in which ionic diodes can be generated, such as nanopore fabrication, reactions leading to interfacial rectification, or filling a microhole asymmetrically with a semi-permeable rectifying material such as porous polymers, two-dimensional nano-material, or microporous metal organic frameworks. The making of rectifying ionic diode devices has been achieved by numerous ways, some of which are described and illustrated below.

2.2.1. Biomimetic Ionic Diodes

Transport of ions occurs in biological ion channel in which the ions will preferably flow in one direction and can therefore be considered as ionic diode. Ion channels in organisms with different structures and functions play essential roles in controlling the ion transport in and out of the cell. For example, electric eels can convert the salt concentration gradient to bioelectricity by employing numerous ion channels in the plasma membrane.[6] Most ion channels with asymmetric structures conduct preferred ion transport in one direction to perform ionic diode functions. A perfect example of biological ion diodes is the outer membrane protein F (OmpF) channel from *Escherichia coli* with an asymmetric pore geometry structure. This case has been studied further due to its charged states in different external conditions.[7]

Figure 2.2. shows the proposed explanation of current rectification phenomena in the OmpF channel under acid||basic configuration. In the side of the protein channel facing the acidic solution, the excess of positive net charge is compensated by corresponding amount of anions. Similarly, the excess of negative

net charge is compensated by corresponding amount of cations on the side of channel facing to the basic solution. In Figure 2.2A under positive polarization in the acid side and negative polarization in the basic side, the predominant charge carriers of each zone migrate outward from the channel heading towards corresponding electrodes, giving rise to a depleted zone in central part of channel. Therefore, there is a rise of electrical resistance due to a lack of ion concentrations. When the polarization is switched in Figure 2.2B, the excess of anions coming from the positive zone try to cross the negative zone of channel and vice versa. The result is an accumulation of charge carriers in the central part of protein channel and giving high conductivity. Thus, the concentration of ions in the central part of channel become much higher than those in bulk solution and produces an increase in current. These properties can be used to pump potassium ions against an external concentration gradient.[8]

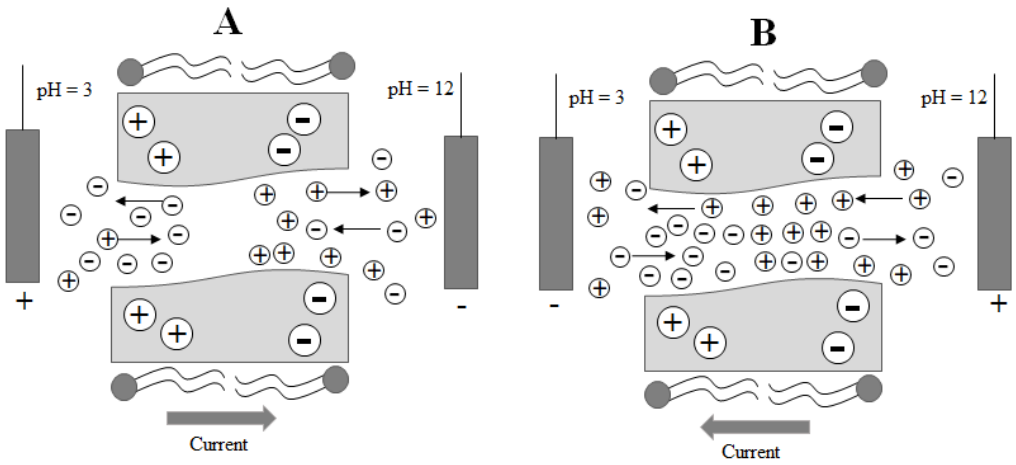

Figure 2.2. Schematic representation of the current rectification in the OmpF channel under (A) positive polarization and (B) negative polarization.[9]

There has been new research in attempting to mimic the selectivity in biological ion pores, namely K^+/Na^+ channels. The selectivity of K^+ ion channel can be ~10^3-10^4 toward Na^+ such as KcsA and is achieved by the presence of carbonyl oxygen atoms in the selectivity filter, which coordinate K^+ and Na^+ differently[10]. The size of synthetic pores must be proportional with diameter of the

diffusing ions (~0.2-0.6 nm) to mimic the chemical selectivity of biological channels[11]. This work emphasizes the idea of selective control of ion flow in nanochannels and has great potential applications such as cation filtration and development of sensitive ion sensors.

2.2.2. Nanofluidic Ionic Diodes

Ionic diode effects with nanochannel geometry have been developed to mimic biological ion channels function and exhibit a preferred ion transport direction. The special character of nanochannel stems from the scale of the nanochannel and the electrical double layer (EDL), which is characterized by Debye length (λ_D). As λ_D is in the range of 1-100 nm under most actual ionic conditions, only when the dimension of the channel is compressed into nanoscale (Figure 2.3) ion transport will be controlled by EDL which provide system with ion selectivity.[12] When the pore/channel diameters are as small as the Debye-length, the electrostatic interactions between the ions or charged molecules in the solution and the surfaces of pores/channels become very strong. The nanochannel device with asymmetric ion transport which can preferentially conduct ion flow in one direction and inhibit ion flow in the opposite direction is similar to a diode in electronics. The diode-like nanosystem with excellent ion transport control may have extensive applications in interdisciplinary subjects, such as physics, chemistry, and biology.[13]

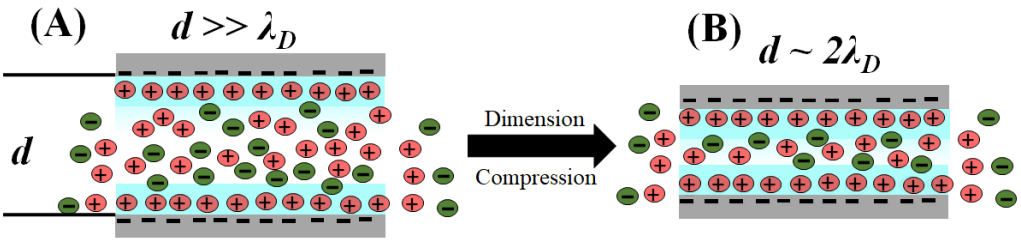

Figure 2.3. Ion transport in channels with different dimensions. A) In a system with a dimension $d >> \lambda_D$, ions diffuse through the channel. B) Ion transport through dimension of the channel ($d \sim 2\lambda_D$) controlled by EDL (light blue area).

The first observation of ionic current rectification in nanoscale was found in quartz nanopipet by Wei et al.[14] Their method used a nanopipet with opening between 20 and 200 nm and recorded the first asymmetric current-voltage current curves in 10 mM KCl electrolyte solution. The nanopipet was produced by pulling clean quartz tubes with a laser puller and the geometrical characteristics were adjusted by controlling the relevant parameters in the puller. However, this behaviour disappeared and ohmic linear current-voltage curve were recorded when the radius of the pipette was enlarged to 20 μm. This behaviour was strongly influenced by the concentration of electrolyte which directly affected by the Debye length. It was concluded that the overlap of the electrical double layer structure contributes to the ionic current rectification phenomenon.

In view of the charge polarity of the nanochannel surface, the ionic diodes can be divided into two types, unipolar and bipolar. Unipolar ionic diode is when there is only a single-polar charge on the ionic diode surface. If a system has both positive and negative charges on the surface, it is called a bipolar ionic diode. The ionic diode effect inside nanochannel exhibited as strong asymmetric ion conduction when switching the voltage bias is utilized. This rectification effect is found to be the result of symmetry-breaking in channel geometry, surface charge distribution, ionic concentration, or a combination of these aspects.[15]

Several types of ionic diode systems have been reported with symmetric and asymmetric nanochannel geometry. The symmetric nanochannel can act as nonlinear ion transport by introducing symmetric breaking. For example, Cheng et al.[16] found the rectified ion transport in a homogenous silica nanochannel, which is placed between two ionic solutions with a concentration gradient. This is because only one side of the nanochannel (facing the low concentration solution) is overlapping with the electrical double layer and yielded ion rectification. Nguyen et al.[17] described the ion rectification in the unipolar ionic diode to the ionic selectivity of the partially charged channel and the different ion distribution in the nanochannel under opposite bias. In Figure 2.4A, the system is in an open state with cations as the primary current carriers while in the closed state, the system forms a

depletion zone in the junction of the charged-neutral region (Figure 2.4B) and leading to ion current diminished.

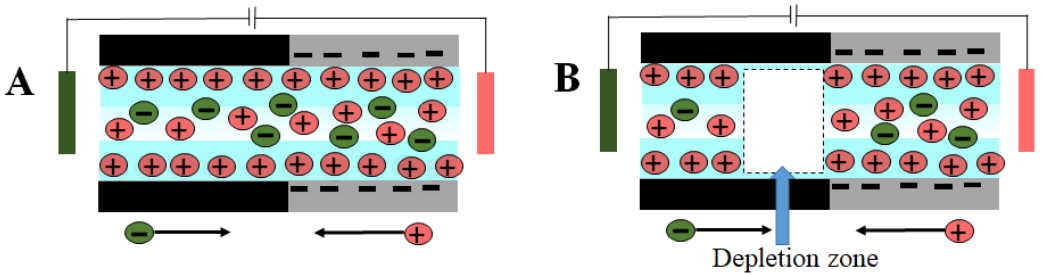

Figure 2.4. Schematic drawing of unipolar ionic diode in A) open state and B) closed state with a formed depletion zone in the junction of the charged-neutral zone.

In perspective of the biological ion channels, asymmetric geometry is an essential character for the ion channels to fulfil functions of physiological properties.[18] The asymmetric geometry of ionic diodes mainly includes conical[19], funnel[20], and bullet-shaped nanochannels. Among these types, the conical-shaped ionic diode is the most extensively explored due to its simplicity and wide applications.[21] Siwy et al.[22] reported asymmetric diffusion through synthetic nanopores in conical nanochannels to rectify ion currents. When the electrical double layer is strongly affected by ionic concentration, the system will result in different ion transport through the nanopore. With the solution concentration gradient, the ionic selective nanopore can also harvest energy from the salt gradient potential. Siwy[23] also reported the typical current-voltage characteristics of a single conical polyethylene terephthalate (PET) measured under symmetric KCl concentrations in both sides. A conical nanopore was prepared by irradiating heavy ions on a 12 μm thick PET film and subsequent chemical etching. A single conical nanopore has large opening diameter of ~600 nm on one side of PET and a small opening diameter, ranging 2 to 15 nm on the side. The chemical etching process produces negatively charged carboxyl groups on the PET film, making the pore become cation selective.

A more direct way to control and produce an asymmetric ion distribution along a nanochannel is by directly creating an asymmetric surface charge. Ionic current rectification can also be generated by asymmetrically shaped nanochannel with charged walls to create bipolar ionic diode devices. Bipolar ionic diodes have been extensively developed by employing the asymmetric surface charge distribution such as the patterning of the charged surface in conical nanochannels. The key challenge for creating this type of bipolar diode is to define different surface charges on the channel walls.

An asymmetric surface charge distribution can also allow ionic current rectification in a nanochannel. Daiguji et al.[24] proposed the idea of a nanofluidic diode consisting surface charges on either half of a nanochannel. Karnik et al.[25] have demonstrated nanofluidic diodes with asymmetric charge distribution by modifying one half of the neutral surface of biotin adsorbed channel with positively charged avidin using diffusion limited patterning (DLP). Meanwhile, Yan et al.[26] achieved surface charge discontinuity in nanopores by fabricating SiO_2/Al_2O_3 heterostructured nanotubes to create nanofluidic diode device. In a related approach, Cheng et al.[27] used a photolithography technique to create nanochannels with SiO_2 and Al_2O_3 that had a much sharper surface charge boundary than the DLP to create nanofluidic triodes.

Several groups have focused on how to control the ionic current rectification phenomena in the conical nanopore. Kovarik et al.[28] reported that the degree of current rectification can be affected by the diameter of the conical pore and rectification ratio increases with decreasing tip diameter. The 35 nm pore exhibits a maximum recitification ratio and the 380 nm pore exhibit nearly diode like current-voltage curves when initially etched and strong rectification obtained after ion current has stabilized.

Changing the sign of surface charge inside the nanopore could also plays a critical role in the ionic current rectification. Siwy et al.[29] demonstrated that adding positive charge (amine groups) to the small diameter conical nanopores yield

different rectifier effect with the polarity opposite with the negatively charge conical nanopores (added with carboxylate groups). He et al.[30] also reported that polyvalent cations like Ca^{2+} and the trivalent cobalt sepulchrate produce localized charge inversion to change the nanopore surface charge profile from negative to positive. Meanwhile, Ali et al.[31] used layer-by-layer deposition of polyelectrolyte into conical nanopore to tune the current rectification ratio. Another work by Wang et al.[32] used the cationic surfactant to tune the ionic current rectification behaviour through a conical nanopore fabricated with track-etching technique. In a further refinement, Yameen et al.[33] used zwitterionic polymer brush to create finely tune the rectifying characteristics of the nanopores and to manipulate the mass and ion transport by simply varying the environmental pH.

2.2.3. Microfluidic Ionic Diodes

Microfluidics is defined as processing or manipulating small (10^{-9} to 10^{-18} litres) amounts of fluids, using channels with dimensions of tens to hundreds of micrometers.[34] Microfluidic devices are capable to meet the criteria of research areas and to integrate and automate many sample handling steps on a microfluidic chip. Microfluidic diode chips may allow precise control of ion transport in analytical systems for various wearable/implantable automated drug delivery, point-of-care diagnostics and energy conversion applications.[35]

Previously other groups have investigated ionic diode phenomena with nanochannels with different coatings and in nanopores that are conical in shape. Miller et al.[36] developed a simple ionic diode device uses a nanocapillary membranes (NCM) with uncoated symmetric channels to a microfluidic channel and a larger solution reservoir. The microfluidic channel also shows nonlinear I-V characteristic curves corresponding to the ionic diode phenomenon. The low current in the closed state of diode is due to formation of an ion depletion zone while the higher current is produced by an ion accumulation zone in the microchannel. In a further refinement, Wang et al.[37] described the method to control rectification ratio using NCM connected to microfluidic channel to fabricate a device with specific rectification factors. The rectification ratio is simply controlled by changing the

ratio of internal diameter between micropore and macropore that are connected to the opposite sides of a nanocapillary membrane.

Different approaches can be used to generate ion current rectification in microscale pores. Yusko et al.[38] introduced a simple method to achieve ion current rectification by electroosmotic-driven flow of liquids using solid-state nanopores to micropores with pores diameters ranging from 10 nm to 2.2 μm. This work demonstrated ionic current rectification in micropores with diameters 500 times larger than Debye length. Therefore, this method extends the concept of fluidic diodes to the micropore range. Qiu et al.[39] also reported the mechanism of ion current mechanism based on electroosmotically induced flow applicable to cylindrical pores with opening diameter between ~300 nm to a few micrometers. They described that current-voltage curves and rectification ratio from a single mesopore can be tuned with controlling via both viscosity and conductivity of solution on both sides of membrane. Their method provides opportunities to use viscosity as a parameter to tune current-voltage curves, rectification degrees, and electrokinetic flow of ions.

Chang et al.[40] developed a new, simple, and cheap ionic current rectification system based on the integration of a biconical microchannels, working electrode, and reference electrode. The modified biconical channel ranges with an outside diameter ranging from 60 to 120 μm can generate the ionic current rectification. Furthermore, the direction of rectification current can be reversed easily by changing the connection the electrodes and the electrochemical work station. He et al.[41] reported micrometer ionic current rectification in micropipette modified by polyelectrolyte brushes with controllable length by surface in situ atom transfer radical polymerization reaction. The critical parameters in polyelectrolyte-modified micropipette have been systematically investigated to observe and explain the generation of the micrometer ionic current rectification. In addition, Zhang et al.[42] fabricated novel ionic current devices based on dual nano- and micropipette and studied their ion transport behaviour electrochemically and theoretically. These simple ionic devices can be used to control ion flux within nanometer-sized and

micrometer-sized dual pipette. Their device also has promising applications in understanding the nano- and microfluidics in fabrication of novel nanodevices and design novel platforms for biomolecules sensing.

The highly charged materials can be patterned at the meso- and microscale opening a new avenue to create rectifying pores with different chemistries. Lin et al.[43] reported ion current rectification can occur in highly charged conical mesopores whose tip diameters are as large as 400 nm approximately 100-fold larger than electric double layer thickness. Ion current rectification resulted from high density of surface at basic conditions as well as the presence of highly mobile hydroxide ions, whose concentration is enhanced for one voltage polarity. Their work provides evidence that highly charged surfaces at mesopores can extend the ion current rectification to the submicron scale. This can lead to the potential use of highly charged large pores for energy and sensing applications. Recently, Lin et al.[44] presented conically shaped mesopore with tip opening diameter 400 nm is filled with high molecular poly-L-lysine to rectify ion current in high ionic strength of 1 M. They also demonstrated that a multipore membrane containing 10^6 pores per cm^2 with poly-L-lysine modified also rectify the current in KCl 1 M. They predicted about the possible application of the poly-L-lysine filled mesopores could be used salinity energy conversion in the future.

2.3. A Materials Approach for Ionic Rectification

Microporous materials have attracted attention in many practical fields such as electronics, energy/environmental, optics, and biotechnological applications. This is due to their regular pore structures which are useful for materials adsorption, storage, removal based on its enhanced surface area. According to IUPAC definition, microporous materials have dimension of pore sizes below 2 nm. Thin free-standing film of microporous materials can be prepared by solvent casting technique on polyethylene-terephthalate (PET) substrate for studies of ionic rectification effect. The key in order to get ionic rectification effect from microporous materials is asymmetric deposition of film onto PET substrate. The

microporous membrane materials have been used for ionic rectification studies will be described below.

2.3.1. Polymers of Intrinsic Microporosity (PIMs)

Most polymers have adequate conformational flexibility to allow to maximize intermolecular cohesive interactions and pack space efficiently. The packing efficiency of a polymer depends upon many factors including its properties in physical state (e.g. crystal, glass, liquid), molecular structure (e.g. flexibility, shape), and recent properties (heat treatment and swelling by solvent). Polymers of intrinsic microporosity (PIMs) are a class of polymer that have macromolecular structures designed to be both rigid and contorted so as to pack space very inefficiently.[45] PIMs attract great interest as a new generation of molecular sieving material because of good chemical stability, good solubility, processability, good thermal and excellent film-forming properties.[46]

A novel type of PIM that provides a highly rigid backbone with Ethanoanthracene - Tröger Base structure (PIM-EA-TB) (see Figure 2.5) has been introduced in 2013. This material with excellent microporosity properties and potential for gas separation applications was produced by poly-condensation. PIM-EA-TB (M_w = 70 kD; BET surface area ca. 1027 m^2g^{-1})[47] is a highly rigid polymer that has two interacting amine sites per repeat unit. The polymer is soluble in chloroform and can be easily cast into optically transparent films with good mechanical strength. PIM-EA-TB is a member of a wider class of PIM materials and may be regarded as mixed cation/anion conductors (due to absence of intrinsic charges). PIM-EA-TB has also demonstrated potential as a membrane for transport of cations and anions due to its intrinsic microporosity character. Madrid et al.[47] have shown that PIM-EA-TB acts as an ionic diode material (pH < 4) when it is deposited asymmetrically (one-sided deposition) onto a 20 µm diameter microhole in a polyethylene-terephthalate (PET) substrate.

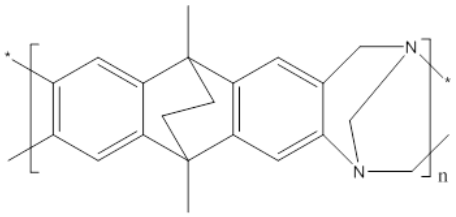

Figure 2.5. The molecular structure of PIM-EA-TB (B) a solvent-cast film (10 cm in diameter) of PIM-EA-TB.

The asymmetric PIM-EA-TB membrane geometry has been demonstrated to be appropriate for ionic diode effects and for the possible future applications such as desalination. It has been showed that pH of aqueous NaCl solution (or more generally the pK_A of the microporous material) is crucial in optimising the rectification ratio. The protonation of PIM-EA-TB (pK_{A1}) observed at pH 4 resulted in the best ionic diode effects. In the future, it would be possible to modify PIMs to generate better characteristics with higher pK_{A1}. It was predicted that a shift of 3 units of pK_{A1} to more neutral would be sufficient to allow for effective desalination in natural seawater. The proposed AC-based desalination application concept will give significant advantages by not having a direct electrolysis associated (only non-Faradaic charging currents at the AC-driven electrodes).

2.3.2. Nafion

Nafion ionomers were developed and produced by the DuPont Company. These materials are generated by copolymerization of a perfluorinated vinyl ether monomer with tetrafluoroethylene (TFE) resulting in chemical structure given in Figure 2.6A. It is well-known that Nafion® (CAS number 66796-30-3) has high proton conductivity and good mechanical, thermal and electrochemical stability.[48] Nafion self-assembles into a "channel structure" that allows cation transport through sulfonate-lined hydrophobic channels (see Figure 2.3B) within a hydrophobic matrix. The negatively charged channels allow permanent uptake and conduction of charged species, in particular cations.

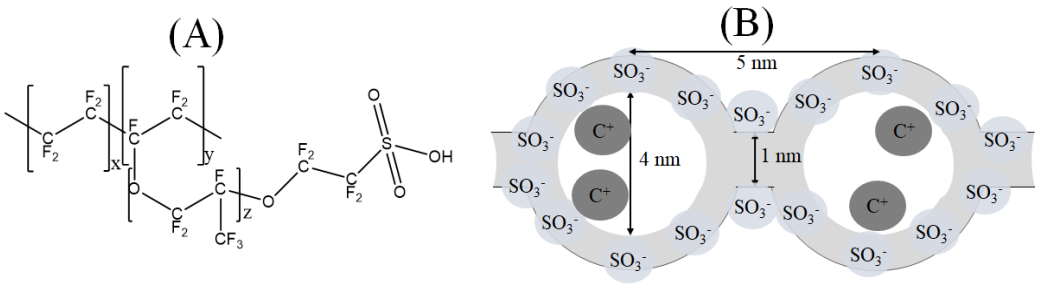

Figure 2.6. (A) Chemical structure of Nafion-117 and (B) schematic representation of cation (C^+) transport Nafion channel formed via self-assembly.

He et al.[49] investigated the behaviour of commercial Nafion 117 thin film can be used to induce ionic diode phenomena. When Nafion is applied as a thin film onto a microhole in a PET substrate, the diode characteristics appears only in asymmetric device compared to the symmetric case with Nafion applied to both sides of substrate. It has been shown that only asymmetric deposition results in current rectification or ionic diode phenomena. The physical reasons for rectification phenomena are associated with Nafion conductivity in the "open" diode state and with the concentration polarization (a diffusional transport overpotential due to a concentration gradient in the electrolyte) in the external electrolyte close to the PET microhole for the "closed" diode state. A cationic diode has been produced with effective rectification ratio for different types of cations. Smaller microholes (5 or 10 μm diameter) have been shown to produce effective ionic diode phenomena and are likely to allow switching times of faster diode.

2.3.3. Cellulose

Natural substances such as cellulose appears to offer very interesting properties to be used as an ionic diode materials. Cellulose possess negative surface charges due to carboxylate functional groups that allows cations to accumulate at the surface. Aaronson et al.[50] explored ionic diode behaviour from α-cellulose (Figure 2.7A) without further modification. They investigated an ionic diode behaviour for asymmetrically deposited cellulose film reconstituted from a mixture of ionic liquid and dimethyl sulfoxide (DMSO) (weight ratio 30:70) as solvent on PET support film with 20 μm diameter microhole. Removal of the solvent (DMSO/ionic liquid) is achieved by usage of anti-solvent such as ethanol or water

leaving a thin layer of reconstituted cellulose. The pore sizes of cellulose film can be adjusted by varying the anti-solvent concentration and also by the drying length time. They reported on ionic rectification effects for asymmetrically deposited α-cellulose membrane immersed in aqueous NaCl solutions and suggesting that membrane can be improved for the future water desalination material.

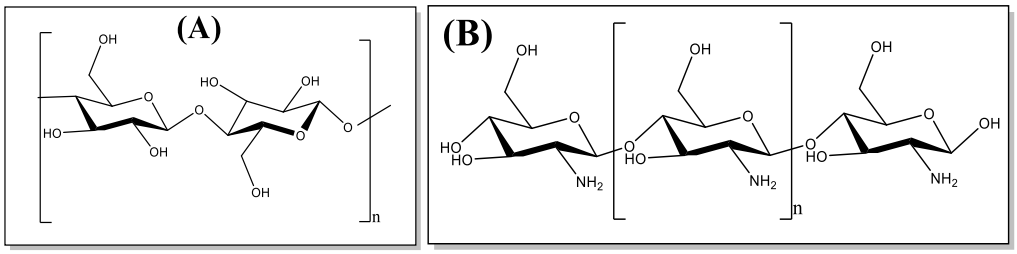

Figure 2.7. (A) Molecular structure of α-cellulose and (B) chitosan.

It is worth expanding the application of biomaterials in ionic process studies. Chemical modification or the insertion of materials into the films can alter the structural and surface characteristics of reconstituted cellulose films. Another work by Aaronson et al.[51] explored chitosan as a doping material for making of cellulose-chitosan composite materials. Chitosan offers an alternative biomaterial with amine functionalities (Figure 2.7B) to provide positive charges when the composite film is protonated. In conclusion, reconstituted α-cellulose films provide cationic diode due to predominant cation conductivity while chitosan-doped cellulose shows anionic diodes effects due to predominant anion conductivity. Chemical crosslinking between chitosan and cellulose will be required in order to keep the membrane stable in acidic pH range for future applications. Furthermore, the switching of diode currents induced by changing of surface charge is also important for signal amplification in sensing.

2.3.4. Metal Organic Frameworks (MOFs)

Metal organic frameworks (MOFs) especially their subclass zeolitic imidazolate frameworks (ZIFs) are compounds formed by the coordination of metal ions with organic ligands displaying porous structures in sub-nanometer size. ZIFs materials have attracted great attention due to its exceptionally stable in organic and alkaline media with applications in gas storage[52,53], photocatalysis[54], catalysis[55],

and biosensors.[56] Most applications of ZIFs are based on interaction between molecule and ZIFs materials within its sub-nanometer channels. Comprehensive understanding of mass transfer and permselectivity through the sub-nanometer channels will facilitate their future applications.

In 2016 Madrid et al.[57] directly grew ZIF-8 [Zn(2-methyl-imidazole)2] "plug" into a 20 μm diameter pore in a PET substrate. The ZIF-8 microporous materials will grow directly from aqueous solution at room temperature. The ZIF-8 materials growth was observed when placing open pore PET film between aqueous solutions of $Zn(NO_3)_2$ and 2-methylimidazole. Initially, the growth of ZIF-8 materials was rapid and after 24 hours the progress of growth more slowly. The most extended of film of ZIF-8 was formed on the zinc(II) solution side. The mechanism of ZIF-8 film due to slow access of 2-methylimidazone through PET film followed by the reaction at the Zn^{2+} side (Figure 2.8). The resulting of ZIF-8 plug has a diameter of about 20 μm. In conclusion, ion current rectification effects was observed through ZIF-8 plug in particular 10 mM ionic strength levels. The rectification effects is similar to that in regular of nanochannel materials although the charge-transporting mechanism was still unclear. Further study of quantitative and qualitative and analysis of phenomena associated with ion flow in ZIF-8 will be required.

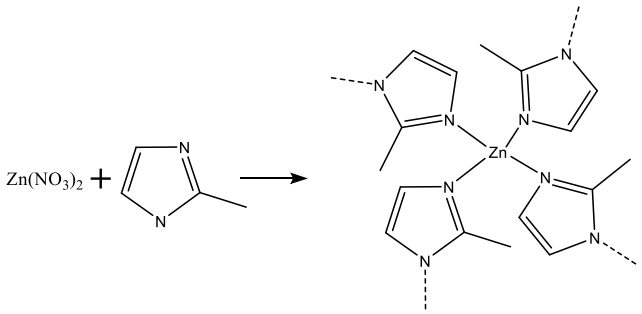

Figure 2.8. Reaction between $Zn(NO_3)_2$ with 2-methylimidazole to form zeolitic imidazolate frameworks (ZIF-8).

2.3.5. Commercial Ion-exchange Membranes

Commercial ionomer films are commonly used as a membrane materials, which are essential in many field of electrochemistry such as electrosynthesis[58],

electrodialysis[59], fuel cell[60], and in desalination[61] application. Recently, a wider range of ionomer film materials attached to a microhole PET substrate were shown to exhibit ionic rectification effects that contribute to ionic diode behaviour. Cationic diode phenomena were demonstrated using cation-conducting membranes for example in Nafion[49] and reconstituted cellulose[50] using solvent casting technique. Therefore, it is interesting to explore ion transport and rectification phenomena using a commercial cation-conducting membrane as a function of ionomer material and diode geometry. In contrast with solvent casting technique using ionomer material, more defined ionic diode geometries are feasible, for example by hot pressing ionomer film with specific thickness onto a PET substrate with microhole.

Tshwenya et al.[62] introduced hot-pressing as a technique for fabricating ionic diodes with defined geometric dimensions from commercial cation conducting film (Fumasep FKS-30) with PET substrates. The hot-pressing approach provides a better defined ionic diode geometries compared to the solvent casting ionomer solution onto the PET substrate. It has been shown that cationic diode effects are obtained at asymmetric structures based on Fumasep FKS-30 ionomer film onto to a PET substrate with a 20 μm diameter microhole. The ionic rectification effect was affected by many parameters such as electrolyte type and concentration, microhole diameter, and differences in electrolyte solution in left and right half-cells for cation transport. Further work will be required to improve rectification ratio value which are reported lower compared to those observed for Nafion. It will be interesting to explore the cation selectivity of cationic diode from Fumasep FKS-30 ionomer material. For future applications, the selective removal of both specific cation and anion could be possible with matching cationic diode and anionic diode on the basis of different types of ionomer materials.

2.3.6. Graphene Oxide

The discovery of graphene by Andre Geim and Konstantin Novoselov in 2004 marks the beginning of a new era in material sciences and inspired the scientific community to investigate the potential applications of this material

extensively. Graphene is commonly referred to as a sheet-like two dimensional (2D) material with sp^2 hybridized carbon atoms arranged in a hexagonal or honeycomb-like structure and its thickness is equal to an atom diameter.[63] The interaction of functional group on the graphene surface provides a novel opportunity for stacking the graphene layers in diverse arrangements. The interaction which is based on contribution from electrostatic forces, hydrogen bonding, and hydrophilic interactions provides a unique feature to prepare flexible free-standing films[64].

Films of graphene oxide also have appropriate porosity for the movement of small species such as ions or small molecules.[65] This is the reason that graphene oxide has been recently developed as an excellent membrane material for a wide range of applications such as molecular sieving[66], desalination[67], humidity sensing[68], and insulation.[69] Graphene oxide membrane has drawn significant attention due to its exceptional molecular sieving properties. The size of ion channel in graphene oxide membrane is typically 13.5 Å when immersed and laminates in water.[70] The size of ion channel can also be precisely controlled down depending on type on the hydrated ions.

Recently, a few papers have reported the excellent cation conducting properties of two dimensional materials in graphene oxide. Karim et al.[71] reported the proton conductivity of graphene oxide was nearly 10^{-2} S cm^{-1}. This result demonstrated the possibility of graphene oxide based on two dimensional proton conductive materials for fuel cell and sensor applications. Sun et al.[72] investigated the selective cations transport of alkali and alkali earth cations through graphene oxide membranes with counter chloride anion. They concluded that the selectivity transport toward different alkali and alkaline earth cations makes graphene oxide membrane a promising material in areas of membrane separations. Another work by Zhang et al.[73] demonstrates a methodology for manipulation of surface charge to control ion transport through graphene oxide membrane. The approach of tuning surface charges to control ion transport in graphene oxide membranes could be of

interest in a variety of applications such as water transport, studies of ion channels and biosensors, and energy conversions.

Two dimensional materials based on nanofluidic diode can also rectify the ionic current rectification in response with light radiation in different wavelength. Wang et al.[74] investigated ion transport based on graphene oxide can be reversibly and rapidly switching controlled by UV-Vis light radiation. These graphene oxide properties has provide new strategy to build smart materials for potential applications in energy, environment, sensing, and healthcare. Recently, Yang et al.[75] reported that active ion transport induced by light illumination through graphene oxide membranes with densely packed sub-nanometer wide lamellar channels. Following the mechanism, they further develop photonic ionic switches, photonic ion diodes, and photonic ion transistors as the fundamental elements for active ion sieving and artificial photosynthesis on synthetic nanofluidic circuits.

2.4. Potential Application of Ionic Rectification

Ionic current devices are emerging as a potential bridge between artificial and biological circuit and sensing systems. The design of ionic current devices has allowed the construction of complex devices by using charged nanostructures, forming ion depletion barriers, and manipulating insulating oxide layers. Ionic current devices with functionalities beyond basic rectification such as transistors, photovoltaic cells, and memristors are currently emerging as the next research frontier. Due to their ability to work in aqueous phase, ionic current devices could find a range of bio-related applications such as sensing, separation, and manipulation of biomolecules.

Ionic diodes are explored as sensing devices with ion transport. The sensing is mainly done by monitoring the transmembrane current changes caused by the variation of surface charge distribution and spatial dimensions during target sensing. By grafting different recognition molecules onto the inner surface of functionalized ionic diodes, the surface charge distribution will be modified due to the presence of the external physical stimuli, such as ions[76], molecules[77], light[78],

and temperature.[79] Siwy et al.[80] developed a prototype for protein sensing based on a conical gold nanochannel. The biosensing system was well evaluated by employing three groups of molecular-recognition agent (MRA/analyte, biotin/streptavidin, protein-G/immunoglobulin (IgG), and an antibody to ricin/ricin). Ali et al.[81] reported an alternative strategy that enables the facile functionalization of the inner channel walls by taking advantage of the existing functional groups to create streptavidin sensors. The positively charged biotinylated poly(allylamine) (PAH) could be easily grafted through electrostatic interaction with the negative carboxyl groups inside the nanochannel. The device could act as a simple and usable streptavidin sensor due to the special recognition between biotin and streptavidin.

The harvesting of solar energy is of current interest around the world. A number of artificial systems have been developed to mimic the light-harvesting functions. Meng et al.[82] has been developed by photovoltaic conversion system based on a conical PET nanochannel array. Zhang et al.[83] demonstrated a hydroenergy harvesting microfluidic generator (MFG) based on the formed porous channel along a patterned micropillar. Inspired by biological ion channel, Chun et al.[84] used nanopore membranes to convert the pressure into electric signals. In addition, Li et al.[85] reported a novel electrokinetic generator by coupling the capillary with water evaporation. The streaming currents are generated in the nanoporous alumina membrane across the fluidic channel when an electrolyte solution flows through it. Therefore, this device can harvest energy from waste heat, wind power, or solar energy.

The Gibbs free energy from mixing different concentrations, such as the salinity gradient between sea water and fresh water, is a huge potential energy source for clean energy production. Among the materials, the single nanopore has drawn much attention due its giant osmotic energy conversion. Siria et al.[86] fabricated a salinity gradient power harvesting device by inserting a boron nitride nanotube (BNNT) through a nanopore drilled in a SiN membrane. In addition, Guo et al.[87] constructed a concentration-gradient-power harvesting system based on an

asymmetric membrane with a single-ion-selective PET conical nanochannel. Furthermore, Feng et al.[88] predicted and estimated power density up 10^6 watts per square meter using a single-layer MoS_2 nanopore by minimizing the ion transport resistance through decreasing the channel length.

Zhang et al.[89] have developed a reverse electrodialysis system based on an anion-selective heterogeneous membrane composed of a porous block copolymer, polystyrene-*b*-poly(4-vinylpyridine), (PS-*b*-P4VP) membrane. A major improvement is the introduction of the particular asymmetric bipolar structure into the energy harvesting process. It is well known that the concentration polarization that widely exists in the traditional ion exchange membrane based reverse electrodialysis process seriously restricts the output power density. In their system, this unfavourable polarization effect can be eliminated by rational design of the channel structure and surface charge pattern. In the electrolyte testing conditions, the porous block copolymer channel was positively charged and the PET channel negatively charged, which formed an asymmetric bipolar structure.

Multipore membranes are also investigated for the salinity gradient power harvesting. Kim et al.[90] fabricated silica nanochannels to investigate the power generation with various combinations of concentrations. Their results indicated that energy conversion efficiency and ion selectivity increase with decreasing concentrations and channel height. They also used anodic alumina nanopores with a nominal pore radius of 10 nm for power generation. By employing self-assembling nanoparticles, Ouyang et al.[91] constructed nanoporous channels using nanofluidic crystal by bottom-up methods and obtained a mixiumum power density of 2.82 ± 0.22 W m^{-2}. Hwang et al.[92] used a mesoporous silica (MPS)-based nanofluidic energy harvesting system and obtained a power density of 2.39 W m^{-2} for NaCl.

2.5. Conclusion

The development of ionic current rectification in nano- and microscale is becoming a hot topic in the intersection of chemistry, physics, and life sciences. This unique phenomenon is important for fundamental studies of ion transport behaviour in solution and also have potential in analytical detection and energy harvesting applications. Currently, most of the fabrication of ionic diode devices requires complex process and their methods are not always fully understood. However, using a single well-defined microporous materials could provide an alternative method to prepare ionic diode devices. Therefore, there is a new opportunity for microporous materials to be developed and investigated to provide higher current, better rectification ratio and device performance for the applications.

The mechanism of ionic transport properties from different dimensional type of microporous materials needs to be systematically explored and investigated for the development of ionic diode devices. The understanding of ionic transport mechanism from each type of microporous materials is the key to develop the new type of ionic diode devices. The most stable and suitable of microporous materials is developed for prototype of water desalination in laboratory scale experimental setting.

2.6. References

1 Guttman, R. *J. Gen. Physiol.* **1944**. *28*, 43-51.

2 Reis, H. *J. Chem. Phys.* **1953**. *21*, 1209-1217.

3 Fuller, C.S. *Rec. Chem. Prog.* **1956**. *17*, 75-93.

4 Lovreček, B., Despic, A., Bockris, J. *J. Phys. Chem*. **1959**. *63*, 750-751.

5 Chun, H., Chung, T.D. *Annu. Rev. Anal. Chem*. **2015**. *8*, 441-462.

6 Xu, J., Lavan, D.A. *Nat. Nanotechnol*. **2008**. *3*, 666-670.

7 Cowan, S.W., Schirmer, T., Rummel, G., Steirt, M., Ghosh, R., Pauptit, R.A., Jansonius, J.N., Rosenbusch, J.P. *Nature*. **1992**. *358*, 727-733.

8 Huang, X., Kong, X.-Y., Wen, L., Jiang, L. *Adv. Funct. Mater*. **2018**. 1801079.

9 Alcaraz, A., Ramirez, P., Garcia-Gimenez, E., Lopez, M.L., Andrio, A., Aguilella, V.M. *J. Phys. Chem. B.* **2006**. *110*, 21205-21209.

10 Doyle, D.A., Cabral, J.M., Pfuetzner, R.A., Kuo, A., Gulbis, J.M., Cohen, S.L., Chait, B.T., MacKinnon, R. *Science*. **1998**. *280*, 5360, 69-77.

11 Tagliazucchi, M., Szleifer, I. *Mater. Today*. **2015**. *18*, 3, 131-142.

12 Daiguji, H. *Chem. Soc. Rev.* **2010**. *39*, 3, 901-911.

13 Cheng, L.-J., Guo, L.J. *Chem Soc. Rev.* **2010**. *39*, 923-938.

14 Wei, C., Bard, A.J., Feldberg, S.W. *Anal. Chem*. **1997**. *69*, 22, 4627-4633.

15 Kwon, H.J., Hong, S.K., Lee, M., Lim, G. *Lab on a Chip*. **2019**. *19*, 2958-2965.

16 Cheng, L-.J., Guo, L.J. *Nano Lett*. **2007**. *7*, 10, 3165-3171.

17 Nguyen, G., Vlassiouk, I., Siwy, Z.S. *Nanotechnology*. **2010**. *21*, 265301.

18 Gouaux, E., MacKinnon, R. *Science*. **2005**. *310*, 1461-1465.

19 Cervera, J., Ramirez, P, Gomez, V., Nasir, S., Ali, M., Ensinger, W., Stroeve, P., Mafe. *Appl. Phys. Lett*. **2016**. *108*, 253701-253705.

20 Nguyen, Q.H., Ali, M., Nasir, S., Ensinger, W. *Nanotechnology*. **2015**. *26*, 485502.

21 Zhang, Z., Kong, X.-Y., Xie, G., Li, P., Xiao, K., Wen, L., Jiang, L. *Sci. Adv.* **2016**. *2,* e1600689.

22 Siwy, Z.S., Kosinska, I.D., Fulinski, A., Martin, C.R. *Phys. Rev. Lett*. **2005**. *94*, 048301.

23 Siwy, Z.S. *Adv. Funct. Mater*. **2006**. *16*, 735-746.

24 Daiguji, H., Oka, Y., Shirono, K. *Nano Lett*. **2005**. *5*, 11, 2274-2280.

25 Karnik, R., Duan, C.H., Castelino, K., Daiguji, H., Majumdar, A. *Nano Lett.* **2006**. *6*, 1735-1740.

26 Yang, R., Liang, W., Fan, R., Yang, P. *Nano Lett*. **2009**. *9*, 3820-3825.

27 Cheng, L.-J., Guo, L. J. *ACS Nano*. **2009**. *3*, 3, 575-584.

28 Kovarik, M.L., Zhou, K., Jacobson, S.J. *J. Phys. Chem. B.* **2009**. *113*, 15960-15966.

29 Siwy, Z., Heins, E., Harrel, C.C., Kohli, P., Martin, C.R. *J. Am. Chem. Soc.* **2004**. *126*, 35, 10850-10851.

30 He, Y., Gillespie, D., Boda, D., Vlassiouk, I., Eisenberg, R.S., Siwy, Z.S. *J. Am. Chem. Soc.* **2009**. *131*, 5194-5202.

31 Ali, M., Yameen, B., Cervera, J., Ramirez, P., Neumann, R., Ensinger, W., Knoll, W., Azzaroni, O. *J. Am. Chem. Soc.* **2010**. *132*, 8338-8348.

32 Wang, L., Yang, Y., Xie, Y., Chen, L., Xue, J., Yan, S., Wang, Y. *Phys. Chem. Chem. Phys.* **2011**. *13*, 576-581.

33 Yameen, B., Ali, M., Neumann, R., Ensinger, W., Knoll, W., Azzaroni, O. *J. Am. Chem. Soc.* **2009**. *131*, 2070-2071.

34 Whitesides, G.M. *Nature*. **2006**. *442*, 368-378.

35 Sun, G., Senapati, S., Chang, H.-C. *Lab Chip*. **2016**. *16*, 1171-1177.

36 Miller, S.A., Kelly, K.C., Timperman, A.T. *Lab Chip*. **2008**. *8*, 1729-1732.

37 Wang, H., Nandigana, V.V.R., Jo, K.D., Aluru, N.R., Timperman, A.T. *Anal. Chem.* **2015**. *87*, 3589-3605.

38 Yusko, E.C., An, R., Mayer, M. *ACS Nano*. **2010**. *4*, 1, 477-487.

39 Qiu, Y., Lucas, R.A., Siwy, Z.S. *J. Phys. Chem. Lett*. **2017**. *8*, 3846-3852.

40 Chang, F., Chen, C., Xie, X., Chen, L., Li, M., Zhu, Z. *Chem. Commun*. **2015**. *51*, 15316-15319.

41 He, X., Zhang, K., Li, T., Jiang, Y., Yu, P., Mao, L. *J. Am. Chem. Soc.* **2017**. *139*, 1396-1399.

42 Zhang, S., Yin, X., Li, M., Zhang, X., Zhang, X., Qin, X., Zhu, Z., Yang, S., Shao, Y. *Anal. Chem.* **2018**. *90*, 8592-8599.

43 Lin, C.-H., Yeh, L.-H., Siwy, Z.S. *J. Phys. Chem. Lett.* **2018**. *9*, 393-398.

44 Lin, C.-Y., Combs, C., Su, Y.-S., Yeh, L.-H., Siwy, Z.S. *J. Am. Chem. Soc.* **2019**. *141*, 3691-3698.

45 McKeown, N.B. *ISRN Materials Science*. **2012**. Article ID 513986.

46 Madrid, E., McKeown, N.B. *Current Opinion in Electrochemistry*. **2018**. *10*, 61-66.

47 Madrid, E., Cottis, P., Rong Y., Rogers A.T., Stone, J.M., Malpass-Evans, R., Carta, M., McKeown, N.B., Marken, F. *J. Mater. Chem. A.* **2015**. *3*, 15849-15853.

48 Jung, H.-Y., Kim, J.W. *Int. J. Hydrog. Energy*. **2012**. *37*, 12580-12585.

49 He, D., Madrid, E., Aaronson, B., Fan, L., Doughty, J., Mathwig, K., Bond, A.M., McKeown, N.B., Marken, F. *ACS Appl. Mater. Interfaces.* **2017**, *9*, 11272-11278.

50 Aaronson, B.D.B., He, D., Madrid, E., Johns, M.A., Scott, J.L., Fan, L., Doughty, J., Kadowaki, M.A.S., Polikarpov, I., McKeown, N.B., Marken, F. *ChemistrySelect*. **2017**. *2*, 871-875.

51 Aaronson, B.D.B., Wigmore, D., Johns, M.A., Scott, J.L., Polikarpov, I., Marken, F. *Analyst*. **2017**. 142, 3707-3714.

52 Wu, H., Zhou, W., Yildrim, T. *J. Am. Chem. Soc.* **2007**. *129*, 17, 5314-5315.

53 Cheng, P., Hu, Y.H. *J. Phys.Chem. C.* **2014**. *118*, 38, 21866-21872.

54 Jing, H.P., Wang, C.-C., Zhang, Y.-W., Wang, P, Li., R. *RSC Advances*. **2014**. *4*, 54454-54462.

55 Jin, R., Bian, Z., Li, J., Ding, M., Gao, L. *Dalton Trans.* **2013**. *42*, 3936-3940.

56 Ma, W., Jiang, Q., Yu, P., Yang, L., Mao, L. *Anal. Chem.* **2013**. *85*, 15, 7550-7557.

57 Madrid, E., Buckingham, M.A., Stone, J.M., Rogers, A.T., Gee, W.J., Burrows, A.D., Raithby, P.R., Celorrio, V., Fermin, D.J., Marken, F. *Chem. Comm*. **2016**. *52*, 2792-2794.

58 Holade, Y., Servat, K, Tingry, S., Napporn, T.W., Remita, H., Cornu, D., Kokoh, B. *ChemPhysChem Rev.* **2017**. *18*, 2573-2605.

59 Zhang, H., Jiang, D., Zhang, B., Hong, J.G., Chen, Y. *Electrochim. Acta*. **2017**. *239*, 65-73.

60 Kusoglu, A., Weber, A.Z. *Chem. Rev.* **2017**. *117*, 3, 987-1104.

61 Geise, G.M., Raul, D.R., Freeman, B.D. *Prog. Plym. Sci.* **2014**. *39*, 1, 1-42.

62 Tshwenya, L., Arotiba, O., Putra, B.R., Madrid, E., Mathwig, K., Marken, F. *J. Electroanal. Chem*. **2018**. *815*, 114-122.

63 Joshi, R.K., Alwarappan, S., Yoshimura, M., Sahajwalla, V., Nishina, Y. *Appl. Mater. Today*. **2015**. *1*, 1-12.

64 Eftekhari, A., Shulga, Y.M., Baskakov, S.A., Gutsev, G.L. *Int. J. Hydrogen Energy*. **2018**. *43*, 2307-2326.

65 Chen, C., Yang, Q.-H., Yang, Y., Lv, W., Wen, Y., Hou, P.-X., Wang, M., Cheng, H.-M., *Adv. Mater*. **2009**. *21*, 3007-3011.

66 Mi, B. *Science*. **2014**. *343*. 740-742.

67 Cohen-Tanugi, D., Grossman, J.C. *Nano Lett.* **2012**. *12*, 3602-3608.

68 Borini, S., White, R., Wei, D., Astley, M., Haque, S., Spigone, E., Harris, N., Kivioja, J., Ryhänen, T. *ACS Nano.* **2013**. *7*, 12, 11166-11173.

69 Tuan, D.V., Kumar, A., Roche, S., Ortmann, F., Thorpe, M.F., Ordejon, P. *Phys. Rev. B.* **2018**. *86*, 121408(R).

70 Abraham, J., Vasu, K.S., Williams, C.D., Gopinadhan, K., Su, Y., Cherian, C.T., Dix, J., Prestat, E., Haigh, S.J., Grigorieva, I.V., Carbone, P., Geim, A.K., Nair, R.R. *Nat. Nanotechnology*. **2017**. *12*, 546-550.

71 Karim, M.R., Hatakeyama, K., Matsui, T., Takehira, H., Taniguchi, T., Koinuma, M., Matsumoto, Y., Akutagawa, T., Nakamura, T., Noro, S.-I., Yamada, T., Kitagawa, H., Hayami, S. *J. Am. Chem. Soc.* **2013**. *135*, 22, 8097-8100.

72 Sun, P., Zheng, F., Zhu, M., Song, Z., Wang, K., Zhong, M., Wu, D., Little, R.B., Xu, Z., Zhu, H. *ACS Nano*. **2014**. *8*, 1, 850-859.

73 Zhang, M., Guan, K., Ji, Y., Liu, G., Jin, W., Xu, N. *Nat. Commun.* **2019**. *10*, 1253.

74 Wang, L., feng, Y., Zhou, Y., Jia, M., Wang, G., Guo, W., Jiang, L. *Chem. Sci*. **2017**. *8*, 4381-4386.

75 Yang, J., Hu, X., Kong, X., Jia, P., ji, D., Quan, D., Wang, L., Wen, Q., Lu, D., Wu, J., Jiang, L., Guo, W. *Nat. Commun*. **2019**. *10*, 1171.

76 Lu, Q., Tang, Q., Chen, Z., Zhao, S., Qing, G., Sun, T. *ACS Appl. Mater. Interfaces*. **2017**. *9*, 38, 32554-32564.

77 Zhang, F., Sun, Y., Tian, D., Li, H. *Angew. Chem. Int. Ed.* **2017**. *56*, 7186-7190.

78 Sun, Y., Ma, J., Zhang, F. Zhu, F., Mei, Y., Liu, L., Tian, D., Li, H. *Nat. Commun*. **2017**. *8*, 260.

79 Wang, R., Sun, Y., Zhang, F., Song, M., Tian, D., Li, H. *Angew. Chem. Int. Ed.* **2017**. *56*, 5294-5298.

80 Siwy, Z., Trofin, L., Kohli, P., Baker, L.A., Trautmann, C., Martin, C.R. *J. Am. Chem. Soc.* **2005**. *127*, 5000-5001.

81 Ali, M., Yameen, B., Neumann, R., Ensinger, W., Knoll, W., Azzaroni, O. *J. Am. Chem. Soc.* **2008**. *130*, 16351-16357.

82 Meng, Z., Bao, H., Wang, J., Jiang, C., Zhang, M., Zhai, J., Jiang, L. *Adv. Mater*. **2014**. *26*, 2329-2334.

83 Zhang, R., Wang, S., Yeh, M.-H., Pan, C., Lin, L., Yu, R., Zhang, Y., Zheng, L., Jiao, Z., Wang, Z.L. *Adv. Mater.* **2015**. *27*, 6482-6487.

84 Chun, K.-Y., Son, Y.J., Han, C.-S. *ACS Nano*. **2016**. *10*, 4550-4558.

85 Li, C. Liu, K., Liu, H., Yang, B., Hu, X. *Mater. Res. Bull*. **2017**. *90*, 81-86.

86 Siria, A., Poncharal, P., Biance, A.-L., Fulcrand, R., Blasé, X., Purcell, S.T., Bocquet, L. *Nature*. **2013**. *494*, 455-458.

87 Guo, W., Cao, L., Nie, F.-Q., Ma, W., Xue, J., Song, Y., Zhu, D., Wang, Jiang, L. *Adv. Funct. Mater*. **2010**. *20*, 8, 1339-1344.

88 Feng, J., Graf, M., Ovchinnikov, D., Dumcenco, D., Heiranian, M., Nandigana, V., Aluru, N.R., Kis, A., Radenovic, A. *Nature*. **2016**. *536*, 197-200.

89 Zhang, Z., Kong, X.-Y., Xiao, K., Liu, Q., Xie, G., Li, P., Ma, J., Tian, Y., Wen, L., Jiang, L. *J. Am. Chem. Soc.* **2015**. *137*, 14765-14772.

90 Kim, D.-K, Duan, C., Chen, Y.-F., Majumdar, A. *Microfluid. Nanofluid*. **2010**, *9*, 1215-1224.

91 Ouyang, W., Wang, W., Zhang, H., Wu, W., Li, Z. *Nanotechnology*. **2013**. *24*, 345401.

92 Hwang, J., Kataoka, S., Endo, A., Daiguji, H. *Lab on a Chip*. **2016**. *16*, 2824-3832.

Chapter 3

Introduction to Electrochemical Techniques

Contents

Chapter Abstract

This chapter mainly introduces the fundamental concepts behind the electrochemical processes and electrochemical techniques including electrode dynamics and electrochemical methods. The discussion about electrode dynamics covers thermodynamics and kinetics of electrochemical reaction. In the thermodynamics section the Nernst equation and electron transfer at the electrode are introduced following the Fermi level energy. In the kinetics section the rate of electron transfer and the link from potential to the Gibbs free energy are explained in order to obtain the Butler Volmer equation. The basic components of electrochemistry experiments are introduced including the use of one-, two-, three, and four-electrode electrochemical systems. Electrochemical methods including cyclic voltammetry, chronoamperometry, and electrochemical impedance spectroscopy (which are used in this thesis) are introduced in this chapter. In this thesis the electrochemical experiments were performed mostly using microhole substrates covered with microporous membrane materials. It is therefore interesting to describe the microelectrode effect, which is similar to the steady state phenomena observed for ionic diodes in the microhole substrates.

3.1. Thermodynamics of Electrochemical Reaction.

Electrochemistry is a powerful tool to probe reactions involving electron transfers and to relate the flow of electrons to chemical changes. Electrochemistry usually deals with chemical reactions that occur at the surface between a conducting electrode and the electrolyte solution. The kinetic and thermodynamic information provide two important aspects in the understanding of electrochemical reactions. Kinetics defines at what speed the reaction happens, while thermodynamics dictates the direction of the reaction and to what extent the reaction will proceed. In electrochemistry, the magnitude of the current often also reflects the rate of the reaction. Several factors may affect the electrochemical reactions, including the species reactivity, the nature of the electrode, the electrode potential, the solution composition, and the mass transport. The detailed information of the electrochemical reactions can be provided by the various of electrochemical techniques.

Thermodynamics describes whether a reaction can occur or not in the equilibrium process achieved between oxidised species Ox and reduced species Red (Equation 3.1). When a suitable electrode is inserted into the solution containing both oxidized and reduced species, the equilibrium condition can be achieved quickly with the fast electron transfer rates between the electrode and the solution. Oxidised species can be reduced at the electrode or reduced species become oxidised. Once the equilibrium is obtained at the surface of the electrode, the rates of oxidation and reduction are exactly the same and thus zero current is obtained.

$$Ox + ne^{-} \rightleftharpoons Red \tag{3.1}$$

During the equilibrium condition, there is a transfer of charged species and electrons linked to the flow of internal current. As a result, there is a net electrical charge between the two phases, the metal electrode and the solution creating a potential difference between two phases (metallic and solution) $(\emptyset_m - \emptyset_{aq})$ which is called electrode potential. This potential has a fixed and precise value and can be measured by introducing a reference electrode to the electrochemical cell. Under

equilibrium conditions, the potential of electrode can be calculated by the Nernst equation described in Equation 3.2.

$$E_{eq} = E^0 + \frac{RT}{nF} \ln \left(\frac{a_{Ox}}{a_{Red}} \right) \quad (3.2)$$

Here, E^o is the standard electrode potential, R is the universal gas constant (8.314 J K^{-1} mol^{-1}), T is the Kelvin temperature, n is the number of electrons transferred, a_{Ox} is the activity of oxidised species, and a_{Red} is the activity of reduced species. The activity of a species dissolved in a solution is proportional to its concentration (equation 3.3). Therefore, the Nernst equation can be expressed in terms of concentration (equation 3.4).

$$a_A = \gamma_A [A] \quad (3.3)$$

$$E_{eq} = E^{o\prime} + \frac{RT}{nF} ln \left(\frac{[Ox]_{bulk}}{[Red]_{bulk}} \right) \quad (3.4)$$

$$\text{with } E^{o\prime} = E^o + \frac{RT}{nF} ln \left(\frac{\gamma_{Ox}}{\gamma_{Red}} \right)$$

Here, γ is the activity coefficient, A is the electrode area (cm^2), $E^{o'}$ is termed formal potential and [Ox]/[Red] is the concentration of oxidized and reduced species at the electrode surface respectively, which are the same as in the bulk solution under equilibrium conditions.

Electron Transfer. The spontaneous electron transfer occurs due to relative energy levels between Fermi level with the electroactive species at the electrode surface. In order to obtain spontaneous electron transfer to occur at the electrode surface, Gibbs free energy must be negative ($\Delta G < 0$) for any electrochemical redox system. ΔG is associated with the cell potential E_{eq} via Equation 3.5.

$$\Delta G = -nFE_{eq} \quad (3.5)$$

The Fermi level energy is minimum thermodynamic work required to add one electron to the electrode. Figure 3.1 illustrates a simple model for how Fermi level (E_F) is affected by potential bias resulting oxidation or reduction of analyte. When the negative potential bias is applied to the electrode, the Fermi level of the electrode is raised above the energy of the lowest unoccupied molecular orbital (LUMO) of analyte and promoting reduction of electroactive species at the electrode surface. In the opposite, under a positive potential bias the Fermi level of the electrode is lowered below the highest occupied molecular orbital (HOMO) of analyte and resulting oxidation of electroactive species at the electrode surface. Therefore, the application of potential to the electrode will change the concentration ratio of oxidised and reduced species in the bulk solution.

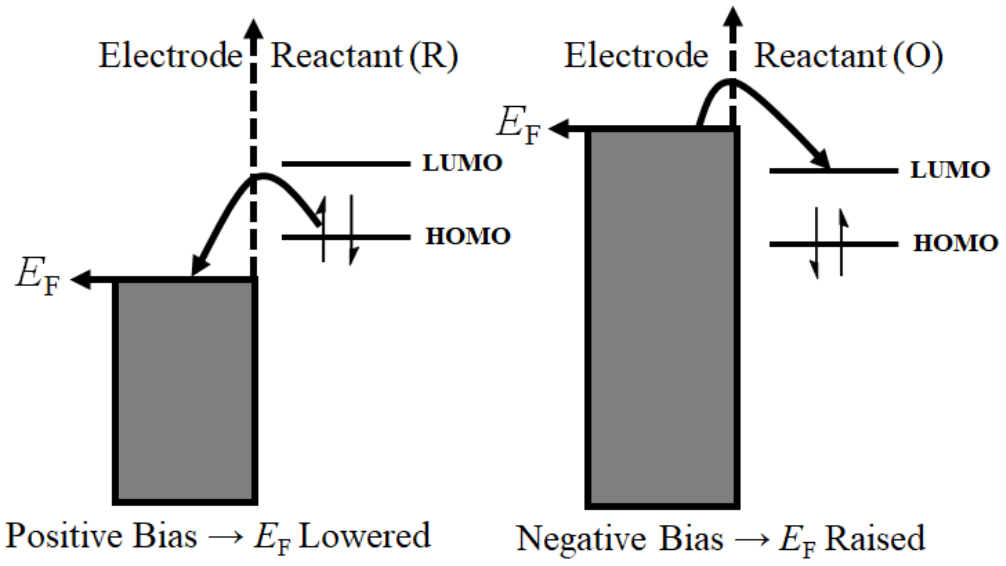

Figure 3.1. Illustration of electron transfer at the electrode surface when a) positive potential bias applied causes E_F lowered than HOMO resulting in analyte oxidation and b) negative potential bias applied causes E_F higher than LUMO resulting in analyte reduction.

3.2. Kinetics of Electrochemical Reaction

The theory of electrode kinetics aims to provide an understanding of the rate of electron transfer in electrochemical reactions. Electron transfer is only one type of rate limiting physical process in electrochemical reactions. There are generally five steps that contribute to the overall kinetics of electrochemical kinetics. First,

reactants O diffuse to the electrode by mass transport. Second, reactants R adsorb onto the electrode surface. Third, the transfer of electrons occurs between the electron and reactant O, giving product R. Fourth, the product R desorbs from the electrode surface. Fifth, the product R diffuses away from the electrode surface by mass transport. A simplistic mechanism for electron transfer process at an electrode surface is illustrated in Figure 3.2.

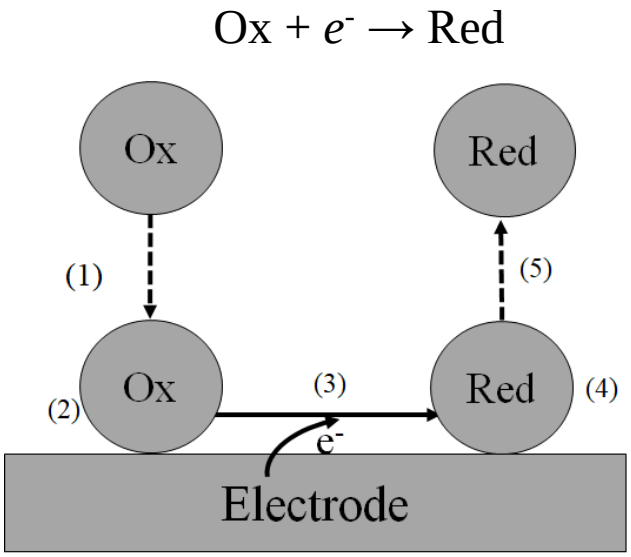

Figure 3.2. Graphical illustration of electron transfer process at an electrode surface simplified to five steps 1) reactant Ox diffuse to the electrode, 2) adsorption of reactant Ox onto the electrode surface, 3) transfer of an electron to reactant Ox, giving product Red, 4) desorption of product Red, and 5) the transport of product R away to the bulk by mass transport.

The overall kinetics reaction rate will generally be limited by the slowest step. In a fast electron transfer reaction, mass transport may be dominating the effective reaction. Mass transport is the movement of material from one location in solution to another, arises either from differences in electrical or chemical potential at the two locations or from movement of a volume element of solution. The mechanism for mass transport are:

1. **Migration**: movement of charged body along an electrical field (for example the charge is carried through the solution by ions according to their transference number)

2. **Diffusion**: the spontaneous movement of a species under the influence of a gradient of concentration (for example from regions of high concentration to regions of lower concentration), aimed to minimize concentration differences.
3. **Convection/stirring or hydrodynamic transport**: this mode of transport is driven by physical movement such as fluid flow and occurs with stirring or flow of the solution and with rotation or vibration of the electrode (forced convection) or due to density gradients (natural convection).

3.2.1. The Rate of Electron Transfer

A redox electrochemical reaction consists of an oxidation and a reduction process. A simple case in the reduction process, oxidised species (Ox) in solution can be reduced into reduced species (Red) by accepting an electron with the rate constants k_{red}. The Ox ions also can be oxidised to Red by removing an electron with rate constant k_{ox} and established with respect of species concentration in Equation 3.6.

$$\mathrm{Ox} + e^- \underset{k_{ox}}{\overset{k_{red}}{\rightleftharpoons}} \mathrm{Red} \qquad (3.6)$$

Here k_{ox} and k_{red} are the first-order rate constants for reduction of Ox (forward) and oxidation of Red (backward) in electron transfer reactions. When a potential bias is applied to the electrode, the electrolysis becomes thermodynamically feasible[1]and the current I will flow due to oxidation of Red or reduction of Ox processes. The magnitude of current for a first order reaction correspond to electrode area (cm^2), Faraday constant F (96485 C mol^{-1}) and flux J of the reactant reaching to the electrode surface area (moles cm^2 s^{-1}) described by Equation 3.7.

$$I = AFJ \qquad (3.7)$$

The flux, J, is quantity of species reacting in the electrode area per second and dependent on the concentration of reactant at the electrode surface. This flux

also can describe as the rate of electrochemical reaction. For the first order reduction of Ox into Red, the flux of Ox to the electrode surface can be described by Equation 3.8.

$$J = k_0[Red]_0 \tag{3.8}$$

Where k_0 is the rate constant for the electron transfer reaction and $[Ox]_0$ is the concentration of reactant at the electrode surface. The magnitude of current can be described as the concentration of species at the electrode surface as Equation 3.9.

$$I = k_0 AF[Ox]_0 \tag{3.9}$$

By combining Equation 3.8 and 3.9, the current for oxidation (anodic) (Equation 3.10) and reduction (cathodic) (Equation 3.11) can be given by the concentration of Ox and Red species as:

$$I_{ox} = FAk_{ox}[Red]_o \tag{3.10}$$

$$I_{red} = -FAk_{red}[Ox]_o \tag{3.11}$$

Here, $k_{ox}[Red]_o$ and $k_{red}[Ox]_o$ correspond to the flux of species Red and Ox to/from the electrode surface, respectively. Therefore, the total current i_{total} is the sum of the anodic and cathodic currents (Equation 3.12 and 3.13):

$$I = I_{ox} + I_{red} \tag{3.12}$$

$$I_{total} = FA(k_{ox}[Red]_o - k_{red}[Ox]_o) \tag{3.13}$$

In order to describe the electron transfer reactions, it is rational to use transition state model[2] in Figure 3.3. This model shows the reaction involves the reactants $[Ox_{(aq)} + e^-_{(m)}]$ need to overcome an energy barrier via a transition state with free energy $G^{\ddagger}$ before becoming product $Red_{(aq)}$.

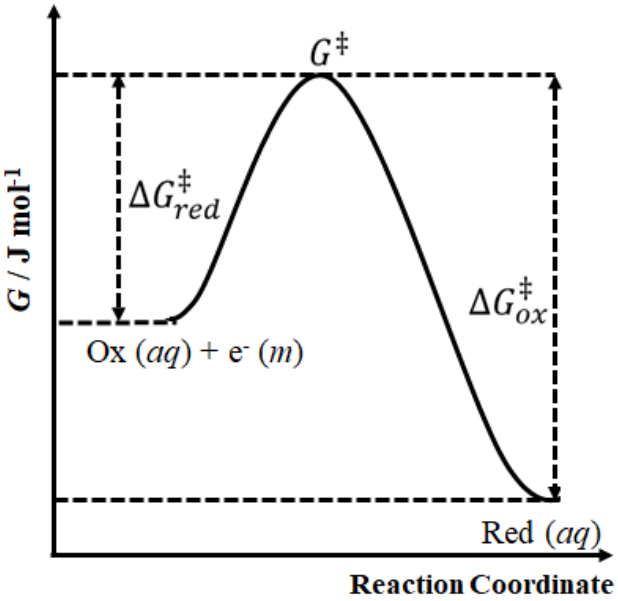

Figure 3.3. Free energy plot for the one electron reduction from O to R, showing the free energy activation of O reduction $\Delta G^{\ddagger}_{red}$ and R oxidation $\Delta G^{\ddagger}_{ox}$ reactions. $\Delta G^{\ddagger}$ represents the free energy of the transition.

The rate of reduction reaction (k_{red}) can be explained in terms of $\Delta G^{\ddagger}_{red}$ as in Equation 3.14.

$$k_{red} = Aexp\left(\frac{-\Delta G^{\ddagger}_{red}}{RT}\right) \tag{3.14}$$

$\Delta G^{\ddagger}_{red}$ is the free energy of activation and A is a frequency factor accounts for the rate of effective collisions of molecule at the electrode surface. For a constant temperature and pressure, the free energy change between the reactants [$O_{(aq)}$ + $e^{-}_{(m)}$] and the transition state $\Delta G^{\ddagger}_{red}$ is given for the reduction ΔG_{red} in Equation 3.15. While the free energy change of oxidation ΔG_{ox} is given by the difference between the free energy of products $R_{(aq)}$ and the transition state in Equation 3.16.

$$\Delta G^{\ddagger}_{red} = G^{\ddagger} - G_{ox} \tag{3.15}$$

$$\Delta G^{\ddagger}_{ox} = G^{\ddagger} - G_{red} \tag{3.16}$$

3.2.2. The Effect of Potential

Previously in Equation 3.16, Gibbs free energy for a one-electron reduction (Ox + e^- → Red) can be written in terms of potential E, corresponding only one electron transfer at the electrode surface. A change in free energy ΔG can be given as a function of the change in potential ΔE where $\Delta E = E\text{-}E^0$ in Equation 3.17.

$$\Delta G = -F(E - E^0) \tag{3.17}$$

The total Gibbs free energy for the reactants G can be described as the sum of the standard Gibbs free energy of the reactants G^0 with the change in potential (Equation 3.19).

$$G = G^0 + \Delta G \tag{3.18}$$

$$G = G^0 - F(E - E^0) \tag{3.19}$$

The curve below on the O + e^- side applies when the electrode potential is equal to E^0. The cathodic and anodic activation energies are $\Delta G^{\ddagger}_{0red}$ and $\Delta G^{\ddagger}_{0ox}$ respectively. If the potential is changed by ΔE to a new value, the relative energy of the electron changes by $-F\Delta E = -F(E - E^0)$, then the O + e^- moves up or down by that amount. The lower curve on the Figure 3.4 (A) shows this effect for a positive ΔE. It is obvious that the barrier for oxidation $\Delta G^{\ddagger}_{ox}$ has become less than $\Delta G^{\ddagger}_{0ox}$ by a fraction of the total energy change.

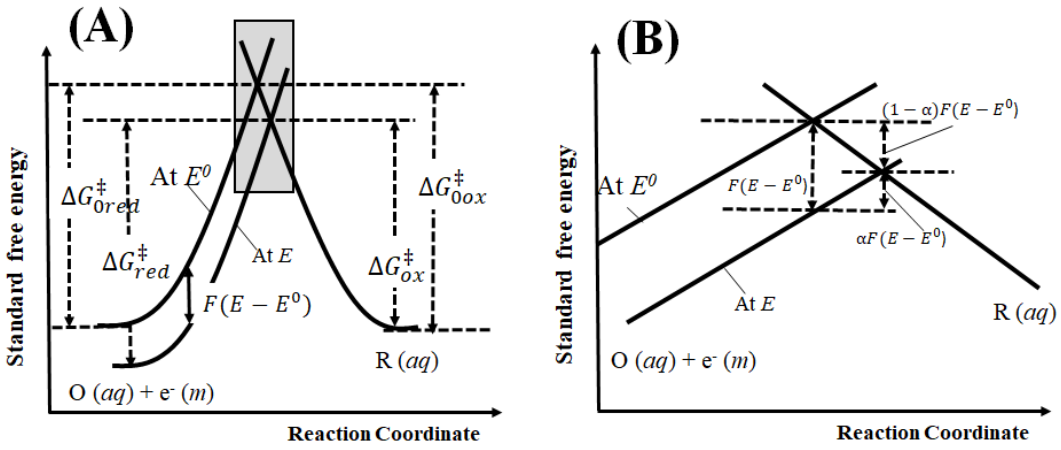

Figure 3.4. Effect of a potential change on standard free energies of activation for oxidation and reduction and (B) the magnified picture of the boxed area in the upper frame.

Equations for $\Delta G^{\ddagger}_{ox}$ and $\Delta G^{\ddagger}_{red}$ can be described in terms of potential. For the anodic process, the free energy of transition state $\Delta G^{\ddagger}_{ox}$ can be described according to Equation 3.20. For the cathodic process, the free energy of transition state $\Delta G^{\ddagger}_{red}$ can be described according to Equation 3.21. The α in Figure 3.4 B has a value between 0 and 1 and reflects to the transition state resembles to the products or reactants more closely. If α close to 0, the transition state resembles to the reactants (Ox + e$^-$) while if α close to 1, the transition state close to the product Red.

$$\Delta G^{\ddagger}_{ox} = \Delta G^{\ddagger}_{0ox} - ((1-\alpha)F(E-E^0) \tag{3.20}$$

$$\Delta G^{\ddagger}_{red} = \Delta G^{\ddagger}_{0red} + \alpha F(E-E^0) \tag{3.21}$$

Equation 3.20 can be finally substituted into Equation 3.13. This equation describes the relationship between rate constant for the oxidation reaction k_{ox} and $\Delta G^{\ddagger}_{ox}$ (Equation 3.22) and similarly for the rate of reduction k_{red} (Equation 3.23).

$$k_{ox} = A_{ox} exp\left(\left(\frac{-\Delta G^{\ddagger}_{ox}}{RT}\right) exp\left(\frac{(1-\alpha)F(E-E^0)}{RT}\right)\right) \tag{3.22}$$

$$k_{red} = A_{red} exp\left(\left(\frac{-\Delta G^{\neq}_{red}}{RT}\right) exp\left(\frac{-\alpha F(E-E^0)}{RT}\right)\right) \tag{3.23}$$

In equilibrium condition, we can assume that concentration in bulk solution of oxidised species $[Ox]_{bulk}$ and reduced species $[Red]_{bulk}$ are similar. Then, $E = E^0$ and $k_{red}[Ox]_{bulk} = k_{ox}[Red]_{bulk}$ so that $k_{red} = k_{ox}$. Thus, E^0 is the potential where the oxidised and reduced rate constants have the same value. The value is called the standard rate constant, k^o, which is independent of potential. Therefore, the rate constant for oxidation and reduction can be simplify into equation 3.24 and equation 3.25.

$$k_{ox} = k^o exp\left(\frac{(1-\alpha)F(E-E^0)}{RT}\right) \quad (3.24)$$

$$k_{red} = k^o exp\left(\frac{-\alpha F(E-E^0)}{RT}\right) \quad (3.25)$$

3.3.3. The Butler-Volmer Equation

The insertion of Equation 3.24 and Equation 3.25 into Equation 3.12 yields to the current-potential characteristics or the Butler-Volmer equation. The substitution of k_{ox} and k_{red} into Equation 3.13 results in an equation for total current due to anodic and cathodic reactions i_{total} (Equation 3.26). Equation 3.26 can be used to determine the current due to anodic or cathodic process at equilibrium, called as the exchange current i^0. i^0 due to anodic and cathodic reactions is given by Equation 3.27 and 3.28, respectively.

$$I_{total} = FAk^o\left([Red]_o exp\left\{(1-\alpha)(E-E^o)\frac{F}{RT}\right\} - [Ox]_o exp\left\{-\alpha(E-E^o)\frac{F}{RT}\right\}\right) \quad (3.26)$$

$$\text{Anodic} : I_{ox} = FAk^0[Red]_0 exp\left\{(1-\alpha)(E-E^0)\frac{F}{RT}\right\} \quad (3.27)$$

$$\text{Cathodic} : I_{red} = -FAk^0[Ox]_0 exp\left\{-\alpha(E-E^0)\frac{F}{RT}\right\} \quad (3.28)$$

Butler-Volmer equation is an important equation to show how net current in the electrochemical system changes with electrode potential. If k^o is large, very little or zero overpotential is needed to induce the electrochemical reaction. However, for the process that have a small value of k^o, a high overpotential is necessary to drive the electron transfer, which indicates an electrochemically irreversible system. This constitutes the classic treatment of electron transfer across

metal | solution interface. In this report (and in contrast to the case of electron transfer) the transfer of ions across an ion conductor | solution interface is investigated. The rate of ion transfer can be generally assumed to be very high (diffusion limited) and there is currently no experimental evidence for the interfacial charge transfer to limit the rate of processes.

3.3. Electrochemical Cells

Electrochemical measurements are made in an electrochemical cell consisting of two or more electrodes and associated electronics for controlling and measuring the current and potential. Here, the basic components of electrochemical cell are introduced.

First, the **Working Electrode** (WE) is the electrode in an electrochemical system on which the electrochemical reaction (reduction or oxidation) being investigated is taking place. Working electrodes can be made of inert materials such as Au, Ag, Pt, glassy carbon (GC), Hg drop, and Hg film electrodes. The size and shape of the working electrode varies and depending on the application.

Second, the **Reference Electrode** (RE) is an electrode, which has a stable and well-known electrode potential and is used as a point of reference in the electrochemical cell for the potential control and measurement. Reference electrodes commonly used are silver-silver chloride electrode (Ag/AgCl/KCl) or the calomel electrode ($Hg/Hg_2Cl_2/KCl$). The high stability of the reference electrode potential is usually reached by employing a redox system with constant (buffered or saturated) concentrations.

Third, the **Counter Electrode** (CE) (or auxiliary electrode) serves to complete the electric circuit. The counter electrode is usually made of an inert material (e.g. Pt, Au, graphite, glassy carbon) and usually it does not participate in the electrochemical reaction. Because the current is flowing between the working electrode and counter electrode, the total surface area of the counter electrode

(source/sink of electrons) should be higher than the area of the working electrode so that it will not be a limiting factor when driving the process under investigation.

There are different electrochemical cell configurations depending on the type of measurement that is required. Most work on the classic electron transfer processes is carried out with three-electrode cell systems. Next, the different cell configurations are described in more detail.

The one-electrode electrochemical cell. When immersing an electrode into an electrolyte solution, a potential develops at the interface between electrode and solution. This causes the exchange of some electrons, but the total amount of charge transferred is usually very low and therefore not practical. The electrode when equilibrated takes on a defined potential (in the presence of a redox system) which can be expressed in the Nernst equation in 3.2. The Nernst equation provides a powerful way to predict how a system will respond to a change of activity/concentration of species in solution or a change in the electrode potential.

The two-electrode electrochemical cell. The simplest electrochemical cell uses two electrodes immersed into the electrolyte system. In a two-electrode cell configuration, CE and RE are shorted on one of the electrodes while the WE and sense electrode are shorted to provide the opposite electrode (see Figure 3.5). The potential across the complete cell is measured. This includes contributions from the CE/electrolyte interface and electrolyte itself. The two-electrode configuration can therefore be used whenever precise control of the interfacial potential is not critical and only the behaviour of the whole cell is under investigation. This configuration is typically used with energy storage or conversion devices like batteries, fuel cells, photovoltaic panels, etc. It is also used in measurements of ultrafast dynamic of electrode processes or electrochemical impedance measurements at high frequencies (>100 kHz). Most practical applications of electrochemistry are based on two electrodes, anode and cathode, immersed in electrolyte media. In this case a current can be measured, but the potential on individual electrodes is not known. Only the total potential across the two electrodes can be measured.

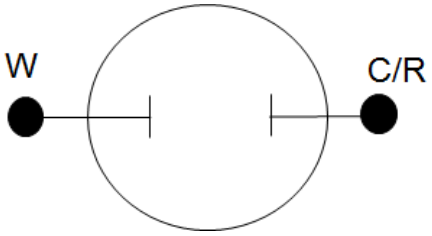

Figure 3.5. Schematic view of the 2-electrode configuration.

The three-electrode electrochemical cell. By introducing a reference electrode and a counter electrode, the potential at the working electrode can be defined as well as the current measured. This classical cell configuration is employed to study electrochemical reactions at many types of working electrodes. The three-electrode cell configuration is the most common electrochemical cell configuration used in electrochemistry (see Figure 3.6). In this case, the current flows from the counter electrode (CE) to the working electrode (WE). The potential difference is controlled between the WE and the CE and measured between RE (kept at close proximity of the WE) and Sense (S). Because the WE is connected with S and WE is kept at fixed and stable potential by controlling the polarization of the CE, the potential difference between RE and WE is controlled all the time. The potential between the CE and WE usually is not measured. This configuration allows the potential across the electrochemical interface at the WE to be controlled with the respect to the RE.

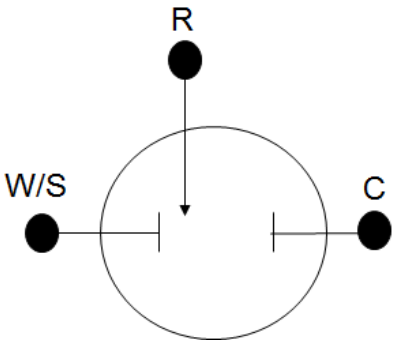

Figure 3.6. Schematic view of the 3-electrode configuration.

The four-electrode electrochemical cell. When applying a potential to a free-standing membrane in between two half-cells, a new configuration is needed. Now the potential across the membrane and the current need to be measured, and therefore the working electrode is replaced by a sense and a current feeding electrode. Figure 3.7 shows that in this case two metal electrodes (e.g. platinum wire) and two reference electrodes (e.g. SCE) are placed in opposite sides of the electrochemical cell. This configuration is needed for ionic diode studies. The four-electrode system is used to measure potential and current at the interfaces between two membranes or non-miscible liquid-liquid junctions. This system can be used to measure resistance of solution or resistance across the surface accurately. This has been used, for example in electrophoresis, in coulometric titration, and in studies of interfaces between immiscible electrolyte solutions.

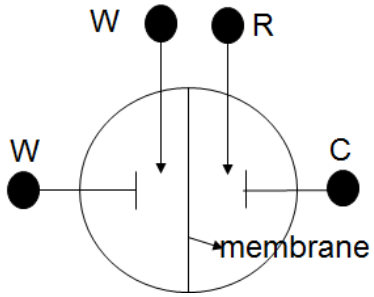

Figure 3.7. Schematic view of the 4-electrode configuration.

In membrane studies sometimes two- and three-electrode configurations are employed when the transport of ions is investigated. This can be fraught with problems as one or two of the electrodes may be polarised and this can take the polarisation away from the membrane. It is very important that all the potential is applied to the membrane and therefore the four-electrode configuration is the only acceptable way to measure membrane processes. There are exceptions, but only for very low currents (as used for example in the study of biological cell membranes and single cell pores). In this report all membrane measurements are performed with the four-electrode configuration.

3.4. Electrochemical Methods

3.4.1. Cyclic Voltammetry

Cyclic voltammetry is a standard tool in electrochemistry and commonly employed to elucidate the reduction and oxidation processes of molecular species. This technique provides substantial information on rapid identification of redox potentials of the electroactive species, and the kinetics and thermodynamics of chemical redox processes. Cyclic voltammetry is usually the first experiment performed in an electroanalytical study[3]. This technique has been used in a wide range of applications with its advantages of simplicity, sensitivity, speed, and low costs among others technique.

Cyclic voltammetry consists of scanning the potential of a working electrode between two potential limits: the initial potential $E_{initial}$ where no faradaic current is observed to the final potential E_{final}. The potential of working electrode is linearly swept forward to the E_{final} and subsequently reverse the potential to the $E_{initial}$. The potential changes with time as shown in Figure 3.8A. The potentiostat measures the current resulting from the applied potential during the potential sweep. The resulting plot of current versus potential is defined a *cyclic voltammogram*. The basic shape of cyclic voltammogram is shown in Figure 3.8B below.

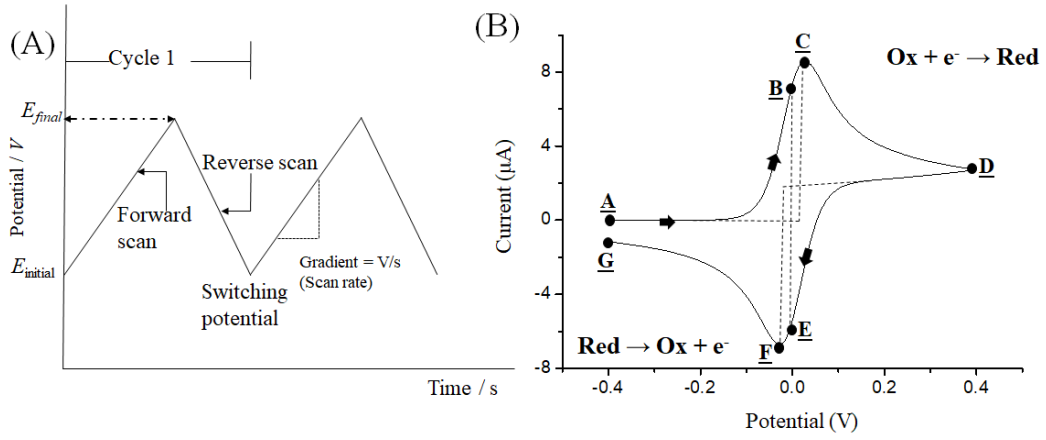

Figure 3.8. (A) A graph of potential against time for a cyclic voltammogram and (B) a cyclic voltammogram plot for reversible electron transfer of reactant Ox forming product Red.

Figure 3.8B shows the cyclic voltammogram for a reversible redox reaction of reactant O forming product R. Initially it is only the species Ox is present. As a potential is scanned positively (anodically) from point **A** to **D**, [Ox] is steadily depleted near the electrode as it is oxidised to R. At point **C**, where the peak anodic current ($i_{p,a}$) is observed, the current is dictated by the delivery of additional R via diffusion from the bulk solution. The volume of solution at the surface of the electrode containing the reduced Ox, called the diffusion layer, continues to grow throughout the scan. This slows down mass transport of Red to the electrode. During scanning to more negative potentials, the rate of diffusion of Ox from the bulk solution to the electrode becomes slower, resulting in a decrease in the current as the scan continues (**C** → **D**). When the switching potential (**D**) is reached, the scan direction is reversed, and the potential is scanned in the negative (cathodic) direction. While the concentration of Red at the electrode surface was depleted, the concentration of Ox at the electrode surface increased, fulfilling the Nernst equation in Equation 3.2. The Red present at the electrode surface is reduced back to Ox as the applied potential becomes more negative. At points **B** and **E**, the concentrations of Ox and Red at the electrode surface are equal, following the Nernst equation, E = $E_{1/2}$. This corresponds to the halfway potential between the observed peaks (**C** and **F**) and provides a straightforward way to estimate the E^o for a reversible electron transfer. The two peaks are separated due to the diffusion of the analyte to and from the electrode[4].

The shape of cyclic voltammogram defines the reversibility of the redox system. If the oxidation process is chemically and electrochemically reversible, the difference between the anodic and cathodic peak potentials, called peak-to-peak separation (ΔEp) (in Equation 3.29) is 57 mV at 25 ^{o}C (2.22 RT/F) and the width at half max on the forward scan of the peak is 59 mV. The peak current for a reversible redox system (at 25 ^{o}C) is given by the *Randles-Sevcik* equation in Equation 3.30.

$$\left|E_p^a - E_p^c\right| = 2.218\frac{RT}{nF} \tag{3.29}$$

$$I_p = 0.446nFAC^o\sqrt{\frac{nF\nu D}{RT}} \tag{3.30}$$

Here n is the number of electrons transferred per redox molecule diffusing to the electrode surface, A is the electrode area (in m^2), C is the concentration (in mol m^{-3}), D is the diffusion coefficient (in m^2 s^{-1}), and v is the scan rate (in V s^{-1}). Accordingly, the current is directly proportional to concentration and increases with the square root of the scan rate. The Randles-Sevcik equation can give indications whether an analyte is freely diffusing in solution and may be used to calculate the diffusion coefficients.

When electron transfer at the electrode surface is slow compared to the mass transport, the process is termed as electrochemically irreversible. In a system of electrochemically irreversible, the product diffuses to the bulk solution instead of reacting back on the surface of the electrode. As a result, peak-to-peak separation is larger than 57 mV comparing to an electrochemically reversible one-electron redox couple. There is intermediate electrochemically system called as quasi-reversible where the chemical reaction depends on both the electron transfer rate and mass transfer rate. In this case, the peak current is not proportional to the square root of the scan rate and peak-to-peak separation depend on the scan rate. Figure 3.9. shows the comparison of the shape of three cyclic voltammogram in reversible, quasi-reversible, and irreversible system.

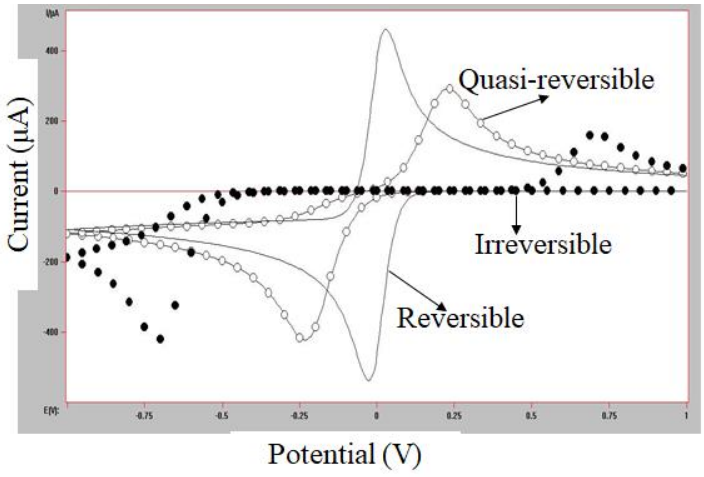

Figure 3.9. Cyclic voltammograms (for reduction) for (—) reversible, (-o-o-) quasi-reversible, and (···) irreversible electron transfer.

3.4.2. Chronoamperometry

Chronoamperometry also known as potential step, is a technique where the current is measured as a function of time. This technique involves stepping the potential of the working electrode from a value at which no faradaic reaction occurs to a potential at which the surface concentration of the electroactive species is effectively zero (Figure 3.10). A stationary working electrode and unstirred solution are used. The resulting current-time dependence is monitored. As mass transport under these conditions is solely by diffusion, the current-time curve reflects the change in the concentration gradient in the vicinity of the surface. This involves a gradual expansion of the diffusion layer associated with the depletion of the reactant, and hence decreased slope of the concentration profile as time progresses (Figure 3.10). Accordingly, the current (at a planar electrode) decays with time as given by the Cottrell in Equation 3.31.

$$I(t) = \frac{nFACD^{\frac{1}{2}}}{\pi^{\frac{1}{2}} t^{\frac{1}{2}}} = kt^{-1/2} \qquad (3.31)$$

The i - $t^{-1/2}$ characteristics is often termed “Cottrell behaviour”. Deviations from such behaviour may occur at long times (usually over 100 s) as a result of natural convection effects or when using microelectrodes with high perimeter-to-area ratio. In the latter case, a time-independent current (proportional to the concentration) is obtained for t > 0.1s due to a large radial diffusion contribution. Similar considerations apply to spherical electrodes whose current response following an applied potential step contain both a time-dependent and a time-independent term.

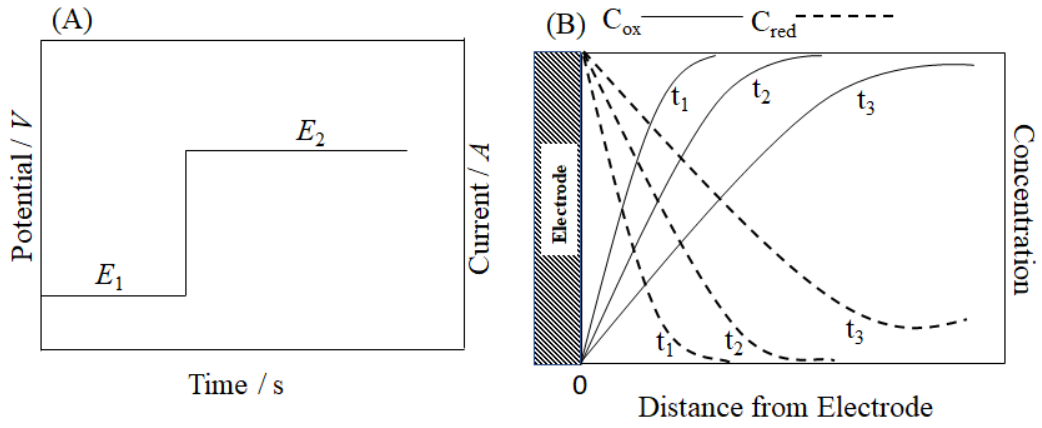

Figure 3.10. (A) Potential step plot from an initial potential; E_1 to a second potential as a functional of time in chronoamperometric experiment and (B) a plot of the variation of concentration C_{ox}/C_{red} as a function of distance from the electrode surface.

Chronoamperometry is often used for measuring the diffusion coefficient of electroactive species or the surface area of the working electrode. Analytical applications of chronoamperometry (e.g. *in vivo* bioanalysis) rely on pulsing of the potential of the working electrode repetitively at fixed time intervals. Chronoamperometry can also be applied to the study of mechanisms of electrode processes.

3.4.3. Electrochemical Impedance Spectroscopy (EIS)

Electrochemical impedance spectroscopy (EIS) is a powerful technique for investigating electrochemical process and widely used for the investigation of both solid and liquid-phase phenomena. This technique has been utilised for purposes such as corrosion analysis, interfacial behaviour of molecules, monitoring the function of batteries and fuel cells amongst many other applications. Impedance (Z) is a measure of ability of a circuit to resist the electrical current flow. The electrochemical impedance is measured by applying a sinusoidal AC potential (V) to an electrochemical cell and then the AC current signal is measured through the cell. Assume that if we change the potential is small enough (typically <10 mV), then the current response (I) will be sinusoid at the same frequency but shifted in phase angle (ϕ) (Figure 3.11A).

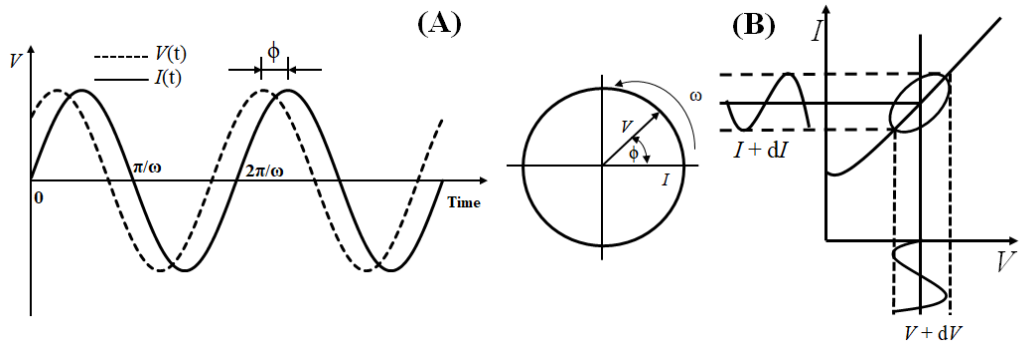

Figure 3.11. (A) Phasor diagram showing the relationship between voltage signals $V(t)$ (--) and alternating current I(t) (—) at a phase angle (ϕ) and frequency ω and (B) Lissajous plot.

In the experimental conditions, the electrochemical impedance is normally measured using excitation AC voltage signal V with small amplitude V_A (volts) applied at a frequency f (Hz or sec^{-1}). The voltage signal V(t) can be expressed mathematically as a function of time (t) with the projection on the y-axis (Figure 3.11 and Equation 3.32).

$$V(t) = V_A \sin(2\pi f t) = V_A \sin(\omega t) \tag{3.32}$$

Where ω is the angular frequency measured in radian s^{-1}. In a linear or pseudolinear system, the current response to a sinusoidal voltage input at the same frequency but shifted in phase. In a linear system, the response current signal I(t) is shifted in phase (ϕ) and has different amplitude I_A can be expressed by the Equation 3.33.

$$I(t) = I_A \sin(\omega t + \phi) \tag{3.33}$$

Therefore, we can calculate the complex impedance (Z^*) as the ratio of input voltage V(t) and output measured current I(t) using the Ohm's Law in Equation 3.34.

$$Z^* = \frac{V(t)}{I(t)} = \frac{V_A \sin(\omega t)}{I_A \sin(\omega t + \phi)} = Z_A \frac{\sin(\omega t)}{\sin(\omega t + \phi)} \tag{3.34}$$

The impedance is expressed in terms of a magnitude (absolute value), Z_A = |Z| and a phase shift (ϕ). If we plot the applied sinusoidal voltage signal on the x-axis of a graph and the sinusoidal response signal *I*(t) on the y-axis, we can obtain a "Lissajous figure" in Figure 3.11B. In order to represent the phase of signals and the relative magnitude more clearly, it is possible to express as a complex function with Euler's relationship (Equation 3.35).

$$\exp(j\phi) = cos\phi + sin\phi \tag{3.35}$$

The potential *V*(t) can be described in Equation 3.36 and the current response *I*(t) can be expressed in Equation 3.37.

$$V(t) = V_A \exp(j\omega t) \tag{3.36}$$

$$I(t) = I_A \exp(j\omega t + \phi) \tag{3.37}$$

Therefore, the impedance is then represented as a complex number and also can be expressed in complex mathematics as a combination of a "real" (Z_{real}) and "imaginary" (Z_{im}) parts in Equation 3.38.

$$Z^* = \frac{V}{I} = Z_A \exp(j\phi) = Z_A(cos\phi + jsin\phi) = Z_{real} + jZ_{im} \tag{3.38}$$

The phase angle (ϕ) at a chosen frequency ω is a ratio of the imaginary and real impedance components described in Equation 3.39.

$$tan\phi = \frac{Z_{im}}{Z_{real}} \; or \; \phi = \arctan\left(\frac{Z_{im}}{Z_{real}}\right) \tag{3.39}$$

Data Representation in Electrochemical Impedance Spectroscopy. If a sinusoidal voltage is applied to a pure resistor of value R, then the measured complex impedance is entirely resistive at all frequencies as Z* = R and the impedance magnitude |Z| = R. If a sinusoidal voltage is applied to a pure capacitor (C), the measured impedance can be calculated to the relationship $Z^* = -j(\omega C)^{-1}$,

where C is the capacitance. The magnitude of the impedance for a pure capacitor can be calculated and obtained in Equation 3.40.

$$V(t) = V_A \exp(j\omega t)$$
$$I(t) = \frac{dQ}{dt} = \frac{d(CV_A)}{dt} = C\frac{dV}{dt}$$
$$I = C\frac{d(V_A \exp(j\omega t)}{dt} = j\omega t C V_A \exp(j\omega t)$$
$$Z = \frac{V(t)}{I(t)} = \frac{1}{j\omega C} = \frac{-j}{\omega C} \quad (3.40)$$

Instead of a simple ideal resistor or capacitor, in a real-life system combines resistor and capacitor elements. One of example is the R | C circuit represented by a parallel combination of an ideal resistor (R) and an ideal capacitor (C) in Figure 3.13A. The impedance of the two parallel branches of R | C circuit are equal to constant resistance *R* and $-j(\omega C)^{-1}$, respectively. According to Kirchoff's Law for a parallel circuit, the potential across both circuit elements are equal, while the total current can be calculated from the sum of the currents flowing through the resistor and capacitor. The current *I*(t) can be calculated as follow and obtained in Equation 3.41.

$$I(t) = \frac{V(t)}{Z^*} = \frac{V(t)}{R} - \frac{\omega C V(t)}{j} = V(t)\left[\frac{1}{R} - \frac{\omega C}{j}\right] = V(t)\frac{1+(\omega RC)^2}{R - j\omega R^2 C} \quad (3.41)$$

The resulting impedance can be expressed in Equation 3.42 is composed with "real" and "imaginary" parts. If the real part is $Z_{real}(\omega) = \frac{R}{1+(\omega RC)^2}$ plotted on the x-axis and the imaginary part $Z_{im}(\omega) = -\frac{\omega R^2 C}{1+(\omega RC)^2}$ on the y-axis, we can obtain a "Nyquist plot" in Figure 3.11B. Figure 3.12 has been annotated to show that low frequency data are on the right side of the plot and higher frequencies are on the left.

$$Z^* = \frac{R}{1+(\omega RC)^2} - j\frac{\omega R^2 C}{1+(\omega RC)^2} \quad (3.42)$$

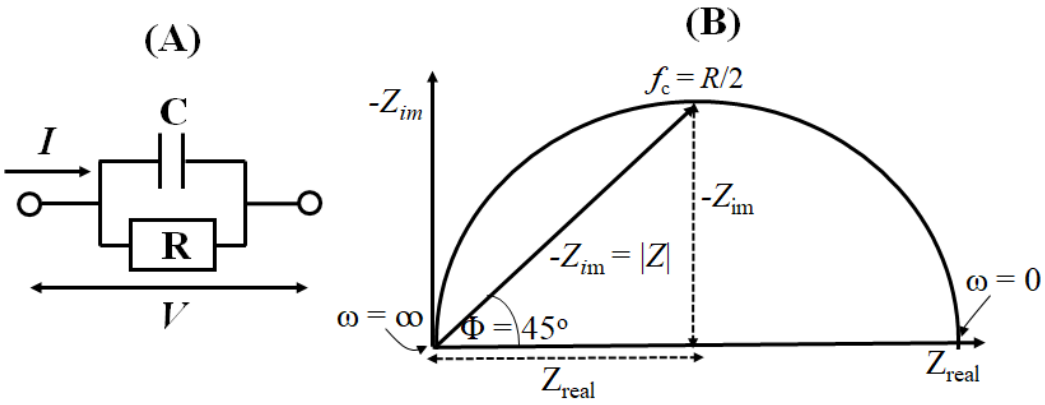

Figure 3.12. (A) An equivalent circuit consists of an ideal resistor (R) and an ideal capacitor (C) and (B) Nyquist plot with impedance factor.

There is a parameter called time constant (τ) derived from τ = RC associated with the circuit, and "characteristics circular" frequency ω = 1/τ and "critical relaxation" frequency $f_C = \frac{1}{2\pi\tau} = \frac{1}{2\pi RC} = 15.9\ Hz$[5]. The impedance is completely capacitive at very high frequency and become completely resistive and approaches to R value at low frequency which equals to the semicircle diameter of Nyquist plot. The phase angle (ϕ) tends towards -90° at high frequency and towards 0° at low frequency and critical frequency f_c corresponds to a midpoint transition where the phase angle (ϕ) is -45° and $Z_{im} = Z_{real} = R/2$.

Nyquist plot can be used to investigate impedance parameters yields into the possible conduction mechanisms or kinetic governing phenomena. If a Nyquist plot shows a perfect semicircle shape, the impedance response corresponds to a single activation energy controlled (or charge transfer) process. However, the information presented in Nyquist plot is not complete because there is no detailed indication of the frequency at which the impedance is measured for every point. For a detailed presentation of the experimental data, the points in the Nyquist plot must be labelled with the corresponding frequency values. The Nyquist plot also makes the determination of low impedance values (at high frequency) is very difficult.

Another form to present impedance data is the Bode plot. The Bode plot shows a plot of the phase angle (ϕ) and the logarithm of the impedance magnitude

as a function of the logarithm of frequency. The Bode plot can show frequency information and tell us about an important low impedance behaviour at high frequency. The transition slope between low frequency and high frequency can provide useful information about the nature of the impedance response if the time constants are well separated. The Bode plot are also sensitive to system parameters and provide a good meaning to compare the model with the experimental results.

3.4.4. Steady State Voltammetry at Microelectrodes

Application of microelectrodes is a growing trend in the field of analytical chemistry. Microelectrodes are defined usually as electrodes with a diameter of less than 50 μm (approaching steady state in < 1 s). These dimensions offer obvious analytical advantages, including the exploration of microscopic domains, measurement of local concentrations profiles, detection in microflow systems, and analysis of very small (microliter) sample volumes. Recent studies about microelectrodes have been aimed at measuring rapid changes in neurotransmitter concentration using carbon fiber microelectrodes[6], measuring the chemical stability of highly reactive species[7], trace electrochemical analysis, analytical sensing, *in vivo* measurements in biological objects, detection in flowing liquids, and surface imaging in scanning electrochemical microscopy[8].

Due to very small total currents at microelectrodes, they offer several other attractive properties that have expanded the possibilities of electrochemistry. The possibility has been noted to work in highly resistive solutions that would develop large ohmic (iR) drop with conventional electrodes. The double-layer capacitance is greatly reduced due to their small surface area, resulting in fast electrochemical cells with small RC time constants. For example, for a microdisk the RC time constant is proportional to the radius of the electrode. The small RC constants allow high-speed voltammetric experiments to be performed at microsecond timescale (scan rates can be higher than 10^6 V/s) and to probe the kinetics of very fast electron transfer and coupling chemical reactions.

The rate of mass transport to and from the electrode increases as the electrode size decreases. The diffusion field at the electrode is spherical rather than

planar and the voltammetric response becomes time independent on a typical multi-second experimental time scale. As a consequence of the increase in mass transport and the reduced charging currents, microelectrodes exhibit excellent signal-to-background characteristics. In addition, steady-state or quasi-steady-state conditions are rapidly achieved and the contribution of convective transport is negligible. The other important properties of microelectrodes in comparison to electrodes of regular size, include: much smaller currents, lower ohmic drop, and higher ratio of faradaic to capacitance currents[9]. Many of the advantages of microelectrodes also apply for microholes in membranes.

In this report most experiments are carried out with microhole substrates covered with microporous membrane materials. Therefore, a microelectrode effect is observed with similar mass transport and steady state phenomena. However, in contrast to the microelectrode electrochemical process, here there are no electron transfer processes. Only ion transport processes across the microhole covered with microporous membrane materials are investigated. This technique is carried out in a two-compartment electrochemical cell with four-electrode configuration. The details for this type of experiment are introduced below and the experiment is developed to allow different type of microporous materials to be investigated.

3.5. References

1 Fisher, A.C. **1996**. *Electrode Dynamics*. Oxford University Press, New York, US.

2 Bard, A.J., Faulkner, L.R. **2001**. *Electrochemical Methods Fundamental and Applications*. 2nd Edition. John Wiley & Sons, New York, US.

3 Wang, J. 2000. *Analytical Electrochemistry 3rd Ed*. New Jersey: John Wiley & Sons

4 Elgrishi, N., Rountree, K.J., McCarthy, B.D., Rountree, E.S., Eisenhart, T.T., Dempsey, J.L. **2018**. *J. Chem. Educ. 95,* 197-206.

5 Lvovich, V.F. 2012. *Impedance Spectroscopy Applications to Electrochemical and Dielectric Phenomena*. John Wiley & Sons, New Jersey, US.

6 Huffman, M.L., Venton, B.J. *Analyst*. **2009**. 134, 1, 18-24.

7 Laborda, E., Olmos, J-M., Torralba, E., Molina, A. **2015**. *Anal Chem*. 87, 1676-1684.

8 Stulik, K., Amatore, C., Holub, K., Marecek, V., Kutner, W. *Pure Appl Chem*. **2000**. 72, 8, 1483-1492.

9 Stojek, Z. *Mikrochim Acta*. **1991**. 2, 353-361.

Chapter 4:

One Dimensional Nanomaterials: Ionic Rectification based on Bacteriophage M13

Contents

Chapter Abstract

The ion conductivity and ion current rectification effects have been investigated when bacteriophage material (M13, wild-type) are deposited as a film onto a poly-ethylene-terephthalate (PET) substrate (6 μm thick with a 20 μm diameter laser-drilled microhole) and tested for potential applications in membranes. The membrane of bacteriophage M13 aggregate is formed under acidic conditions (in aqueous 10 mM acids) and acts as a microporous anion conductor with micropores described by the packing of cylindrical virus particles. In combination the semi-permeability of phage membrane, and asymmetric deposition of bacteriophage M13 on the PET film substrate leads to anionic diode behaviour. Typical values of rectification ratio obtained from experiments are around 10 (determined at switching potential +/-1V) in aqueous 10 mM mineral acids. A rectification minimum is consistently obtained at 0.5 mM concentration of cationic guest species (aqueous Cu^{2+}, Co^{2+}, Ag^{+}) in aqueous 10 mM acids. However, an equivalent rectification minimum for an anionic guest species (indigo carmine) is obtained at a much lower concentration of 5 μM. It is suggested that the behaviour of the anionic diode asymmetrically deposited onto PET substrate is linked to cation exclusion effects on ion transport through membrane micropores.

Chapter Publication

Part of this chapter have been published in:

B. R. Putra, K. S.-Karpińska, P. Kudła, H. Yin, J. A. Boswell, A. M. Squires, M. A. D. Silva, K. J. Edler, P. J. Fletcher, S. C. Parker, F. Marken. Bacteriophage M13 Aggregation on a Microhole Poly(ethylene terephthalate) Substrate Produces an Anionic Current Rectifier: Sensitivity toward Anionic versus Cationic Guests. *ACS Appl. Bio. Mater*. **2020**, 3, 1, 512-521.

Acknowledgement

Dr. Katarzyna Szot-Karpińska and Dr. Patryk Kudła from Institute of Physical Chemistry, Polish Academy of Sciences, Poland are acknowledged for supplying bacteriophage M13 for ionic diode studies based on phage material membranes.

4.1. Introduction

This chapter focuses on ion transport behaviour through bacteriophage M13 films deposited onto a 6 μm thick poly-(ethylene-terephthalate) (PET) substrate with a 20 μm microhole. The normal wild-type M13 bacteriophage used in this study exists in nature as filamentous nanofiber with 6.6 nm diameter, 880 nm length, and a large surface area and typically 18700 nm^2 (Figure 4.1A).[1,2] From a structural perspective, M13 bacteriophages are dominated by the 2700 copies of the pVIII coat proteins representing 87% of its total mass and 99% of the total virus surface.[3] The distance between two adjacent pVIII coat proteins units is approximately 2.7 nm with 10 pVIII proteins contributing the one repeat length (Figure 4.1C). Considering the cylindrical shape of bacteriophage M13 geometry with given the radial diameter 6.6 nm, the exposed surface area per pVIII protein is readily estimated as 5.6 $nm.^2$ The pVIII coat protein at M13 phage has a positive region (inwardly directed to interact with embedded DNA) and at the opposite end a negative region (outward directed) to define the virus surface.[4] These major coat proteins in M13 phages can be written as a sequence of 50 amino acids, some of which are responsible for the surface charges.[5,6]

The iso-electric point of M13 bacteriophage is at approximately 4.2 consistent with the negative charge at neutral pH on the phage surface.[7] The pK_A of bacteriophage M13 particles is connected with the isoelectric point, which is dependent on the outside protonation of the protein pVIII. The pVIII protein in the cylindrical section of the phage shows a slight excess positive charge internally with some more negatively charged functional groups exposed to the outside of the virus. The exposed charged groups on the outside surface of pVIII protein are the NH_2 terminus, Glu2, Asp4, Asp5, Lys8, Asp12, and Glu20 (Figure 4.1B). At a neutral pH 7, Lys would have positive charge and both charges of Asp and Glu would be negative (net -3). However, at a pH of approximately 2 with the presence of aqueous 10 mM acid, only the positive charge (+2) at pVIII protein surface should remain. This excess positive charge on the surface of pVIII protein defines a microchannel (see the small circle in Figure 4.1D) that is formed when packing the cylindrical virus particles.

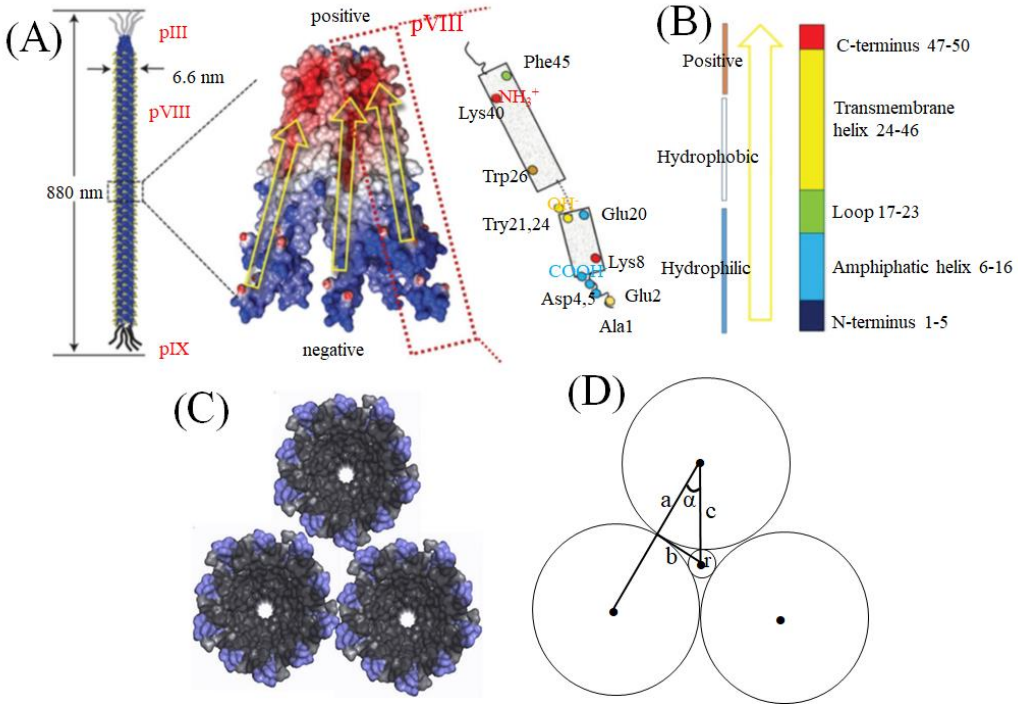

Figure 4.1. (A) Schematic drawing of the M13 bacteriophage (adapted from [4] with permission). (B) Major pVIII coat protein of phage M13 with packing of positive excess charge internally as interacting with DNA and negative excess charge externally as interacting with electrolyte. (C) Vertical cross-sectional view of three virus particles (in cross section) packing to give a central microchannel. (D) Calculation of the microchannel diameter from cross-sectional view of phage M13.

Bacteriophage materials, due to their ability to replicate precisely, can provide extraordinarily stable nanostructures in order to create structurally well-defined nanomaterials at the molecular limits. Phage materials have been used for many applications such as development of phage display[8] and sensor[9] based on the end/surface groups being covered with proteins with specific selectivity. The uniform surface of bacteriophage M13 could offer a well-defined surface charge for future membrane applications based on major coat protein pVIII, if the virus particles can be aggregated into dense microporous films. Aggregation of phage particles is the first important step in the formation of M13 phage membranes. In this chapter, the geometry of M13 phage membranes can be estimated by assuming a closely compacted packing of cylindrical M13 virus particles.

In Figure 4.1D, the diameter of the forming microchannel (2r) from densest packing of M13 virus particles for ion transport can be related to the diameter of the virus particles (2a = 6.6 nm) with the angle $\alpha = 30^{o}$. The radius is given by r = c-a, which can be translated as $r = a/\cos\alpha - a = a(1/\cos\alpha - 1)$. This suggests that r is 0.51 nm (15.5% of c), therefore the diameter for the ion conducting channel from the densest packing of M13 virus particles is approximately 2r = 1 nm. This size of channel from packing of M13 virus particles is narrow, but sufficient for the ion transport. In a 10 mM aqueous solution, a typical Debye layer can be estimated by $\kappa^{-1} = 0.3/I^{0.5} = 3$ nm (I is the ionic strength[10]), and therefore strong cation exclusion phenomena inside the channel can be expected at pH 2. The aggregation of M13 virus particles should result a semi-permeable membrane which has anion conductor characteristic in aqueous electrolyte solution.

In this chapter, it is demonstrated that the aggregation of M13 wild-type phage can form membrane-forming aggregates with treatment of aqueous 10 mM acids. The intrinsic micro-channel structure formed between cylindrical M13 phage material provides the pathways for ion transport especially for anions. The asymmetric deposition of the M13 bacteriophage material on a microhole in a PET film substrate followed by aqueous 10 mM acid results in ionic rectification effects and in particular in anionic diode behaviour. As anions and cations interact in these microchannels due to the potential-driven process, different effects for cationic and anionic guest species have been observed (rectification minima).

4.2. Experimental

4.2.1. Chemical Reagents

A wild bacteriophage M13 KE lysate was supplied from New England Biolabs, NEB. In order to be used in the experiment, the M13 phage were multiplied on *Escherichia coli* ER2738 (NEB) according to the NEB protocol.[3] The concentration obtained after following the NEB protocol for the multiplied M13 phage was 1.04×10^{14} plaque-forming units per mL (PFU/mL). Hydrochloric acid, nitric acid, sulphuric acid, perchloric acid, phosphoric acid, agarose, copper (II) perchlorate, cobalt (II) perchlorate, silver nitrate, and indigo carmine were obtained

from Sigma-Aldrich Ltd. and used without further purification. Aqueous solutions were prepared in volumetric flasks with ultrapure water resistivity of 18.2 MΩ cm (T = 20 +/- 2 ^{o}C) under ambient conditions from an ELGA Purelab Classic System for water filtration.

4.2.2. Instrumentation

M13 phage imaging was performed with Transmission Electron Microscopy (TEM) instrument of JEOL JEM-2100 Plus with 200 kV maximum operating voltage. Scanning Electron Microscopy (SEM) was performed with a JEOL JSM-6480LV SEM. The zeta-potential for the bacteriophage M13 solution was measured on a Zetasizer Nano ZS (Malvern Instruments Ltd, Malvern, UK). Scattering analysis for the bacteriophage M13 and HCl-treated phage M13 solution was perfomed using small angle X-ray scattering (SAXS) system from Anton Paar. The scattering vector (Q) was calculated using $Q = 4 \pi \sin\theta/\lambda$, where θ is half of the scattering angle, λ is the x-ray wavelength (1.54 Å). 1D scattering patterns of intensity *vs*. *Q* were fitted to a cylinder fit with SASView 4.2.2.

Electrochemical data (for both voltammetry and chronoamperometry) were recorded at T = 20 ± 2 ^{o}C on a potentiostat system (Ivium Compactstat, Netherland). A classic 4-electrode electrochemical cell configuration was employed during the electrochemical experiments. The membrane separates two tubular half-cells (15 mm diameter), one with Pt wire working and KCl-saturated calomel (SCE) sense electrode, and the other one with SCE electrode and Pt wire counter electrode. In electrochemical measurements the working electrode was always located on the side of the bacteriophage M13 film deposit.

4.2.3. Procedures of Bacteriophage M13 Deposition

During the electrochemical studies of bacteriophage M13, 6 µm thick the polyethylene-terephthalate (PET) films with laser-drilled 20 µm diameter microhole were used as substrates for phage M13 deposit. Before deposition of bacteriophage M13, a microscopy glass slide was pre-coated with a thin layer of 1% agarose gel. The PET film was placed onto the gel to prevent bacteriophage

M13 solution entering/crossing the microhole. Approximately 10 μL volume of bacteriophage M13 solution (1.04×10^{14} PFU/mL) was applied to the surface and with a glass rod the bacteriophage M13 solution was spread evenly over ca. 1 cm^2 of the PET surface. After drying of the bacteriophage M13 deposit, 10 μL volume of bacteriophage M13 was applied once again to the PET film. Finally, the PET film was removed from the agarose gel and stored under dry conditions. For electrochemical measurements the M13 phage film was mounted in a U-cell between the two glass flanges with the help of some Dow-Corning vacuum grease as sealant. Reproducibility of currents are generally good for multiple devices typically at ±10 %, with variations probably mostly due to slight variations in the film thickness. New M13 phage films were employed for each set of experiments. In order to ensure the reproducibility in both current and rectification effect, each new M13 phage film has been tested in aqueous 10 mM HCl before using it in the experiment.

4.3. Result and Discussion

4.3.1. Characterisation of Bacteriophage M13

Table 1 shows the data from Dynamic Light Scattering (DLS) measurements obtained with Malvern Zetasizer Nano ZS. When bacteriophage M13 in aqueous 10 mM NaCl, it shows a negative zeta potential -18 mV. From the DLS measurements, the average size of virus particle is approximately 168 nm assuming spherical particles. This average size is consistent with dissolved cylindrical material where length and diameter of M13 phage materials are very different.[11] In fact, the DLS measurement also reports the hydrodynamic diameter of M13 phage particles, including the shell of ions and water around the particles, rather than the bare M13 phage particle size. In comparison, the Z-average diameter tends to be increased in aqueous 10 mM HCl consistent with aggregation of M13 phage particles. Also, the zeta potential changes from -18.0 mV to +20.6 mV gives indication of protonation of pVIII protein on the surface of M13 phages linked to negative counter anions weakly binding to the surface of virus particles.

Table 4.1. Data obtained from dynamic light scattering for zeta potential measurements and diameter of M13 phage particles treated with 10 mM NaCl and in 10 mM HCl (errors expressed as standard deviation for triplicate measurements).

Sample		Z-average diameter / nm	Zeta-potential / mV
M13 bacteriophages	in NaCl 10 mM	168 ± 20	-18.0 ± 2.4
	in HCl 10 mM	1145 ± 152	+20.6 ± 3.7

Figure 4.2A shows the image of electron optical measurements using M13 phages stained with uranyl acetate and suggest a highly filamentous structure. The M13 phage materials dissolved and deposited from distilled water appears to be widely distributed and opened in Figure 4.2A. When M13 phage treated with 10 mM aqueous HCl in Figure 4.2B and C aggregation of filamentous phage can be seen and the formation of bundles of filamentous material was observed.

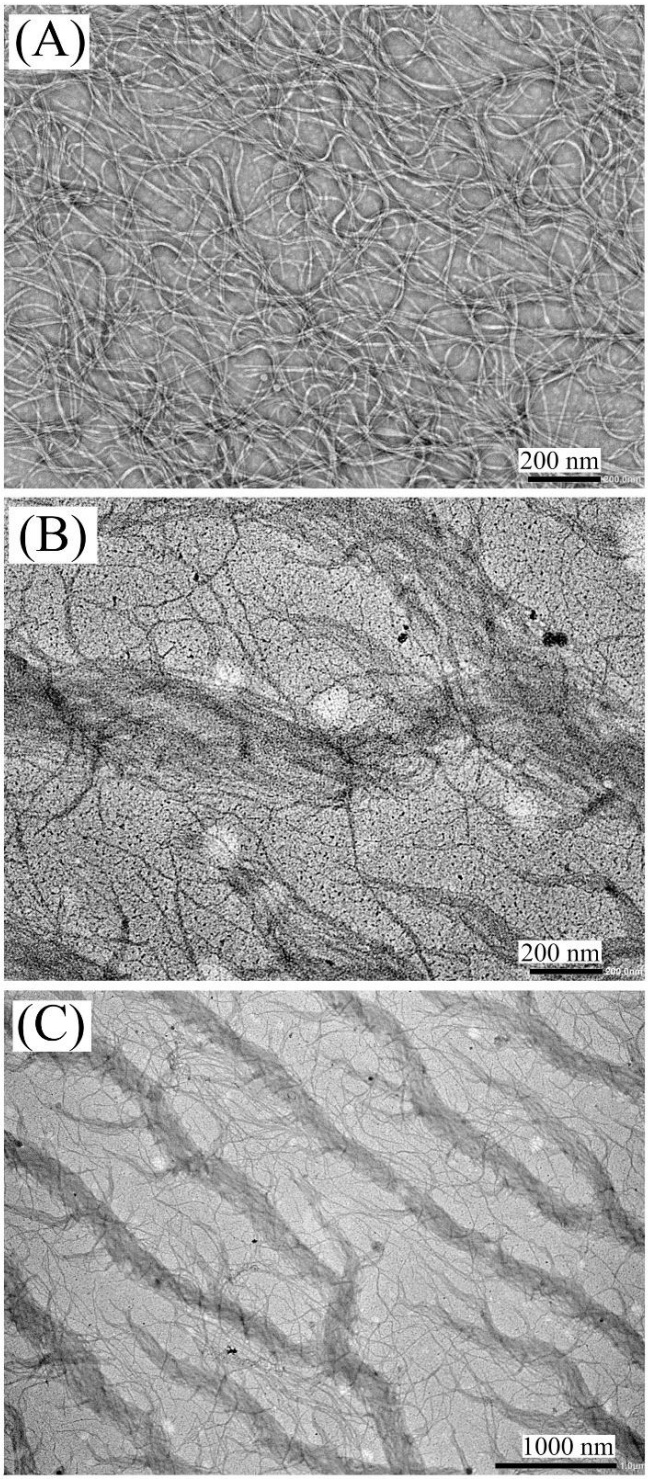

Figure 4.2. (A) TEM image for M13 phage 1.04×10^{14} PFU/mL deposited onto 20 μm diameter microhole of PET substrate. TEM images for M13 phage deposited and aggregated when exposed to aqueous 10 mM HCl with (B) 200 nm and (C) 1000 nm scale.

In order to obtain the geometric properties of filamentous M13 phage, SAXS experiment was performed in the absence and in the presence of 10 mM HCl. It can be seen in Figure 4.3 that data sets were obtained in water (blue dot data) and with the treatment of 10 mM HCl (green dot data). When the experimental data sets were compared with the modelling software SASView[12], both these data sets fit into the cylindrical model of M13 phage. For the data sets obtained in water samples, the diameter of M13 phage is 7.2 +/- 0.8 nm with a typical length of 24 +/- 6 nm. When the M13 sample was treated with HCl 10 mM, data fitting from modelling software SASView suggests a diameter of 7.1 +/- 1.1 nm and a length of 19 +/- 5 nm. These observation on both diameter and length of M13 phages are in good agreement of the literature value of 6.6 nm in diameter with the apparent length of 31.5 nm.[13]

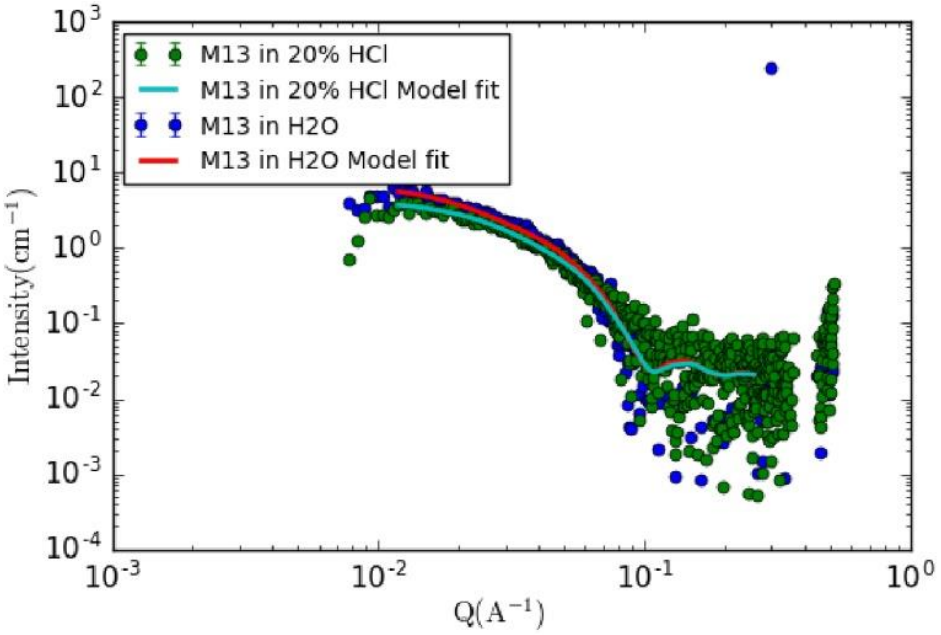

Figure 4.3. SAXS data for M13 phage in water (blue points) and treated with aqueous 10 mM HCl (green points). Cylinder model fits are shown to closely agree for the two data sets. Limit Q plotting range to the fitting range (~0.08 – 0.5).

In Figure 4.4, the asymmetry of M13 phage deposit between the bottom of the PET film (Figure 4.4A) and the top of PET film (Figure 4.4B) can be observed by imaging the phage film with scanning electron microscopy. Before imaging with the scanning electron microscopy, the M13 phage deposits were exposed to 10 mM

HCl in order to demonstrate the aggregation of virus particles to give a dense asymmetric deposit. The cross-sectional image from M13 phage deposit in Figure 4.4C suggests uneven films with the thickness about 10 μm.

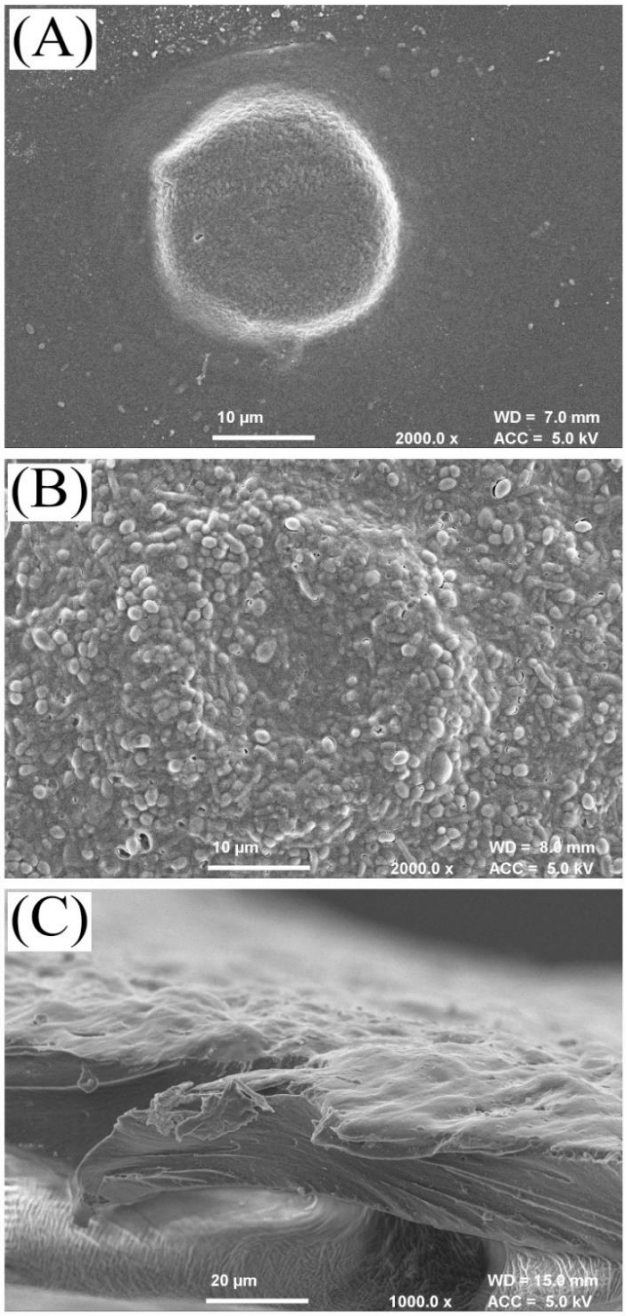

Figure 4.4. (A) SEM image for M13 phage 1.04×10^{14} PFU/mL deposited from aqueous dispersion onto 20 μm diameter microhole PET substrate (and aggregated by exposure to 10 mM HCl). Figure shows the bottom view of M13 phage deposit onto 20 μm diameter microhole PET. (B) SEM image from top view of M13 phage aggregation deposit by exposure to aqueous 10 mM HCl. (C) SEM cross-sectional image from freeze-fracture of the approximately 10 μm thick phage deposit on PET.

4.3.2. Characteristics of M13 Phage Deposits Lead to Ionic Rectifier Behaviour: Observation in Aqueous Acids

When the M13 phage film was exposed to neutral or alkaline aqueous electrolyte, it does not form mechanically stable films and the deposits simply dissolve after this treatment. However, when M13 film was exposed to acidic solution environments in particular 10 mM acid concentration, a permanent membrane-like material was obtained, which behaves like an anion conductor when it was investigated during electrochemistry experiments. Figure 4.5A shows the classic 4-electrode measurement cell with M13 phage deposited asymmetrically onto a poly-ethylene-terephthalate (PET) film with a 20 μm diameter microhole with the film always facing to the working side. The thickness of the M13 phage deposit is not well-controlled and estimated here to be approximately 10 μm with two times deposition of M13 phage onto the PET substrate. When the M13 phage film was made thicker with additional deposition, the current response did not significantly change the behaviour, although thinner films with less deposition of M13 phage were observed to be mechanically more fragile. Then the M13 phage film was placed between two electrolyte reservoirs with the working and sense electrode on the right compartment always facing the M13 film (see Figure 4.5A) and the reference and counter electrode in the left compartment. In this experiment configuration, the potential is applied between reference and sense electrodes (both SCE) and the corresponding current flows between working and counter electrode through M13 phage film.

Figure 4.5B shows the investigation of the behaviour of the M13 phage deposits during cyclic voltammogram experiments. The empty microhole filled with 10 mM HCl produces an Ohmic response (R = 118 kΩ), which correlated to the specific resistivity of the aqueous HCl electrolyte with contributions both from the cylindrical region and access of diffusion-migration ions within the microhole.[14] There are two distinct potential domains are observed when the M13 phage deposit used in the voltammetric investigation. In the positive potential range, the ion flux through M13 phage deposit decreases considerably consistent with a “closed” diode state. In the negative potential range, the current is similar to that observed for the

empty microhole filled with aqueous acid solution consistent with an “open” diodes state. This type of behaviour is typically observed for ion conductors with anion semi-permeable characteristics such as chitosan doped cellulose[15] and consistent with the protonated M13 phage material only enabling mobile anions to flow through the microchannels in between densest packing of the virus particles. Protonation of pVIII protein on the phage surface leads to a Debye layer with mobile anion counter charges, which are present within channels between cylindrical strands of the M13 phage deposit (see Figure 4.6). Cation transport through the channel between cylindrical strands of M13 phage deposit is inhibited due to cation exclusion.

In order to obtain the ionic current rectification effects from M13 phage materials, the asymmetric deposition of the M13 phage deposit onto the PET substrate is important to induce the anionic diode behaviour. Experiments with symmetric deposition of ionomer onto the PET substrate only result in Ohmic behaviour but with the current much less rather than that obtained with the empty microhole.[16] Also, the effect of increasing the aqueous electrolyte concentration on the side of the working electrode drastically decrease the rectification effect has been reported by using negatively charged carbon nanofibers (CNFs) deposited as a film onto a PET substrate.[17]

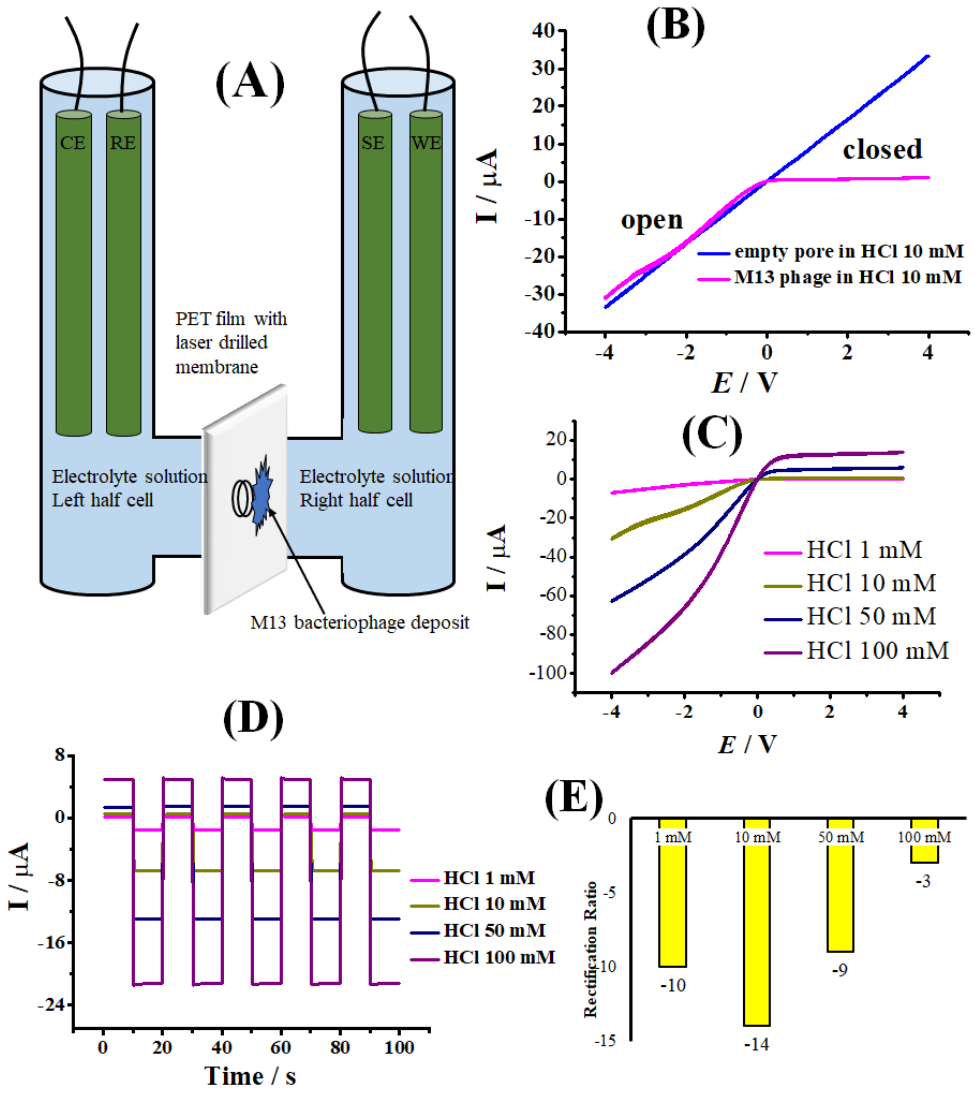

Figure 4.5. (A) Schematic description of the classic 4-electrode measurement cell with an asymmetrically deposited M13 phage onto a 6 µm thick PET film with 20 µm diameter microhole. (B) Cyclic voltammogram with scan rate 50 mVs^{-1} in aqueous 10 mM HCl comparing the empty microhole (behaving like a resistor) and the microhole with asymmetrically deposited M13 phage onto a PET (behaving like an anionic diode). (C) Cyclic voltammetry (scan rate 50 mVs^{-1}) data with asymmetrically deposited M13 phage deposit) immersed in 1, 10, 50, and 100 mM HCl. (D) Chronoamperometry responses (switching between -1V and +1V) immersed in aqueous HCl with concentration of 1, 10, 50, and 100 mM HCl on both sides compartment.

It is necessary to more closely consider the processes occurring during anion transport through M13 phage deposits and the effects of electrolyte concentration within the microhole region in the PET film, in order to better explain the observed diode effect.[18] When positive potentials are applied to the working electrode, anions

diffuse from bulk solution in the counter electrode compartment to the PET microhole and therefore penetrate the M13 phage film deposits. This leads to the electrolyte depletion phenomenon and this results in a high resistance area within the microhole region (see Figure 4.6, in closed state). The effect of ion depletion eliminates HCl from the microhole region of PET substrate and this is related to the loss of protonation at some protein surfaces also within the M13 phage film. With the deprotonation of protein surface, the adjacent phage material is locally affected and further increasing the resistance and severely reducing the flow of current. When negative potentials are applied to the working electrode, anions are driven through the phage material from the right compartment to the left compartment resulting in an increasing in electrolyte concentration within the microhole region and therefore locally a lower resistance (see Figure 4.6, in open state). Protons also re-enter from the counter electrode compartment to the previously depleted region in the M13 phage deposits to provide a more positive charge at protein surface and thus improved anion conductivity.

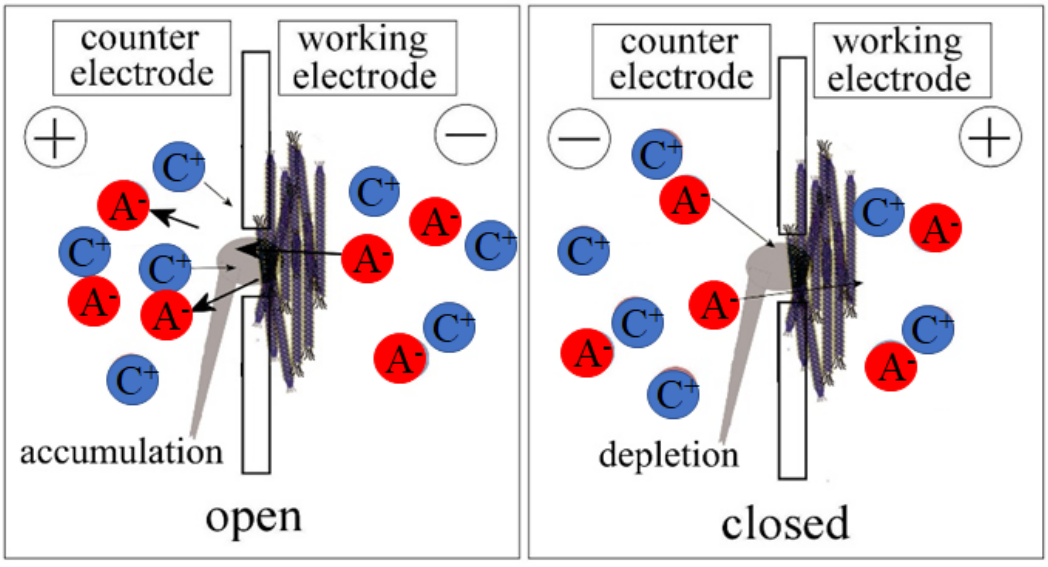

Figure 4.6. Schematic depiction of the case open and closed state of anionic diode from bacteriophage M13 deposit. The ion movement and accumulation/depletion effects induced in the bacteriophage M13 diode by externally applied potentials.

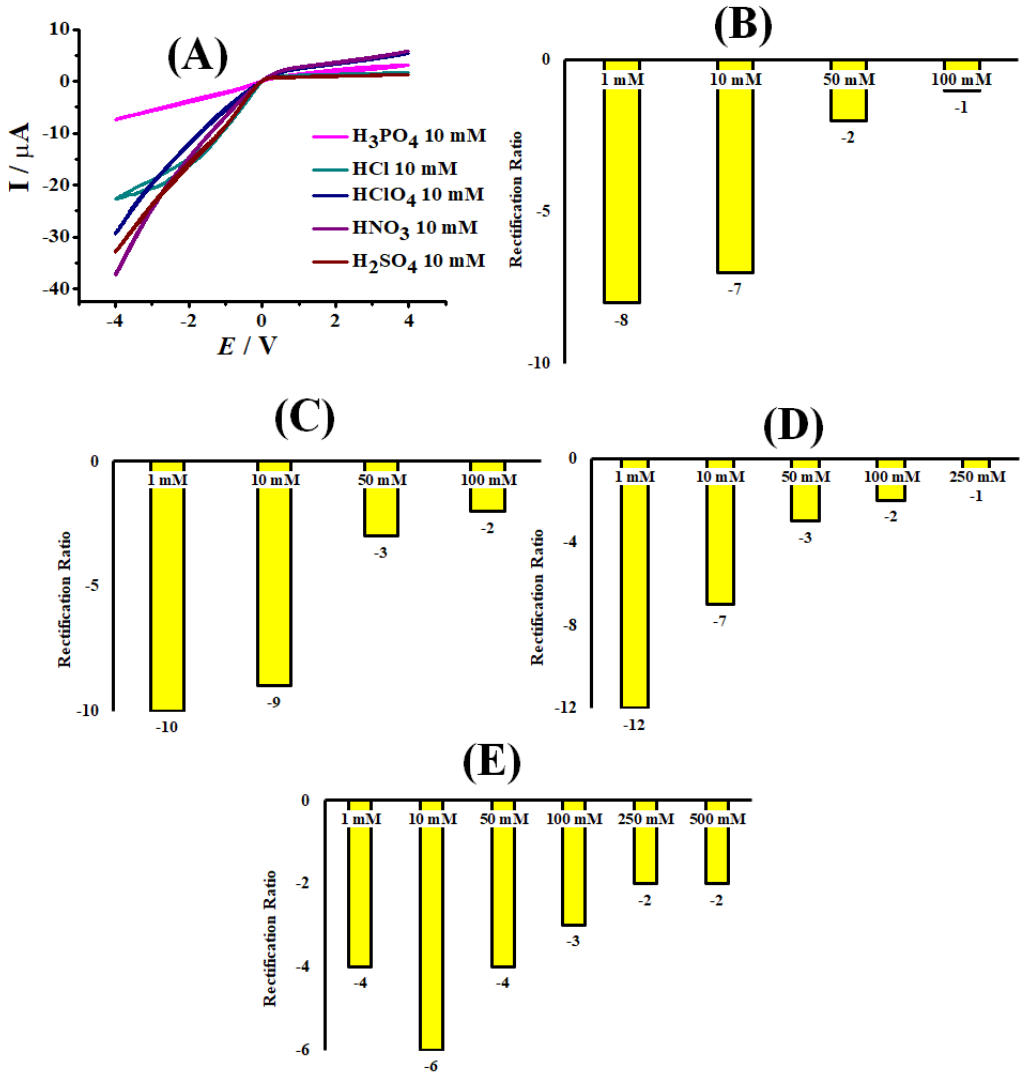

Figure 4.7. (A) Cyclic voltammograms (scan rate 100 mVs^{-1}) in aqueous 10 mM mineral acids H_3PO_4, $HClO_4$, H_2SO_4, HNO_3 in asymmetrically deposited M13 phage onto a PET substrate. The bar plots of rectification ratio data (obtained by chronoamperometry at +1V and -1V) in aqueous 10 mM mineral acids for (B) HNO_3, (C) $HClO_4$, (D) H_2SO_4, and (E) H_3PO_4.

In order to describe the resulting ionic current rectification effects from anionic diode M13 phage deposit, it is possible to calculate the rectification ratio using chronoamperometry data at switching potential +/-1 V. Figure 4.5D shows transient phenomena at chronoamperometry data for different HCl concentrations from 1-100 mM. Transient phenomena can be described by the time for on/off switching at chronoamperometry data. This is relatively short, approximately 1 s, consistent with fast-moving protons. Figure 4.5C shows a significant decrease of in rectification ratio by an increasing in concentration of aqueous HCl, although

generally the ion flux through M13 phage deposits is increased. This is probably caused by loss of semi-permeability within the M13 phage deposit at higher ionic strength of electrolyte solution. This is the reason for this decrease in ionic current rectification effects. The approximate Debye length can be calculated at an ionic strength of HCl I = 0.1 M is reduced to $\kappa^{-1} = 0.3/I^{0.5}$ = 0.95 nm and more cations can enter the microchannels within M13 phage deposits. The reduction of Debye length in microchannel causes the decrease in the anionic diode effect.

When similar experiments (voltammetry and chronoamperometry) were repeated for different types of inorganic acids (HNO_3, $HClO_4$, H_2SO_4, and H_3PO_4) for concentrations ranging from 1 mM to 100 mM or higher with M13 phage deposits, a very similar picture arises for all cases. Figure 4.7 shows a summary of voltammetry and rectification ratio data indicating that maximum rectification occurs at 1 mM or 10 mM electrolyte concentration for all cases of different types of inorganic acid with a rectification ratio of typically 10 (at switching potential +/- 1V during chronoamperometry). In general, an increase in ionic strength of different type of inorganic acids leads to a loss in ionic current rectification effect caused by semi-permeability of M13 phage deposits. There is considerable interest in investigating the additional effects of ionic current rectification behaviour of M13 phage deposits with other additional ionic solution species (interferences). In the next sections of this chapter, the focus is on the impact of additional cationic species in acidic condition on the ionic current rectification effect with M13 phage deposit.

4.3.3. Ionic Rectifier Effect on M13 Phage Deposits: Case for an Additional Cationic Guest

Initial exploratory experiments were conducted with Fe(III) or Cu(II) cations in aqueous 10 mM hydrochloric acid. Experiments with these species indicated that they have a negligible effect in the ion transport within the M13 phage material, probably due to the formation of anionic complexes such as $FeCl_4^-$ or $CuCl_4^{2-}$. The appearance of voltammetric data (cyclic voltammetry and choronoamperometry) and the calculated rectification ratio were essentially

unaffected. However, when the experiments were using aqueous 10 mM $HClO_4$ without presence of chloride, an additional cationic species added into aqueous acidic media in the working electrode compartment can result in a characteristic change in ionic rectifier behaviour.

The diode characteristics with M13 phage deposits is altered when the experiments were using 10 mM $HClO_4$ electrolyte solution with an additional Cu^{2+} cations in mM concentration range. Figure 4.8 shows a summary of voltammetric data for additional $Cu(ClO_4)_2$ in a concentration range from 62 μM to 5 mM added into the working electrode compartment with the M13 phage deposit always on this side. Initially, the current in the open state of the diode in negative applied potential range decreases with Cu^{2+} addition. A minimum in current response in open state of diode in negative applied potential range is reached with 0.5 mM $Cu(ClO_4)_2$ was added into the working electrode compartment. The minimum current in open state of M13 phage diode corresponds to the minimum value in the rectification ratio. Figure 4.8 shows the plot of the rectification ratio using M13 phage deposits with natural logarithm of Cu^{2+} in mM concentration range for switching potential +/-1 V (Figure 4.8C) and for +/-4 V (Figure 4.8D). The higher voltage (+/-4 V) applied during chronoamperometry gives more clear representation of the anionic diode characteristics with M13 phage deposits. It can be assumed that the change in semi-permeability of phage films is triggered with the addition of Cu^{2+} into the micropore channels created by $HClO_4$ treatment to M13 phage deposits. When the added concentration of $Cu(ClO_4)_2$ reached 0.5 mM, the anionic diode effect of M13 phage deposits is almost lost (the rectification ratio is at minimum). This is possibly due to Cu^{2+} binding to amine and/or carboxylate sites at the pVIII protein surface of M13 phage and decreasing the surface charge thus lowering the anion conductivity. The anionic diode unexpectedly is recovered when the Cu^{2+} concentration further increased. The rectification ratio in switching potential +/- 1 V and +/- 4V is also recovered when the added concentration of Cu^{2+} above 0.5 mM.

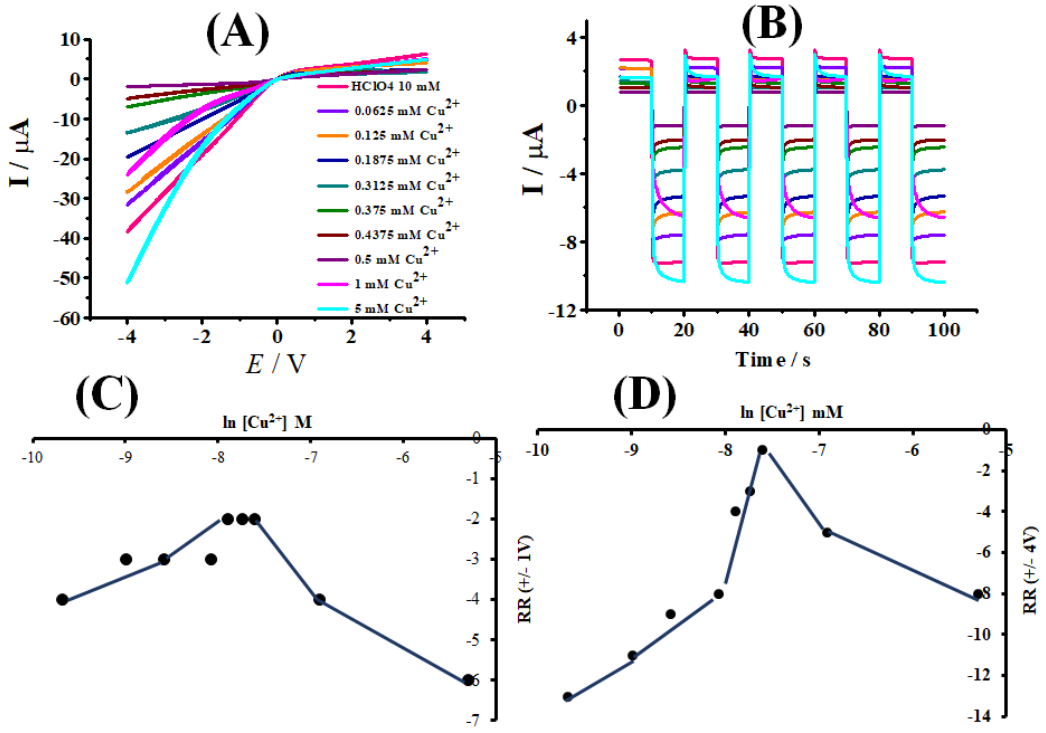

Figure 4.8. (A) Cyclic voltammograms (scan rate 50 mV s^{-1}) for asymmetrically deposited M13 phage on a 20 µm diameter PET microhole immersed in 10 mM $HClO_4$ with additions of different concentrations of Cu^{2+}. (B) As before, but for chronoamperometry data (switching between -1 and +1 V). (C) Plot of rectification ratio (at switching potential +/-1 V) versus copper concentration. (D) As before but for switching potential +/-4 V versus copper concentration. Lines in Figure C and D are shown to guide the eyes.

The ion flux through M13 phage deposits can be investigated as a function of time in chronoamperometry experiments. Figure 4.8B shows chrono-amperometry data as a function of current response to added $Cu(ClO_4)_2$ concentration in 10 mM $HClO_4$ media. In the presence of $HClO_4$ media without added Cu^{2+} in the working electrode compartment, there is a fast transient with equilibrium reached almost instantly. This is due to proton diffusion through microchannel of M13 deposit being relatively fast and changes in phage protonation are rapidly adjusted after switching the potential during chronoamperometry experiment. When the small amounts of Cu^{2+} are added into $HClO_4$ media, the transient phenomena at both positive and negative currents display falling transient characteristics. This implies that the current is initially high then drops down to a dynamic equilibrium value and consistent with a low population of less mobile Cu^{2+}

in the M13 phage deposits competing with the process of faster protonation at the protein surface. However, when the added concentration of Cu^{2+} is beyond 0.5 mM, the current transients at chronoamperometry data show rising characteristics at the applied negative potential. The concentration of Cu^{2+} above 0.5 mM is sufficiently high to dominate the charge at the pVIII protein surface of M13 phage and to give a Cu^{2+} based anionic diode system with slower transient characteristics.

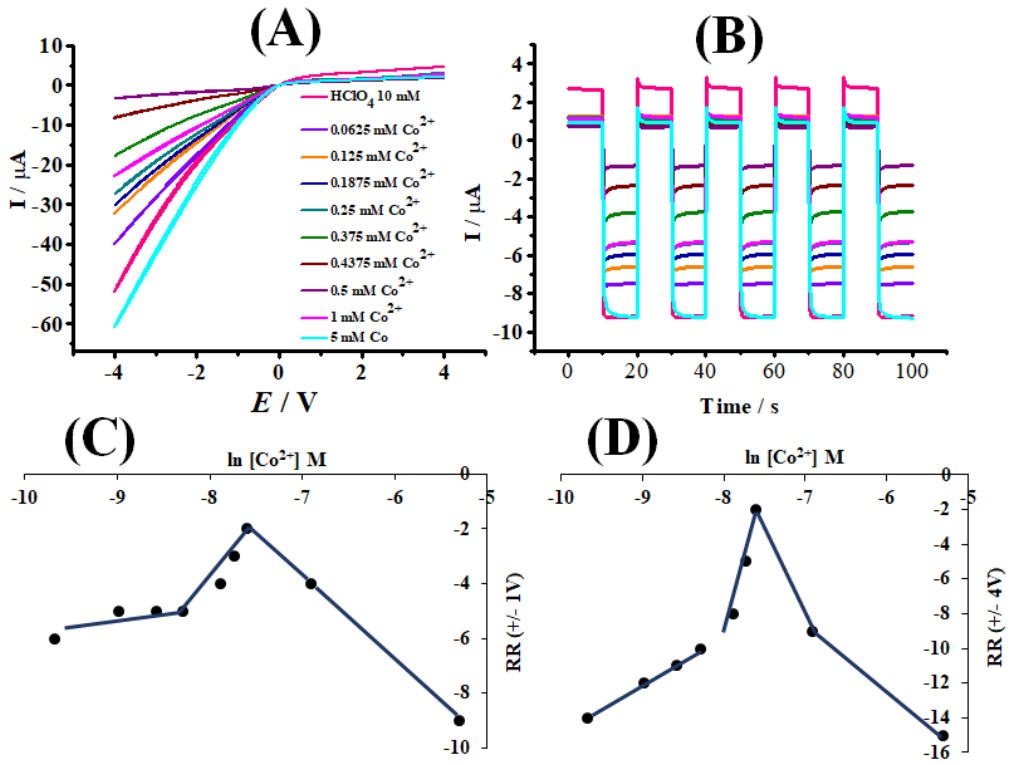

Figure 4.9. (A) Cyclic voltammograms (scan rate 50 mV s^{-1}) for asymmetrically deposited M13 phage on a 20 µm diameter PET microhole immersed in 10 mM $HClO_4$ with additions of different concentrations of Co^{2+}. (B) As before, but for chronoamperometry data (switching between -1 and +1 V). (C) Plot of rectification ratio (at switching potential +/-1 V) versus cobalt concentration. (D) As before but for switching potential +/-4 V versus cobalt concentration. Lines in Figure C and D are shown to guide the eyes.

Figure 4.9 shows voltammetric data for added Co^{2+} into 10 mM $HClO_4$ media obtained under similar conditions compare to those for Cu^{2+} experiments. The characteristics obtained from Co^{2+} are very similar to those observed for Cu^{2+}. When the Co^{2+} concentration increased, the ionic current rectification effect for M13 phage deposits is lost and at concentration Co^{2+} beyond than 0.5 mM the

anionic diode effect is restored, similar with rising transient phenomena during chronoamperometry. It can be assumed that both cation species of Cu^{2+} and Co^{2+} have similar effect on the protonated protein surface at M13 phage films, presumably as weakly interacting guests within the micropore channels of the M13 virus deposit.

In order to restore the original characteristics of ionic diode effect of M13 phage deposits, it is possible to re-immerse the phage film into pure 10 mM $HClO_4$ after addition of both Cu^{2+} and Co^{2+} ions. This is due to the binding coordination of both Cu^{2+} or Co^{2+} being probably weak and insignificant to the virus protein in order to chemically alter the surface of M13 phage deposits.

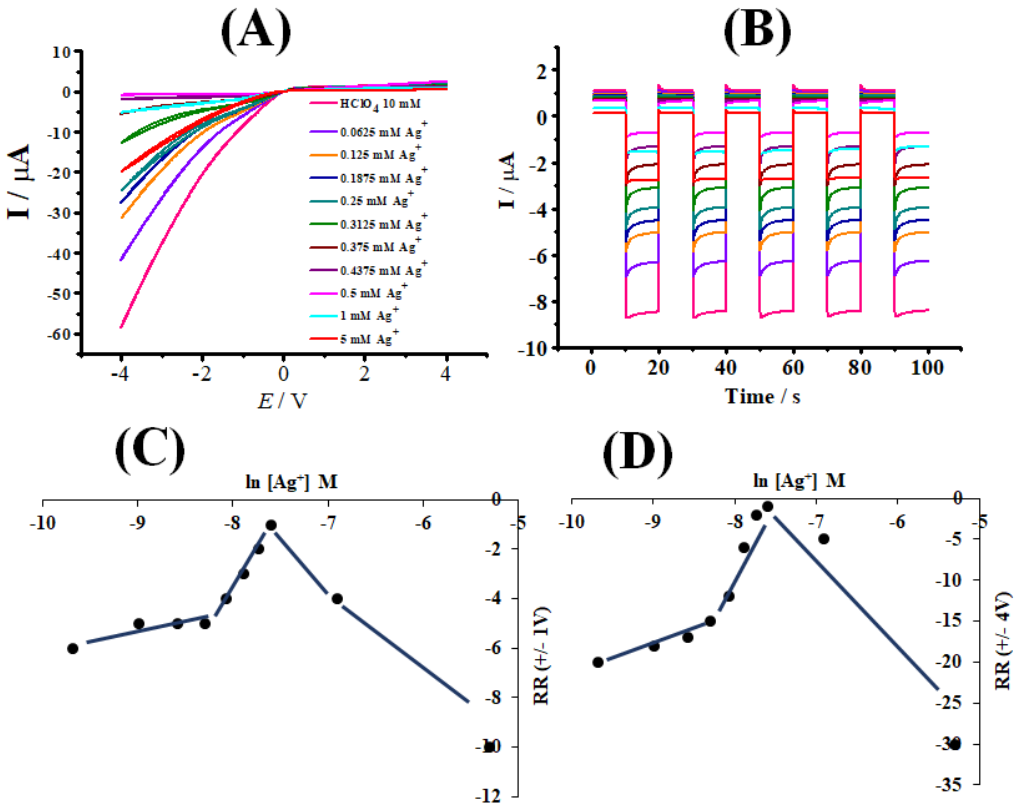

Figure 4.10. (A) Cyclic voltammograms (scan rate 50 mV s^{-1}) for asymmetrically deposited M13 phage on a 20 µm diameter PET microhole immersed in 10 mM $HClO_4$ with additions of different concentrations of Ag^+. (B) As before, but for chronoamperometry data (switching between -1 and +1 V). (C) Plot of rectification ratio (at switching potential +/-1 V) versus silver concentration. (D) As before but for switching potential +/-4 V versus silver concentration. Lines in Figure C and D are shown to guide the eyes.

A permanent change at protein surface of M13 phage deposit occurs when using Ag^+ as added cation in 10 mM $HClO_4$ media. Figure 4.10 summarises the ionic diode effect characteristics from M13 phage deposits as a function of added Ag^+ cations in 10 mM $HClO_4$ media into the working electrode compartment. It has been observed that there is a similarity between added Ag^+ with Co^{2+} or Cu^{2+} in the initial decrease of diode current response and rectification ratio to a minimum value. The current response of M13 phage diode is then followed by an increase when going beyond to the concentration of 0.5 mM Ag^+ (Figure 4.10A). The shape of transient responses from chronoamperometry (see Figure 4.10B) remains rising even the concentrations of Ag^+ at higher than 0.5 mM, but the change of diode current response from M13 deposits is also permanent with no recovery after going back to aqueous 10 mM $HClO_4$. Both effects indicate that a more permanent modification of the protein surface of M13 phage deposits and lack of competition between Ag^+ with mobile protons. It is suggested that Ag^+ tends to create bonds with amines and carboxylate moieties at the protein surface of M13 phage deposits and further modification possibly by chemical oxidation. Details of M13 phage modification at protein surfaces with Ag^+ are currently unknown but interaction of M13 with silver nanoparticles in order to enhance the fluorescence effect of M13 virus complexes has been reported by Huang et al.[19] The similarity between Cu^{2+}, Co^{2+}, and Ag^+ in the voltammetric response of the diode effect for M13 phage deposit indicates closely related mechanisms between these cations. This can be related with weak binding of these cations into the electrical double layer (affecting the Debye length) inside the microchannel formed from aggregation of M13 phage particles. Next, it is shown that a negatively charged aromatic guest species contributes to significantly different ionic diode characteristics when acting as a guest species inside the microchannel of the M13 phage aggregate.

4.3.4. Ionic Rectifier Effect on M13 Phage Deposits: Case for an Additional Anionic Guest

Next, the investigation is continued to the indigo carmine anion in order to study the ionic diode effect in the presence of hydrophobic guest molecules in ion flow within microchannel in M13 phage deposits. Hydrophobic molecules such as

indigo carmine (see molecular structure in Figure 4.11) are likely to bind to the protonated protein surface of M13 phage deposit. Therefore, indigo carmine should strongly affect ion flow within the microchannel of M13 phage and the ionic current rectification characteristics. These phenomena are explained in Figure 4.11A with adding indigo carmine in micromolar concentration range into 10 mM $HClO_4$ media into the working electrode compartment. The concentration effect of ionic diode characteristics towards indigo carmine at M13 phage deposits is 100 times stronger compared to that for cationic guests such as Ag^+ in Figure 4.10. When adding more indigo carmine to the working electrode compartment, the ionic diode current in the open state at negative potential range decreases to a minimum value at approximately 5 μM indigo carmine. The ionic diode current at negative potentials are then restored when the added concentration of indigo carmine goes beyond 5 μM. In this case, indigo carmine can directly change the charge of the protein surface of M13 phage deposits and reduce the population of mobile perchlorate anions in the microchannel space between filamentous virus particles.

Figure 4.11B shows the transient phenomena at chronoamperometry data to reveal fast switching process at potential +/-1 V between closed and open state of ionic diodes for M13 phage deposits. These transient phenomena are consistent with rapid proton exchange with indigo carmine molecules in the M13 phage deposits in the depletion region close to the microhole in PET. When the added concentration of indigo carmine higher than 5 μM, the current response of anionic diode effect is partially restored. These phenomena suggest that indigo carmine molecules remain mobile within the microchannel space between M13 virus particles and can contribute to the current response in ionic rectification effect. Figure 4.11C shows the chronoamperometry data of added indigo carmine to the 10 mM $HClO_4$ media at M13 phage deposits. In general, it has been observed that the rising current transients at chronoamperometry give indication of absence of competition to the proton uptake/release in the depletion zone within the microhole of PET.

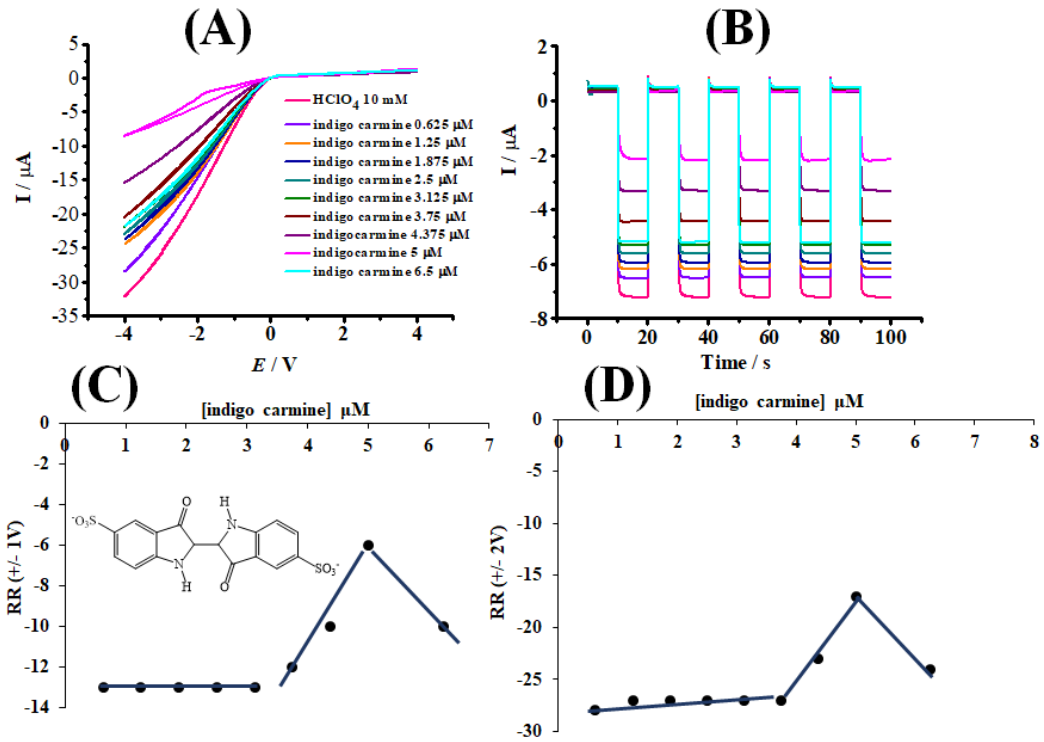

Figure 4.11. (A) Cyclic voltammograms (scan rate 50 mV s^{-1}) for asymmetrically deposited M13 phage on a 20 µm diameter PET microhole immersed in 10 mM $HClO_4$ with additions of different concentrations of indigo carmine. (B) As before, but for chronoamperometry data (switching between -1 and +1 V). (C) Plot of rectification ratio (at switching potential +/-1 V) versus indigo carmine concentration. (D) As before but for switching potential +/-4 V versus indigo carmine concentration. Lines are shown to guide the eyes.

The closed state of anionic diode of M13 phage deposits appears fundamentally insensitive for all cases of cationic and anionic guests in ion flow within microchannel space between virus particles. This is probably due to perchlorate anion diffusion dominating the process of ion accumulation and depletion effect towards the microhole in the PET substrate. However, the ion transport through microchannels in the M13 virus deposit is critical and changes in diode current in the open state of the diode in negative potential area are detected as a function of bound guest species.

The low concentration of indigo carmine (anionic guest) for binding within the microchannel of M13 phage deposits is consistent with the fact that anion semi-permeability of virus membrane is observed. Guest anions such as indigo carmine molecules can easily enter to the microchannel and bind to the protein of M13 phage

at surface deposits. The changes at proteins of M13 deposits modifies the surface charge leading to loss of anionic diode character. Figure 4.12 shows the explanation about the increase of ionic diode current by considering excess indigo carmine molecules as a mobile species similar to the perchlorate permeation through the M13 phage deposit.

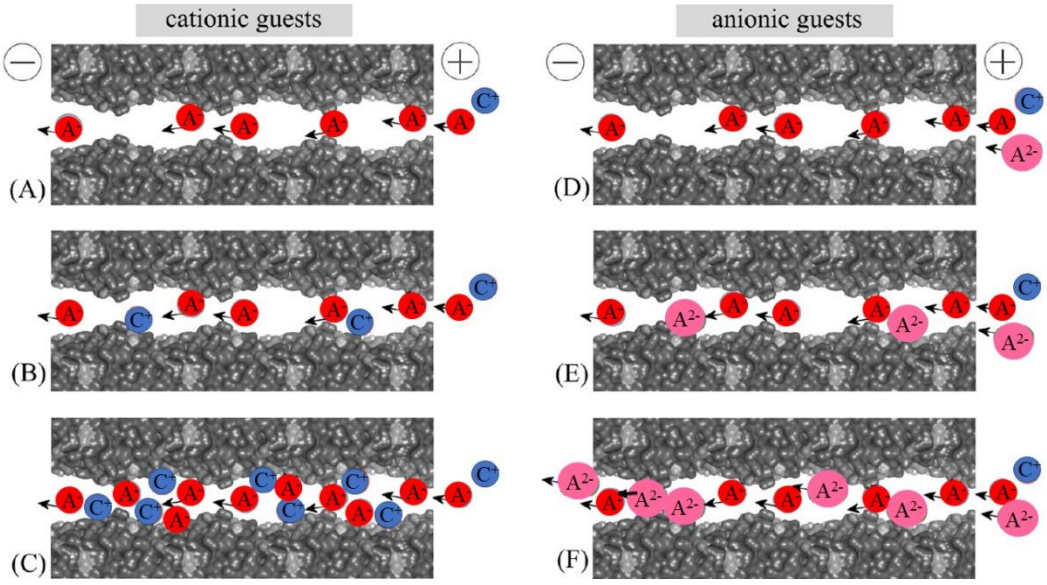

Figure 4.12. (A-C) Schematic illustration of a cationic guest species entering a microchannel initially with a blocking effect and then at higher concentration with a current enhancing effect. In (D-F) the case of an anionic guest is illustrated with initially a blocking effect followed at higher concentration with a current enhancing effect.

Based on Figure 4.12 (A-C) the access for the cationic guest species such as Cu^{2+}, Co^{2+}, or Ag^{+} to the anion selective virus film is initially at lower concentrations inhibited. The cationic guest species at concentration 0.5 mM can then enter and bind with the protein of M13 phage material. The threshold of 0.5 mM is insensitive to the chemical nature of the cations. When the cations bind to the M13 protein within the microchannel, initially it can lower the rate of transport, but then at higher concentrations the ionic diode effect restores. This could be due to dominating anion transport with excess cation binding. When the guest species either cationic or anionic is added into the counter electrode compartment of electrochemical cell, the effects towards ionic current diode remain negligible. Therefore, the contact between either cationic or anionic guest species with M13

protein virus at the surface appears to require effective exposure of the virus film to the guest ionic solution.

The specificity of binding effects to the M13 virus surface, the binding to a wider range of guest species either cationic or anionic, and the potential of the M13 phage deposits to function as a "diode sensor" with specific binding ability are still unexplored and many questions remain unanswered. Further work will be required to develop and quantify process at the M13 virus surface, based on condition of double layers, and the effects of virus surface modifications on ionic diode characteristics.

4.4. Conclusions

It has been shown that M13 phage material can aggregate with treatment in 10 mM acid and at a pH acidic of the isoelectric point at virus protein surface in order to make semi-permeable membranes. The resulting membrane of M13 phage material forms microchannel spaces between filamentous virus particles with cationic surface charges for anion conduction. Semi-permeability of M13 membranes from the aggregation of virus particles and cation exclusion effect within the microchannel is weakened when the concentration of outside electrolyte is increased.

The investigation using cyclic voltammetry and chronoamperometry technique of asymmetrically deposited M13 phage films with 20 μm diameter microhole on a PET substrate results in anionic diode behaviour. The magnitude of anionic diode effect can be quantified in terms of the rectification ratio by using chronoamperometry techniques. The effects on the rectification ratio of cationic and anionic guest species in the microchannels inside the M13 phage deposits are investigated. Cationic guest species such as Cu^{2+}, Co^{2+}, and Ag^{+} only gradually enter the micropore space within M13 phage deposits presumably due to cation exclusion phenomena inside the microchannel. All three cations (Cu^{2+}, Co^{2+}, and Ag^{+}) show a similar minimum rectification effect at 0.5 mM concentration, which is linked to access and surface attachment of the cationic species to the protein

surface of M13 phages. In comparison, anionic guest molecules such as indigo carmine provide a minimum of rectification effect at 0.5 μM and this is due to the blocking effect of indigo carmine binding in micropores inside M13 phage deposits. When the concentration of indigo carmine increased, the mobility of ions inside microchannels become higher with most binding sites inside the M13 micropores occupied and therefore the ionic diode effect restores.

Bacteriophage materials offer a very interesting nano-building block for membranes and in the future a more systematic surface modification approach will be possible to develop more suitable and robust membrane materials also for applications in neutral solution environments. This could lead to innovative desalination and water purification technology or to new types of sensors. Further work will be required to further explore the effects of electrolytes either cationic or anionic guest species and surface modifications towards protein surface functionality at M13 phage deposits.

4.5. References

1 Szot-Karpinska, K., Lesniewski, A., Jonsson-Niedziolka, M., Marken, F., Niedziolka-Jonsson, J. *Sens. Actuators B Chem.* **2019**, *287*, 78–85.

2 Yang, S. H., Chung, W.-J., McFarland, S., Lee, S.-W. *The Chemical Record*. **2013**. *13*, 43-59.

3 Smith, G.P., Petrenko, V.A. *Chem. Rev*. **1997**, *97*, 391-410.

4 Chung, W.J., Lee, D.Y., Yoo, S.Y. *Internat. J. Nanomedicine* **2014**, *9*, 5825–5836.

5 Lee, B.Y., Zhang, J.X., Zueger, C., Chung, W.J., Yoo, S.Y., Wang, E., Meyer, J., Ramesh, R., Lee, S.W. *Nature Nanotechnol.* **2012**, *7*, 351–356.

6 Jazwinski, S.M., Marco, R., Kornberg, A. *PNAS* **1973**, *70*, 205–209.

7 Cao, B.R.; Xu, H.; Mao, C.B. *Microsc Res Tech.* **2011**, *74*, 627–635.

8 Johnsson, K., Ge, L. *Curr. Top. Microbiol. Immunol.* **1999**. *243*, 87-105.

9 Goldman, E. R., Pazirandeh, M. P., Mauro, J. M., King, K. D., Frey, J. C., Anderson, G. P. *J. Mol. Recognit.* **2000**. *13*, 382-387.

10 Atkins, P.W.; de Paula, J., *Physical Chemistry*, Oxford University Press, Oxford, 2006, p. 168.

11 Marvin, D.A., Hale, R. D. *J. Mol. Biol.* **1994**. *235*, 260-286.

12 www.sasview.org.

13 Specthrie, L., Bullitt, E.; Horiuchi, K.; Model, P.; Russel, M.; Makowski, L. *J. Molecular Biology.* **1992**, *228*, 720–724.

14 Brown, R., Madrid, E., Castaing, R., Stone, J.M., Squires, A.M., Edler, K.J. Takashina, K., Marken, F. *ChemElectroChem* **2017**, *4*, 1172–1180.

15 Aaronson, B.D.B.; Wigmore, D.; Johns, M.A.; Scott, J.L.; Polikarpov, I.; Marken, F. *Analyst* **2017**, *142*, 3707–3714.

16 Mathwig, K., Aaronson, B.D.B., Marken, F. *ChemElectroChem* **2018**, *5*, 897–901.

17 Tshwenya, L. Marken, F., Arotiba, O.A. *ChemElectroChem* **2019**, *6*, 3145–3153.

18 He, D., Madrid, E., Aaronson, B.D.B., Fan, L., Doughty, J., Mathwig, K., Bond, A.M., McKeown, N.B., Marken, F. *ACS Appl. Mater. Interfaces* **2017**, *9*, 11272–11278.

19 Huang, S., Qi, J., deQuilettes, D.W., Huang, M., Lin, C.-W., Bardhan, N.M., Dang, X., Bulovic, V., Belcher, A.M. *Small* **2019**, *15*, 1901233.

Chapter 5

Two Dimensional Nanomaterials: Ionic Rectification based on Graphene Oxide

Contents

Chapter Abstract

A film of graphene oxide is applied to a 6 μm thick poly-ethylene-terephthalate (PET) substrate with 20 μm diameter microhole and immersed in aqueous electrolyte solution and shows strong cationic diode effects. Strong cationic diode effects are observed even at high ionic strength (0.5 M) of electrolyte solution. The nanochannels in graphene oxide contributes to the cation transport to give cationic diode effects through the graphene oxide deposit. The parameters that have been investigated during this cationic diode study using graphene oxide membranes were (i) switching between open and closed states, (ii) microhole size effects, and (iii) time dependent phenomena. Data are explained based on a simplified model theory for migration-diffusion within the microhole region. Competition between Na^+ transport and field-driven heterolytic water splitting are observed in aqueous NaCl solution but shown to be significant only at very low ionic strength (<1 mM). Therefore, nanostructured graphene oxide is demonstrated to exhibit close to ideal behavior for future application in ionic diode desalination of seawater.

Chapter Publications

Part of this chapter have been published in:

B. R. Putra, K. J. Aoki, J. Chen, F. Marken. Cationic Rectifier Based on a Graphene Oxide-Covered Microhole: Theory and Experiment. *Langmuir*, **2019**, 33, 2055-2065.

Acknowledgement

Prof. Koichi J. Aoki and Prof. Jingyuan Chen from University of Fukui Japan are acknowledged for providing the theoretical model for ionic diode studies based on graphene oxide membranes.

5.1. Introduction

This chapter focuses on ion transport behaviour through graphene oxide films deposited onto a 6 μm thick poly-(ethylene-terephthalate) (PET) substrate with a 20 μm microhole. Recently, graphene oxide (a subclass of two-dimensional materials) emerged as highly interesting class of nanomaterial that offer exciting prospects for new applications.[1] Graphene oxides have been proposed as an effective water purification membrane component due to good chemical and mechanical stability.[2] Graphene oxide materials also can be formed into layered membranes that offer selectivity in salt separation and transport.[3]

Molecular structures of graphene oxides (see drawing in Figure 5.1A) lead to the possibility of interaction of cations with π-electrons of the graphene oxide layer. This type of interaction is expected to influence the transport of cations within the nanopores of graphene oxide membrane.[4] The previous electrochemical studies of ion transport using graphene oxide membrane and its composites have been suggested a relatively high proton conductivity.[5,6] It has been proposed that the distinctive properties of the graphene oxide nanosheet structure should be linked to the presence of nanochannels and different types of structural regions. First, the regions of pristine graphene causing strong interactions between interlayer of nanosheet inside the membrane. Second, the regions of oxidized graphene allowing proton and water transport through membrane nanochannel. Third, the holes and defects in the nanosheet helping to make more effective ion transport through the graphene oxide membrane. A review has appeared summarizing graphene oxide membrane transport phenomena with tunable semi-permeability properties.[7]

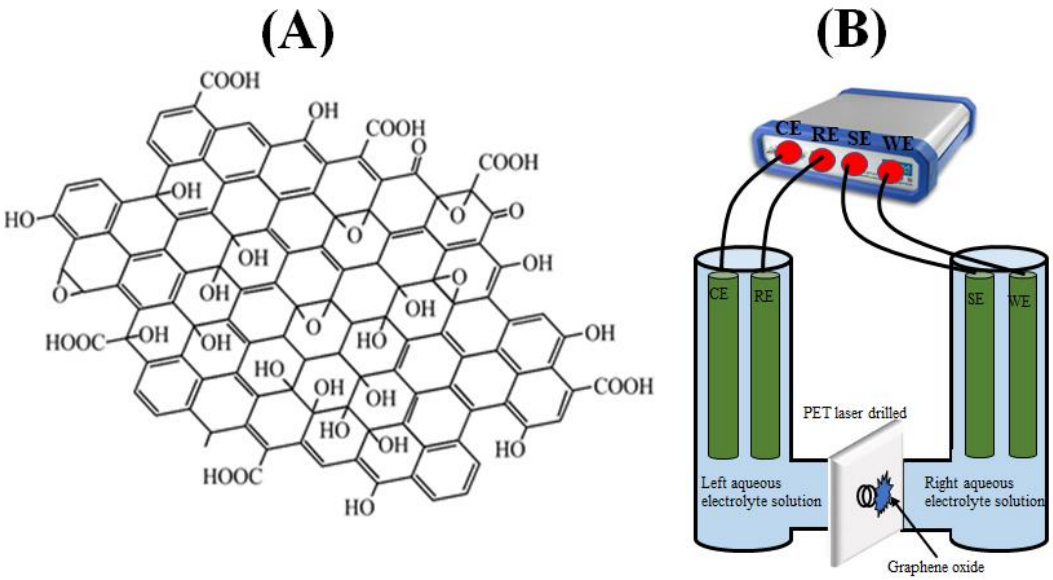

Figure 5.1. (A) Schematic representation of a graphene oxide structure and (B) Schematic description of the classic 4-electrode cell for membrane voltammetry (counter electrode CE, reference electrode RE, sense electrode SE, working electrode WE) with graphene oxide deposits on 20 μm diameter microhole PET film with 6 μm thickness.

Most of the published work on graphene oxide membranes focuses on desalination with filtration and ion retention effects rather than potential driven processes of water treatment using a membrane. Graphene oxide membranes could potentially function as a "molecular pump" for water, if the potential driven ion transport associated with the water transport could be performed uni-directional or "diode-like". From the previous investigations, the diode-like behaviour has been reported for graphene oxide materials interfaced with graphene and coated with electrolyte[8]. In this chapter, the diode-like behaviour or ionic rectification effect is observed when graphene oxide materials deposited asymmetrically onto 6 μm thick poly-ethyleneterephthalate (PET) with 20 μm diameter microhole.

In order to investigate the ionic rectification effect for graphene oxide deposits, a four-electrode cell was employed in the experiments. The conventional two-compartment four-electrode configuration (see in Figure 5.1B) allows the potential to be applied to the graphene oxide membrane and current measured

during the ionic rectification studies. In the initial studies using aqueous HCl, it is assumed that the ion transport is dominated by proton transport through the graphene oxide deposit. Then the studies were continued to investigate the rectification effects with different aqueous electrolytes and with different ionic strengths. The rectification effects are shown to be dominated by cation transport in semi-permeable graphene oxide even under relatively high ionic strength electrolyte conditions. It is shown that only under lower ionic strength electrolyte conditions (<1 mM), there is a significant level of competing water heterolysis to protons and hydroxide as a competing process to ion insertion and transfer via graphene oxide.

Here it is assumed as an initial hypothesis that the diode effect is dominated by the diffusion-migration conditions within the asymmetrically deposited graphene oxide onto microhole in the PET film. This process is based on graphene oxide, which acts as a very good semi-permeable materials for cation conduction with good anion rejection even at high ionic strength. To rationalize the observations with cyclic voltammograms and the current rectification effects, a simplified theoretical model based on analytical theory is adopted.

5.2. Experimental

5.2.1. Chemical Reagents

Graphene oxide (2 mg/mL, dispersion in H_2O, Aldrich 763705), concentrated hydrochloric acid (37%), agarose, and rhodamine B (97%) were obtained from Sigma-Aldrich Ltd. and used without further purification. Aqueous solutions were prepared with deionized water with resistivity of 18.2 MΩ cm under ambient conditions from an ELGA Purelab Classic System for water filtration.

5.2.2. Instrumentation

Microscopy imaging was performed using JEOL JEM-2100 Plus Transmission electron microscopy (TEM) instrument with 200 kV maximum operating voltage. A Carl Zeiss Confocal Scanning Microscope LSM 880 with airyscan and multiphoton laser was used in order to obtain fluorescence images. An

Ivium Compactstat potensiostat system (The Netherlands) was used to record all electrochemical data (voltammetry, chronoamperometry, and impedance experiments) at T = 20 ± 2 °C. A classic 4-electrode electrochemical cell configuration was employed during the electrochemical experiments. The membrane separates two tubular half-cells (15 mm diameter, see Figure 5.1B), one with Pt wire working and KCl-saturated calomel (SCE) sense electrode (right in Figure 5.1B) and the other with SCE reference electrode and Pt wire counter electrode (left in Figure 5.1B). In electrochemical measurements, the working electrode was always located on the side of the graphene oxide film deposit. In some measurements, additional battery powered pH-probes (Voltcraft PH-100ATC) were positioned in left and right compartment close to the graphene oxide membrane.

5.2.3. Procedures of Graphene Oxide Deposition

During the electrochemical studies of graphene oxide, polyethylene-terephthalate (PET) films of 6 μm thickness with laser-drilled 20 μm diameter microhole were used as substrates for graphene oxide deposit. Before deposition of graphene oxide, a microscopy glass slide was pre-coated with a thin layer of 1% agarose gel. The PET film was placed onto the gel to prevent graphene oxide solution from entering/crossing the microhole. Approximately 4 μL volume of graphene oxide solution (2 mg/mL in water) was applied to the PET film and with a glass rod the graphene oxide was spread evenly over ca. 1 cm^2 of the PET surface. After drying in room temperature, the PET film contains graphene oxide was removed from the agarose gel and stored under dry conditions. For electrochemical measurements the film was mounted in a U-cell (Figure 5.1B) between the two glass flanges with the help of some Dow-Corning vacuum grease as sealant.

5.3. Summary of Theory for Ionic Diodes (Koichi Aoki and Jingyuan Chen)

The mechanism of ionic diode phenomena in electrically conducting solution system can often be related to more than one mechanism, for example in $KClO_4$ precipitation[9]. The behaviour of ionic diodes using asymmetrically deposited semipermeable material is dependent on the geometry of the microhole

and materials employed. The critical part of the ionic diode mechanism based on semipermeable membrane is due to diffusion-migration of ions within a cylindrical microhole region in contact with graphene oxide deposit at one end and in contact to bulk electrolyte solution at the other end (see Figure 5.2A). The microhole is positioned as a cylindrical space between a graphene oxide deposit as semi-permeable membrane and a hypothetical dividing surface indicating the interface to the bulk electrolyte (see area *S* in Figure 5.2A). A theoretical model was developed for the case of a cation (or proton) exchange membrane, which during current flow affects concentration gradients of both the cation and the anion in the microhole region (whilst maintaining electroneutrality). A voltage is applied to the two solution compartments (here indicated as a simplified two-electrode system). As current flows driven by potential, the electrolyte concentration within the microhole region changes. In other words, the charge is carried with mobile ions outside of the microhole depending on the direction of the current; the mobile ion being the cation within the membrane in the left direction (Figure 5.2A), being in the bulk electrolyte in the right direction. The current is controlled by an electric resistance within the microhole, which is variable and dependent on the applied voltage. This switching of resistivity with applied potential is observed as “open” and “closed” states of the ionic diode or ionic rectifier.

The simplified theory predicts the diode current , $I = -AFf$, as given by

$$I = (AF^2D\phi_L/LRT)(c_m - c_s e^{-u})/(1 - e^{-u}) \quad (1)$$

When $|u|$ is an extremely large value (the diode is open), Eq. 1 for $u > 0$ tends to

$$I = (AF^2D/LRT)c_m \phi_L \quad (2)$$

while that for $u < 0$ (the diode is closed) goes to

$$I = (AF^2D/LRT)c_s \phi_L \quad (3)$$

Both expressions for the current at high overpotential represent a linear (Ohmic) characteristic in the variation of I with ϕ_L, although a point of undefined current remains at $u = 0$. The comparison of Eq. 2 and 3 suggests the asymmetric current-voltage curves. By taking the ratio of Eq. 2 to 3, the rectification ratio is estimated as c_m/c_s, which is the concentration ratio of the mobile ion in the ion-exchange membrane ion to that in the bulk. A plot of the current versus potential based on equation 1 is shown in Figure 5.2B. Here, c_s = 10 mM has been selected with $D = 10^{-9}$ m^2s^{-1} and $A = \pi r^2$ with a microhole radius r = 10 μm. The apparent membrane concentration c_m = 0.2 M is selected to approximately represent the conditions in experimental data (*vide infra*). Note that the currents are predicted to scale linearly with microhole area A or with r^2 with all other parameters remaining. The rectification ratio is predicted to be independent of microhole diameter.

Since the applied voltage necessarily includes an additional voltage loss from the solution and the membrane as well as further access diffusional losses, the equations given above have to be considered only as a first approximation. The voltage drop is given by $V = I\,(R_{\text{microhole}} + R_{\text{additional}})$, where $R_{\text{microhole}}$ is the resistance ϕ_L/I as given in Eq. 1. So far as difference in the slope is concerned, in the linear domain, Eq. 2 and 3 are valid. In other words, diffusion-only processes can contribute only to the restricted potential domain of $|V| < 0.1$ V. Concentration profiles within the microhole are expressed by

$$c/c_s = [(c_m/c_s)(1-e^{-xu/L}) + e^{-xu/L} - e^{-u}]/(1 - e^{-u}) \qquad (4)$$

Calculated concentration profiles are plotted against x/L in Figure 5.2C for four values of ϕ_L. When electric migration does not contribute to the current, the profile is a line ($\phi_L = 0$, not shown), as is obvious for conventional steady-state diffusion. With an increase in the contribution of the electric field by positive voltage, the cations and anions move largely toward $x = 0$, exhibiting concave curves and causing accumulation of salt into the microhole. The application of the opposite voltage causes a depletion of salt in the microhole (Figure 5.2C). Note that currents in Figure 5.2B should scale with the square of microhole radius.

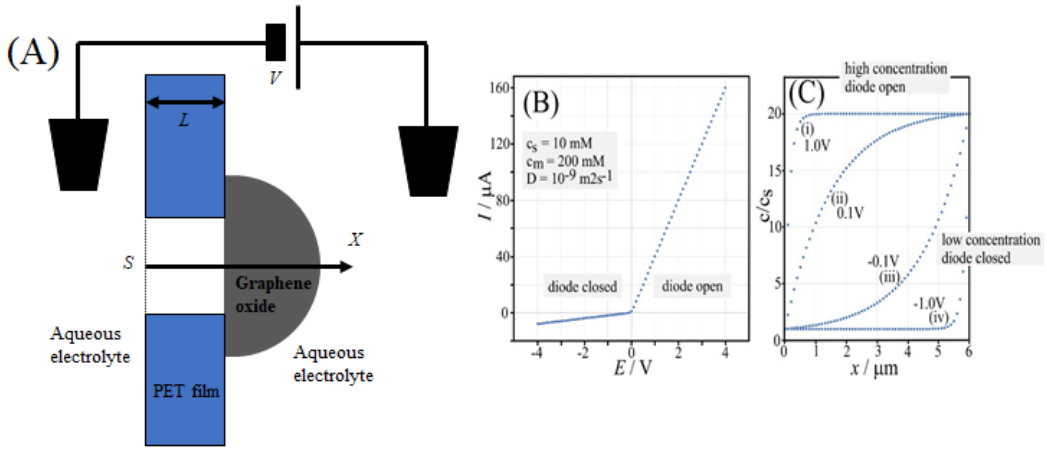

Figure 5.2. (A) Definition of the cylindrical geometry within the microhole based on surface S and length x. Note that the graphene oxide is always situated in the working electrode and therefore a positive applied potential is associated with cation moving from the right into the left compartment. Figure (B) and (C) taken from Langmuir 2019, 35, 2055-2065 and developed by Koichi Aoki and Jingyuan Chen. (B) Plot of calculated current from Equation 1 versus applied potential for the case $c_m = 200$ mM and $c_s = 10$ mM. (C) Plot of concentration profiles calculated from Eq (4) at $\phi_L = 1.0$ V, 0.1 V, -0.1 V -1.0 V for $L = 6$ µm.

There are some limitations to quantitative insights due to simplifications made in the present model: (A) If the microhole is so narrow that electric migration force varies with the distance normal to x-direction (e.g. in nanopores), it is necessary to take into account the surface effects such as zeta potential. This subject is beyond the present work. (B) The model does not include mass transport or polarization in the two outer domains of the microhole ($x < 0$ and $x > L$). Diffusion in the outer domains will have to be taken into account due to access diffusion effects. That is, the assumption that c_s = constant at $x = 0$ is not strictly valid and in reality the depletion of salt in the microhole will progress well below $c/c_s = 1$ (see Figure 5.2C), if the applied potential is sufficiently negative. (C) The assumption of the Laplace equation validity rather than the Poisson's equation validity is based on the equi-concentrations of the anion and the cation (electroneutrality), which is fulfilled at micrometer scale. The Debye length in 10 mM aqueous solution is only

ca. 4 nm. This length is too short to consider a domain of x for the difference in concentrations. Therefore, the Laplace equation is valid.

Comparison of theory and data obtained for graphene oxide (*vide infra*) shows that equations 1 and 4 are beneficial mainly at qualitative level due to some oversimplifications, but the description of the underlying rectification mechanism and the conditions within the microhole region are very useful to rationalize and predict the observed ionic diode effects.

Table 5.1. Nomenclature

A	area of the cross-section of the microhole
c	concentration of the cation in the microhole
c_m	concentration of the cation in the adjacent cationic exchange membrane
c_s	concentration of the cation in the adjacent solution bulk
D	diffusion coefficient of the cation or anion
f	flux of the cation in the x-direction
F	Faraday constant
I	total current
L	thickness of the film through which the microhole is made
R	gas constant
R_h	resistance in the hole, defined by ϕ_L/I
T	absolute temperature
u	dimensionless potential, $\phi_L F/RT$
x	axis along the hole
V	voltage between the two cells
ϕ	electric potential in the solution
ϕ_L	electric potential at $x = L$

5.4. Results and Discussion

5.4.1. Formation and Characterisation of Graphene Oxide Deposit with Fluorescence Imaging

Figure 5.3A shows the typical of transmission electron micrograph from commercial graphene oxide material dispersed in aqueous solution typically consists of 2-10 μm size of single and few-layer nanosheets. In order to achieve asymmetric deposition and to stop penetration of graphene oxide below the microhole, agarose gel substrate was used to deposit colloidal suspension of graphene oxide nanosheets onto a PET film with 20 μm diameter microhole. A fluorescent film of graphene oxide was obtained when it was mixed with small amounts of rhodamine B dye to give better visualization using fluorescence microscopy. Figure 5.3B shows the stacked image of the microhole region with graphene oxide deposit in the x-y plane using the fluorescence microscopy. The microhole region seems bright according to the white region in Figure 5.3B due to the light refraction effects and also the red region in Figure 5.3B indicates the fluorescence in this region is improved. The continuous graphene oxide film coated over the microhole (with an average thickness ca. 9-12 μm) can be seen in the cross-sectional data.

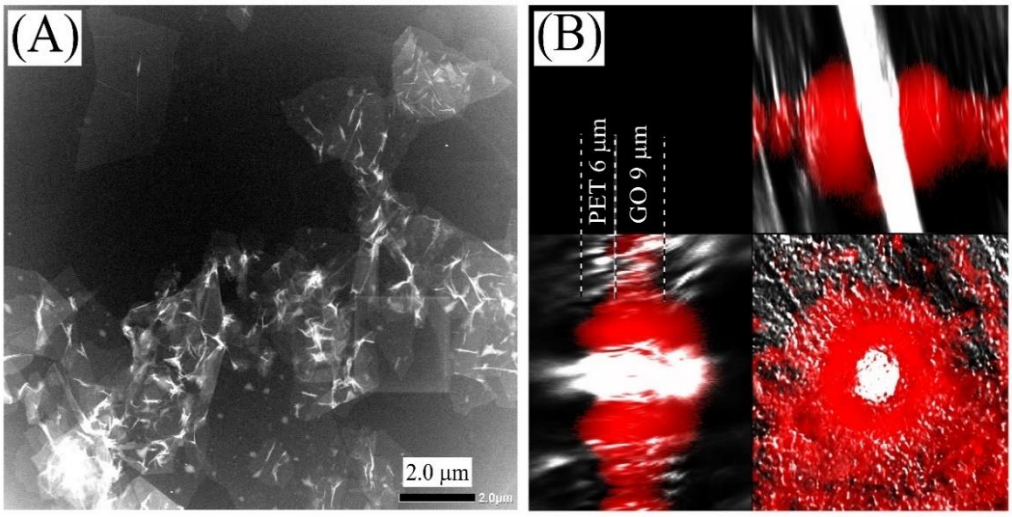

Figure 5.3. (A) Image of scanning transition electron microscopy (STEM) showing flakes of graphene oxide flakes typically 2 to 10 μm size and (B) the orthogonal fluorescence image stack based on a graphene oxide film with rhodamine B dye. The thickness of the graphene oxide (GO) layer is estimated as 9-12 μm with the 20 μm hole is clearly seen.

5.4.2. Electrochemical Characterisation of Ionic Diode Effects Based on Graphene Oxide Deposit

Figure 5.4A shows the current responses for a graphene oxide deposit (always placed on the side of the working electrode compartment; see Figure 5.1A) when it is immersed into HCl 10 mM on both sides. When the amount of graphene oxide is doubled, the current reproducibility is particularly insensitive. This current observation is in agreement with the diode character following the simplified theoretical idea of electrolyte accumulation/depletion within the microhole rather than the potential drop across the graphene oxide deposit. When both compartments were filled with aqueous 10 mM HCl, the current response increases in the positive applied potential to the film and only a much less current is observed with a negative applied potential. The current response from both positive and negative applied potential appear to be consistent with the developed theory in Figure 5.2B. This behavior characteristic can be described as ionic diode or ionic current rectification.

In Figure 5.2B, the theory suggests for cation concentration in the bulk solution (c_s) equals to 10 mM and the cation concentration in the graphene oxide membrane (c_m) 200 mM a rectification ratio of 20. When compared to the experiment in Figure 5.4F, there is good compatibility with a rectification ratio of 28 using HCl 10 mM. However, one still has to be careful with oversimplifying assumptions in the theory. An additional effect occurs at both the graphene oxide – electrolyte interface and the access diffusion of ions region close to surface *S* (Figure 5.2A). In Figure 5.4A, three consecutive potential cycles with scan rate 50 mVs^{-1} suggest nearly the behaviour of time independence or steady state. When the scan rate is increased to 500 mVs^{-1} in Figure 5.4B, the voltammogram shows a slight loop in the current at positive applied potential indicating the current increases with time. In Figure 5.4C with faster scan rate 4000 mVs^{-1}, every subsequent potential cycle shows an increasing current. As a result, the steady-state character is lost when the experiment runs typically at a scan rate of 4000 mVs^{-1} or a typical time regime of 1 s. Also, in this high scan rate, a small negative current peak appears at -0.3 V suggesting that a “switching” process between open and closed diode occurs approximately over 0.2 s. This switching time is likely to be

connected with the diffusion of cations and anions to and from the microhole region based on the assumption of a diffusion-migration mechanism. This is also confirmed by changes in switching time data for different microhole diameters in Figure 5.5B. However, Li et al.[10] also reported the related “hysteresis” effects for nano-fluidic diodes based on nanopipettes of typically 60 nm orifice diameter on a similar time scale.

Wang et al.[11] also observed similar phenomena in single conical nanopores and can be attributed to time-dependent compositional changes within the nanopore double layer. The similar behaviour of time-dependent compositional changes could also occur within the graphene oxide film and then resulting in phenomena like those observed in Figure 5.4C. Clearly, these phenomena are the sign of the development of significant concentration gradients within the graphene oxide film, but currently not readily accessible by experiment.

In Figure 5.4E shows the chronoamperometry data to indicate the switching speed of the ionic diode behaviour. The switching of diode occurs within 1 s from positive applied potentials to negative applied potentials and take approximately 10-20 s for steady state to be fully reached. Figure 5.4F shows a plot of the rectification ratio (absolute current at switching potential +/- 1V) *versus* HCl concentration based on chronoamperometry data. It is clearly observed that at higher concentration of HCl, a decline of rectification ratio occurs. This phenomenon could be associated with the gradual loss of semipermeability graphene oxide membrane which was assumed in theoretical model to be retained.

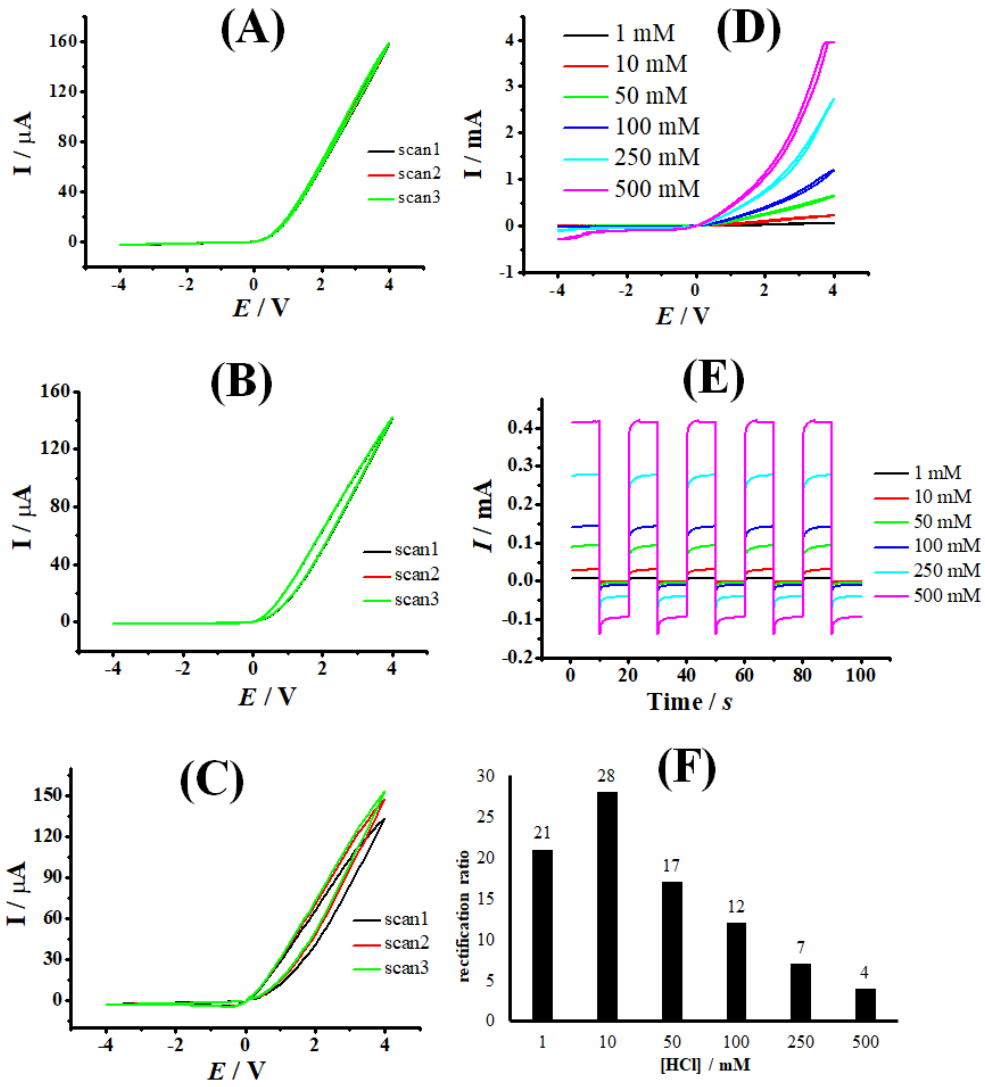

Figure 5.4. (A) Cyclic voltammograms of graphene oxide deposit with 3 cycles at scan rate 50 mVs^{-1} on a 20 µm diameter microhole in a PET substrate immersed in 10 mM aqueous HCl. (B) As above, with scan rate 500 mVs^{-1}. (C) As above, with scan rate 4000 mVs^{-1}. (D) As above, scan rate 50 mVs^{-1} for a HCl concentration of 1, 10, 50, 100, 250, 500 mM. (E) Chronoamperometry data stepping from +1 V to -1V. (F) Plot of the rectification ratio (the absolute of the current at +1 V divided by the current at -1 V) *versus* concentration.

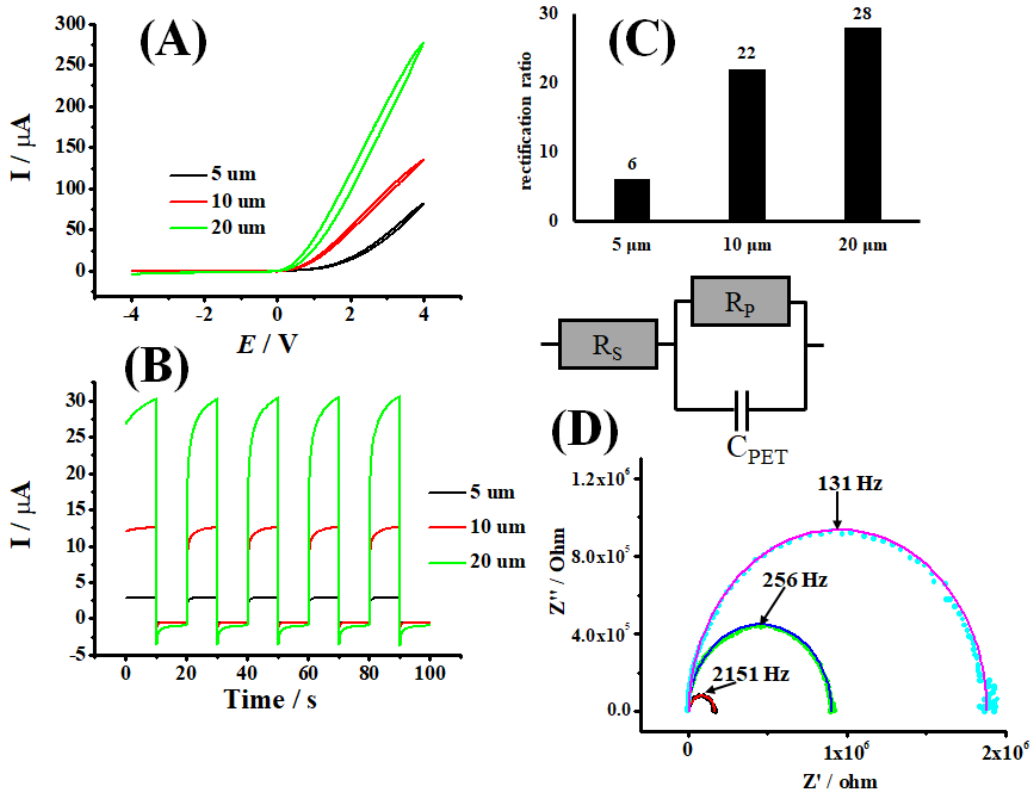

Figure 5.5. (A) Cyclic voltammograms data with scan rate 50 mVs^{-1} for a graphene oxide deposit on a 5, 10, 20 µm diameter microhole in a PET substrate immersed in 10 mM aqueous HCl, (B) Chronoamperometry data stepping from +1 V to -1V, (C) Plot of the rectification ratio (+/-1 V) *versus* microhole diameter. (C) Impedance data (frequency range 50 kHz to 0.5 Hz, amplitude 100 mV, bias 0.0 V; for 5, 10, and 20 µm diameter microhole) showing experimental data points and a line for fitting results.

It is important to investigate the case of different microhole diameters of PET substrate in the experimental observation. The cyclic voltammetry data for 5, 10, and 20 µm diameter of microhole using aqueous 10 mM HCl has been presented in Figure 5.5A. The currents increase linearly with the increasing microhole diameter, but not quadratic as predicted by the theory. Therefore, the access diffusion of ions towards the microhole especially in smaller diameter microholes cannot be completely ignored. The chronoamperometry data in Figure 5.5B shows a faster switching in time constant is observed with small diameter microhole devices which is associated with both access diffusion of ions and diffusion inside

of the cylindrical region in the microhole. The time for ions diffusion-migration process within the microhole are only dependent on the length *L* and unlikely to change with microhole diameter. The access diffusion of ions from the external microhole (dependent on *r*) is affected and therefore can explain the decrease in switching time for slower microhole diodes. By using the equation 5 has been proposed by Oldham and Myland[12], one can find how long it takes to reach the current transient within 2% of steady state diffusion at microelectrodes.

$$\text{time to 2\% within steady state} = 2500\ \frac{r^2}{\pi D} \qquad (5)$$

In this equation *r* is the microhole radius in m and *D* is the diffusion coefficient assumed to be approximately 10^{-9} m^2s^{-1}. This suggest that a time to steady state within 2% approximately 5s, 20 s, and 80 s for a microhole diameter of 5, 10, and 20 μm, respectively, consistent with data in Figure 3.5B. The impedance data in Figure 5.5C have been obtained at 0.0 V as well as at -1.0 V and at +1.0V in Table 5.2. The impedance data from Table 5.2 also confirm that a change in 10 mM HCl electrolyte concentration occurs locally in the vicinity of the microhole during ionic diode switching.

From the Table 5.1, it is clear that the capacitance C_{PET} of the PET film remains constant under all conditions with different bias voltage and microhole diameters. The resistance R_S shows an increase with smaller microhole diameter which is dominated by the ion concentration in solution phase in the vicinity of the microhole. The R_P resistance also increases for smaller microhole diameters connected with PET film polarization and associated with both graphene oxide deposit resistivity and electrolyte resistivity within the microhole region. When switching the diode from open (+1.0 V) to closed state (-1.0 V) causes both R_S and R_P change. This suggests that the electrolyte solution plays a significant role in the changes of R_S and R_P value. The other possible of additional effects to the changes of R_S and R_P value are coming from charge carrier concentration gradients within the graphene oxide and from the graphene oxide | electrolyte interface.

Table 5.1. Summary of impedance data obtained in aqueous 10 mM HCl with frequency range 50 kHz to 0.5 Hz, amplitude 100 mV, bias -1.0 V, 0.0 V, or +1.0 V; for 5, 10, and 20 μm diameter microhole.

microhole diameter	R_S / Ω	R_P / Ω	C_{PET} / nF
Bias 0 V			
20 μm	2273 ± 10	166.8 ± 12	0.54 ± 0.001
10 μm	5921 ± 22	900 ± 28	0.55 ± 0.001
5 μm	8320 ± 42	1876 ± 58	0.67 ± 0.001
Bias +1.0 V (open diode)			
20 μm	1260 ± 3	32.2 ± 3.5	0.53 ± 0.001
10 μm	1562 ± 7	161.9 ± 8.6	0.5 ± 0.001
5 μm	6467 ± 27	800 ± 40	0.32 ± 0.001
Bias +1.0 V (closed diode)			
20 μm	9992 ± 97	192.6 ± 0.26	0.56 ± 0.001
10 μm	14620 ± 200	2900 ± 4.3	0.5 ± 0.001
5 μm	17870 ± 280	13880 ± 10	0.35 ± 0.001

In the Figure 5.5C the rectification ratio shows an upward variation for higher diameter of microholes when investigated as a function of microhole diameter. This behavior is not following the simplified theory which predicts a constant rectification ratio in different diameter of microhole. This phenomenon can be associated with the behaviour of diffusion-migration ions from external to the microhole region or within the graphene oxide deposit. In order to explain ionic rectifier effects based on the electrolyte-based processes within the microhole region, the proposed simplified theoretical model provides a good model system. However, processes within the graphene oxide cannot be ignored and to improve the theory and better predict the characteristics of ionic diode system such as rectification ratio and switching time, more work will be required in future.

5.4.3. Cases for Na^+ versus H^+ Selectivity at Graphene Oxide Based Ionic Diodes

In order to better understand the processes in ionic diodes based on the graphene oxide and also to explore the possibility to be used in desalination, different ionic strength of aqueous NaOH and NaCl are investigated. In previous studies, for example in ionic diode based on cellulose materials[13], the pH of the solution and type of electrolyte were essential parameters affecting the ionic diode effect. Figure 5.6A shows the cyclic voltammogram data for the graphene oxide diode in different ionic strength of aqueous NaOH. The ionic rectification effects are very similar to those observed in Figure 5.4D for aqueous HCl and the shape of the cyclic voltammogram response are consistent with a cationic diode which open state only in the positive potential range. In Figure 5.6B shows the chronoamperometry data and rectification ratio data are presented in Figure 5.6C. In general, rectification effects for aqueous NaOH are still maintained even at higher ionic strength (500 mM). In conclusion, the rectification effects at different concentration of aqueous NaOH are considerable and almost independent with ionic strength, but generally lower than aqueous HCl.

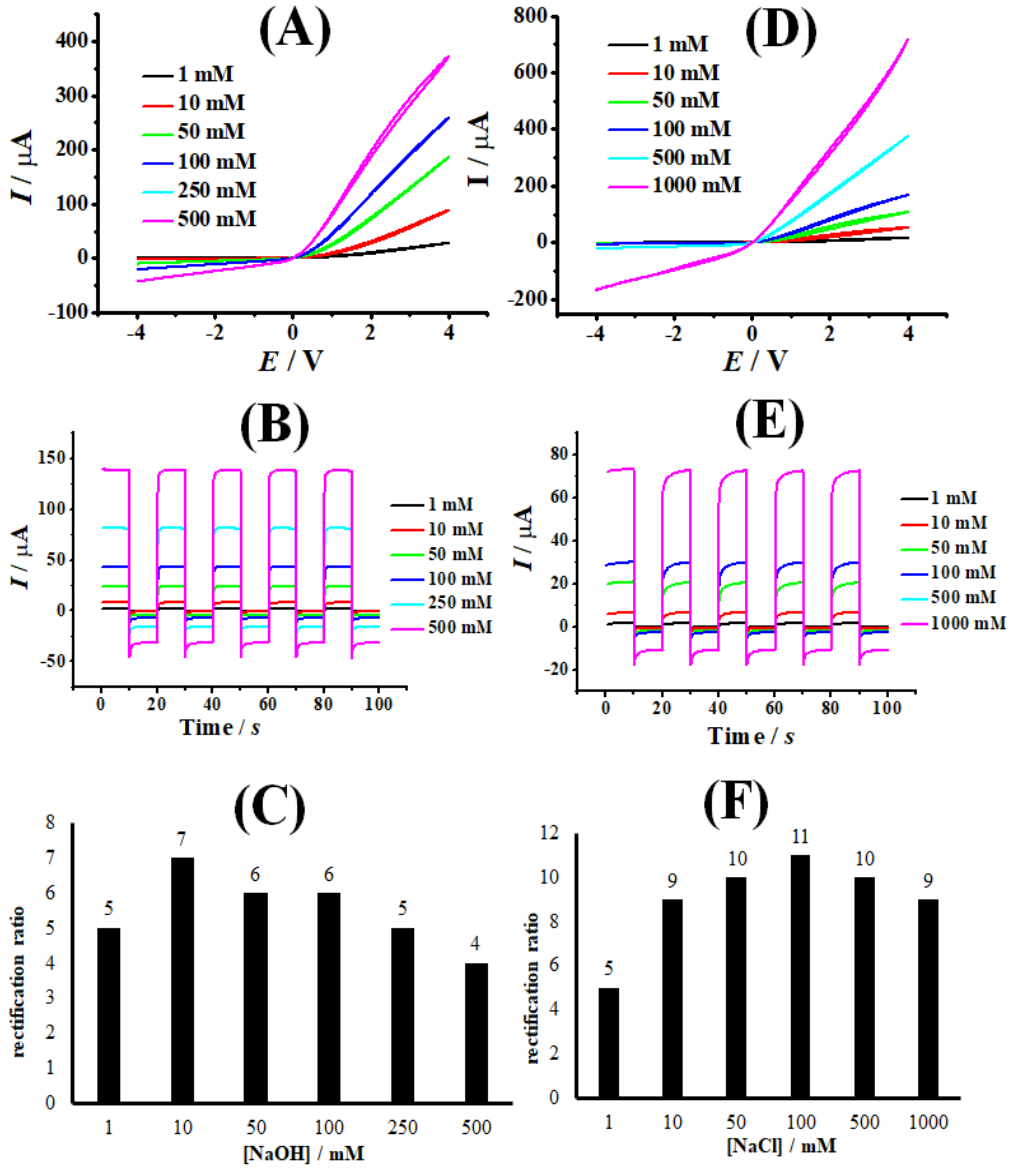

Figure 5.6. (A) Cyclic voltammograms with scan rate 50 mVs^{-1} for a graphene oxide deposit on a 20 µm diameter microhole in a PET substrate immersed in 1, 10, 50, 100, 250, and 500 mM aqueous NaOH. (B) Chronoamperometry data stepping from +1 V to -1V. (C) Plot of the rectification ratio (the absolute of the current at +1 V divided by the current at -1 V) *versus* NaOH concentration. (D) Cyclic voltammograms with scan rate 50 mVs^{-1} for a graphene oxide deposit on a 20 µm diameter microhole in a PET substrate immersed in 1, 10, 50, 100, 500, and 1000 mM aqueous NaCl. (E) Chronoamperometry data stepping from +1 V to -1V. (F) Plot of the rectification ratio (the absolute of the current at +1 V divided by the current at -1 V) *versus* NaCl concentration.

In Figure 5.6D shows cyclic voltammogram data for aqueous NaCl in different ionic strength with concentration range from 1 mM to 1000 mM. The data from cyclic voltammetry and chronoamperometry (in Figure 5.6B) suggest a substantial rectification effect observed over the entire concentration range and most effective effects in the 100 mM range. These findings are encouraging in terms of future desalination applications, but also unusual when compared to ionic diodes based on other types of semipermeable ionomer materials for example in Nafion[14] suggests substantially higher mobility for protons, where the rectification effect strongly inhibited at higher ionic strength. Figure 5.7B shows the data comparison of ionic diode effects from 10 mM HCl, 10 mM NaOH, and 10 mM NaCl. It is obvious that for aqueous HCl both open diode currents and rectification ratio (Figure 5.7C) data are higher than NaOH and NaCl. While the open diode currents and rectification ratio for NaOH and NaCl are essentially identical. This effect can be associated with the cation mobility for both protons (H^+) and Na^+ in graphene oxide deposit dominating the resistance for the open diode. The mobility in aqueous media for proton (36.23×10^{-8} $m^2V^{-1}s^{-1}$) and for Na^+ (5.19×10^{-8} $m^2V^{-1}s^{-1}$) s at 298 K[15]. These data suggest that proton has higher mobility than Na^+, but here this is likely to be moderated by the host interactions within the graphene oxide deposit.

More experimental insight needed to reveal the cation selectivity in transport across the film which responsible for the current response in ionic diode based on graphene oxide. It is possible that proton transport could dominate in ion transport process across graphene oxide film based on Na^+ cations electrolyte media. In ionic diode based on Fumasep FKS-30 film[16], the heterolytic water dissociation process has recently been proven to occur under similar conditions. In the heterolytic water dissociation process occurs the localized formation of H^+ and OH^- as a potential-driven catalytic process at membrane surfaces. This process has been observed in different materials for example when catalyzed by graphene oxide derivatives[17] or nanosheet MoS_2[18]. This competing process between protons and Na^+ in ion transport process through graphene oxide film should lead to measurable pH gradients between right compartment and left compartment. Therefore, additional experiments are performed here with two pH probes placed close to each

side of membrane independently in order to monitor the local pH in the right and in the left solution compartments. This process aims to measure *in situ* local pH of graphene oxide membrane during ionic diode operation. The schematic drawing of experimental setup to measure local pH has been presented in Figure 5.7A. When the experiment is running during the "open diode" operation (applying +4V at a certain time) either Na^+ transport or H^+ transport in aqueous 10 mM NaCl are reasonable. This process should result in either no pH change or a change to higher pH (more alkaline) on the right and lower pH (more acidic) on the left, respectively at a certain time of experiment.

It is possible to calculate the effect of a proton current flow through graphene oxide film when the diode is opening by applying + 4V for 10 minutes (see Figure 5.7D). In terms to calculate the pH in the right and in the left compartment, it is necessary to assume a fixed volume V of ca. 0.01 dm^3 where pH changes occur close to the graphene oxide membrane surface. Equations 6 and 7 express the shift in pH (from an initial value $pH_{initial}$) in the right compartment (where protons are lost) in the left compartment (where protons are gained). The other parameters are the time-average absolute current I, the time t = 600 s, and the Faraday constant F = 96487 C mol^{-1}.

$$pH_{left} = -\log_{10}(10^{-pHinitial} + It/FV) \quad (6)$$

$$pH_{right} = 14 + \log_{10}(10^{-(14-pHinitial)} + It/FV) \quad (7)$$

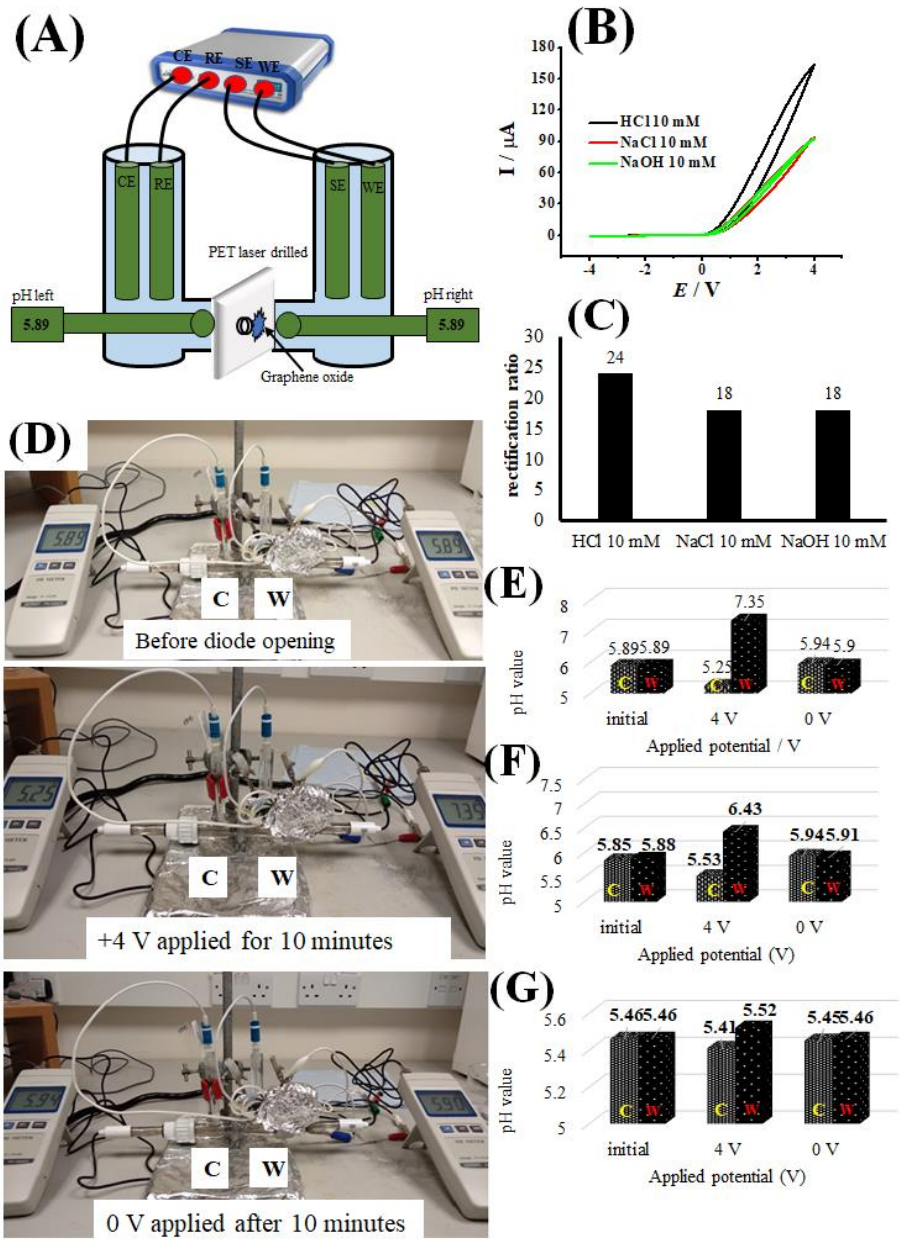

Figure 5.7. (A) Schematic drawing of the 4-electrode measurement cell fitted with two additional pH meters on both compartments, (B) Cyclic voltammograms with scan rate 50 mVs^{-1} for a graphene oxide deposit on a 20 µm diameter microhole in a PET substrate immersed in 10 mM HCl, NaCl, and NaOH, (C) Plot of the rectification ratio (the absolute of the current at +1 V divided by the current at -1 V) *versus* 10 mM HCl, NaCl, and NaOH, (D) Photographs showing the measurement cell with 1 mM NaCl before diode opening, after 10 minutes +4V open diode operation, and after further 10 minutes 0V closed diode operation. Also shown are bar plots for pH changes in both compartments observed under these conditions for (E) 1 mM NaCl, (F) 10 mM NaCl, and (G) 100 mM NaCl.

In Figure 5.7D for the case of a 1 mM NaCl electrolyte, the average current at an applied voltage of 4 V was 17 x 10^{-6} A over 600 s, which (with $pH_{initial}$ = 5.89) translates to pH_{left} = 4.9 and pH_{right} = 9.0. When the experimental results in Figure 5.7E compared with the predicted theory, the trend is indeed observed, but it shows also that the effect is less strong. This suggests that during the open diode experiment, it occurs the competition of Na^+ transport and H^+ transport through graphene oxide film. In the case of 10 mM NaCl (Figure 5.7F) the observed current was 45 x 10^{-6} A at applied voltage 4 V for 600 seconds. These parameters give values for pH_{left} = 4.5 and pH_{right} = 9.4. The increase in NaCl concentration from 1 mM to 10 mM decreases the production rate of protons and hydroxide during applying 4V for 600 seconds. Finally, for aqueous 100 mM NaCl electrolyte the observed average current was 112 x 10^{-6} A at 4 V applied voltage for 600 seconds, which translates to pH_{left} = 4.1 and pH_{right} = 9.8. The observed values in Figure 5.7G shows pH_{left} = 6.4 and pH_{right} = 6.7 suggest a minimal contribution from production of proton and hydroxide during applying 4V for 600 seconds.

Therefore, transport of Na^+ cation at relatively high ionic strength using graphene oxide material offer good efficiency and consistent with desalination purposes. It has been reported that the ionic diode effect can be developed into an ionic current rectifier for low energy desalination based on alternating current (AC) excitation using capacitive electrode. For this purpose, it would ideal to develop a device combining a Na^+ ionic rectifier as a cationic diode for example using graphene oxide materials and a Cl^- ionic rectifier as an anionic diode to transfer both cations and anions uni-directionally and irreversibly across a membrane.

5.5. Conclusions

It has been shown that ionic current rectification phenomena or ionic diode effects can be obtained for asymmetrically deposited graphene oxide on a PET substrate with the protons transport is facile. The first part of results section focuses on the proton transport through graphene oxide film with the best rectification ratio achieved using 20 μm microhole diameter in aqueous 10 mM HCl. Therefore, during proton transport through graphene oxide film, the accumulation and

depletion phenomena in the microhole region are primarily responsible for the diode effects. The cationic diode effect remaining even at higher concentrations of hydrochloric acid, which can be attributed to the porosity effects and sustained semi-permeability in the graphene oxide film. The second part of results section discusses the effects of aqueous NaOH and NaCl and performance of diodes based on graphene oxide film. It is clear that the similar behaviour was observed in aqueous NaOH and NaCl with Na^+ transport currents are dominant even at relatively low concentrations of Na^+ with minimal competition due to proton transport through graphene oxide film. The system seems promising especially in desalination application, but still needs to be investigated in more depth and a wider range of aqueous electrolyte systems.

In conclusion, graphene oxide material can be readily deposited to be developed into a novel ionic current rectifier or cationic diode device. In order to get better insight into the various aspects of the mechanism of ionic diode device, the simplified theoretical model also developed. The simplified model here based only on phenomena in the electrolyte solution within the microhole region and could be refined by including phenomena within the graphene oxide and within the access diffusion region. The methodology employed in this study possible to be used for screening a wider range of materials and discovery of suitable anionic diodes to complement the cationic rectifier behaviour of graphene oxide in desalination.

5.6. References

1 Loh, K.P., Bao, Q.L., Eda, G. Chhowalla, M. *Nature Chem.* **2010**, *2*, 1015–1024.

2 Joshi, R.K., Carbone, P. Wang, F.C., Kravets, V.G., Su, Y., Grigorieva, I.V., Wu, H.A., Geim, A.K., Nair, R.R. *Science.* **2014**, *343*, 752–754.

3 Sun, P., Zhu, M., Wang, K., Zhong, M., Wei, J., Wu, D., Xu, Z., Zhu, H. *ACS Nano.* **2013**, *7*, 428–437.

4 Sun, P., Zheng, F., Zhu, M., Song, Z., Wang, K., Zhong, M., Wu, D., Little, R.B., Xu, Z., Zhu, H. *ACS Nano.* **2014**, *8*, 850–859.

5 Karim, M.R., Hatakeyama, K., Matsui, T., Takehira, H., Taniguchi, T., Koinuma, M., Matsumoto, Y., Akutagawa, T., Nakamura, T., Noro, S., Yamada, T., Kitagawa, H., Hayami, S. *J. Amer. Chem. Soc.* **2013**, *135*, 8097–8100.

6 Zarrin, H., Higgins, D., Jun, Y., Chen, Z. Fowler, M. *J. Phys. Chem. C.* **2011**. *115*, 42, 20774-20781.

7 Sun, P., Wang, K., Zhu, H. *Adv. Mater.* **2016**. *28*, 2287–2310.

8 Jana, S.K., Banerjee, S., Bayan, S., Inta, H.R., Mahalingam, V. *J. Phys. Chem. C.* **2018**, *122*, 11378–11384.

9 Putra, B.R., Carta, M., Malpass-Evans, R., McKeown, N.B., Marken, F. *Electrochim. Acta* **2017**, *258*, 807–813.

10 Li, Y., Wang, D., Kvetny, M.M., Brown, W., Liu, J., Wang, G. *Chem. Sci*. **2015**. *6*, 588-595.

11 Wang, D., Kvetny, M., Liu, J., Brown, W., Li, Y., Wang, G. *J. Am. Chem. Soc.* **2012**. *134*, 8, 3651-3654.

12 Oldham, K. B., Myland, J. C. *Fundamentals of Electrochemical Science*, Academic Press, London. 1994, p. 278.

13 Aaronson, B.D.B., Wigmore, D., Johns, M.A., Scott, J.L., Polikarpov, I., Marken, F. *Analyst*. **2017**. *142*, 3707-3714.

14 He, D., Madrid, E., Aaronson, B.D.B., Fan, L., Doughty, J., Mathwig, K., Bond, A.M., McKeown, N.B., Marken, F. *ACS Appl. Mater. Interfaces*. **2017**. *9*, 12, 11272-11278.

15 Atkins, P.W., de Paula, J., Keeler, J. *Physical Chemistry*, 11th ed., Oxford University Press, Oxford, 2018, p. 702.

16 Tshwenya, L., Arotiba, O., Putra, B.R., Madrid, E., Mathwig, K., Marken, F. *J. Electroanal. Chem.* **2018**, *815*, 114–122.

17 Manohar, M., Das, A.K., Shahi, V.K. *Industrial Engineer. Chem. Res*. **2018**, *57*, 1129–1136.

18 Li, J., Morthensen, S.T., Zhu, J., Yuan, S., Wang, J., Volodine, A., Lin, J., Shen, J., Van der Bruggen, B. *Separation Purification Technol.* **2018**, *194*, 416–424.

Chapter 6

Two Dimensional Nanomaterials: Ionic Rectification based on TiO_2 Nanosheets

Contents

Chapter Abstract

A lamellar structure in a film deposit of titanate nanosheets (approx. 1.8 nm layer thickness and 200 nm size) can be filled with the electrolyte creating semi-permeable channels that intrinsically contain tetrabutylammonium cations. The persistent deposits of titanate nanosheets are readily formed with approximately 10 μm thickness on a 6 μm thick poly(ethylene-terephthalate) (PET) substrate with a 20 μm diameter microhole by evaporation of a colloidal solution. The titanate nanosheet films exhibit a point of zero charge (pzc) of -37 mV, consistent with the formation of a cation conducting (semi-permeable) deposit when films are immersed into an aqueous solution. The ionic current rectification behaviour for titanate nanosheet films is observed (as cationic diode behaviour) at a sufficiently low ionic strength (below 100 mM) in aqueous electrolyte solution. The currents in titanate nanosheet studies were observed because of the electrolyte transport as well as interfacial water heterolysis processes (causing additional proton transport). The water heterolysis mechanism is observed for all types of electrolyte cations, especially for Ca^{2+} and Mg^{2+} ions. Water heterolysis causes ion current blocking, mainly due to localised hydroxide-induced precipitation processes. The ionic diode effect can be inverted from cationic into anionic by using aqueous NBu_4^+ solution.

Chapter Publications

Parts of this chapter have been published in: B. R. Putra, C. Harito, D. V. Bavykin, F. C. Walsh, W. T. Wahyuni, J. A. Boswell, A. M. Squires, J. M. F. Schmitt, M. A. D. Silva, K. J. Edler, P. J. Fletcher, A. E. Gesell, F. Marken. Processes associated with ionic current rectification at a 2D-titanate nanosheet deposit on a microhole poly(ethylene terephthalate) substrate. *J. Solid State Electrochem.* **2019**, 23, 4, 1237-1248.

Acknowledgement

Dr. Christian Harito, Dr. Dmitry V. Bavykin, Prof. Frank C. Walsh from the University of Southampton are acknowledged for providing the titanate nanosheet materials used in this study and for helpful discussion.

6.1. Introduction

This chapter focuses on ion transport behaviour through lamellar titanate nanosheets deposited onto a poly-(ethylene-terephthalate) substrate (PET with 6 μm thickness) with a microhole (20 μm diameter). The lamellar structure of 2D-titanate nanosheet deposits has been shown to be electrochemically active depending on the pH and intercalated guest species[1]. The titanate nanosheet materials used this study have been developed according to the method of Sasaki and coworkers[2,3]. The resulting titanate nanosheet colloidal solutions are stable and readily deposited from solution into thin films.

During the synthesis, titanate nanosheet materials can be produced in two steps[4]; first, TiO_2 reacts with cesium salts to give an intermediate solid lepidocrocite-type product; second, the product is exfoliated with tetrabutylammonium[5] cations to give a stable colloidal solution of negatively charged titanate nanosheets. The surface charge of the colloid has a point of zero charge (p.z.c.) at approximately pH 4 [6]. The titanate nanosheet colloidal solutions contain single unit cell thick titanate layers, which are typically 200 nm in diameter[7]. When the deposits of this colloid are dried under ambient conditions, a lamellar-structured gel is formed with typically 1.7 nm to 1.8 nm unit cell spacing according to the x-ray diffraction pattern[8]. This spacing is consistent with the thickness of unit cell layer approximately 1.2 nm to 1.3 nm sandwiched between electrolyte layers of typically 0.5 nm. These types of gels can collapse back to the anatase crystal form at high temperature, but at room temperature these lamellar nano-structures of titanate nanosheet persist for a long time. In contrast to polymer materials (with 3D-channels), the nanosheet lamellar materials can swell and change the ion channel pore size in response to the external solution environment.

In order to investigate ion transport through the lamellar titanate nanosheets, deposits of the titanate are studied here on a poly-ethylene-terephthalate (6 μm thick PET) substrate with a single 20 μm diameter hole. The ion transport has been investigated previously using semi-permeable material and shows the ionic diode or ionic current rectification effect for example in Nafion[9], polymer intrinsic of

microporosity[10], cellulose[11], and the commercial ionomer Fumasep[12]. The ionic current rectification effect allows to distinguish cation transport (cationic diodes for cation conductors) and anion transport (anionic diodes for anion conductors) based on membrane semi-permeability.

The ionic diode effect can be explained based on a combination of ion conductivity and concentration polarization phenomena in asymmetrically deposited films in the microholes[13]. Figure 6.1 shows a schematic summary of the accumulation and depletion of ion transport phenomena in the semi-permeable ionomer asymmetrically coated onto the microhole. A four-electrode cell[14] is employed, and at positive polarization on the working electrode, the current flows consistent with ion accumulation in the microhole region. With the polarization switched to negative at the working electrode, the current is blocked due to ion depletion in the microhole region. This behaviour leads to an ionic current rectification effect. However, when the ionomer is deposited symmetrically on both sides of the microhole, ion transport from the left or from the right compartment remain similar and a simple resistance behaviour is observed rather than the current rectification effect. A case for cationic diode (cation conductor) is illustrated in Figure 6.1.

In this chapter, the ion transport behaviour in the inter-lamellar region of titanate nanosheets is investigated using different type of electrolyte. The semi-permeability of titanate nanosheet deposits allows cation transport and causes cationic diode effects when it immersed in electrolyte below 100 mM concentration. This cationic diode effect is investigated in different types of cation and anion of electrolytes. The cationic diode behaviour can be inverted into anionic diode in the presence of tetrabutylammonium cations.

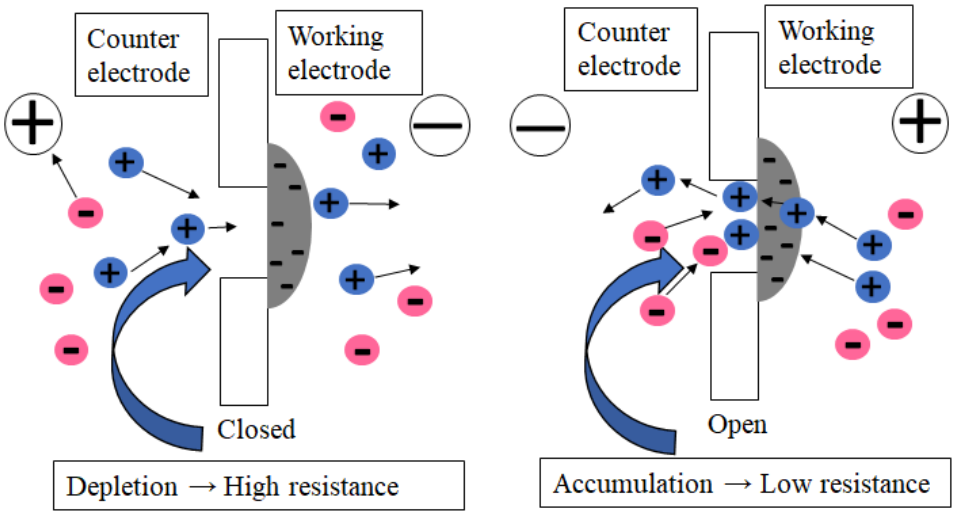

Figure 6.1. Schematic depiction of the case of a "cationic diode" effect from a semi-permeable cation conductor. In the closed state, the flow of cations is limited by ion depletion within the microhole region of the PET film causes high resistance. In the open state, the ion accumulation occurs due to over-supply of cations through the semi-permeable cation conductor within the microhole region of the PET film causes low resistance.

6.2. Experimental

6.2.1. Chemical Reagents.

Titanate nanosheets material was prepared and synthesized by Harito *et al.*[15,16] as described according to Sasaki *et al.*[17] method. Hydrochloric acid, sodium chloride, potassium chloride, lithium chloride, ammonium chloride, tetrabutylammonium chloride, magnesium chloride, calcium chloride, sodium hydroxide, sodium nitrate, sodium perchlorate, sodium sulphate were obtained in analytical grade from Sigma-Aldrich or Fischer Scientific and used without further purification. Phosphate buffer saline (PBS) was prepared with NaH_2PO_4, Na_2HPO_4, and NaCl and adjusted to pH 7. Aqueous solutions were prepared with deionised water with the resistivity of 18.2 MΩ cm (at 22°C) from an ELGA Purelab Classic System.

6.2.2. Instrumentation.

An Ivium Compactstat potensiostat system (The Netherlands) was used to record an electrochemical data (voltammetry and chronoamperometry) at $T = 20 \pm 2$ °C. A classic 4-electrode membrane electrochemical cell was used in whole experiment in order to get an electrochemical data. The membrane separates two

tubular half-cells (15 mm diameter, see Figure 6.2B), one with platinum wire working and saturated calomel (SCE) sense electrode, and the other with SCE reference electrode and platinum wire counter electrode. During the electrochemical measurements the working electrode (platinum wire) was always located on the side of titanate nanosheets films. A Carl Zeiss Confocal Scanning Microscope Fluorescence was used in order to get a fluorescence imaging. In Figure 6.3, Rhodamine B dye was mixed with titanate nanosheets colloidal solution, and then applied to the PET films in order to get a fluorescence imaging. In some measurements, an additional battery powered pH-probes (Voltcraft PH-100ATC) were positioned in left and right compartment close to the titanate membrane.

6.2.3. Procedures of Titanate Nanosheets Deposition.

The zeta-potential for the colloidal titanate solution shows the value on average of -32.5 mV with the average size of 216 nm measured using a Zetasizer Nano ZS (Malvern Instruments Ltd, Malvern, UK)[26]. Approximately 10 µL aqueous titanate nanosheets colloidal solution (2.56 gL^{-1}) was applied to a PET film on a glass substrate in order to form films of titanate nanosheets on PET substrates (20 µm diameter hole in 6 µm thick PET from Laser Micromachining Ltd., Birmingham, UK). Before depositing the aquoeus titanate nanosheets solution, the glass substrate should be pre-coated with a thin layer of 1% agarose gel by solution-casting to stop material penetrating through the PET microhole. A volume of 10 µL titanate nanosheets colloidal solution was then applied to the surface over PET to give a 1 cm^2 film coating, which after drying produced a thin uniform coating. In order to get symmetric deposition of titanate nanosheets on both sides of the PET film, the deposition was repeated on the back side of the PET. The stacked fluorescence images were obtained in a symmetric (double-sided) and an asymmetric (one-sided) of TiO_2 films deposition (Figure 6.3).

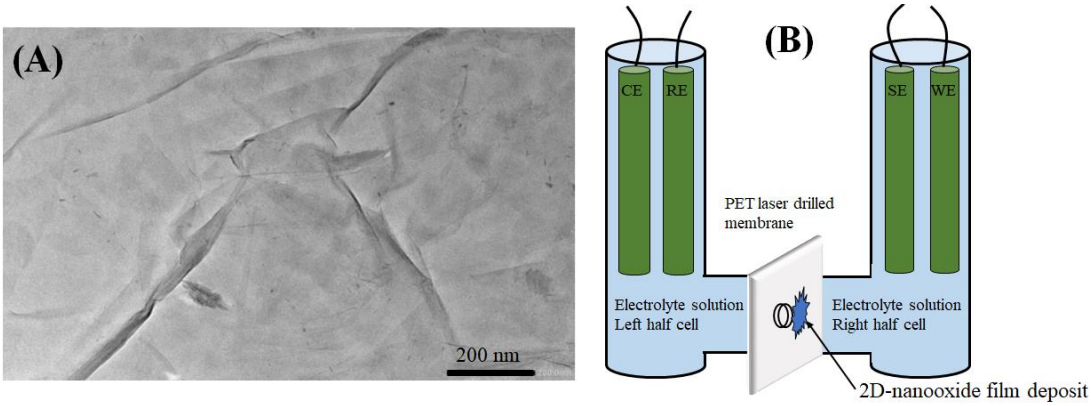

Figure 6.2. (A) A typical TEM image of the titanate nanosheets material and (B) Schematic description of the experiment with 4-electrode control (WE = working electrode, SE = sense electrode, CE = counter electrode, RE = reference electrode) of the applied potential and TiO_2 nanosheets deposit on the side of the working electrode.

6.3. Results and Discussion

6.3.1. Characterisation of Titanate Nanosheets Film.

A uniform ~5-10 µm thick film of titanate nanosheets with a rhodamine B dye deposited on a 20 µm diameter microhole in a PET substrate has been observed using fluorescence microscopy. Figure 6.3 shows orthogonal images from fluorescence microscopy from titanate nanosheets deposit with the top view with the focus on PET layer. From the Figure 6.3 A, symmetric deposition shows that the 20 µm microhole was partially-filled with titanate nanosheets material. There are two layers of titanate nanosheets on opposite sides of the PET which can be clearly identified. However, from the Figure 6.3B for asymmetric deposition, the layer deposit of titanate nanosheets material (ca. 5-10 µm thick) can only be seen only in one side. Due to the light reflecting effect, the size of deposit is not completely resolved.

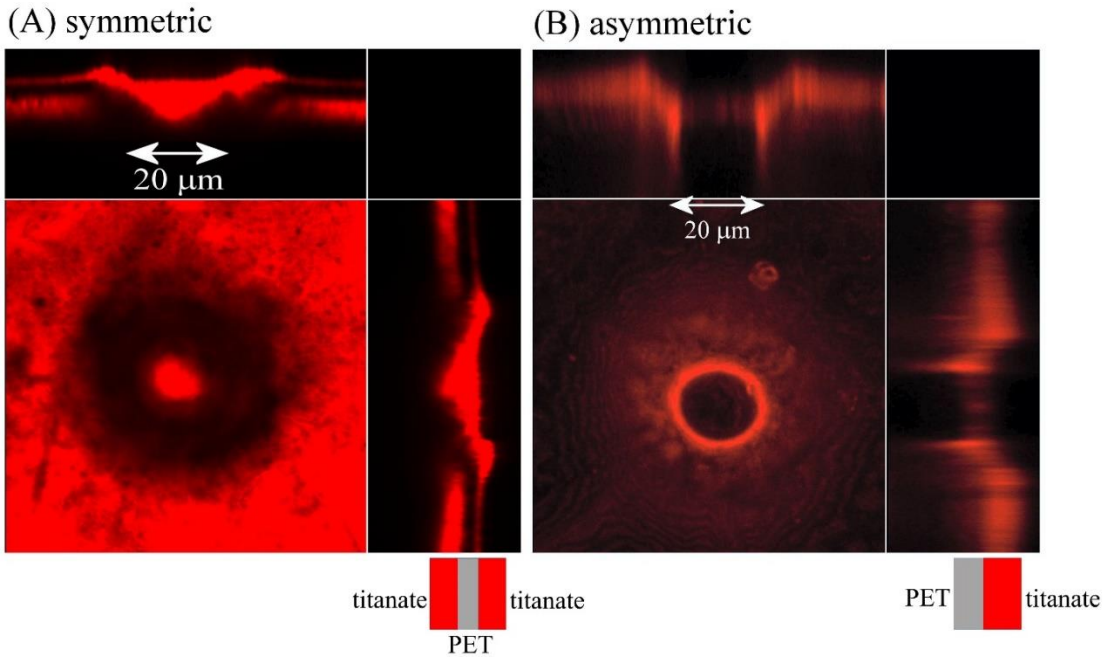

Figure 6.3. The orthogonal fluorescence image stacks based on TiO_2 nanosheets deposits dyed with rhodamine B for (A) symmetric (applied from both sides) and (B) asymmetric (applied form only one side) to the PET substrate with 20 μm diameter microhole.

6.3.2. The Ion Transport Through Lamellar Titanate Nanosheets Deposits: Case for Na^+ Transport

The typical cyclic voltammetry data for titanate nanosheets membrane-coated or uncoated PET over a potential range of +4 V to -4 V applied immersed in 10 mM NaCl on both sides is shown in Figure 6.4A. Here, three different cases are shown: (i) an empty 20 μm diameter hole of PET film, (ii) a symmetric deposition of titanate nanosheets deposited symmetrically on both sides of PET film, and (iii) an asymmetric deposition of titanate nanosheets only one side of PET film. For the case (i) an empty microhole, the currents are mainly due to the specific resistivity of the aqueous NaCl electrolyte solution filling the microhole of PET and giving a constant resistance[18]. When the deposit has been applied on both sides of PET (symmetric case), the titanate nanosheets restricts the ion flows in both negative and positive applied potentials and therefore the current decreases at cyclic voltammogram. Interestingly, when the titanate nanosheet applied only one side (asymmetric case), ionic current rectification effect is observed leading to a higher current at positive applied potentials and a lower current at negative applied

potentials. From the Figure 6.1, it can be seen that the case of an open state of cationic diode at positive applied potential and a closed state cationic diode at negative applied potential for the negatively charged titanate nanosheets material. The open state of diode is due to ion accumulation and closed state of diode caused by ion depletion in the microhole region. Then, ionic current rectification effect are investigated in aqueous NaCl electrolyte solution with concentration range 1-1000 mM.

The data of cyclic voltammetry for asymmetrically deposited titanate nanosheets immersed in 1-1000 mM aqueous NaCl solution has been presented in Figure 6.4B. The currents due to ion flow are rectified in the positive applied potentials and therefore titanate nanosheets deposit must conduct cations through its lamellar spacing. When the concentration of NaCl is increased from 1 to 1000 mM, a well-defined voltammetric response from titanate nanosheets deposit is observed. When the NaCl concentration is below than 100 mM, the current in the positive potential range is higher than the current in the negative potential range. This phenomenon has been similarly observed in the other semi-permeable materials such as Nafion[9] and Fumasep FKS-30[12] and consistent as cationic diode behaviour. Chronoamperometry data in Figure 6.4C shows more clearly effect of the currents on different NaCl electrolyte concentration and the switching time for the cationic diode. From the chronoamperometry data, the rectification ratio can be calculated by dividing the absolute currents at +1V with at -1V in Figure 6.4D. In general, when the concentration of NaCl increases causes an increasing current in both the open and closed state of diode. The concentration range of NaCl solution from 50 mM to 100 mM shows the optimum rectification effect. When the concentration of NaCl above 100 mM or higher ionic strength, the rectification ratio is going lower due to loss of titanate semi-permeability and starting of anion transport through the titanate nanosheets film.

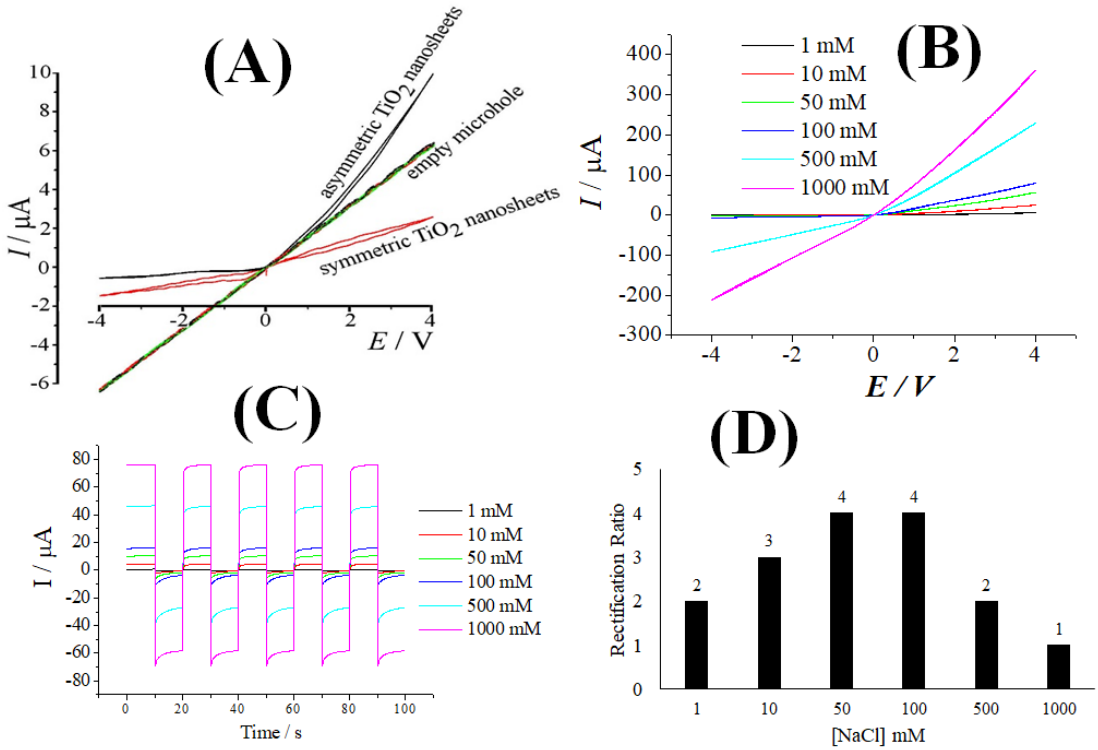

Figure 6.4. (A) Cyclic voltammograms (scan rate 50 mV s^{-1}) for (i) an empty microhole, a symmetric deposition of titanate, an asymmetric deposition of titanate (microhole diameter 20 µm) immersed in 10 mM NaCl, (B) Cyclic voltammograms of asymmetric titanate nanosheets deposition (scan rate 25 mVs^{-1}) in aqueous NaCl, (C) chronoamperometry responses of asymmetric titanate deposition (stepping from +1 V to -1 V) immersed in aqueous NaCl with concentration of 1, 10, 50, 100, 500, 1000 mM NaCl on both sides. (D) rectification ratios from chronoamperometry data at +/- 1 V.

6.3.3. The Ion Transport Through Lamellar Titanate Nanosheets Deposits: Case for Electrolyte Cations *versus* Anions

In order to better understand the processes in cationic diodes based on titanate nanosheets, different type of cations and anions transport are investigated. The data summary for cyclic voltammogram, chronoamperometry, and rectification ratio bar plots for aqueous 10 mM HCl, NaCl, KCl, LiCl, NH_4Cl, $MgCl_2$, and $CaCl_2$ are presented in Figure 6.5A-C. All electrolyte cations systems show different conductivities, but there are distinct changes in current magnitude depending on the type of cation. The open state of diode generates higher current in case of monovalent cations such as H^+, Li^+, Na^+, K^+, and NH_4^+ compared to those for divalent cations such as Mg^{2+} and Ca^{2+}. These phenomena are consistent with a higher mobility for monovalent cations relative to divalent cations. However, water

heterolysis processes in the titanate deposit can also affected by the ability of cation to bind/transfer and will be investigated in further studies below. From the Figure 6.5A-B, it can be concluded that protons gave the highest currents and the best rectification ratio among the other of mono-valent cations.

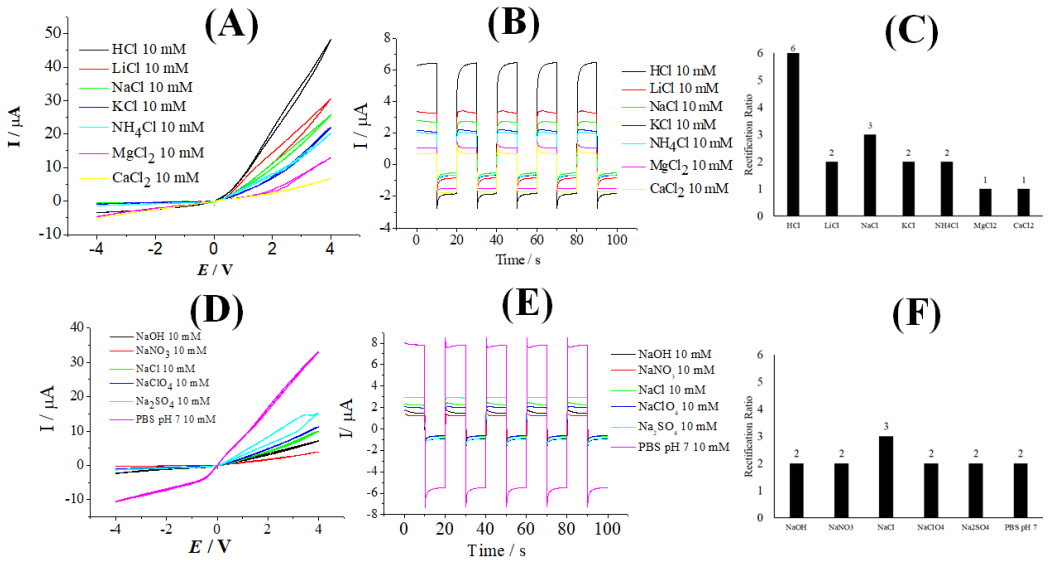

Figure 6.5. Data for asymmetric titanate nanosheets deposition. (A) Cyclic voltammograms (scan rate 25 mVs^{-1}), (B) chronoamperometry data (stepping from +1 V to -1V), (C) rectification ratio (+/- 1V) immersed in aqueous HCl, LiCl, NaCl, KCl, NH_4Cl, $MgCl_2$, and $CaCl_2$ (10 mM on both sides), (D) Cyclic voltammograms (scan rate 25 mVs^{-1}), (E) chronoamperometry data (stepping from +1 V to -1V), (F) rectification ratio (+/- 1V) immersed in aqueous NaOH, $NaNO_3$, NaCl, $NaClO_4$, Na_2SO_4, and phosphate buffer saline (PBS) pH 7 (all 10 mM on both sides).

Next, the effects of anion transport through lamellar titanate deposits are investigated. The data summary from cyclic voltammogram, chronoamperometry, and a rectification ratio bar plot for aqueous 10 mM NaOH, $NaNO_3$, NaCl, $NaClO_4$, Na_2SO_4, and phosphate buffer saline (PBS) pH 7 are presented in Figures 6.5D-E. Similar levels of rectification effect are observed for all different type of electrolyte anions. When the higher-valent anions (SO_4^{2-} and PO_4^{3-}) have been used in the studies, the currents for the open diode become significantly higher but effects of the type of anion on the rectification ratio value seem too small. It is obvious that at a higher anion concentration ions can enter into the inter-lamellar space of titanate nanosheets deposit and significantly change the rate of anion transport. This

indicates that even when the cation transport appears dominant, there could be always a contribution from anion transport as well. The collapse of the internal double layer is likely due to highly charged sulphate and phosphate anions. Therefore, the titanate nanosheets nano-channels can open up leading to both cation and anion transport. As a result, this effect can give rise to a higher ion current at both applied potentials and less semi-permeability of titanate nanosheets membrane. Figure 6.5E shows chronoamperometry data of transients both rising and falling with transient features mainly observed in the first 0.5 s of the data. During the transient period, not only the concentration gradients in the solution developing in the surrounding area of the microhole, but also that concentration gradients may also changing within the nanosheets material. The chronoamperometry data may provides current traces that are associated with compositional changes in the inter-lamellar titanate space. It is currently difficult to distinguish the effect of anion electrolyte and to provide a more detailed of these effects into the interlayer of titanate nanosheets.

6.3.4. The Ion Transport Through Lamellar Titanate Nanosheets Deposits: Case for Competing Cation and Proton Transport

There are three types of processes that can be associated with current generation through the asymmetrically deposit of titanate nanosheets. First, the current observation from flow of cations through lamellar of titanate nanosheets deposit. Second, the current observation from flow of anions especially under the high concentration conditions (these can enter into inter-lamellar space leading to collapse of internal double layer structure). Third, the current observation from the potential-driven water heterolysis process is possible leading to the formation of additional mobile protons and mobile hydroxide. The latter process will result in changes of proton and hydroxide ions leading to the a pH gradient in solution. From the investigation of ion transport process through the titanate deposit as reported in Figure 6.5, it is not immediately clear whether potential-driven water heterolysis process can contribute to or even dominate the observed currents.

One way of directly monitoring the simultaneous formation of protons and hydroxide during potential-driven water heterolysis process is by placing a Pt-disk electrode as a secondary working electrode (WE2) into the two-compartment cell. During the measurement, the potential of Pt-disk electrode will be fixed at proton reduction in order to observe the ion transport through titanate nanosheets deposit. The current observed at WE2 will be generated by hydrogen evolution from protons at the surface of Pt-disk electrode. A schematic drawing with Pt-disk electrode placed in the vicinity of the membrane and in the left counter electrode compartment has been presented in Figure 6.6. Initially, a cyclic voltammetry experiment was performed in 3 cycles using the three electrodes system in the left compartment to observe the onset potential for hydrogen evolution at Pt-disk electrode. Cyclic voltammetry data for 10 mM HCl are shown in Figure 6.6A and the inset shows that the onset potential of hydrogen evolution at -0.4 V vs. SCE (indicated by a black arrow). Next, the 5-electrode membrane cell is operated in cyclic voltammetry mode with the collector (Pt-disk electrode) potential fixed at the onset potential of hydrogen evolution. Protons transport processes associated with the open state of diode during positive applied potentials causes an increase in proton concentration at the location of Pt-disk electrode and thereby leads to a current.

The schematic drawing consist of both the generator current (WE1, membrane) and the collector current (WE2) as shown in Figure 6.6. For the case of 10 mM HCl in Figure 6.6A, the magnitude of current in the collector Pt-disk electrode approaching to the magnitude of current in the generator (membrane) with the opposite sign. Therefore, the cyclic voltammetry data for the proton transport in Figure 6.6A provide proof of working methodology. Cyclic voltammetry data are also shown for 10 mM LiCl in Figure 6.6B. The significant proton transport in LiCl is observed with the magnitude of current in the collector electrode almost mirroring the magnitude of current in the generator (membrane). This indicates that the transport of Li^+ is likely to be accompanied by proton transport during the water heterolysis process at titanate nanosheets. Similar results have been observed for NaCl (Figure 6.6C), KCl (Figure 6.6D), and NH_4Cl (Figure 6.6E). This suggests

that there is proton formation during water heterolysis processes for electrolytes in aqueous solution leading to current generation at the collector electrode. The current is generated from the proton transport through the titanate film.

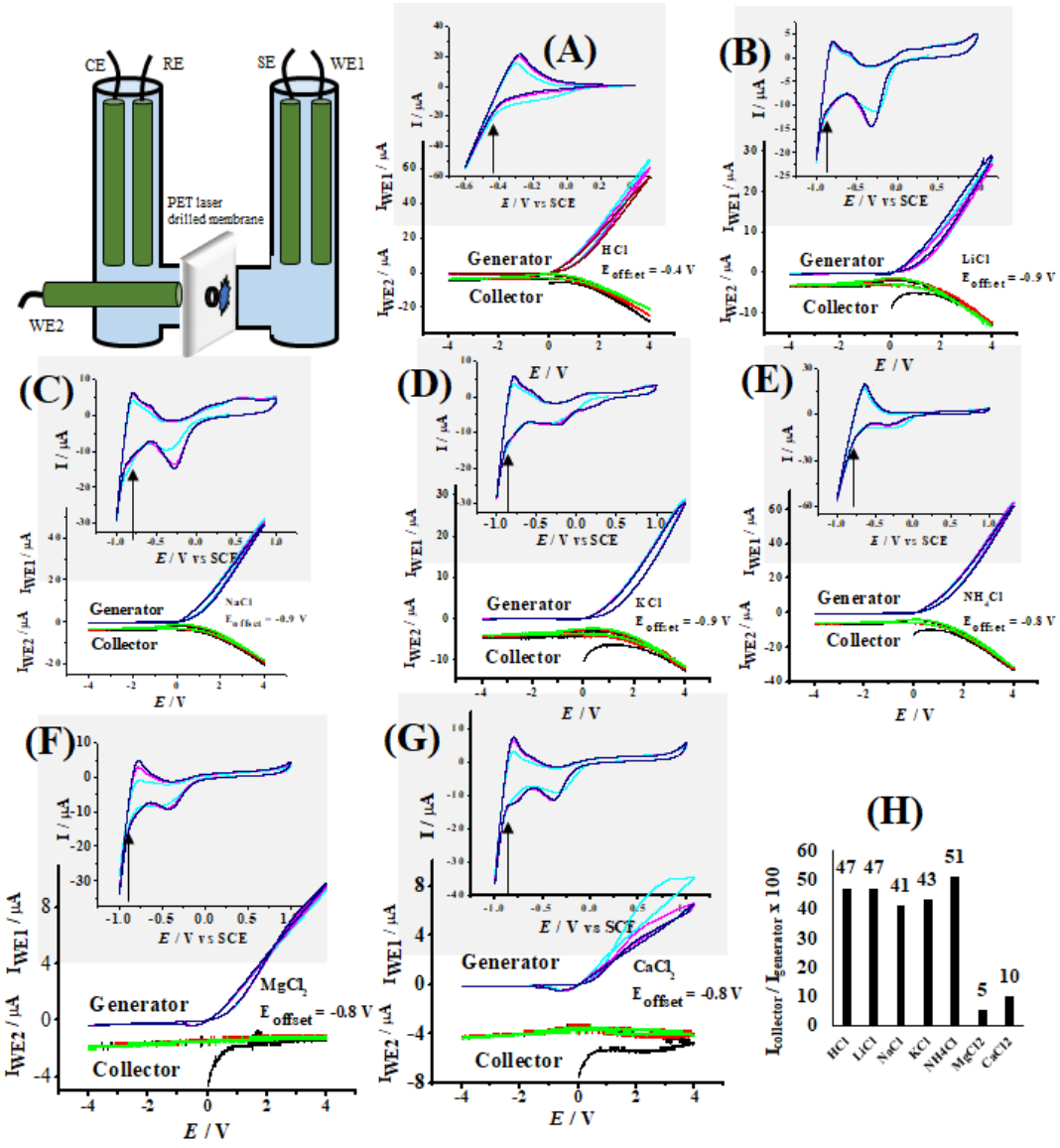

Figure 6.6. Schematic drawing showing the 5-electrode cell with additional (working electrode 2 (WE2), 3 mm diameter platinum disk) collector electrode for detection proton flux. Cyclic voltammogram data sets for (A) 10 mM HCl, (B) 10 mM LiCl, (C) 10 mM NaCl, (D) 10 mM KCl, (E) 10 mM NH_4Cl, (F) 10 mM $MgCl_2$, and (G) 10 mM $CaCl_2$ with the scan rate 50 mVs^{-1} at WE2 showing onset of hydrogen evolution (black arrow) and the generator-collector voltammogram (three consecutive potential cycles, scan rate 50 mVs^{-1}) and (H) Bar graph comparing the ratio of collector current and generator current (at +4V; in %) for different electrolyte solution.

The generator currents observed in $MgCl_2$ (Figure 6.6F) and for $CaCl_2$ (Figure 6.6G) are much lower compared with those for monovalent cations. This can be explained due to proton formation and transport through the titanate film. The voltammogram shapes from current generator for both divalent cation (Ca^{2+} and Mg^{2+}) are complex and give indication of some blocking of the diode as the potential is scanned into the positive potential range. When the potential scanning is going into negative for both Mg^{2+} and Ca^{2+}, small transient peaks are seen which could be associated with an "unblocking" process. These phenonema are due to hydroxide formation during water heterolysis process and leading to a localised pH changes at the titanate film surface. The combination of hydroxide ions with Mg^{2+} or Ca^{2+} forming $Mg(OH)_2$ or $Ca(OH)_2$, which would be the cause of the blocking effect at the titanate nanochannel. However, it is still difficult to quantify the importance of the this blocking effect and the relative importance of proton versus electrolyte cation transport at the titanate nanochannel. Therefore, direct pH measurements at the titanate membrane were used in order to give more evidence for these processes.

Figure 6.7 illustrates the configuration of two battery controlled pH probes based on glass membrane incorporated into the 4-electrode electrochemical cell. The reading from pH probes gives the information about an average of local pH close to the PET film on the left and on the right of cell compartment. In both compartments each pH probe was placed close to the PET film in order to sense the pH changes in the membrane. The photograph in Figure 6.7A shows the system before starting the experiment (no applied voltage). When 10 mM NaCl solution was placed in the left and right cell compartments, the pH solution is close to neutral. When cationic diode is opened by applying +4 V, an average current of approximately 23 μA flows and the pH value on both pH probe start to divert. After applying constant +4 V during 10 minutes (see Figure 6.7B), the pH in the left compartment reaches 6.56 (more acidic) and in the right compartment 6.91 (less acidic). Figure 6.7C-D outlines a bar graph for pH data for experiments in 1 mM NaCl and in 10 mM NaCl before and after applying constant +4V during 10 minutes. The pH changes were found to be less significant when used 100 mM

NaCl solution in the experiment. This behaviour could be explained with water hetrolysis process in the titanate membrane.

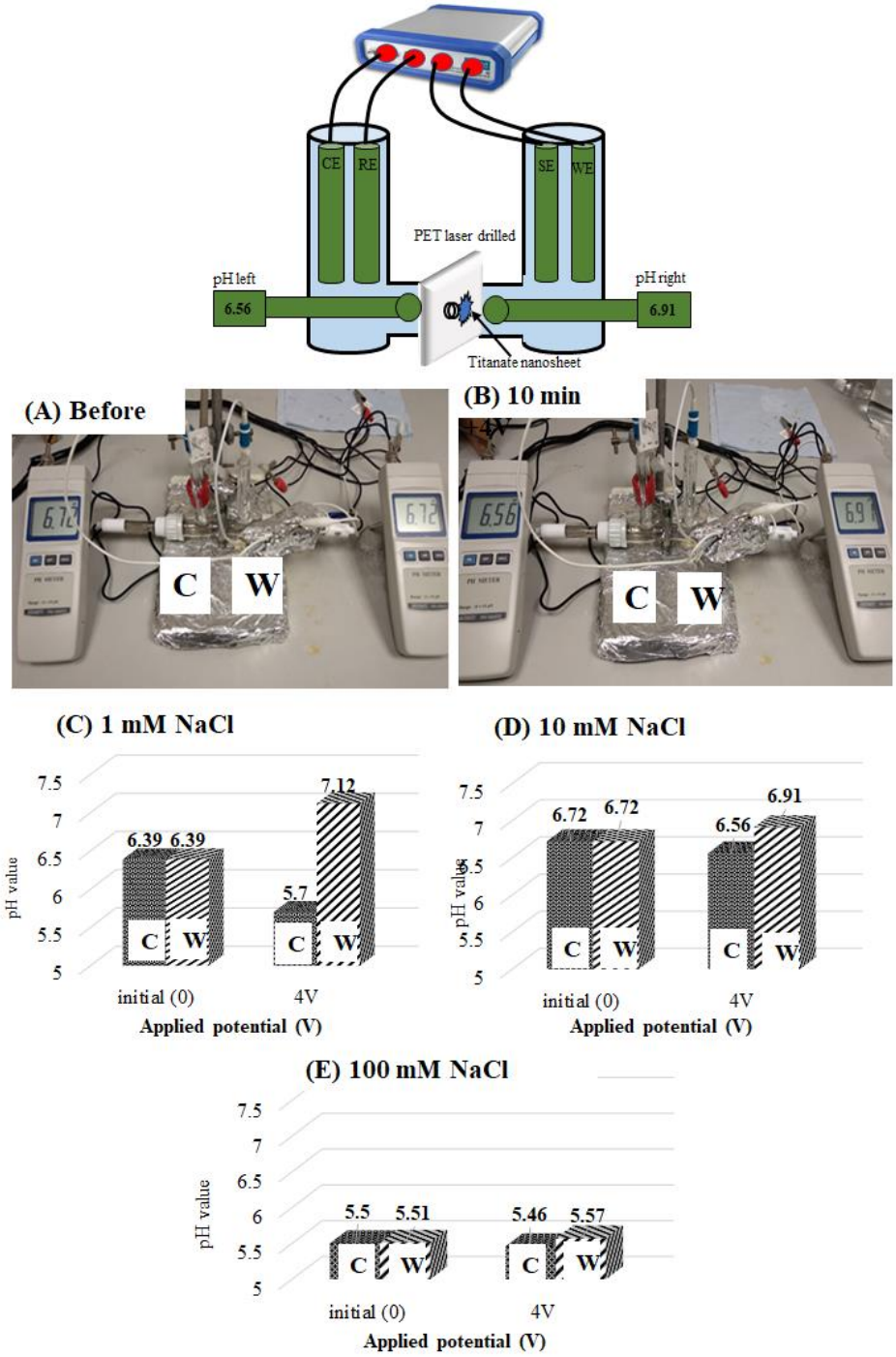

Figure 6.7. Illustration of the experimental system using 2 pH probes to sense protons on both sides of PET film. (A) The photograph shows the experimental cell with right compartment (working electrode and sense electrode) and left compartment (counter electrode and reference electrode. Bar graphs for the pH changes effect at 10 minutes applying +4 V for (C) 1 mM NaCl (10 μA), (D) 10 mM NaCl (23 μA), and (E) 100 mM NaCl (65.4 μA).

In order to calculate the effect of current flow through the titanate film, it is necessary to assume a fixed volume V of ca. 0.01 dm^3 where pH changes occur close to the membrane surface. The protonic current can be estimated in terms of an upper limit for the pH changes in the right/left compartment when the diode is opening (applying +4 V during 10 minutes). Equations (1) express the shift in pH (from the initial value $pH_{initial}$) in the right compartment (where protons are lost) and (2) in the left compartment (where protons are gained).

$$pH_{left} = -\log_{10}(10^{-pHinitial} + It/FV) \quad (1)$$

$$pH_{right} = 14 + \log_{10}(10^{-(14-pHinitial)} + It/FV) \quad (2)$$

Parameters in these equations are the time-average absolute current $I = 10.2 \times 10^{-6}$ A, time t = 600 seconds, and the Faraday constant F = 96487 C mol^{-1}. In Figure 6.7C for the case of a 1 mM NaCl electrolyte, the average current $I = 10.2 \times 10^{-6}$ A at an applied voltage of 4 V was 10 μA over 600 s, which (with $pH_{initial}$ = 6.39) translates to pH_{right} = 8.8 and pH_{left} = 5.2. When the experimental results in Figure 6.7C compared with the predicted theory, the trend is indeed observed. In Figure 6.7D for the case of 10 mM NaCl the observed average current was 23×10^{-6} A at 4 V applied voltage during 600 seconds. These parameters gives pH_{left} = 4.8 and pH_{right} = 9.2.

Based on the experimental data a less strong change in pH (and therefore less competition between Na^+ transport and water heterolysis processes) occurs at the higher NaCl concentration. Additional experiments for 100 mM NaCl in Figure 6.7E suggest even lower pH shift even at higher currents (65.4 μA). Water heterolysis processes appears to be strongly electrolyte concentration dependent and probably insignificant at electrolyte concentrations of 10 mM or higher. Instead of protons, sodium (Na^+) ions dominate the ion transport through titanate films in high concentration of NaCl. Although the experiment gives direct evidence for the water heterolysis process, the data provide only qualitative insights during and further work will be required to provide a quantitative measure of the water heterolysis process conclusively under these conditions.

6.3.5. The Ion Transport Through Lamellar Titanate Nanosheets Deposits: Case for Interference of NBu_4^+ with Proton Transport

In order to create single-layer nanosheets, NBu_4^+ cations are required in order to the exfoliate the interlayer of titanate with a bulky tetraalkylammonium reagent. NBu_4^+ cations are present when depositing titanate nanosheets onto the PET film and they characterise the ability of the titanate lamellae to conduct ions. Therefore, it is important to also study the ionic current rectification and the ion conductivity of NBu_4^+ cations on the titanate nanosheets. Initially, the experiment uses both 10 mM HCl electrolyte in the two-compartment cell as shown in Figure 6.8A. The response is consistent with a typical cationic diode as in Figure 6.8A black line. When adding NBu_4Cl stepwise in specific concentration into the right compartment previously filled with 10 mM HCl, NBu_4^+ cations can equilibrate with the titanate nanosheets deposit and change the ability of the lamellar structure to conduct ions. Cyclic voltammograms in Figure 6.8A demonstrate a systematic decrease in ionic current and rectification ratio (Figure 6.8C) as the added concentration of NBu_4Cl into HCl 10 mM increases. Ultimately, when adding 50 mM NBu_4Cl into HCl 10 mM, the current in the positive potential is the lowest and the current in the negative potential range is the highest (the diode is inverted). The switching of the open diode state from positive potential to negative potential is a strong indication for a change from a cationic diode to an anionic diode. Figure 6.8B shows chronoamperometry data also confirmed the switching from cationic to anionic diode. The current transient at chronoamperometry data in Figure 6.8B shows a rising current when opening the diode. When 50 mM NBu_4Cl is added into the HCl 10 mM, the diode behaviour switches and the rising current transient is observed in the negative potential domain.

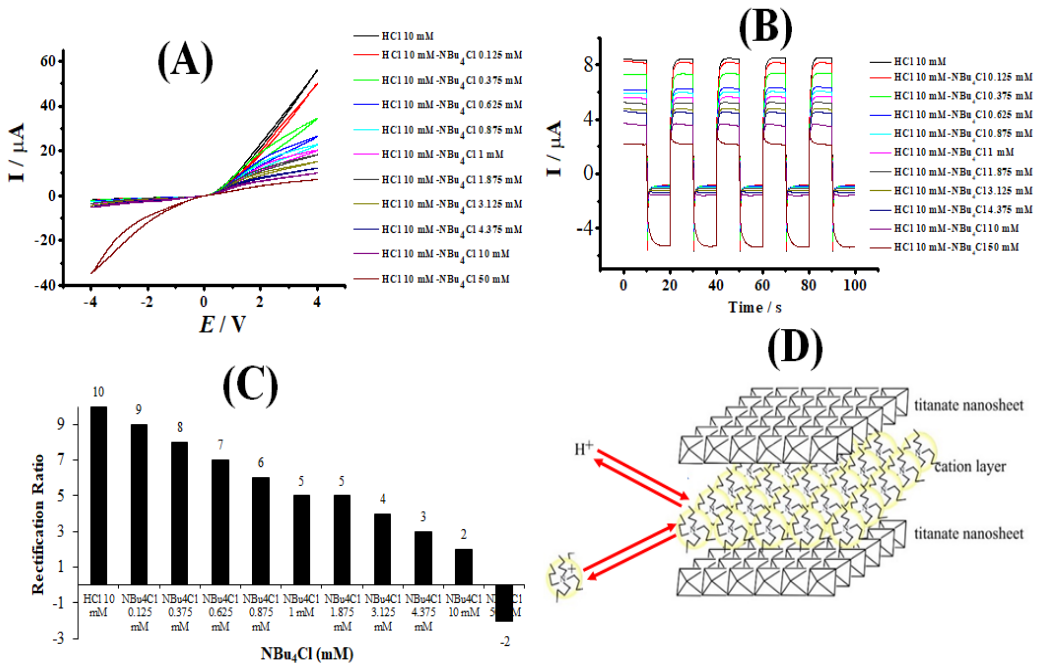

Figure 6.8. (A) Cyclic voltammograms of asymmetric TiO_2 nanosheets deposits with scan rate 25 mVs^{-1} in aqueous electrolyte for 10 mM HCl on the left compartment and 10 mM HCl, 10 mM HCl + 0.12 mM NBu_4Cl, 10 mM HCl + 0.37 mM NBu_4Cl, 10 mM HCl + 0.62 mM NBu_4Cl, 10 mM HCl + 0.87 mM NBu_4Cl, 10 mM HCl + 1 mM NBu_4Cl, 10 mM HCl + 1.87 mM NBu_4Cl, 10 mM HCl + 3.12 mM NBu_4Cl, 10 mM HCl + 4.37 mM NBu_4Cl, 10 mM HCl + 10 mM NBu_4Cl, 10 mM HCl + 50 mM NBu_4Cl, on the right compartment, (B) chronoamperometry data (stepping from +1 V to -1V) immersed in aqueous electrolyte, (C) rectification ratio calculation from chronoamperometry data at +/- 1 V, (D) schematic illustration of the competition of protons and tetrabutylammonium cations intercalates into titanate nanosheets interlayer.

The ion transport in the titanate lamellar structure can be explained based on the equilibration of competing cation in the titanate double layer. Both protons and NBu_4^+ can be bound into the interlayer titanate nanosheets (Figure 6.8D). When there is no NBu_4^+ to bind into the interlayer, protons or other cations can bind and conduct through the titanate deposit. However, when adding NBu_4^+ cations into interlayer titanate, these will bind and block the transport of other cations or protons. When the added concentration NBu_4^+ is 1 mM, both the curent in the open state and rectification ratio decreased to the half of original HCl 10 mM. When NBu_4Cl added more to the interlayer titanate, it is possible to "invert" the diode behaviour. This can be described with surplus of NBu_4Cl binding into the inter-lamellar space of titanate resulted a net anionic transport due to mobile chloride

mechanism is being activated. Further work will be needed to more understand this switch from cationic to anionic current rectification.

6.4. Conclusions

It has been shown that ionic current rectification phenomena or ionic diode effects can be obtained for asymmetrically deposited titanate nanosheets on a PET substrate, as long as the semi-permeable character due to cation transport is maintained. The first part of the results section from this chapter focuses on the ion transport of aqueous NaCl through the titanate nanosheets film, which is found to be very fundamental and therefore useful for explaining and introducing the ionic diode effect. The second part of results section discusses the effects of aqueous cations on the currents and on the performance of diodes based on titanate nanosheets films. It is shown that the currents for monovalent cations are considerable higher than those for divalent cations, presumably due to a higher mobility of the monovalent cations. This is an unusual and unexpected result suggesting that selectivity for certain types of ions is possible. The third part of results section explains the effects of aqueous anions on the performance of ionic diodes based on titanate nanosheets films. The currents in the positive potential range at "open" diode state appear to be considerably higher with increasing of the anion size. In phosphate buffer solution containing mixed cations (K^+ and Na^+) the highest ion currents were observed in the potential range corresponding to the "open" diode state. This is the first demonstration of the use of titanate nanosheets in ionic diodes systems.

The fourth part of results section explains competition between cation and proton transport through lamellar titanate nanosheets using 5-electrode measurements. The five-electrode membrane cell is operated in cyclic voltammetry with the collector (second working electrode) potential fixed at the onset potential (-0.4 V vs SCE). Proton transport associated with the open diode state (at positive applied potential) causes an increase in proton concentration at the location of second working electrode and leads to a current. Data observed for divalent cations (Mg^{2+} and Ca^{2+}) shows that the shape of voltammetric signal is more complex and

indicate of some diode blocking as the potential is scanned into the positive range. This phenomenon is caused by localized pH changes at the surface of titanate film. Water heterolysis occurs at the surface of titanate film and causes locally the formation of hydroxide then in combination with Mg^{2+} or Ca^{2+} causes blocking of titanate nanochannels forming $Mg(OH)_2$ and $Ca(OH)_2$. It will be necessary to observe more quantitatively contributions of the relative contributions of proton and electrolyte cation transport to the diode current.

It has been shown that NBu_4^+ cations can compete with the other cations to bind into interlayer titanate and eventually switch the diode from cationic to anionic due to an increase in positive charge in the lamellar space. For application purposes such as in desalination, the interaction between lamellar structures with NBu_4^+ guest cations need to enhanced in order to maintain effective rectification at higher ionic strengths. Therefore, the inter-lamellar space of titanate needs to be better designed to maintain a higher rectification effect with maintaining its semi-permeability. This can be accomplished by tuning the concentration and structure of the tetraalkylammonium guest cations.

6.5. References

1 Matsumoto, Y., Funatsu, A., Matsuo, D., Unal, U., Ozawa, K. *J. Phys. Chem. B.* **2001.** 105, 44, 10893–10899.

2 Sasaki, T. *Supramolecular Sci.* **1998**. *5*, 3-4, 367–371.

3 Chen, X., Mao, S.S. *Chem. Rev.* **2007.** *107*, 7, 2891–2959.

4 Sasaki, T., Watanabe, M. *J. Am. Chem. Soc*. **1998**. *120*, 19, 4682–4689.

5 Maluangnont, T., Matsuba, K., Geng, F., Ma, R. Yamauchi, Y., Sasaki, T. *Chem. Mater.* **2013**. *25*, 15, 3137–3146.

6 Yuan, H., Besselink, R., Liao, Z., ten Elshof, J.E. *Sci. Rep*. **2014.** *4,* 4584–4589.

7. Wahyuni, W.T., Putra, B.R., Harito, C., Bavykin, D.V., Walsh, F.C., James, T.D., Kociok-Kohn, G., Marken, F. *Electroanalysis.* **2018**. *30,* 7, 1303–1310.

8 Sasaki, T., Ebina, Y., Kitami, Y., Watanabe, M., Oikawa, T. *J. Phys. Chem. B*. **2001**. 105, 26, 6116–6121

9 He, D., Madrid, E., Aaronson, B., Fan, L., Doughty, J., Mathwig, K., Bond, A.M., McKeown, N.B., Marken, F. *ACS Appl. Mater. Interfaces.* **2017**, *9*, 11272-11278.

10 Madrid, E., Cottis, P., Rong Y., Rogers A.T., Stone, J.M., Malpass-Evans, R., Carta, M., McKeown, N.B., Marken, F. *J. Mater. Chem. A.* **2015**. *3*, 15849-15853.

11 Aaronson, B.D.B., He, D., Madrid, E., Johns, M.A., Scott, J.L., Fan, L., Doughty, J., Kadowaki, M.A.S., Polikarpov, I., McKeown, N.B., Marken, F. *ChemistrySelect*. **2017**. *2*, 871-875.

12 Tshwenya, L., Arotiba, O., Putra, B.R., Madrid, E., Mathwig, K., Marken, F. *J. Electroanal. Chem*. **2018**. *815*, 114-122.

13 Mathwig, K., Aaronson, B.D.B., Marken, F. *ChemElectroChem*. **2018.** *5*, 897–901.

14 Madrid, E., Rong, Y.Y., Carta, M., McKeown, N.B., Malpass-Evans, R., Attard, G.A., Clarke, T.J., Taylor, S.H., Long, Y.T., Marken, F. *Angew. Chem. Inter. Ed.* **2014**. *53*, 40, 10751–10754.

15 Harito, C., Bavykin, D.V., Light, M.E., Walsh, F.C. *Composites B : Engineering*. **2017**. *124*, 54–63

16 Martins, A.S., Harito, C., Bavykin, D.V., Walsh, F.C., Lanza, M.R.V. *J. Mater. Chem. C*. **2017**. *5*, 3955–3961.

17 Sasaki, T., Ebina, Y., Kitami, Y., Watanabe, M., Oikawa, T. *J. Phys. Chem. B*. **2001**. *105*, 6116–6121.

18 Brown, R., Madrid, E., Castaing, R., Stone, J.M., Squires, A.M., Edler, K.J., Takashina, K., Marken, F. *ChemElectroChem*. **2017**. *4*, 1172–1180

Chapter 7
Three Dimensional Nanomaterials: Ionic Rectification based on a PIM-EA-TB | Nafion "Heterojunction"

Contents

Chapter Abstract

Ionic diode phenomena were observed based on a Nafion cation conductor and a Polymer of Intrinsic Microporosity (PIM-EA-TB with EA = Ethanoanthracene and TB = Tröger Base) interfaced at a 6 μm thickness polyethylene-terephthalate (PET) film with 20 μm diameter microhole. Ionic diode phenomena occur at asymmetric ionomer | aqueous electrolyte microhole interfaces and show improved diode characteristics and current rectification in aqueous NaCl. The effects of creating the PIM-EA-TB | Nafion micro-interface are investigated and suggested to lead to novel sensor architectures. Further work with this heterojunction has been exploited in diode mechanisms in a potassium diode sensor context. The mechanism of potassium diode sensing is based on a precipitation reaction of potassium cations with perchlorate anions to give insoluble $KClO_4$ at the interface of PIM-EA-TB | Nafion heterojunction. The blocking process due to the $KClO_4$ layer is suggested to be dynamic/fast and potentially useful as a diode sensor mechanism based on a solubility product dependent precipitation.

Chapter Publication

Part of this chapter have been published in:

First paper: B. R. Putra, B. D. B. Aaronson, E. Madrid, K. Mathwig, M. Carta, R. M.-Evans, N. B. McKeown, F. Marken. Ionic Diode Characteristics at a Polymer of Intrinsic Microporosity on a Microhole Poly(ethylene-terephthalate) Substrate. *Electroanalysis*. **2017**, 29, 10, 2217-2223.

Second paper: B. R. Putra, M. Carta, R. M.-Evans, N. B. McKeown, F. Marken. Potassium Cation Induced Ionic Diode Blocking for a Polymer of Intrinsic Microporosity | Nafion "Heterojunction" on a Microhole Substrate. *Electrochimica Acta*. **2017**. *258*, 807-813.

Acknowledgement

Dr. Mariolino Carta, Dr. Richard Malpass-Evans, and Prof. Neil B. McKeown from University of Edinburgh, UK are acknowledged for providing PIM-EA-TB materials for ionic diode studies based on PIM-EA-TB | Nafion "heterojunction" membranes.

7.1. Introduction

In this chapter the focus is on the ion transport through heterojunction membrane devices based on deposition Nafion onto one side of 20 μm diameter microhole in a poly-ethylene-terephthalate (PET) film and deposition of PIM-EA-TB on the opposite side of the PET (Figure 7.1). The resulting membrane device is named by PIM-EA-TB | Nafion "heterojunction" and observed to give ionic current rectification phenomena similar to those obtained with asymmetrically deposited Nafion onto a 20 μm diameter microhole onto a PET substrate.[1] Commercial Nafion ionomer (see molecular structure in Figure 7.1), when deposited onto a 20 μm diameter microhole in a PET film, was found to provide ionic current rectification effects not only for acidic environments, but also for neutral solutions of NaCl or KCl.[2] The cation conduction through the Nafion film was observed to be uni-directional due to the asymmetric geometry of the deposit on the PET substrate. The PIM-EA-TB deposit opposite to the Nafion can help improving the perfomance and selectivity of the ionic diode device as well as defining a PIM-EA-TB | Nafion interface.

The polymer of intrinsic microporosity PIM-EA-TB (see molecular structure in Figure 7.1) is a member of a wider class of PIM materials.[3] This is a solution processable polymer, which behaves as microporous material due to highly rigid and contorted polymer/molecular chains that prevents packing and ensure microporosity.[4] This polymer offers a novel class of porous materials with high internal porosity and surface area with excellent processibility.[5,6,7] Generally, polymers based on PIM materials provide highly rigid molecular polymer structures that pack space poorly and therefore provide porous solid films. Further benefits from the molecularly rigid structure of PIM materials are good solubility in certain organic solvents (e.g. chloroform)[8] as well as high thermal stability.[9]

It has been observed that the ionic current rectification effects change as a function of pH for the PIM-EA-TB materials when this microporous polymer was asymmetrically deposited onto a 20 μm diameter microhole of a PET substrate.[10] Protonation of the tertiary amine in the neutral PIM-EA-TB structure at

approximately pH 4 was found to convert the polymer into an anion conducting structure.[10] Therefore, when PIM-EA-TB is immersed into aqueous electrolyte (e.g. NaCl), it can be considered mainly neutral with both Na^+ and Cl^- conducting through its microporous structure. However, PIM-EA-TB can be predominantly positively charged when protonated to give exclusively Cl^- conducting behaviour (e.g. when immersed into aqueous electrolyte HCl).

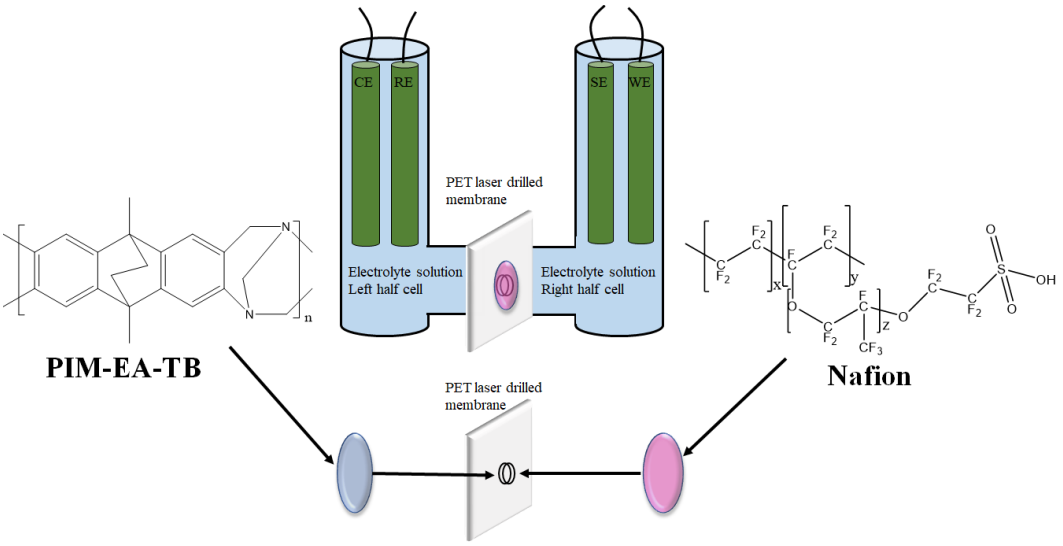

Figure 7.1. Schematic description of the classic 4-electrode measurement cell with a 6 μm thick PET film containing microhole (20 μm diameter) covered with deposits of PIM-EA-TB and Nafion (see molecular structures).

In this chapter, it is demonstrated that the Nafion deposit on the microhole in PET can be complemented by an opposite PIM-EA-TB deposit (Figure 7.1) in order to enhance the ionic current rectification effects in this heterojunction membrane. This constitutes a new type of heterojunction membrane device with ionic diode characteristics, in which both the "open" and the "closed" state of diode can be affected by the PIM-EA-TB film. In the first part of the results chapter, the improved diode characteristics and rectification are observed in aqueous NaCl solution. The focus here is on cationic diode effect for this PIM-EA-TB | Nafion heterojunction. The application could be in desalination in NaCl electrolyte or to provide more ion selective diodes for analytical applications. The interface of PIM-EA-TB | Nafion is critical to define a new reaction zone in which "sensing processes" can be restricted to lead to strong amplification/switching effects, for

example when analyte causes localised switching of the state of the diode form closed to open. In the second part of this results chapter, K^+ cations are investigated as mobile species in Nafion deposits. Cationic diode characteristics are observed with $NaClO_4$ in contact to a PIM-EA-TB deposit. The PIM-EA-TB deposit allows $KClO_4$ precipitation reactions to occur in a defined region at the PIM-EA-TB | Nafion "heterojunction" interface. The accummulation of K^+ at the PIM-EA-TB | Nafion interface was used to generate "inverted" diode characteristics with a perchlorate (ClO_4^-) triggered precipitation reaction leading to potential for sensor applications. Finally, a process sensitive to potassium, K^+, with an additional Na^+ as competing cation is investigated using the PIM-EA-TB | Nafion "heterojunction".

7.2. Experimental

7.2.1. Chemical Reagents

Nafion®-117 (5% in a mixture of lower aliphatic alcohol and water), concentrated hydrochloric acid (37%), sodium chloride, rhodamine B (97%), and eosin Y were obtained from Sigma-Aldrich or Fisher Scientific and used without further purification. Solutions were prepared under ambient conditions in volumetric flasks with ultra-pure water of resistivity 18.2 MΩ cm from ELGA Purelab Classic system.

7.2.2. Instrumentation

An Ivium Compactstat potensiostat system (The Netherlands) was used to record all electrochemical data (voltammetry, chronoamperometry, and impedance experiments) at T = 20 ± 2 ^oC. A classic 4-electrode electrochemical cell configuration was employed during the electrochemical experiments. The membrane separates two tubular half-cells (15 mm diameter, see Figure 7.1), one with Pt wire working and KCl-saturated calomel (SCE) sense electrode (right in Figure 7.1) and the other with SCE reference electrode and Pt wire counter electrode (left in Figure 7.1B). In electrochemical measurements the working electrode was always located on the side of Nafion films. Fluorescence imaging experiments were performed on a Carl Zeiss Confocal Scanning Microscpore. For fluorescence

analysis, rhodamine B was mixed with Nafion-117 solution and eosin-Y was mixed with PIM-EA-TB (2% in chloroform), which were then applied to opposite sides of the PET films.

7.2.3. Fabrication Procedure of PIM-EA-TB | Nafion "Heterojunction"

A two-step solution casting method was employed in order to obtain Nafion and PIM-EA-TB deposits on PET substrates (obtained with 20 μm diameter hole in 6 μm thick PET from Laser-Micro-Machining Ltd., Birmingham, UK). Before deposition of PIM-EA-TB, a microscopy glass slide was pre-coated with a thin layer of 1% agarose gel. The PET film was placed onto the gel to prevent PIM-EA-TB solution from entering/crossing the microhole. A volume of 10 μL PIM-EA-TB solution (2% in chloroform) was applied to the surface and with a glass rod the PIM-EA-TB solution was spread evenly over the PET to give a 1 cm^2 film, which after drying produced a thin uniform coating typically 10 μm thickness. Next, the PET film was turned around and coated with a volume of 10 μL Nafion solution from the opposite side. Confocal fluorescence microscopy was used in order to take the orthogonal image stacks of Nafion and PIM-EA-TB films. Figure 7.2 shows the stacked images of Nafion and PIM-EA-TB film with red coloration indicating rhodamine B in Nafion and yellow coloration indicating eosin Y in PIM-EA-TB. Three layers corresponding to Nafion with (ca. 6 μm thick), PET (ca. 6 μm thick), and PIM-EA-TB (ca. 10 μm thick) are shown (partially obscured by the shadowing effects).

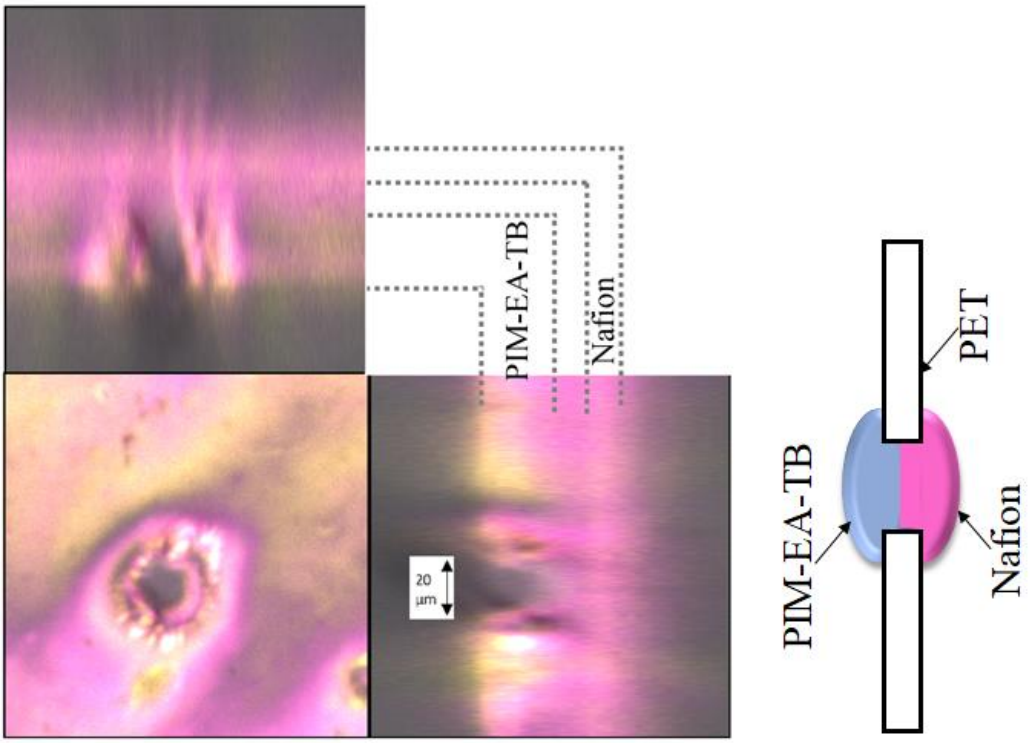

Figure 7.2. Orthogonal fluorescence image stacks showing the cross-section and the top view (central slice) based on PIM-EA-TB | Nafion heterojunction. Nafion was stained with rhodamine B (associated with red color) and PIM-EA-TB was stained with eosin Y (associated with yellow color).

7.3. Results and Discussion

The first part of the results chapter introduces and characterises the PIM-EA-TB | Nafion "heterojunction". Measurements were performed as a function of NaCl and HCl concentration in both sides on the membranes. Within the first part of the results chapter, the PIM-EA-TB | Nafion heterojunction will be investigated in a range of ionic diode architectures to assess whether they can bring improvements to the rectification effect. The rectification effects will be compared with different types of aqueous electrolyte solutions and as a function of concentration. This is a new type of PIM-EA-TB | Nafion heterojunction and is likely to lead to novel ionic diode characteristics.

7.3.1. Ionic Rectification Effects as a Function of NaCl or HCl Concentration: Symmetric Case

It has been reported previously that ionic current rectification behaviour occurs for Nafion deposited asymmetrically onto 6 μm thick film of poly-(ethylene-terephthalate, PET) with 20 μm diameter microhole[2]. Electrochemical techniques (cyclic voltammetry and chronoamperometry) were employed. From the chronoamperometry data rectification ratio values of 10 to 20 were extracted (obtained by dividing the current at +1 V by the current at -1 V) for both aqueous HCl and aqueous NaCl. It was observed that the rectification ratio increased significantly when the concentration of aqueous electrolyte was increased on the Nafion side. However, when the electrolyte concentration was increased on the opposite side, the opposite effect occurred (the rectification ratio decreased significantly). This behaviour was explained with the ionic diode mechanism based on a semi-permeable membrane. In the open state (positive applied potential) electrolyte accumulates in the microhole. In the closed state with negative applied potential, the electrolyte deplets and the current is dependent on the transport of cations in the aqueous phase close to the microhole. For potential future applications of the ionic diode or rectifier device, the membrane resistivity is preferred to be low (at open diode), to be high (at closed diode), and fast switching from open to closed diode (or vice versa) is desirable in order to achieve high ionic rectification effect with minimum energy losses.

A new type of interface is created when a film of PIM-EA-TB (see structure in Figure 7.1) deposited on the opposite side to Nafion onto a PET film with 20 μm diameter microhole. The electrochemical investigation using cyclic voltammetry and chronoamperometry experiment is investigated in this chapter. Figure 7.3A shows data for PIM-EA-TB | Nafion immersed in aqueous NaCl for 1 mM, 10 mM, and 100 mM solution on both sides. Data of voltammetric responses are recorded over a +/-4 V potential range with a scan rate 25 mV s^{-1}. When the concentration of NaCl was increased from 1-100 mM on the side of the Nafion deposit, the current at the positive applied potential area (open diode) was significantly increased. Therefore, the rectification ratio for NaCl with concentration ratio 1-100 mM using

a PIM-EA-TB | Nafion is also increased (see Figure 7.3C). The magnitude of currents for NaCl cases at open diode at positive applied potential seems to be slightly higher than to those reported for Nafion only by He et al.[2] Consequently, this new type of interface, a PIM-EA-TB | Nafion is interesting to be explored to optimise the ionic current rectification effect.

The experiment is continued with an aqueous HCl in a concentration range 1-100 mM in contact with both of PIM-EA-TB and Nafion films as shown in Figure 7.3D. When using Nafion only, generally aqueous HCl caused a higher current for the open diode at positive applied potential due to the higher mobility of protons across the semi-permeable membrane. For the PIM-EA-TB | Nafion heterojunction, it is obvious that the currents for both open and closed diodes are higher than those for Nafion only (almost approaching 1 mA in the open state for NaCl 100 mM; see Figure 7.3D). The rectification ratio for Nafion only has been reported for HCl 1-100 mM as 13, 15, 7, while using PIM-EA-TB | Nafion "heterojunction" for HCl in the same concentration range gave 19, 35, and 35 (see Figure 7.3F). Therefore, the rectification ratio using the PIM-EA-TB | Nafion "heterojunction" is improved (roughly doubled) compared using Nafion only.

A further interesting result is a new limiting current observed stabilising at potentials positive of approximately 1 V for 10 mM HCl solution (see Figure 7.3D). This phenomenon can be explained when considering the ion transport conditions for open and closed state of the diode as explained by for a Nafion | aqueous electrolyte interface by He et al.[2] The overall behaviour of the diode at open and closed states is dominated by the Nafion layer only allowing cation transport through its microhole channels. In the open state of the diode using Nafion, the cation transport is hindered primarily by the resistance in the Nafion ionomer and then salt concentration can build up in the aqueous side. While in the closed state of the diode using Nafion, the cation transport is hindered mainly in the aqueous phase by diffusion-migration access to the Nafion ionomer. When using a PIM-EA-TB | Nafion "heterojunction", in the closed state of the diode (at negative applied potentials) cations have to access and enter via the PIM-EA-TB first to then conduct

through the Nafion. Without PIM-EA-TB layer (for Nafion only) in the closed state of the diode, the diffusion-migration access of cations from the aqueous phase to the Nafion ionomer would limit the ion transport. However, when using PIM-EA-TB only and the pH is above than 4 and the polymer is mainly neutral[10] and only some NaCl will enter and access the film of microporous polymer to conduct to the Nafion film. In the presence of PIM-EA-TB with Nafion on the opposite side and at pH < 4 the microporous polymer will be protonated, cation transport is believed to be slow and mainly chloride transport will be dominating in PIM-EA-TB for aqueous HCl electrolyte. Nevertheless, this microporous polymer still remains as poor cation/proton conducting material and this causes a low current in the closed state at negative applied potentials (see in Figure 7.3D in 1 mM HCl).

In the case of an open state of diode at positive applied potentials, a similar approach applies with flow of cations fast across from Nafion side to PIM-EA-TB layer and fast transfer of chloride within the polymer of intrinsic microporosity. This phenomenon causes salt accumulation inside the microhole especially at the PIM-EA-TB | Nafion interface (see Figure 7.3G in open state). When the pH of solution is above 4, an additional chloride can enter and access the PIM-EA-TB microporous structure to increase conductivity of the cation transport. While the pH of solution is lower than 4, this causes poor conductivity for cation inside the microporous structure of PIM-EA-TB layer. For the case of 1 mM HCl a new limiting current observed at positive applied potential approximately +1 V and shows that PIM-EA-TB blocks the cation transport or current even when Nafion is highly conducting under these conditions. In general, the current in the open state of the diode for Nafion only is lower than that for the current in the open state of the diode for the PIM-EA-TB | Nafion "heterojunction". Both, Nafion on the side of the working electrode compartment and PIM-EA-TB on the side of the counter electrode compartment operate synergistically to provide an improved or modified ionic current rectification effect.

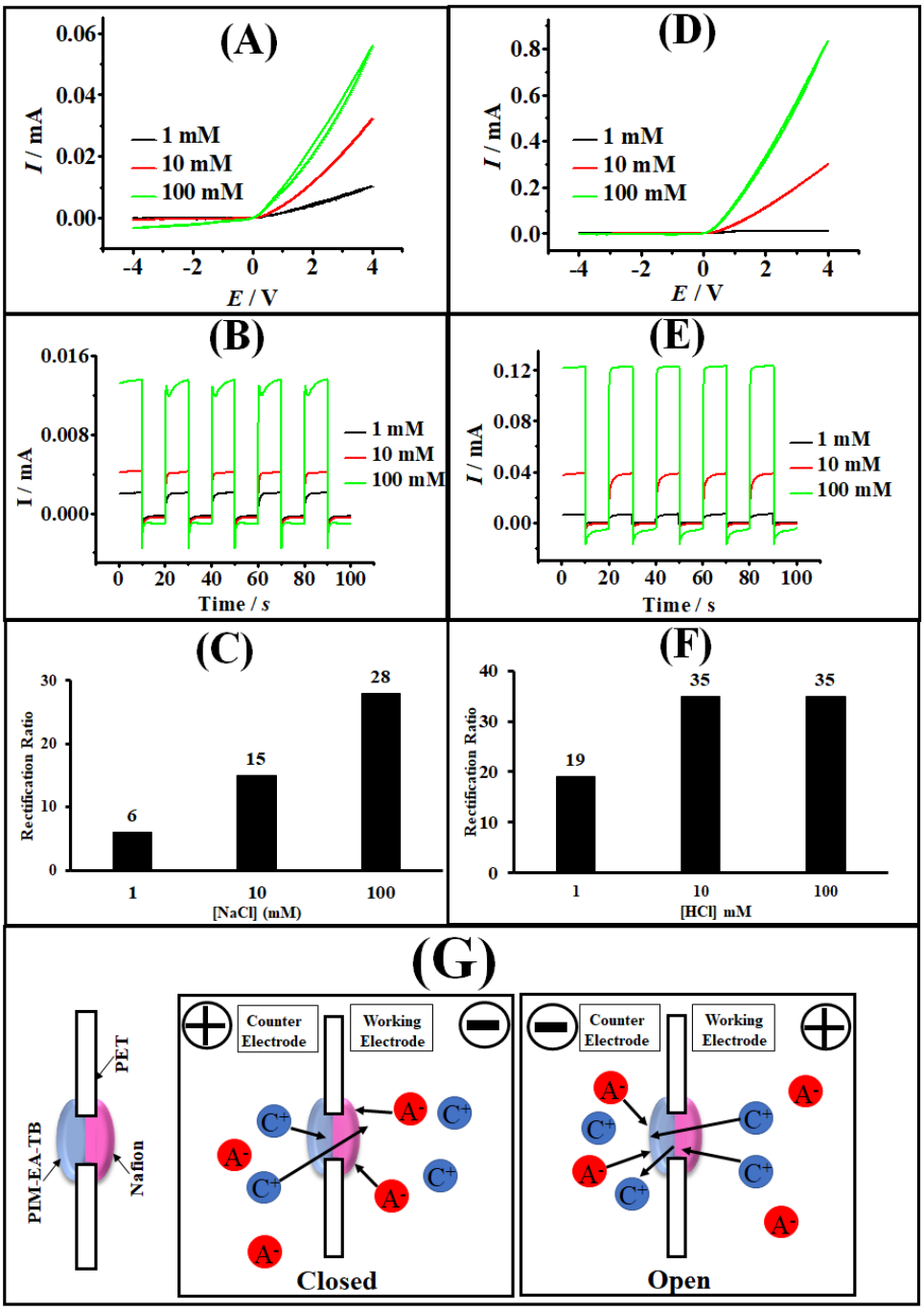

Figure 7.3. (A) Cyclic voltammograms with scan rate 25 mVs^{-1} for a PIM-EA-TB | Nafion heterojunction immersed in aqueous NaCl (1, 10, 100 mM) on both sides. (B) As before, but with chronoamperometry data (stepping from +1 V to -1 V). (C) As before, but with rectification ratio at +/1 V. (D) Cyclic voltammograms with scan rate 25 mVs^{-1} for a PIM-EA-TB | Nafion heterojunction immersed in aqueous HCl (1, 10, 100 mM) on both sides. (E) As before, but with chronoamperometry data (stepping from +1 V to -1 V). (F) As before, but with rectification ratio at +/1 V. (G) Schematic drawing of ion flow in closed and open diode states based on PIM-EA-TB | Nafion heterojunction.

7.3.2. Ionic Rectification Effects as a Function of NaCl or HCl Concentration: Asymmetric Case

New phenomena were observed when placing the PIM-EA-TB | Nafion heterojunction in contact with different aqueous electrolytes (10 mM HCl and 10 mM NaCl) as an asymmetric case. Figure 7.4A shows the data from cyclic voltammetry with different scan rates from 25, 50, 100, 250, 500, and 1000 mV s^{-1} using PIM-EA-TB in contact with 10 mM HCl and Nafion in contact with 10 mM NaCl. It has been shown that at elevated scan rates (higher than 100 mV s^{-1}) generally the currents in the open state of diode (positive applied potential) are lower and a limiting current in the open diode state is observed as well. This phenomenon is expected when the PIM-EA-TB film is exposed to acidic media (see Figure 7.3D). The current in the open state of the diode passing through the protonated PIM-EA-TB is limited by cation (sodium) mobility in the Nafion side (working electrode compartment). At slower scan rates (below 100 mVs^{-1}) the PIM-EA-TB is probably deprotonated and thereby allowing cations (Na^+) to pass through the microporous polymer structure (see Figure 7.4D).

Normal diode characteristics are restored (see Figure 7.4E) when placing Nafion in contact with 10 mM HCl and PIM-EA-TB in contact with 10 mM NaCl (switching the sides). However, the currents at the open state of diode are lower when compared to the symmetric case for both sides containing 10 mM HCl using PIM-EA-TB | Nafion "heterojunction" (see Figure 7.3D). Figure 7.4 D and H explain the phenomena of open and closed state of diodes of 10 mM NaCl-10 mM HCl (or vice versa) schematically. It can be considered that the PIM-EA-TB | Nafion "heterojunction" is consistent with a sodium pump or "sodium diode" in Figure 7.4D whereas the drawings in Figure 7.4H suggest a proton pump or "proton diode".

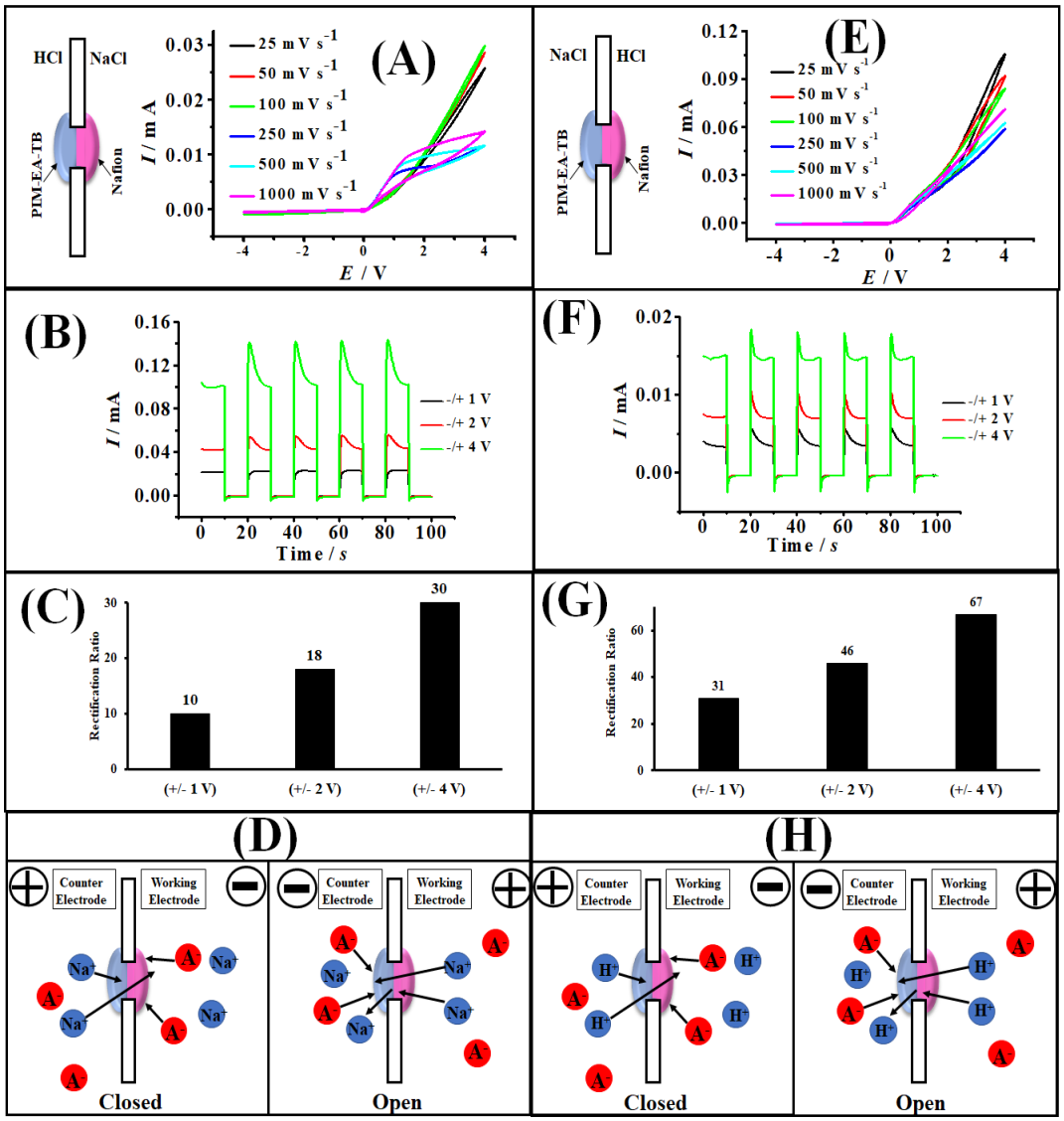

Figure 7.4. (A) Cyclic voltammograms for a PIM-EA-TB | Nafion heterojunction with scan rate 25, 50, 100, 250, 500, 1000 mVs^{-1} immersed in 10 mM HCl – 10 mM NaCl. (B) As before, but with chronoamperometry data (switching at +/- 1, 2, and 4 V). (C) As before, but with rectification ratio at +/- 1, 2, and 4 V. (D) Schematic drawings explaining the open and closed diode behaviour for the case HCl in contact with PIM-EA-TB and NaCl in contact with Nafion. (E) Similar with case (A) but NaCl in contact with PIM-EA-TB and HCl in contact with Nafion. (F) As before, but with chronoamperometry data (switching at +/- 1, 2, and 4 V). (G) As before, but with rectification ratio at +/- 1, 2, and 4 V. (H) Schematic drawings explaining the open and closed diode behaviour for the case of NaCl in contact with PIM-EA-TB and HCl in contact with HCl.

In Figure 7.4A, when investigating the cyclic voltammogram of PIM-EA-TB | Nafion "heterojunction" with 10 mM HCl-10 mM NaCl case at a high scan rate of 1000 mVs^{-1}, a small cathodic peak can be seen emerging at approximately 0 V. This small peak is associated with the switching time of the diode of PIM-EA-

TB | Nafion “heterojunction” for the case of switching condition from open state to closed state. In the open state of heterojunction diode, sodium cations flow through the Nafion film then permeate to the PIM-EA-TB film and possibly pushing protons out from the microporous polymer structure. When the diode is switched from open state to closed state, the protons have to re-enter the microporous structure of PIM-EA-TB film, which leaves a short period of current flow (due sodium cation removal and protons re-entering the PIM-EA-TB layer). Further details about this phenomenon can be observed when investigating chronoamperometry current data as a function of time.

7.3.3. Ionic Rectification Effects as a Function of Time

Figure 7.5B shows the the chronoamperometry data for HCl 10 mM-HCl case when using the PIM-EA-TB | Nafion “heterojunction” with switching potentials of +/- 1 V. Transient phenomena (current spikes) are observed for both closed (cathodic current) and open (anodic current) diodes. Both phenomena can be explained with an accumulation and decrease in proton concentration in the PIM-EA-TB film (in the counter electrode compartment). More complex transient phenomena are observed in both closed (cathodic current) and open (anodic current) diodes in chronoamperometry data for the case of 10 mM NaCl – 10 mM NaCl as shown in Figure 7.5B. Both currents when the diode is opening and closing (for switching potentials from +1 V to -1V) are associated with an initial fast spike followed by another slower rise in anodic or cathodic current, respectively. This phenomenon can be associated with fast anion (chloride) transport followed by slower accumulation of both sodium and chloride ions to fully develop the concentration profile across the interface of PIM-EA-TB | Nafion “heterojunction”.

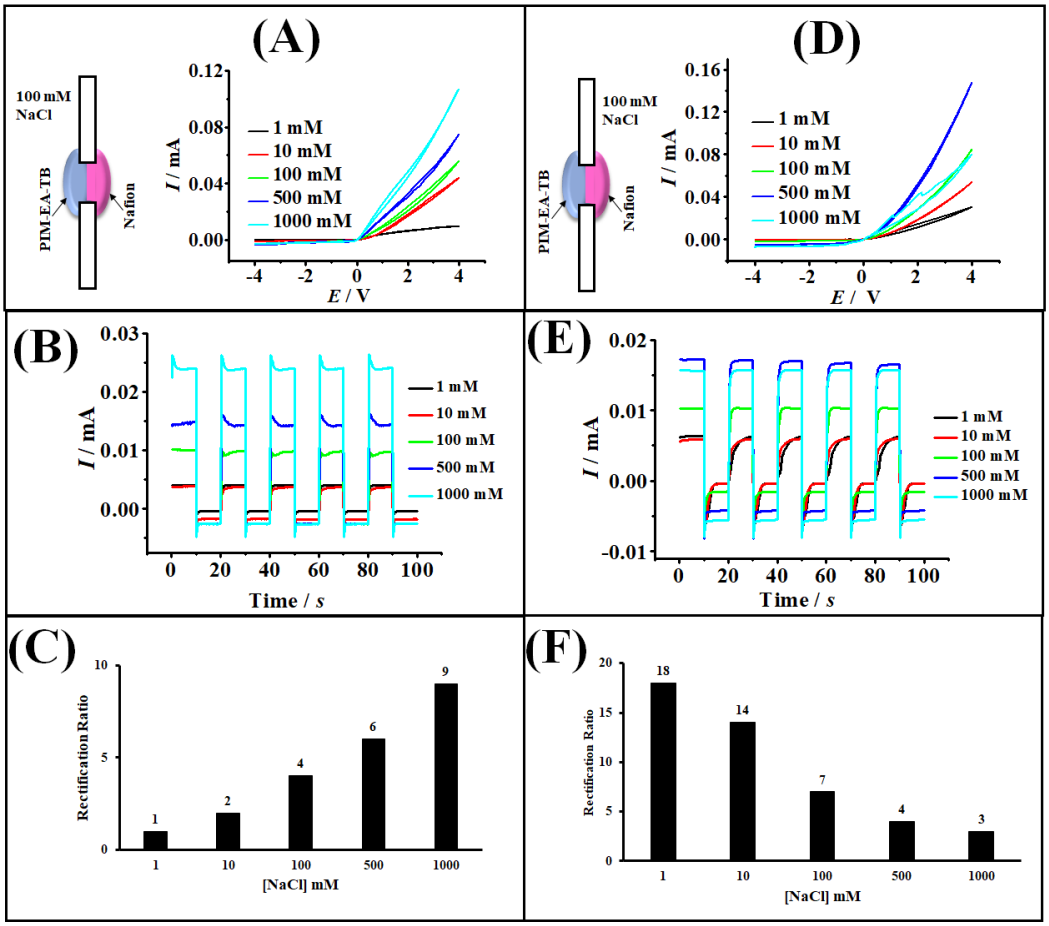

Figure 7.5. (A) Cyclic voltammetry data for a PIM-EA-TB | Nafion heterojunction (scan rate 25 mVs^{-1}) with 100 mM NaCl in contact to PIM-EA-TB and 1, 10, 100, 500, 1000 mM HCl in contact to Nafion. (B) As before, but with chronoamperometry data (stepping from +1 V to -1 V). (C) As before, but with rectification ratio at +/- 1 V. (D) Similar with case (A) but 100 mM NaCl in contact to Nafion and 1, 10, 100, 500, 1000 mM HCl in contact to PIM-EA-TB. (E) As before, but with chronoamperometry data (stepping from +1 V to -1 V). (F) As before, but with rectification ratio at +/- 1 V.

Figure 7.5A shows voltammetric data (scan rate 25 mV s^{-1}) for the case of a fixed 100 mM NaCl concentration in contact with PIM-EA-TB and various concentration (1-1000 mM) of NaCl in contact with Nafion. When the concentration of NaCl increases on the side of Nafion, the rectification ratio clearly improves (Figure 7.5C) mainly due to a higher conductivity of ions across the Nafion film. The currents observed with 1000 mM NaCl on the Nafion side approach 1 mA (through a 20 μm diameter microhole). The opposite behaviour is observed when the concentration of NaCl increased (see Figure 7.5D) with a strong loss of rectification effect in a concentration range of 1-1000 NaCl mM. An increase

of concentration of NaCl in this concentration range is probably also increasing the salt concentration in the PIM-EA-TB microporous structure. The high concentration of salt in the PIM-EA-TB structure can block the ion transfer across heterojunction membrane and give detrimental effects in the closed state of the diode. It can be concluded that both materials Nafion and PIM-EA-TB perform different tasks during ion transfer across the dual-material membrane in the ionic diode investigation. Nafion films receive the positive charge carriers (Na^+ or H^+) and needs high conductivity and the PIM-EA-TB layer holds the return of positive charge carriers inside the microporous structure. Both of these tasks performed by Nafion and PIM-EA-TB materials are influenced by the type and concentration of aqueous electrolyte in contact to the microporous polymer deposits.

7.3.4. Characterisation of "Normal" Cationic Diode Effects as a Function of KCl and $NaClO_4$ with a PIM-EA-TB | Nafion "Heterojunction"

Figure 7.6A shows cyclic voltammetry data for the case of aqueous electrolyte ($NaClO_4$) in contact with a Nafion layer and aqueous electrolyte (KCl) in contact with PIM-EA-TB film. In the open state of the diode (positive applied potential) there is a fast transport of Na^+ from aqueous electrolyte $NaClO_4$ to the semi-permeable Nafion film. In contrast, in the closed state of the diode (negative applied potential) there is only a limited rate of K^+ transport to the Nafion. Figure 7.6D shows a schematic description of these processes in the open and closed state of the PIM-EA-TB | Nafion "heterojunction". Cyclic voltammetry data in Figure 7.6A show currents when the diode is open at positive potentials applied on the Nafion side with cationic rectifier characteristics. The magnitude of the currents in the open state of the diode are affected by the electrolyte concentration of both KCl and $NaClO_4$ in a concentration range of 1-100 mM. Based on studies that have been reported by Mathwig et al.[1] and He et al.[2], this phenomenon is probably caused by the high conductivity of Na^+ within the Nafion deposit in the open state of the diode at positive applied potential domain.

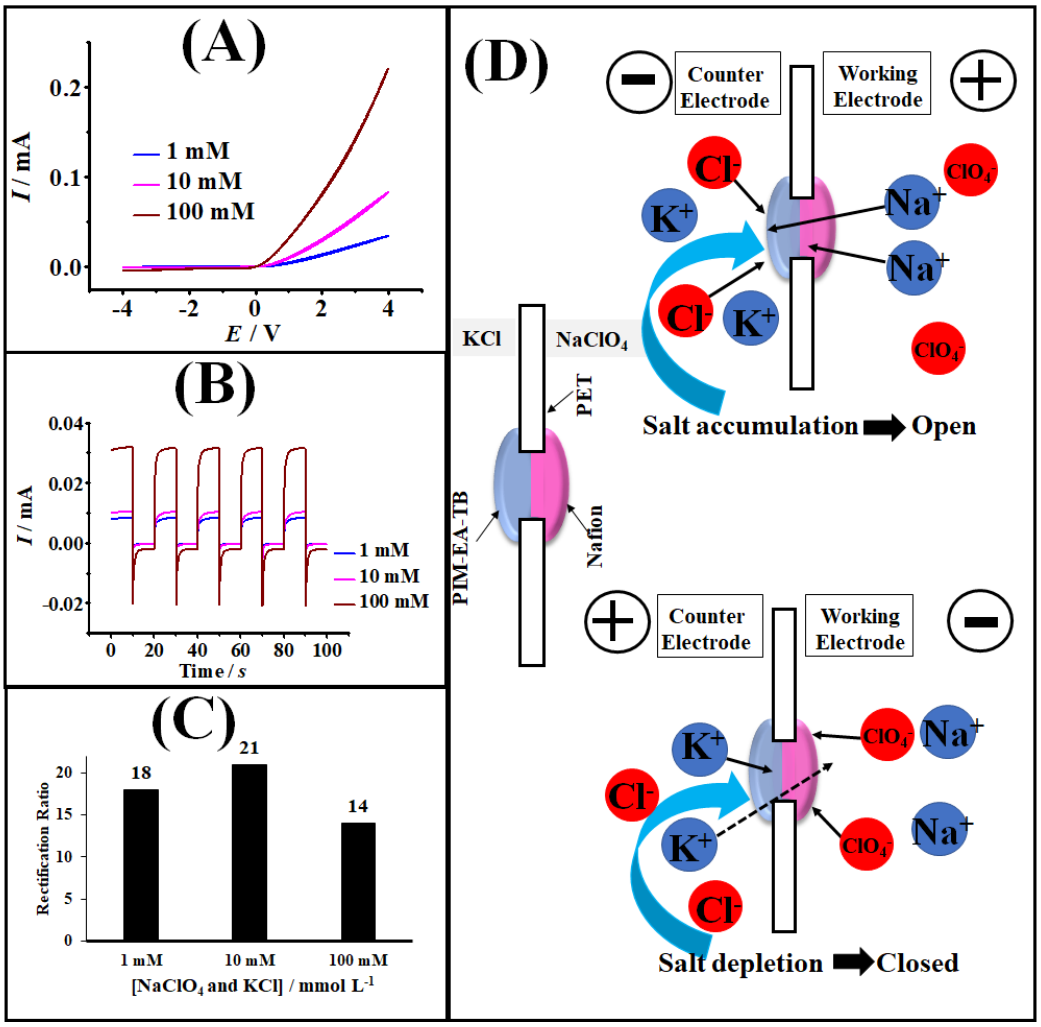

Figure 7.6. (A) Cyclic voltammograms for a PIM-EA-TB | Nafion hetero-junction (scan rate 25 mVs^{-1}) with both concentration of KCl (counter electrode compartment) and $NaClO_4$ electrolyte (working electrode compartment) are 1, 10, and 100 mM. (B) As before but with chronoamperometry data (stepping from +1 V to -1 V). (C) As before, but with rectification ratio at +/- 1 V. (D) Schematic drawings explaining the open and closed diode behaviour for the case of KCl in contact with PIM-EA-TB and $NaClO_4$ in contact with Nafion.

In the closed state of diode (negative applied potentials to the Nafion side), there is low level of K^+ transport with a resulting rectification ratio of typically 20 (calculated as the ratio of absolute currents (*I*) at +1V divided by that at -1V; see in Figure 7.6C). Figure 7.6B shows additional chronoamperometry data consistent with cyclic voltammetry data in Figure 7.6A. The chronoamperometry data primarily represent the switching time from open to closed state of the diode (or vice versa) or the time constant, which can be estimated here as typically 1 s. This time constant is correlated with the development of the diffusion-migration layer of

ions is solution and within the films of PIM-EA-TB and Nafion. The mechanism of the cationic diode is not affected by the fact that there are two different anions in electrolyte media, perchlorate in the working electrode compartment and chloride in the counter electrode compartment. The cationic diode mechanism is dependent solely on sodium cation transport in the open state at positive applied potential and potassium cation transport in the closed state at negative potential potential on the Nafion side. Then, the position of two electrolyte solutions, KCl in the counter electrode compartment and $NaClO_4$ in the working electrode compartment are exchanged.

7.3.5. PIM-EA-TB | Nafion "Heterojunction" Deposits: "Inverted" Cationic Diode Effects and KCl Concentration Effects

Figure 7.7A shows cyclic voltammetric data with scan rate 25 mV s^{-1} for the heterojunction membrane when aqueous KCl solution in contact with Nafion layer and aqueous $NaClO_4$ solution in contact with PIM-EA-TB film. The data show that there is a change in cation transport across Nafion from dominated by Na^+ flow in electrolyte $NaClO_4$ solution to now dominated by K^+ flow in electrolyte KCl solution. In the open state of diode at positive applied potentials to the working electrode compartment, K^+ ions conduct through the Nafion film into the counter electrode compartment with $NaClO_4$ solution. The high concentration of potassium ions (K^+ enrichment) inside the interface of PIM-EA-TB | Nafion microporous structure is anticipated under the open state of diode. The concentration of $NaClO_4$ is fixed at 100 mM at PIM-EA-TB film in order to investigate the effects of K^+ precipitating with ClO_4^-. It can be assumed that aqueous electrolyte $NaClO_4$ permeates through PIM-EA-TB structure (with 1-2 nm pore size[10]) and concentration of $NaClO_4$ within the electrolyte and within the microporous polymer are similar. However, the exact concentration of $NaClO_4$ is currently unknown within the PIM-EA-TB microporous structure.

Figure 7.7A shows cyclic voltammogram data that reveal new characteristics of PIM-EA-TB | Nafion heterojunction in the open state of diode at positive applied potentials to the working electrode compartment. In the presence

of 0.1 mM KCl only, the current at positive applied potential increases to approximately 30 μA but then collapses and settles at a significantly lower level of about 3-4 μA. Then the current at positive applied potential has superimposed a considerable noise in the open state of diode. When the concentration of aqueous KCl increased further to 1 mM and 10 mM at the Nafion side, the current peak at positive applied potential is lowered to approximately 11 μA and 8 μA, respectively. This current peak at positive applied potential must be associated with the formation of insoluble $KClO_4$ (see Figure 7.7G) at the interface of the PIM-EA-TB | Nafion microporous structure. The formation of $KClO_4$ salts inside the PIM-EA-TB | Nafion structure is responsible for the blocking of the ion flow across the microporous membrane. When the concentration of KCl is higher than 10 mM, the "blocking phenomena or currents" are observed at lowered potential and this suggests that the conditions of $KClO_4$ precipitation in the presence of a higher concentration of KCl are more easily reached.

The observation of a peak associated with $KClO_4$ precipitation at the open state of diode suggests that the solubility product for $KClO_4$ is reached inside the PIM-EA-TB | Nafion interface. The solubility product of $KClO_4$[11] translates to $K_{SP} = [K^+] \times [ClO_4^-]$ at 25 ^oC equals to 1.05×10^{-2} mol^2 dm^{-6}. The concentration of $NaClO_4$ within the interface of PIM-EA-TB | Nafion microporous structure is approximately 0.1 mol dm^{-3} and close to the bulk $NaClO_4$ electrolyte concentration. Therefore, the concentration of K^+ ions inside the interface of PIM-EA-TB | Nafion microporous structure at the moment when the current peak is observed at the open state of diode is likely to be close to 0.1 mol dm^{-3}. During the process of open state of diode in the positive applied potential at the Nafion side, first cations predominantly from the KCl solution are accumulated to the Nafion film and pushed into the PIM-EA-TB layer in order to produce locally higher concentrations inside the microporous structure. The precipitation peak current is observed even for the concentration of 0.1 mM KCl on the Nafion side during the open state of diode. Therefore, the interface of PIM-EA-TB | Nafion microporous structure seems to be feasible for a three order of magnitude accumulation effect of K^+ in a concentration range of KCl from μM to mM.

When the current for higher concentrations of KCl is increased even further at positive applied potential, it remains effectively suppressed with some superimposed noise in the open state of the diode. This phenomenon indicates that in the $KClO_4$ blocking layer there is a dynamic process inside the interface of PIM-EA-TB | Nafion microporous structure. When the potential in the working electrode compartment is switched to negative, a negative current is observed in the cyclic voltammetry data. This negative current is still consistent with the closed state of diode but appears a bit higher when compared to the blocked current in the positive applied potentials during the open state of diode. Therefore, the rectification ratio is indeed inverted from positive into negative as an increasing of KCl concentration in the Nafion side (see Figure 7.7C). The inversion of the rectification ratio occurs when the concentration of aqueous electrolyte KCl at the working electrode compartment is approximately 100 mM as shown in Figure 7.7B and 7.7C.

Figure 7.7B shows chronoamperometry data for KCl (Nafion) and $NaClO_4$ (PIM-EA-TB) with complex $KClO_4$ blocking behaviour. This is compared to chronoamperometry data without precipitation in Figure 7.6B. In Figure 7.7B, the rectification ratio remains positive for a low concentration of KCl in a concentration range of 0.1-10 mM with transients phenomena in chronoamperometry data similar to those observed in Figure 7.6B. When the concentration of KCl is 100 mM in Figure 7.7B, there is a slow blocking transient is seen with positive applied potential (+1V) to the Nafion side. In Figure 7.6B, when the KCl concentration of 500 and 1000 mM in the working electrode compartment, the blocking transient at positive applied potential becomes much faster. The rectification ratio reaches -64 at 1000 mM KCl concentration in the working electrode compartment. Therefore, the development of of a blocking layer of $KClO_4$ is associated with a systematic behaviour based on KCl concentration in the working electrode compartment during the open state of diode.

Additional data are shown for a fixed concentration of 500 mM $NaClO_4$ at the PIM-EA-TB side with a concentration range 0.1-1000 mM of KCl at the Nafion

side (see Figure 7.7D and 7.7E). Figure 7.7D shows cyclic voltammetry data with a clear $KClO_4$ precipitation point in the concentration range of KCl 1-1000 mM at the Nafion side. The higher perchlorate concentration at PIM-EA-TB side lowers currents at the positive applied potential and it decreases the voltage necessary for the formation of $KClO_4$ blocking. In Figure 7.7E, the chronoamperometry data show the transient phenomenon for time-dependent switching/blocking of the diode at +1V and -1V applied potentials. For 500 mM $NaClO_4$ at PIM-EA-TB side, the diode inversion from the positive (+2) to negative (-9) in rectification ratio is happening at lowered concentration of KCl at approximately 10 mM.

During the $KClO_4$ blocking events at the interface of PIM-EA-TB | Nafion, the shape of the peaks in the cyclic voltammetry data can be interpreted as the gradual formation of a physical barrier towards ion transport inside the microporous structure. Figure 7.7A shows a sharp decrease in current at positive applied potential due to rapid nucleation and growth presumably due to $KClO_4$ crystals inter-growing at the PIM-EA-TB | Nafion interface and followed by a more gradual closing of the physical barrier inside the microporous structure. It is unlikely that a 100% transport blockage can happen with K^+ ions inside the PIM-EA-TB | Nafion microporous interface as this should result in the "re-opening" of the heterojunction at the negative applied potential due to $KClO_4$ dissolving back into solution (see Figure 7.7G at closed state). Therefore, a process of dynamic $KClO_4$ precipitation/ dissolution appears possible inside the microporous structure of PIM-EA-TB | Nafion during open and closed states of the diode. The current noise in the positive applied potential domain during the open state of the diode is probably due to fluctuations in the $KClO_4$ blocking layer at PIM-EA-TB | Nafion microporous interface.

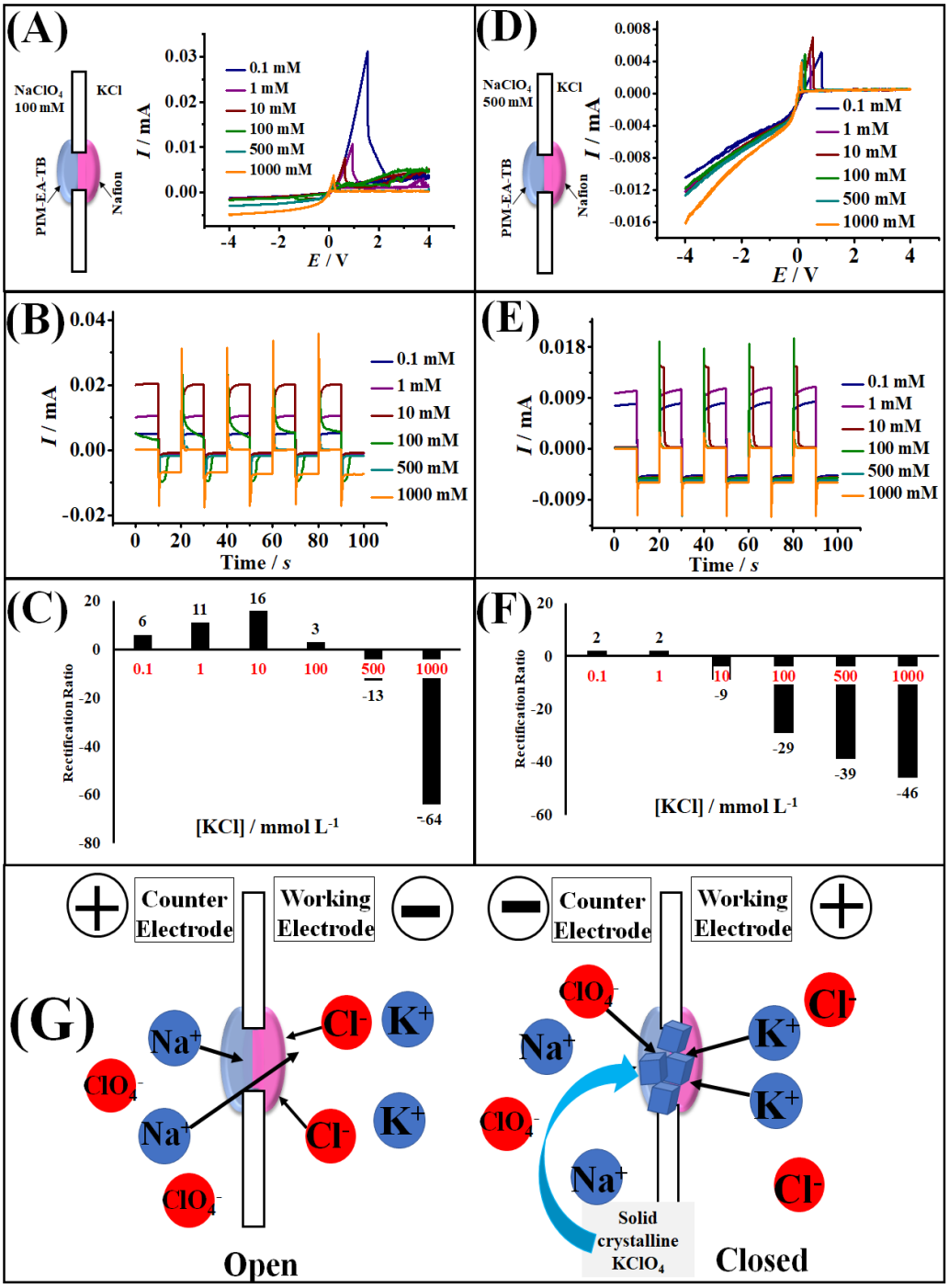

Figure 7.7. (A) Cyclic voltammograms for a PIM-EA-TB | Nafion heterojunction (scan rate 25 mVs^{-1}) with 100 mM $NaClO_4$ in contact with PIM-EA-TB and 0.1, 1, 10, 100, 500, 1000 mM KCl in contact with Nafion. (B) As before but with chronoamperometry data (stepping from +1 V to -1 V). (C) As before, but with rectification ratio at +/- 1 V. (D) Similar with case (A) but 500 mM $NaClO_4$ in contact to PIM-EA-TB. (E) As before, but with chronoamperometry data (stepping from +1 V to -1 V). (F) As before, but with rectification ratio at +/- 1 V. (G) Schematic drawings explaining the open and closed diode behaviour for the case of KCl in contact with Nafion and $NaClO_4$ in contact with PIM-EA-TB.

7.3.6. PIM-EA-TB | Nafion "Heterojunction" Deposits: Sodium Cation Interference During $KClO_4$ Blocking

The gradual formation of the $KClO_4$ blocking layer during the open state of diode is caused by a precipitation reaction at the location of the PIM-EA-TB | Nafion interface. This is likely to be influenced by the involvement of other mobile cations such as sodium. Figure 7.8C and Figure 7.8 D show the effects of NaCl with fixed concentration added to the working electrode compartment (Nafion side). The concentration of $NaClO_4$ placed in counter electrode compartment (PIM-EA-TB side) was maintained. In the open state of the diode at positive applied potentials, there is now a flux competition between K^+ and Na^+ cations through the Nafion film (see Figure 7.8G). Due to the competition between Na^+ and K^+ in the Nafion film, the local concentration of K^+ at the interface of PIM | Nafion microporous structure is likely to be lowered at positive applied potential domain in the presence of sodium cations.

Figure 7.8A shows data from cyclic voltammetry experiments (scan rate 25 mV s^{-1}) in the presence of of fixed 10 mM NaCl with addition of 0.1-1000 mM KCl concentration in the working electrode compartment (with fixed 100 mM $NaClO_4$ in counter electrode compartment). The magnitude of currents (see Figure 7.8A) at positive applied potentials (open state of diode) has increased compared to the cyclic voltammetric data without added 10 mM NaCl into the working electrode compartment (Figure 7.7A). The presence of Na^+ ions in the KCl media in the working electrode compartment tend to be correlated with an additional cation flow through the Nafion film resulting in higher currents in the positive applied potential domain (in the open state of the diode). The position of the $KClO_4$ blocking peak at positive applied potentials appears to shift more positive when the K^+ concentration is lowered with an increasing of Na^+ concentration in the working electrode compartment. When the Na^+ concentration reaches 30 mM with a low K^+ concentration (see Figure 7.8D), the $KClO_4$ blocking peak is too far to be detected in the positive potential range during the open state of diode.

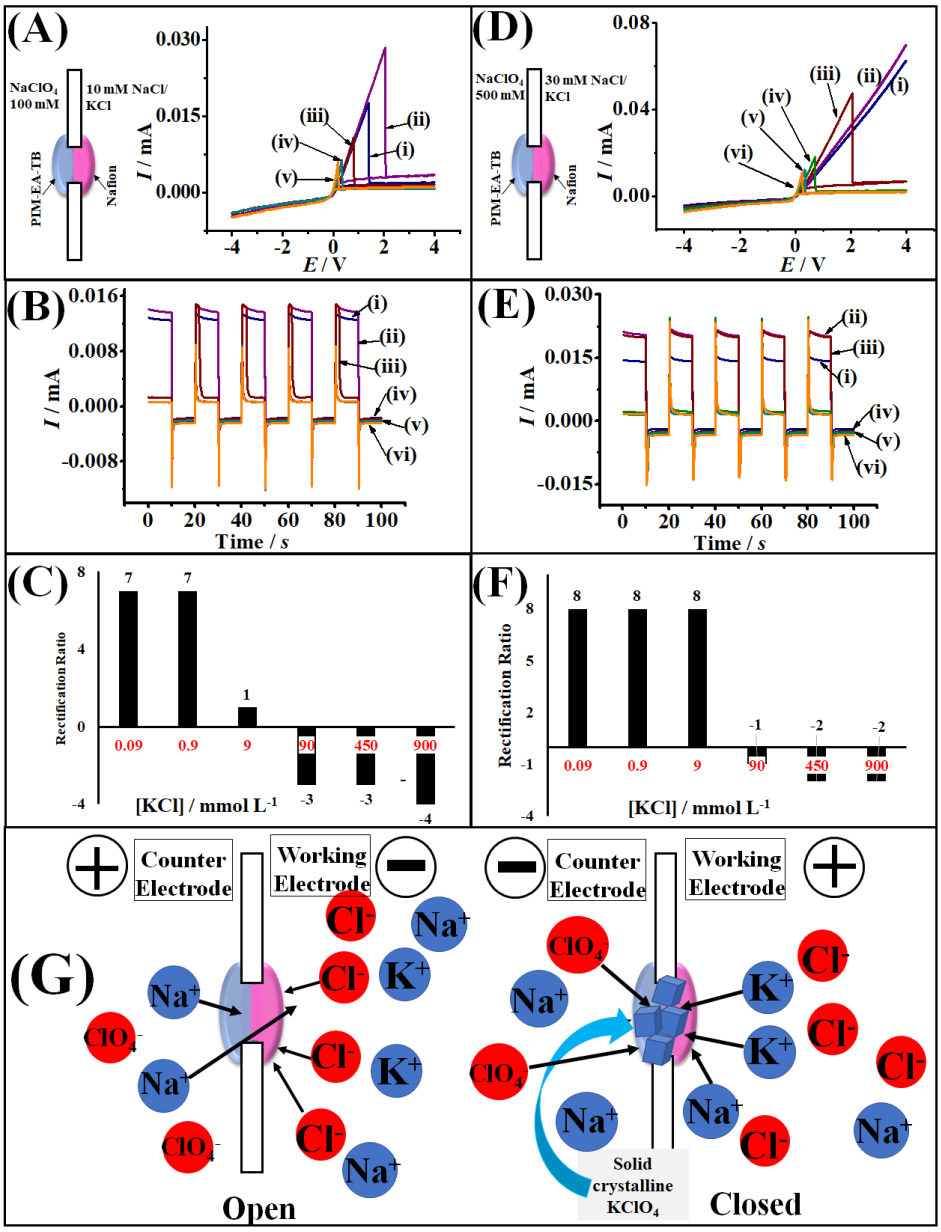

Figure 7.8. (A) Cyclic voltammograms for a PIM-EA-TB | Nafion hetero-junction (scan rate 25 mVs^{-1}) with 100 mM $NaClO_4$ in contact with PIM-EA-TB and (i) 10 mM NaCl/ 0.09 mM KCl, (ii) 10 mM NaCl/ 0.9 mM KCl, (iii) 10 mM NaCl/ 9 mM KCl, (iv) 10 mM NaCl/ 90 mM, (v) 10 mM NaCl/ 450 mM KCl, (vi) 10 mM NaCl/ 900 mM KCl electrolyte. (B) As before, but with chronoamperometry data switching between +1 V and -1V. (C) As before, but with the rectification ratio at +/-1 V. (D) Similar with case (A) but with 500 mM $NaClO_4$ in contact with PIM-EA-TB and (i) 30 mM NaCl/ 0.07 mM KCl, (ii) 30 mM NaCl/ 0.7 mM KCl, (iii) 30 mM NaCl/ 7 mM KCl, (iv) 30 mM NaCl/ 70 mM, (v) 30 mM NaCl/ 350 mM KCl, (vi) 30 mM NaCl/ 700 mM KCl electrolyte. (E) As before, but with chronoamperometry data switching between +1 V and -1V. (F) As before, but with the rectification ratio at +/-1 V. (G) Schematic drawings explaining the open and closed diode behaviour for the case of KCl competing with NaCl in contact with Nafion and $NaClO_4$ in contact with PIM-EA-TB.

Chronoamperometry data (Figure 7.8B and 7.8E) and rectification ratio plots (Figure 7.8C and Figure 7.8F) reveal the effects added Na^+ ions in KCl solution in the working electrode compartment. The inverted rectification ratio with an additional Na^+ in the working electrode compartment during the open state of the diode is shifted from ca. 9 mM KCl in 10 mM NaCl media (see Figure 7.8C) to about 70 mM KCl in the presence of 30 mM NaCl (see Figure 7.8F). In order to reach the $KClO_4$ blocking effect at the heterojunction membrane, when Na^+ transport occurs in parallel during the open state of diode, a higher concentration of K^+ in the electrolyte is needed. With increased Na^+ concentration in the KCl media at working electrode compartment, the currents after the precipitation peak (blocked) at positive applied potentials are still very low due to $KClO_4$ blocking layer occurs in the interface of PIM-EA-TB | Nafion heterojunction. Therefore, both transport of K^+ ion and Na^+ ion are blocked through the interface of PIM-EA-TB | Nafion heterojunction due to $KClO_4$ precipitate as a physical barrier inside the microporous structure.

7.4. Conclusions

It has been demonstrated that "heterojunctions" can be fabricated by deposition of Nafion onto one side of a 20 μm diameter microhole in PET film and deposition of PIM-EA-TB onto the opposite side. This produces ionic current rectification effects with the resulting device shows interesting ionic diode behaviour. The use of a PIM-EA-TB material helps defining an interface where processes such as salt precipitation could occur. It affects the access of cations and anions to the PIM | Nafion heterojunction. This device could be of interest in the improvement of the performance of ionic diode systems.

The first part of result chapter discusses about the effects of ionic rectification in cases where the electrolytes solutions are symmetric or asymmetric for the case of NaCl and HCl at different concentrations. It has been shown that the rectification ratio (as defined as the absolute ratio of the currents at +1 V and at -1 V) is higher for HCl than for NaCl due to the higher mobility of protons in aqueous

media. In the second part of results section, the effects of ionic rectification as a function of HCl and NaCl concentration are discussed. It can be concluded that at positive applied potential consistent with the open state of ionic diode, the heterojunction can be considered as cationic diode. This is the case when Nafion in contact to aqueous NaCl solution (sodium diode) and when Nafion in contact with aqueous HCl solution (proton diode).

The third part of the results section describes an investigation of the effects of time on ionic rectification. From the current responses, it can be concluded that Nafion and PIM-EA-TB perform different tasks contributing to the ionic diode behaviour. Nafion acts as an acceptor for charge carriers (for example sodium ions) and needs high conductivity (to suppress resistive losses in the diode), while PIM-EA-TB blocks the return of charge carriers, which is depending on type and electrolyte concentration in contact with PIM-EA-TB deposit. In a word, the Nafion is key to performance of the diode in the "open" state and the PIM-EA-TB is key to the performance of the diode in the "closed" state. Therefore, the usage of PIM-EA-TB material is not only contributing to the stabilisation of the diode geometry, but it can also be used to improve the diode behaviour in the PIM | Nafion heterojunction.

The fourth part of the results section focuses on the investigation of conventional cationic diode effect and mechanisms based on Nafion in contact with $NaClO_4$ and PIM-EA-TB in contact with KCl. The observed cationic diode behavior is mainly a reflection of Na^+ conductivity within Nafion in the open state of the diode. In the closed state K^+ is blocked from moving into the opposite compartment. In this part the function of the ionic diode is demonstrated and explained without additional complexity from precipitation reactions.

The fifth part of the results section is based on the discussion of the "inverted" cationic diode effect, when the two electrolyte solutions are exchanged. This introduces an entirely new type of ionic diode based on interfacial precipitation. By switching the electrolyte solution from one compartment to the

other, now KCl solution is in contact with Nafion and $NaClO_4$ solution is in contact with the PIM-EA-TB deposit. When the diode is in the "open" state, ion flow occurs in the form of potassium cation moving across towards the perchlorate containing electrolyte. It has been shown that a new type of precipitation peak based on formation of $KClO_4$ blocking layer at the interface of PIM-EA-TB | Nafion "heterojunction" was observed in cyclic voltammetry data. It can be concluded that the formation of a $KClO_4$ blocking layer is dependent on systematic KCl concentration in the compartment opposite to that with perchlorate electrolyte. This is an entirely new mechanism and therefore a major achievement in this study.

The sixth part of the results section introduces interference effects of other ions during the $KClO_4$ blocking process. It is likely that other ions and ionic strength effects are affecting diode function for example in the presence of cations such as sodium, Na^+. In order to explore this effect, Na^+ has been added to KCl and now there is a competition between Na^+ and K^+ ion flux conduct through Nafion film. A higher of K^+ concentration is needed in order to reach the precipitation point because there is shifting of the inversion point of diode from 9 mM KCl to 70 mM KCl. It can be concluded that not only K^+ ion flux is blocked but also Na^+ flux is blocked across the heterojunction. The main achievement here is the realization that interference effects need to be considered when developing ionic diode sensors.

7.5. References

1 Mathwig, K., Aaronson, B.D.B., Marken, F. *ChemElectroChem*. **2018**. *5*, 897-901.

2 He, D., Madrid, E., Aaronson, B.D.B., Fan, L., Doughty, J., Mathwig, K., Bond, A. M., McKeown, N.B., Marken, F. *ACS Appl. Mater. Interf.* **2017**, *9*, 11272–11278.

3 Madrid, E., Cottis, P., Rong, Y., Rogers, A. T., Stone, J. M., Malpass-Evans, R., Carta, M., McKeown, N. B., Marken, F. *J. Mater. Chem*. **2015**. *3*, 15849-15853.

4 Taylor, R. G. D., Bezzu, C. G., Carta, M., Msayib, K. J., Walker, J., Short, R., Kariuki, B. M., McKeown, N. B. *Chem. Eur. J*. 2016. *22*, 2466-2472.

5 Carta, M., Malpass-Evans, R., Croad, M., Rogan, Y., Jansen, J. C., Bernardo, P., Bazzarelli, F., McKeown, N. B. *Science* **2013**, *339*, 303–307.

6 McKeown, N. B., Budd, P. M. *Macromolecules*. **2010**. *43*, 12, 5163-5176.

7 McKeown, N. B., Budd, P. M. *Chem. Soc. Rev*. **2006**. *35*, 675-683.

8 Budd, P. M., Ghanem, B. S., Makhseed, S., McKeown, S., Msayib, K. J., Tattershall, C. E. *Chem. Commun.* **2004**, 230–231.

9 Li, F. Y., Xiao, Y., Chung, T.-S., Kawi, S. *Macromolecules* **2012**, *45*, 1427–1437.

10 Madrid, E., Rong, Y., Carta, M., McKeown, N.B., Malpass-Evans, R., Attard, G.A., Clarke, T.J., Taylor, S.H., Long, Y.T., Marken, F. *Angew. Chem. Int. Ed.* **2014**, *53*, 10751-10754.

11 D.R. Lide (ed.), CRC Handbook of Chemistry and Physics, 74th edition, CRC Press, London, 1993-1994, p. 8-49.

Chapter 8
Application of Ionic Rectification for Water Purification: Desalination with a Nafion Cationic Diode

Contents

Chapter Abstract

A proof-of-principle (prototype) device of desalination or salination process driven by AC-electricity has been developed based on asymmetrically deposited Nafion ionomer on a 100 microhole array. The cationic diode material is combined with a commercial Fumasep FAS-130 film as an anion-conducting membrane. The prototype utilizes a 3D-printed four-chamber system with two internal chambers to extract and/accumulate the salt in order to demonstrate desalination or salination processes. The desalination or salination processes are shown in three operational modes (device configurations) for an aqueous 250 mM NaCl solution. A 50% degree of desalination/salination is achieved before membrane deterioration occurs. Due to experimental restrictions such as (i) material resistivity lowering the rectification effect, (ii) rectification ratio limitations for the 100 microholes array, and (iii) insufficient stability of ionomer membranes under AC-square-pulse-driven operation, the charge efficiency is estimated to be only 12% over 18 hours experiment time. However, the process is entirely new and this chapter describes the new technology for future desalination/salination applications with some perspectives for improvements.

Chapter Publication

Part of this chapter have been published in:

B. R. Putra, E. Madrid, L. Tshwenya, O. A. Arotiba, F. Marken. An AC-driven desalination/salination system based on a Nafion cationic rectifier. *Desalination*. **2020**, *480*, 114351.

8.1. Introduction

The focus of this chapter is on developing a proof-of-principle (prototype) device based on ionic diode mechanism using a Nafion cationic rectifier coupled with an anionic resistor network in order to achieve both desalination and salination processes in aqueous NaCl electrolyte. The combination of ionic rectifier and ionic resistor in order to form desalination circuit system driven by AC-electricity has been previously proposed as a concept by Madrid et al.[1] Commercial Nafion ionomer has been used previously for diode studies as reported by He et al.[2] Nafion has sufficient chemical robustness to be suitable as cationic rectifier material for developing a proof-of-concept ionic diode desalination system. Figure 8.1 shows the schematic drawing of the basic mechanism for the underlying concentration polarisation for the case of Nafion as a cation conducting semipermeable material. The concentration of electrolyte locally in the microhole will increase (accumulation state) by applying positive potential polarization on the Nafion side. Thus cations readily flow through the ionomer into the microhole in the PET film region. When the opposite polarisation (negative potential) is applied on the Nafion side, the concentration of cations (and therefore of electrolyte) become depleted contributing to highly resistive conditions within the microhole region in the PET film.[3] This rectifier effect from Nafion as a semipermeable material asymmetrically deposited onto PET film can be investigated with cyclic voltammetry or chronoamperometry techniques under AC electrical stimulation. In cyclic voltammetry experiments, the potential is applied and slowly scanned from zero to positive and to negative potentials. The Nafion membrane results in potential-dependent ionic current flow. The steady state (or time independent) current is expected during the cyclic voltammetric measurements due to the small size of the microhole (20 μm diameter) employed during ionic rectification studies. In contrast, the time dependence or transient current can be investigated directly for any given step potential during chronoamperometry experiments. Both of these techniques, voltammetry and chronoamperometry, can be employed to reveal and study ionic rectification phenomena for the desalination system driven by AC-electricity.

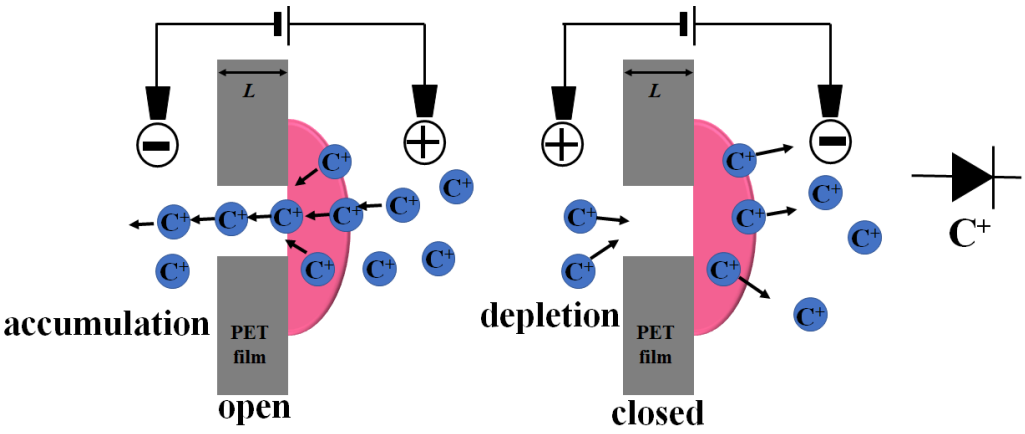

Figure 8.1. The schematic representation of the case of open cationic diode, the closed cationic diode, and the symbol for the cationic diode using negatively charged semipermeable membrane.

The suggested desalination circuit driven by AC-electricity works in a similar way to that of an electrical rectifier with two active chambers and for two opposite polarisations (see Figure 8.2). This system can be configured in three distinct ways for operational modes in desalination (salt removal) or salination (salt accumulation) processes. Figure 8.2A shows that the bottom chamber undergoes desalination when cations are removed via Nafion cationic diode and anions are removed through an anion conductor in order to balance the charge, whereas the top chamber is blocked. When the potential of the external voltage is reversed, the bottom chamber is blocked and the top chamber now has to provide a desalination path. The net result from both chambers is salt removal and resulting in a net salt concentration increases in the outside reservoirs (not shown in Figure 8.2).

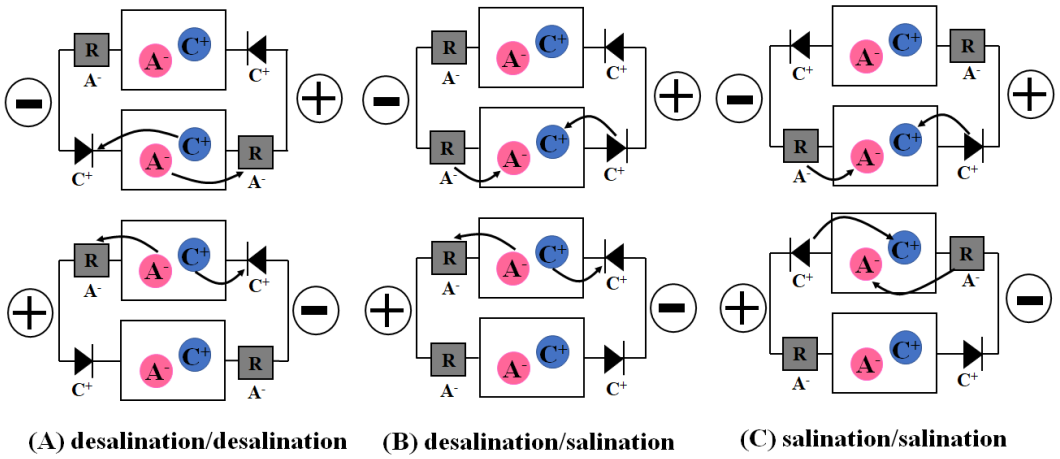

Figure 8.2. (A) Schematic representation of an ionic circuit for simultaneous desalination in two active chambers with external alternating applied potential. The outside electrolyte reservoirs are not shown. (B) As before, but for desalination/salination. (C) As before, but for salination/salination.

When one of the cationic diodes in the both chambers is inverted (see Figure 8.2B), a combination of desalination/salination system can be obtained, in which one chamber loses salt with the second chamber accumulating salt. Finally, in Figure 8.2C, when both of cationic diodes are inverted resulting in a salination/salination system with a net of salt removal from the outside reservoirs and salt accumulation in both chambers. In this chapter, it is the first time that these three types of operational modes for the ionic rectifier system are demonstrated. The ionic rectifier system consists of cationic diodes based on Nafion ionomer material with corresponding anionic resistors (based on commercial Fumasep FKS-130 ionomer films). The testing of the ionic rectifier system with three operational modes with aqueous electrolyte NaCl solution shows that the proposed concept works, but also that significant limitation exist from experimental problems, especially the degradation of ionic resistor materials. Fumasep FAS-130 film as an ionic resistor material failed under square-wave potential polarization conditions in the higher NaCl concentration range. In order to develop better performance for desalination based on the ionic diode mechanism, further challenges must be tackled such as finding more robust materials for ionic resistors.

In the 21st century and beyond, desalination process are essential in providing fresh water to supply drinking water and irrigation system for daily human activity.[4] A range of water purification technologies have been developed and refined including electrolytic desalination[5], capacitive desalination[6,7], electrodialysis[8], forward osmosis[9], and reverse osmosis[10], as well as new innovative microfluidic systems for desalination.[11] There are different types of water purification technology already available depending on the type of water source, the location/mobility of the desalination system, the use of sunlight[12], and the scale of water treatment.[13] The new ionic diode technology may offer a low cost, low energy, and low maintenance alternative to provide safe fresh water in remote or disaster-struck area where fresh water is in short supply.

8.2. Experimental

8.2.1. Chemical Reagents

Poly-ethylene-terephthalate (PET) films of 6 μm thicknesss with laser-drilled micropores (20 μm diameter of each microholes) with 10 × 10 array configuration were obtained from Laser-Micro-Machining Ltd., Birmingham UK (see Figure 8.3B). Fumasep FAS-130 as ionomer film for anionic exchange membrane applications was obtained from www.fuelcellstore.com. Nafion®-117 (5% in a mixture of lower aliphatic alcohol and water) and sodium chloride were obtained from Sigma-Aldrich (UK) and used without further purification. All reagents used in solution preparation for the experiments were of analytical or reagent grade. Solutions were prepared under ambient conditions in volumetric flasks with ultra-pure water of resistivity 18.2 MΩ cm from an ELGA Purelab Classic system. A light microscope GX microscope GXML 3230 was used to take the image of single 20 μm diameter hole of PET (Figure 8.3A) and 10 × 10 microhole array configuration of PET substrate (see Figure 8.3B and 8.3C).

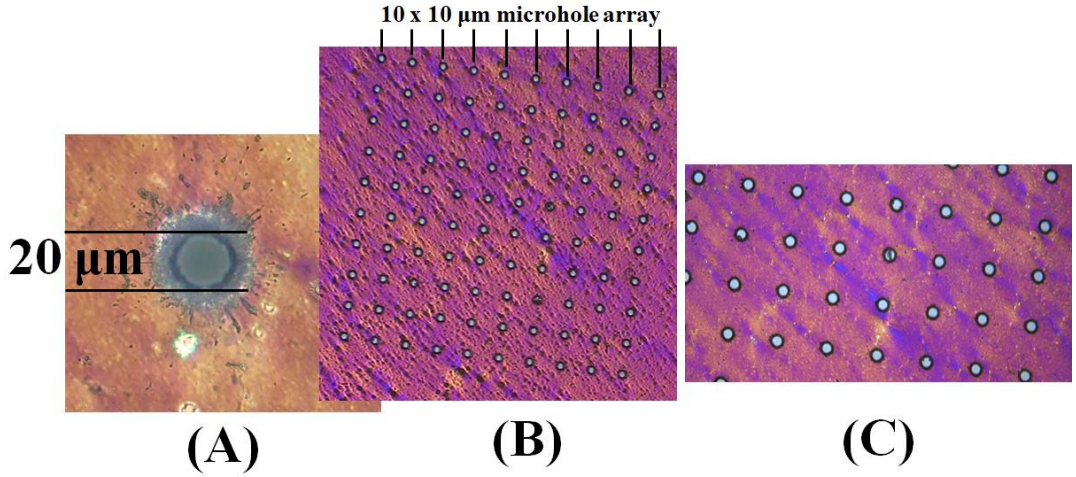

Figure 8.3. (A) Optical image showing a single 20 µm diameter microhole. (B) 10 × 10 array of microholes in a 6 µm thick poly-ethylene-terephthalate (PET) film. (C) As before but with the higher magnification. The gap between individual microholes in the array corresponds to 5 times of microhole diameters or 100 µm.

8.2.2. Instrumentation

An Ivium Compactstat potensiostat system (The Netherlands) was used to record all electrochemical data (voltammetry, chronoamperometry, and impedance experiments) at T = 20 ± 2 °C. The 3D-printed salt solution reservoir (from www.i.materialize.com) employed in this desalination study is shown in Figure 8.4B. There are two inner small chambers separating two outer water reservoirs. Figure 8.4A shows the desalination compartment with a Pt wire working and saturated calomel (SCE) sense electrode placed into the right reservoir, and an SCE reference and a Pt wire counter electrode placed into the left reservoir. The two reservoirs and two chambers were filled with NaCl solution using filling ports. A Mettler Toledo Seven Easy Conductivity Meter Conductivity was used for conductivity measurements to monitor NaCl content in the salt solution reservoir. In order to measure the conductivity of NaCl solution, the desalination process was stopped, a 1 cm^3 sample was taken, and after conductivity testing (in the inverted conductivity probe) the sample was returned for further desalination. Solution conductivity in both chamber 1 and chamber 2 were monitored in 18 hours of the experiment.

8.2.3. Protocol for Nafion Diode Assembly

A volume of 10 µL Nafion solution was applied to a PET film on a glass substrate (pre-coated with a thin layer of 1% agarose gel to avoid Nafion penetrate through the microholes) by solution-casting in order to form films of Nafion simultaneously on 100 microhole PET substrates. With a glass rod the Nafion solution was spread evenly over the PET film to give a 1 cm^2 coating on the top of 100 microholes. Then, after drying, the coated PET film was peeled off from the 1% agarose substrate to give asymmetric Nafion deposits. A piece of 1 cm^2 Fumasep FAS-130 film was cut out and placed in between of a laminating plastic pouch with 0.5 cm diameter hole in order to form a semipermeable membrane for anion transport. A stable film of Fumasep FAS-130 was obtained after lamination and then assembled into the desalination system. Both Fumasep films and Nafion diodes were sealed in with some Dow-Corning vacuum grease as a sealant.

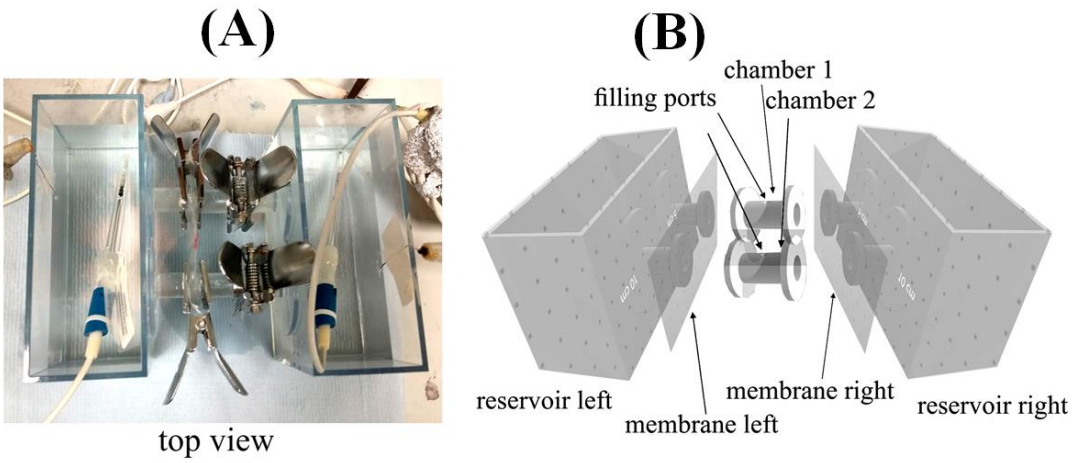

Figure 8.4. (A) Photograph in top view of the cell in operation. A 4-electrode potentiostat (sense paired with working electrode in one side and counter paired with reference electrodes in the other side) was employed to drive the external potentials to the compartments. (B) Schematic drawing of a 3D-printed 4-chamber electrochemical cell for desalination and salination in chamber 1 and 2.

8.3. Results and Discussion

8.3.1. Characterisation of Asymmetrically Deposited Nafion for Single-hole and Multi-hole Ionic Diodes

Initially, a four-electrode electrochemical cell is employed to characterise the behaviour of the ionic diode from asymmetrically deposited Nafion onto single-hole or multi-hole PET substrates. A four-electrode experimental set-up is shown in Figure 8.5A with the 6 μm thick poly-ethylene-terephthalate (PET) film with 20 μm diameter laser-drilled hole sandwiched between two electrolyte-filled compartments. The asymmetrically deposited Nafion on the PET substrate was placed in the right compartment facing the working electrode. Figure 8.5B shows current responses form the cyclic voltammetry (scan rate 0.1 V s^{-1}) in 0.25 M NaCl in both compartments for a single microhole cationic diode and for an array of 10 × 10 microholes in the PET substrate. The ionic current rectification effect is observed for both of these cases with "open" state of diode with positive applied potential and "closed" state of diode with negative applied potential domain. It is interesting to scale the diode current from asymmetrically deposited Nafion onto single microhole ×100 (see Figure 8.5B, green line) to explore possible interactions between the individual of 20 μm diameter microholes in the 10 × 10 array on the PET substrate. The 10 × 10 microhole arrays on the PET substrate shows a current approximately a factor 2 lower (Figure 8.5B blue line) compared to the anticipated behaviour of 100 individual cation ionic diodes (Figure 8.5B green line). This could be related to some interactions such as access of diffusion migration in ion flow towards multiple microholes even with a 5 × diameter gap (100 μm) in between individual microholes.

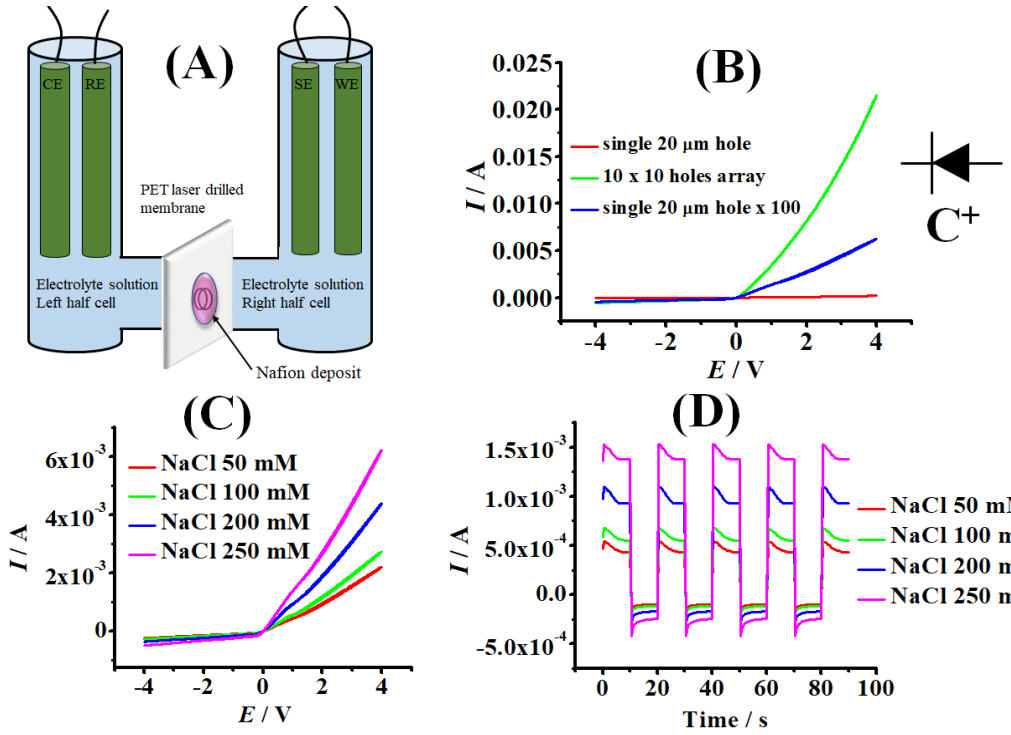

Figure 8.5. (A) Schematic description of the experiment with 4-electrode control (WE = working electrode, SE = sense electrode, CE = counter electrode, RE = reference electrode) of the applied potential and Nafion deposit on the side of the working electrode. (B) Cyclic voltammograms (scan rate 0.1 Vs^{-1}) for a single microhole with 20 µm diameter hole, a 10 × 10 microhole array, and a single 20 µm diameter microhole with the current axis scaled ×100, all coated with asymmetrically deposited Nafion and immersed in 0.25 M NaCl on both sides. (C) Cyclic voltammograms (scan rate 0.1 Vs^{-1}) for a microhole array in asymmetrically deposited Nafion and immersed in 50, 100, 200, and 250 mM NaCl. (D) As before, but with corresponding chronoamperometry data for +/-1 V.

Figure 8.5C and 8.5D shows the cyclic voltammetry and chronoamperometry data for aqueous NaCl electrolyte on both sides in a concentration range of 50, 100, 200, and 250 mM using asymmetrically deposited Nafion on a 10 × 10 array of microholes. The performance of the ionic current rectification of Nafion diode array is changing with the electrolyte concentration as shown in Figure 8.5C and 8.5D. The current in open state of diode at positive applied potential increases with concentration in a range of 50-250 mM NaCl (see in Figure 8.5C), but the rectification ratio from chronoamperometry data (calculated from the absolute current ratio at +1 V and -1 V) remains approximately 4 (50-100 mM) to 5 (200-250 mM) in this NaCl concentration range. Then, the effects of an

additional ionic resistor based on commercial Fumasep FAS-130 anion semi-permeable membrane are investigated in series with Nafion diode network.

8.3.2. Characterisation of the Nafion Ionic Diode – Ionic Resistor Network

In order to achieve desalination, an anion semi-permeable film is required to couple anion transport to the cation transport in the Nafion cationic diode. In this experiment, after unsuccessful attempts to employ thinner anion conducting films, a Fumasep FAS-130 (with 130 μm thickness) was selected in order to achieve anion transport. However, these anion conducting films are rapidly degrading under AC-polarisation conditions during the desalination process. Therefore, the anion conductor currently represent the weakest component in the proposed desalination system. Figure 8.6A shows cyclic voltammetry data for the anionic resistor (Fumasep FAS-130) in 0.05, 0.1, 0.2, and 0.25 M NaCl on both sides. Resistive behaviour for 0.25 M NaCl is observed with typically 387 Ω. In Figure 8.6A, the experiments were performed with a scan rate of 0.1 V s^{-1}. A weak peak feature is observed probably due to some non-steady state diffusion.

Figure 8.6B shows the cyclic voltammetric data for a combination of the anionic resistor (Fumasep FAS-130) with the cationic diode (asymmetrically deposited Nafion onto 10 x 10 array of PET substrate) in 50-250 mM NaCl. From the cyclic voltammetry data, it is clear that diode-like behaviour (cationic diode) is maintained using aqueous electrolyte NaCl in a concentration range of 50-250 mM. However, the additional resistance from the anion conducting membrane (Fumasep FAS-130) reduces the rectification ratio to approximately 2 or less for higher NaCl concentrations. The obvious reduction of the rectification ratio here is due to the loss of applied potential on the diode. The Nafion diode exhibits an approximate resistance of 709 Ω in aqueous 250 mM NaCl. When the Nafion diode was combined with a Fumasep-FAS130 film, the apparent resistance increases to 2860 Ω (estimated from the slope of *I-V* curve at a potential of +1 V). This increase in resistance when going from Nafion diode to Nafion diode-ionic resistor network can explain the loss in rectification ratio. Both positive and negative potential polarisation are needed to drive a complete rectifier system consisting of cationic

diode and anionic resistor. Therefore, two branches consisting of Nafion cationic diode and anionic resistor (Fumasep FAS-130) are combined to allow operation of ion removal or accumulation in both chambers during both positive and negative polarisation.

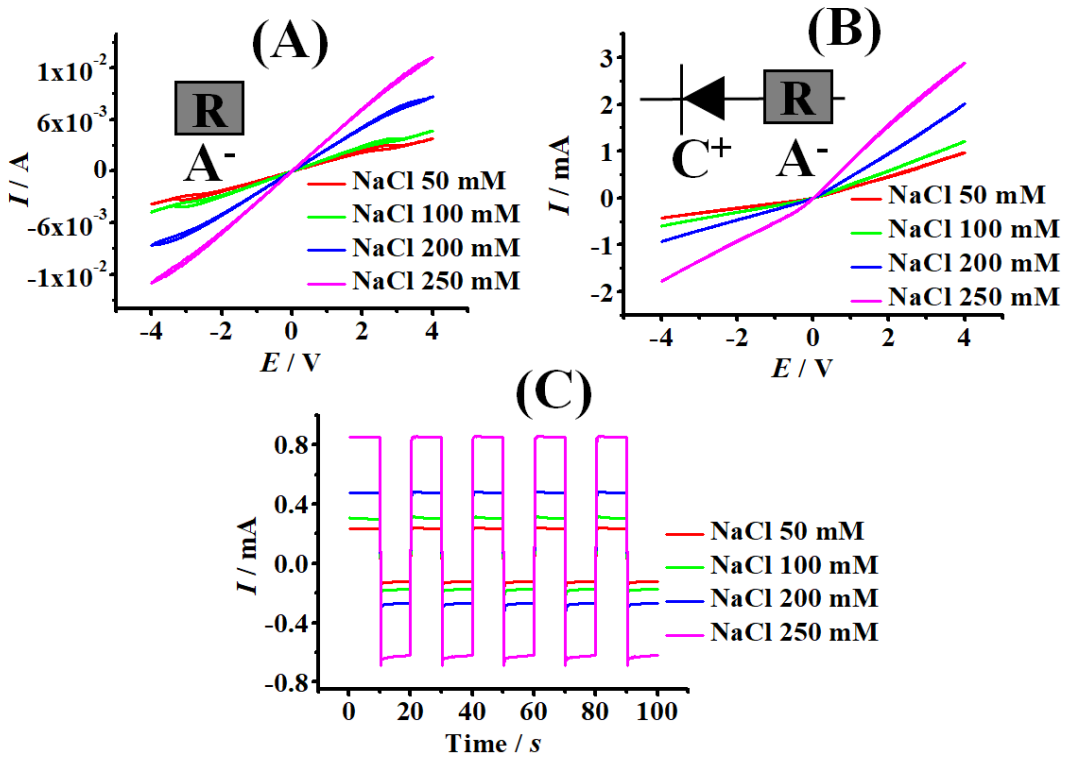

Figure 8.6. (A) Cyclic voltammograms (scan rate 0.1 Vs^{-1}) for a 10 mm diameter Fumasep FAS-130 ion conducting film immersed in 50, 100, 200, and 250 mM NaCl on both sides. (B) As before, but cyclic voltammograms for a Nafion cationic diode microarray in series with a Fumasep FAS-130 film. (C) Corresponding chronoamperometry data obtained for +/-1 V.

8.3.3. Operation of the Ionic Rectifier in Desalination/Desalination Mode

Figure 8.7A shows a schematic drawing of the ionic rectifier with two "active" chambers (indicated as boxes) in both desalination mode using alternating positive and negative polarization. Externally, there are two reservoirs in the left and right compartment for the driver voltage using reference electrode (SCE) to be applied in order to remove both Na^+ and Cl^- from two active chambers. From the configuration shown in Figure 8.7A it can be seen that salt removal occurs from the two chambers in both cases: with applying an alternation of positive and negative

voltage to the salt reservoir. Therefore, the saltwater in both active chambers should be desalinated (desalination mode).

Figure 8.7 B shows cyclic voltammetry data (scan rate 0.1 Vs^{-1}) for aqueous NaCl electrolyte in a concentration range of 50-250 mM in a complete rectifier system (Nafion diode coupled with ionic resistor). Figure 8.7B shows data with some asymmetry in the current-voltage curve suggesting some degree of imperfection in the two branches with ionic diodes and ionic resistors. Figures 8.7C and 8.7D show chronoamperometry data obtained for switching potential at +/-1V and +/-4V with currents reaching 1 to 2 mA. It is possible to monitor the desalination effect at both chambers with time when operating the full cell with +/-4V and pulse times of 10 s. In this case (desalination mode), the experiment was running 18 hours by applying an alternating positive and negative polarization. Table 8.1 shows the conductivity of aqueous electrolyte 0.25 M NaCl in both active chambers undergo desalination. The experiment was repeated twice in order to ensure reproducibility of the desalination phenomena at both active chambers (C1&C3 is conductivity is the first chamber and C2 & C4 is conductivity in the second chamber).

Table 8.1. Table summarising the conductivity of 0.25 M NaCl for chamber 1 and 2 with the twice experiment in desalination/desalination mode. C1 and C3 are conductivity of 250 mM NaCl in the first chamber and C2 and C4 are conductivity of 250 mM NaCl in the second chamber.

Time/	**Conductivity (mS/cm)**					
hours	**C1**	**C2**	**C3**	**C4**	**(C1+C3)/2**	**(C2+C4)/2**
0	24.6	24.6	24.6	24.6	24.6	24.6
3	23.7	22.6	22.6	22.8	23.2	22.7
6	22.3	19.9	19.4	21.3	20.8	20.6
9	16.3	16.0	18.2	17.5	17.2	16.8
12	14.4	13.5	15.3	15.6	14.8	14.5
15	12.0	12.5	13.7	13.2	12.8	12.9
18	10.1	10.7	11.7	11.5	10.9	11.1

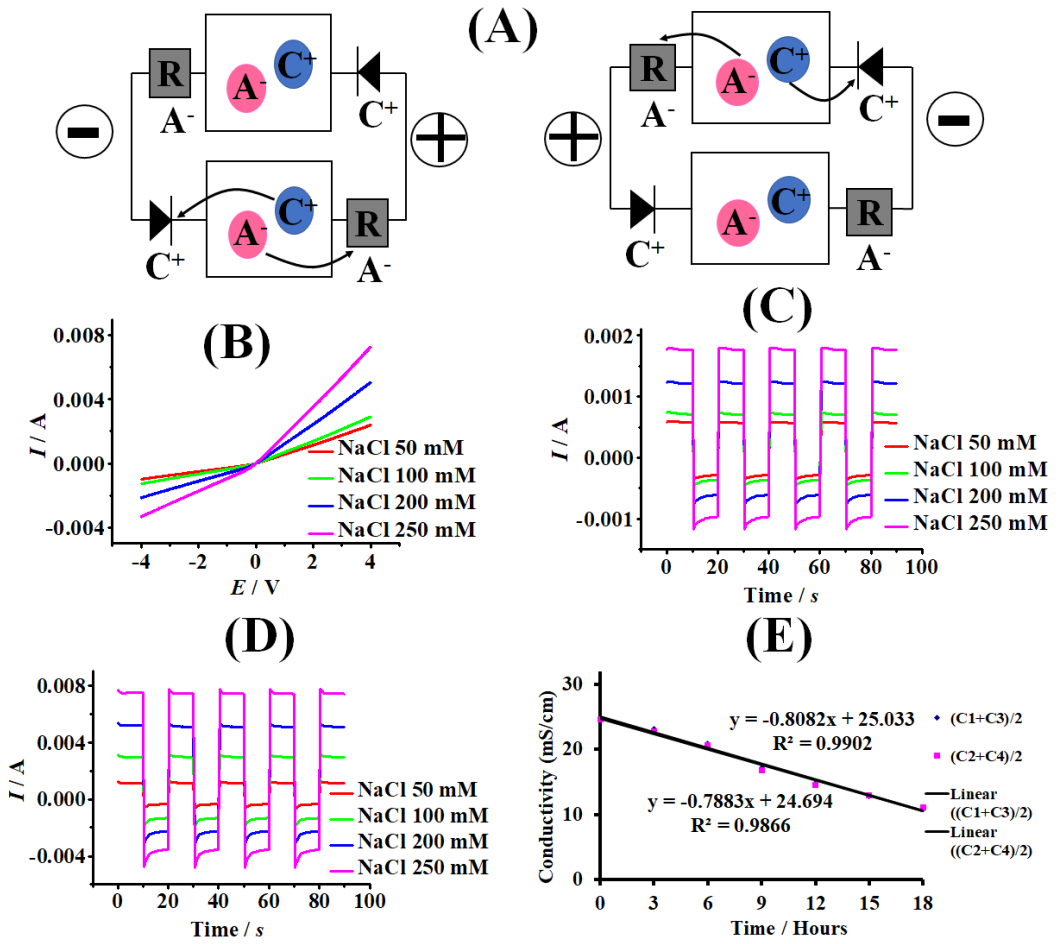

Figure 8.7. (A) Schematic drawing of mechanism for desalination mode in both chambers. (B) Cyclic voltammograms (scan rate 0.1 Vs^{-1}) for two-chamber desalination mode with 50, 100, 200, and 250 mM NaCl in both outer chambers. (C) Corresponding chronoamperometry data for +/-1 V. (D) Corresponding chronoamperometry data for +/- 4 V. (E) Plot of the specific conductivity in the two desalination chambers versus time (error bars estimated for two repeat experiments).

Figure 8.7E shows the plot of conductivity data versus time of experiment over 18 hours for the two chambers initially filled with 0.25 M NaCl. The initial specific conductivity for 0.25 M NaCl approximately 25 mS cm^{-1}, in a good agreement with the anticipated specific conductivity measured by a conductometer. With the desalination driven by switching potential at +/-4 V over 18 h (AC-driven desalination), there is a clear removal of salt from 25 mS cm^{-1} to approximately half of the initial concentration 11.7 mS cm^{-1}. This occurs in both chambers simultaneously. The charge occurs over 10 seconds in the first chamber was 0.08 C and in the second chamber was 0.04 C (from chronoamperometry data in Figure

8.7D). The total charge occurs for both chambers was 0.12 C per 20 seconds by switching potential +/- 4V at the chronoamperometry investigation. This total charge can be translated into the charge in a minute (0.36 C), in an hour (21.6 C), and in 18 hours experiment (388 C) for both chambers. The charge per each chamber over 18 hours experiment can be estimated as 194 C. The salt removal during the 18 h experiment can be estimated as 50% desalination (0.125 mol dm^{-3}) due to the conductivity decrease. Then, the theoretical charge can be calculated for a 50% desalination (remove 0.125 mol dm^{-3} in a volume of 2 cm^3 or 2.5 x 10^{-4} mol NaCl) by multiplying with the Faraday constant (96500 C mol^{-1}) consistent with 24 C in each chamber. This indicates that the efficiency of the current system for 50% salt removal (desalination) is only about 12% in terms of NaCl removal per charge transported. This could be improved in the future with a better rectification system. The energy consumption of 50% desalination of NaCl per chamber by applying +/- 4V over 18 hours is 776 Watt second cm^{-3}, which can be translated as 216 Watt hour for a litre of solution. From this experiment, in order to achieve 50% desalination of salt solution, the energy consumption was 108 Watt hour of a litre of NaCl. This compares to large scale desalination plants for example in reverse osmosis technology operating at 3-10 Watt hour for a litre of water.[14] Therefore, the energy consumption for the current ionic diode desalination process is significantly high. But this also is connected to material resistance and a relatively low rectification ratio during this process. However, it is expected that improvements can be achieved for this technology in the future.

8.3.4. Operation of the Ionic Rectifier in Desalination/Salination Mode

Then, one of the desalination branches is reversed to operate in a salination mode with applying +/- 4V over 18 hours experiment as shown in Figure 8.8A. Table 8.2 shows the conductivity of aqueous electrolyte 0.25 M NaCl in two active chambers undergoing desalination and salination in 18 hours. The experiment was repeated twice in order to ensure reproducibility of the desalination and salination phenomena in both active chambers (C1&C3 is conductivity is the first chamber and C2 & C4 is conductivity in the second chamber). Figure 8.8B shows the cyclic voltammetry data, approximately current-voltage (*I*-*V*) curve linear characteristics

are observed consistent with both branches of the system operating with similar efficiency. Figure 8.8C and 8.8D also suggest similar conditions based on chronoamperometry data at switching potential +/- 1V and +/- 4V similar to those observed in Figure 8.7.

Table 8.2. Table summarising the conductivity of 250 mM NaCl for chamber 1 and 2 with the duplicate experiment in desalination/salination mode. C1 and C3 are conductivity of 250 mM NaCl in the first chamber and C2 and C4 are conductivity of 250 mM NaCl in the second chamber.

Time/ hours	Conductivity (mS/cm)					
	C1	C2	C3	C4	(C1+C3)/2	(C2+C4)2
0	30.1	30.1	30.3	30.3	30.2	30.2
3	26.6	33.7	27.9	34.4	27.3	34.1
6	23.9	38.7	24.5	37.5	24.2	38.1
9	20.5	40.3	21.3	39.1	20.9	39.7
12	16.93	41.9	20.6	41.7	18.8	41.8
15	15.27	43.5	18.3	43.4	16.8	43.5
18	13.92	45.8	16.8	45.9	15.4	45.9

In this case, the first chamber undergoes desalination (as before) and the second chamber undergoes salination (the specific conductivity value of aqueous electrolyte NaCl increases when monitoring the salt concentration). The decrease in conductivity in one chamber and increase in conductivity in the other chamber appear balanced in agreement with a desalination/salination process over the 18 hours experiment. The desalination coupled with salination mode of operation could be useful in preventing build-up of waste salt in the environment. It might be feasible to concentrate and recover salt with an enhanced salt concentration in the one of the active chambers at the same time as operating a desalination process.

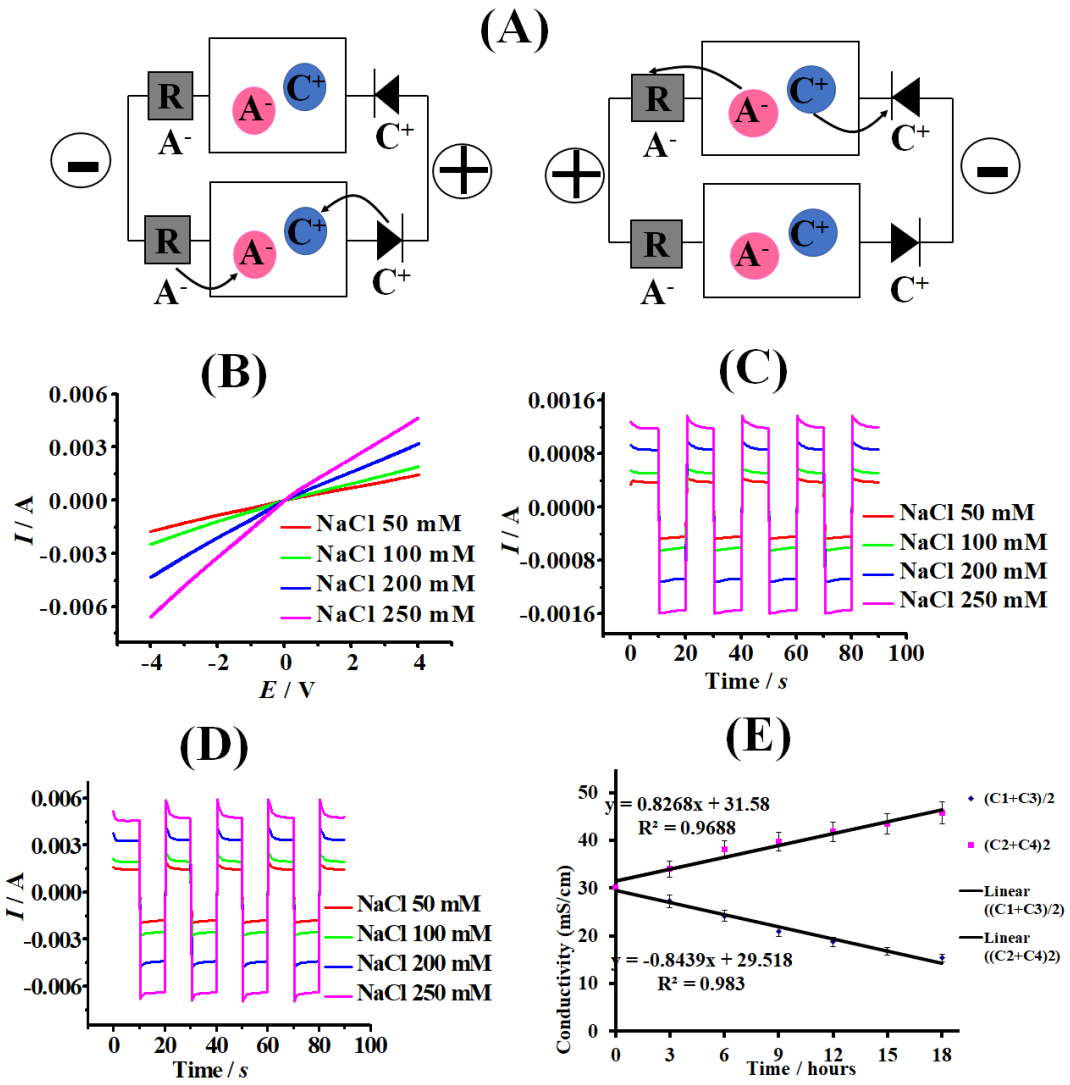

Figure 8.8. (A) Schematic drawing for mode of desalination at chamber 1 and salination at chamber 2. (B) Cyclic voltammograms (scan rate 0.1 Vs^{-1}) for two-chamber desalination/salination with 50, 100, 200, and 250 mM NaCl in both outer chambers. (C) Corresponding chronoamperometry data for +/-1 V. (D) Corresponding chronoamperometry data for +/- 4 V. (E) Plot of the specific conductivity in the desalination and salination chambers versus time (error bars estimated for two repeat measurements).

8.3.5. Operation of the Ionic Rectifier in Salination/Salination Mode

In order to achieve a salination/salination operational mode, it is possible to also invert the second branch in the ionic rectifier system to concentrate the salt at both active chambers. Table 8.3 shows the conductivity of aqueous electrolyte 0.25 M NaCl in both active chambers undergo salination mode in 18 hours. Figure 8.9A shows a schematic of schematic drawing from salination/salination configuration

in both active chambers. Figure 8.9B shows a little bit asymmetry of cyclic voltammetry data in the opposite effect observed in the desalination/desalination system as shown in Figure 8.7B. However, the chronoamperometry data at switching potential +/- 1V (Figure 8.9C) and at +/- 4V (Figure 8.9D) show current transients in agreement with the desalination/salination experiments as shown in Figure 8.8C and Figure 8.8D.

Table 8.3. Table summarising the conductivity of 250 mM NaCl for chamber 1 and 2 with the duplicate experiment in salination/salination mode. C1 and C3 are conductivity of 250 mM NaCl in the first chamber and C2 and C4 are conductivity of 250 mM NaCl in the second chamber.

Time/ hours	Conductivity (mS/cm)					
	C1	C2	C3	C4	(C1+C3)/2	(C2+C4)/2
0	25.2	25.2	27.7	27.7	26.5	26.5
3	25.9	28.9	34.6	35.1	30.3	32.0
6	28.0	32.1	38.2	38.5	33.1	35.3
9	31.7	35.3	42.8	42.0	37.3	38.7
12	38.6	39.2	44.6	44.2	41.6	41.7
15	41.7	42.8	49.7	49.0	45.7	45.9
18	45.4	46.1	54.5	53.3	50.0	49.7

Figure 8.9E shows the plot of specific conductivity for both active chambers increasing over 18 hours experiment. This implies that both active chambers indeed received salt (salination process) with a similar efficiency. Therefore, the configuration of ionic rectifier system coupled with ionic rectifier network can be employed for both salination and desalination with a similar efficiency.

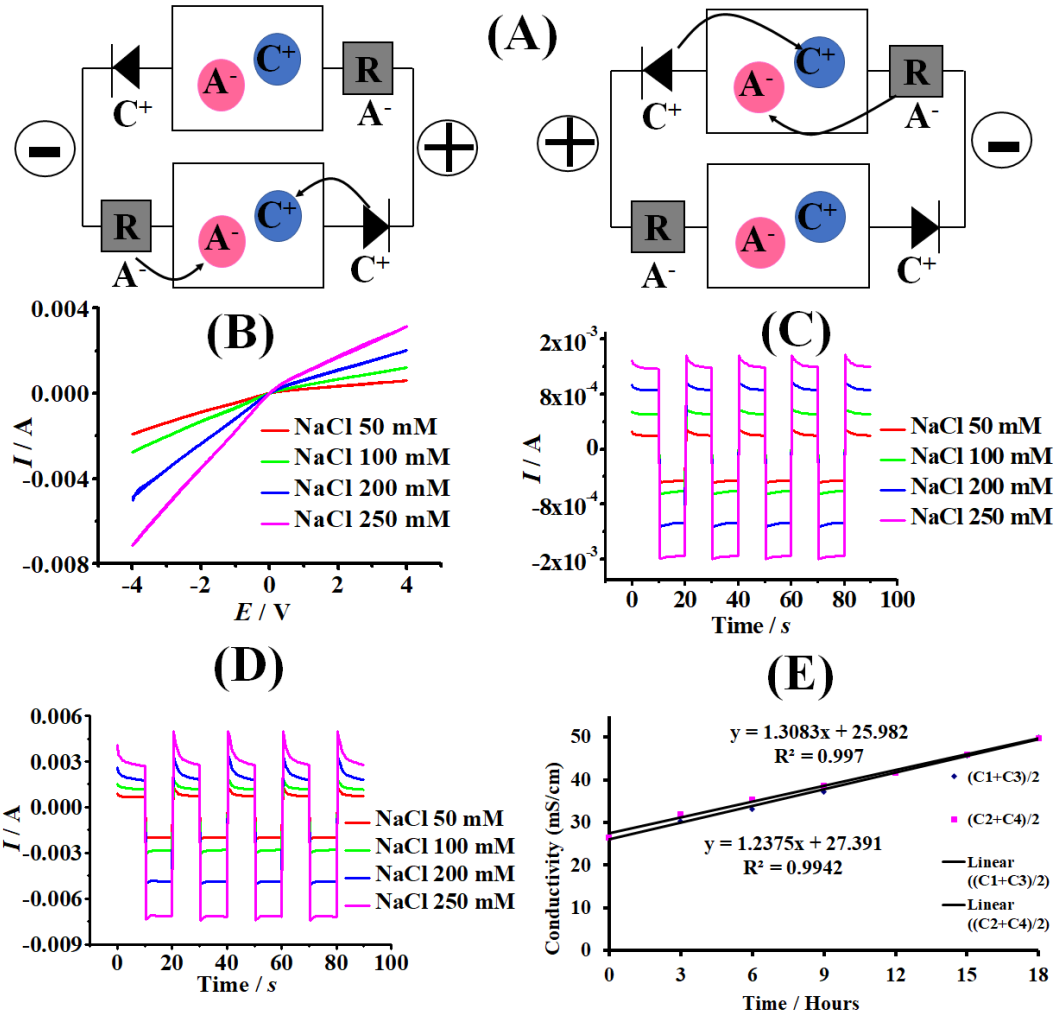

Figure 8.9. (A) Schematic drawing for mode of salination in both chambers. (B) Cyclic voltammograms (scan rate 0.1 Vs^{-1}) for two-chamber desalination with 50, 100, 200, and 250 mM NaCl in both outer chambers. (C) Corresponding chronoamperometry data for +/-1 V. (D) Corresponding chronoamperometry data for +/- 4 V. (E) Plot of the specific conductivity in the two desalination chambers versus time (error bars for two repeat measurements each).

8.4. Conclusions

The mechanism has been investigated for an ionic diode desalination system based on a 3D-printed 4-chamber experimental system with asymmetrically deposited Nafion onto 10 × 10 microhole array in a PET substrate coupled with Fumasep FAS-130 as an ionic resistor. A square wave AC-driving potential is applied using two driver (reference) electrodes by switching potential +/- 4V over 18 hours duration of the experiment. In the future, ideally these driver electrodes can be replaced with simple capacitive electrodes to avoid chemical side reactions.

The cationic diode effect based on asymmetrically deposited Nafion onto 10 × 10 microhole array in PET substrate can be used to either achieve desalination (removal of salt) or salination (concentration of salt). Proof-of-principle of ionic diode mechanism for both salination and desalination operating in tandem is provided at both active chambers over 18 hours experiment. The Fumasep FAS-130 anion conductor which degrades rapidly (over 20 hours square wave pulse operation) is a particular weak part of the current ionic diode desalination system. Therefore, better development in the anion conductor would help to improve the reliability and durability in making the device also reducing the energy consumption due to resistivity.

In this current ionic diode desalination system, particular weakness needs to be resolved in the future such as degradation of the anionic resistor even for thicker materials. This can be improved with applying sine-wave driving potentials or with other better anion conducting materials. The resistivity in the anionic resistor could be improved with using better materials and also with a higher active surface area. The performance of Nafion cationic diodes could be improved with operating a higher number of diodes in parallel to reduce the resistivity. The usage of driver electrode could be further optimised to increase rectification by applying higher voltages. In spite of that, a first proof-of-principle with clear evidence for both desalination and salination processes is demonstrated using Nafion cationic diode and Fumasep FAS-130 ionic resistor network. This system promises water purification technology without any moving parts and without production of electrolytic waste products.

8.5. References

1 Madrid, E., Cottis, P., Rong, Y., Rogers, A. T., Stone, J. M., Malpass-Evans, R., Carta, M., McKeown, N. B., Marken, F. *J. Mater. Chem. A.* **2015**. *3,* 15849–15853.

2 He, D., Madrid, E., Aaronson, B. D. B., Fan, L., Doughty, J., Mathwig, K., Bond, A. M., McKeown, N. B., Marken, F. *ACS Appl. Mater. Interfaces.* **2017**. *9*, 11272–11278.

3 Mathwig, K., Aaronson, B. D. B., Marken, F. *ChemElectroChem*. **2018.** *5*, 897–901.

4 Subramani, A., Jacangelo, J. C. *Water Res.* **2015**. *75*, 164–187.

5 Al-Amshawee, S., Yunus, M. Y. B., Azoddein, A. A. M., Hassell, D. G., Dakhil, I. H. Hasan, H. A. *Chem. Engineer. J.* **2020**. 380, 122231.

6 Cheng, Y., Hao, Z., Hao, C., Deng, Y., Li, X., Li, K., Zhao, Y. *RSC Adv*. **2019**. 9, 24401–24419.

7 Jia, B., Zhang, W. *Nanoscale Res. Lett.* **2016**. *11*, 64.

8 Pan, S.-Y., Snyder, S. W., Lin, Y. J., Chiang, P. C. *Environ. Sci.: Water Res. Technol*. **2018**. *4*, 613–638.

9 Ang, W. L., Mohammad, A. W., Johnson, D., Hilal, N. *J. Water Progress Eng*. **2019**. *31*, 100886.

10 Yang, Z., Zhou, Y., Feng, Z., Rui, X., Zhang, T., Zhang, Z. *Polymers*. **2019**. *11*, 8 1252.

11 Roelofs, S. H., van den Berg, A., Odijk, M. *Lab on a Chip*. **2015**. *15*, 3428–3438.

12 Shekarchi, N., Shahnia, F. *Internat. J. Energy Res*. **2019**. *43*, 3, 1357–1386.

13 Elimelech, M., Phillip, W. A. *Science*. **2011**. 333, 6043, 712–717.

14 Alkaisi, A., Mossad, R., Sharifian-Barforoush, A. *Energy Procedia*. **2017**. *110*, 268–274.

Chapter 9

Conclusions & Future Work

Contents

9.1 Conclusions

In this thesis, the electrochemical behaviour (ionic current rectification phenomena) for different types of ion conducting microporous structure materials has been explored with its application linked to future water desalination technology. Broadly, three types of microporous materials have been investigated based on (i) one-dimensional, (ii) two-dimensional, and (iii) three-dimensional pore systems. All of these show good performance as long as semi-permeability can be achieved. The ionic diode mechanism is similar in all cases and based on electrolyte accumulation (open diode) and depletion (closed diode) within the region of a microhole in the substrate.

The aggregation of bacteriophage M13 (one dimensional microporous materials) is observed in the presence of aqueous 10 mM acid and acts as an anion conductor membrane. Semi-permeability has been shown to lead to ionic current rectification phenomena. Ionic current rectification effects for M13 membranes was investigated when phage materials were asymmetrically deposited as a film onto a poly-ethylene-terephthalate (PET) substrate with 20 μm diameter microhole. M13 phage films form microchannel spaces between filamentous virus particles with positive surface charges (in acid) for anion conduction. The effects of the anionic diode behaviour for M13 phage deposits have been investigated with cationic (Cu^{2+}, Co^{2+}, and Ag^{+}) and anionic (indigo carmine) guest species. The cationic guest species only gradually enter the microchannel space within M13 phage deposits and show very similar minimum rectification effects at 0.5 mM concentration. Cation exclusion phenomena inside the M13 microchannel space have been proposed. In contrast, indigo carmine shows a minimum of rectification at 0.5 μM due to the blocking effect of indigo carmine binding into the micropore space of M13. The anionic diode effect for M13 deposits restores when the concentration of indigo carmine increased presumably due to the increasing conductivity inside microchannel spaces with most binding sites inside the M13 micropores occupied by the guest ions.

Ionic current rectification phenomena also have been investigated with graphene oxide (two dimensional microporous materials) when asymmetrically deposited onto a PET substrate with 20 μm diameter microhole. The ionic rectification phenomena from graphene oxide films show strong cationic diode effects in different types of aqueous electrolyte solutions, and even at higher ionic strength (up to 0.5 M). The best rectification ratio from graphene oxide films was achieved in aqueous 10 mM HCl (compared with NaOH and NaCl with similar concentration). The cationic diode effects observed in aqueous NaOH and NaCl solutions are related to dominant Na^+ transport with minimal contribution from proton transport even at low concentrations of electrolyte Na^+ through graphene oxide film. This result seems promising for removing Na^+ from saltwater in desalination application, but exploratory work on graphene oxide desalination suggests that the cationic diodes are not robust and deteriorate too quickly to be applicable. Improved graphene oxide materials still need to be investigated.

Cationic diode effects can also be obtained for titanate nanosheets (two dimensional microporous materials) when asymmetrically deposited onto a PET substrate with microhole. Cationic transport and semi-permeability are observed. It has been shown that the currents for monovalent cations are considerably higher compared to those for divalent cations, presumably due to a higher mobility of the monovalent cations through 2D titanate nanosheet film. The effects of aqueous electrolyte anions on the performance of cationic diode based on titanate nanosheet films have been investigated. With increasing of electrolyte anion size, the currents at open state of diodes appear to be higher, especially in phosphate buffer solution containing mixed cations (K^+ and Na^+). The competition between cation and proton transport through lamellar titanate nanosheet are demonstrated using a 5-electrode measurement. In this experiment, the second working electrode (collector) is fixed at the onset potential for hydrogen evolution (-0.4 V vs SCE) in order to give information about competing transport between cations and protons through titanate nanosheet film. The shape of voltammetric signals observed for divalent cations (Mg^{2+} and Ca^{2+}) shows more complex behaviour with indication of diode blocking (due to local hydroxide levels at the membrane surface) as the potential is scanned

into the positive region. This phenomenon is caused by water heterolysis that occurs at the surface of the titanate film. Combination of hydroxide ions with Mg^{2+} or Ca^{2+} causes blocking of titanate nanochannels. The presence of NBu_4^+ cations in interlayer spaces of 2D-titanate nanosheets can compete with the other cations and eventually switch the diode from cationic to anionic due to increasing positive charge in the lamellar space.

Ionic current rectification phenomena have been investigated as well in "heterojunctions" of three-dimensional microporous materials when Nafion was deposited onto one side of a 20 μm diameter microhole in PET film and PIM-EA-TB was deposited onto the opposite side. This produces cationic diode effects. The deposition of a PIM-EA-TB material helps defining a polymer|polymer interface where processes such as salt precipitation occur. NaCl and HCl at different concentrations have been investigated and, in general, the rectification ratio for HCl is higher than that for NaCl due to the higher mobility of protons in aqueous media.

The investigation of Nafion in contact with $NaClO_4$ and PIM-EA-TB in contact with KCl provided evidence for a "conventional" cationic diode effect. In the open state of diode, the observed current is mainly a reflection of Na^+ conductivity within Nafion, while in the closed state K^+ ions are blocked when moving into the opposite compartment. However, when the two electrolyte solutions are exchanged the "inverted" cationic diode effect appears and introduces an entirely new type of ionic diode based on interfacial precipitation of $KClO_4$. Now KCl solution is in contact with Nafion and $NaClO_4$ solution is in contact with the PIM-EA-TB deposit. The potassium cations flow occurs across towards the perchlorate containing electrolyte in the "open" state of diode. This results in precipitation of $KClO_4$ as blocking layer. Characteristic blocking peaks are observed in cyclic voltammetry data. The formation of this blocking layer is dependent on KCl concentration in the Nafion compartment. This is an entirely new mechanism and a possible way to sense potassium with a cationic diode or "heterojunction".

In the final part of this work, a prototype device for desalination or salination process driven by AC-electricity has been developed based on asymmetrically deposited Nafion ionomer on a 100 microhole array. This prototype device is based on a 3D-printed 4-chamber experimental system. The prototype device combines asymmetrically deposited Nafion film on a 10 × 10 microhole array on a PET substrate with Fumasep FAS-130 as a complementary anionic resistor. Two driver (reference and counter) electrodes were used to apply a square wave AC-driving potential by switching potentials +/- 4V over 18 hours of the experiment. By switching the potential +/- 4V over 18 hours partial desalination (removal of salt) or salination (concentration of salt) can be achived. The desalination or salination processes in both active chambers are shown in three operational modes using an aqueous 250 mM NaCl solution. A 50% degree of desalination/salination is achieved before severe membrane deterioration occurs. The Fumasep FAS-130 anion conductor which degrades rapidly (over 20 hours square wave pulse operation) is a particular weak part of the current ionic diode desalination system. Therefore, improvement in the anion conductor would help making the ionic diode desalination device more durable and also reducing the energy consumption in future processes.

9.2. Future Work

Although the research presented in this thesis provides many new insights into ionic current rectification phenomena with different types of microporous materials, there still remain many areas into which this investigation could be expanded. The following sections highlight some suggested areas of future research in the areas of ionic current rectification based on microporous materials and water desalination prototype based on ionic diode technology.

Bacteriophage M13. The ionic current rectification investigation study towards bacteriophage M13 raises more questions about the ability of the phage surface to interact with specific cations and anions. Further work will be required to explore effects of different electrolytes and its surface modifications. The observed ionic rectification phenomena are currently too weak for developing into realistic

applications (e.g., for desalination or for sensors), but improvements in the semipermeability of phage materials are possible, and specificity in binding could be high. In the future, specially modified phage materials could be employed in membrane separation (e.g. water purification) and developed also with sensor function for neutral, anionic, or cationic species.

Graphene Oxide. The cationic diode effect from graphene oxide film appears promising in particular for future desalination application, but this has to be investigated in more detail and for a wider range of aqueous electrolyte systems. The effects of graphene oxide structure and chemically modified graphene oxide needs to explored towards better ionic current rectification phenomena. A more quantitative theoretical description and better insight into the various aspects of diode mechanism needs to be investigated by including phenomena within the graphene oxide and within the access diffusion region. Importantly, the graphene oxide films need to be more robust to stop deterioration of films under AC-driven desalination conditions.

Titanate Nanosheets. A more quantitative observation will be required to explain the relative contributions of proton and electrolyte cation transport to the ionic diode current. At the moment, the ability of lamellar structures of titanate nanosheets is poor to maintain effective rectification ratio at higher ionic strength. Therefore, the inter-lamellar space of titanate nanosheets needs to be better designed in order to maintain semipermeability to achieve higher rectification effect. Further work can be directed toward the effects of inter-lamellar guests on the mechanism and the use of nanosheet materials in desalination and sensing.

PIM-EA-TB | Nafion Heterojunctions. Further work will be required to explore effects of film thickness and types of materials for both Nafion and for PIM-EA-TB in ionic current rectification. Improved ionomer selectivity on both sides of the heterojunction could be used to develop ionic diodes, for example targeting Mg^{2+}, Ca^{2+}, and/or more complex cations and anions. A wider range of PIMs and ionomers could be investigated to further optimize ionic diode performance. The

precipitation mechanims could be studied for other types of ions. The ionic diode sensor device could be made more selective to provide better sensitivity in electroanalytical detection applications in the future.

Water desalination prototype. In the future, the rectification efficiency needs to be improved with scale (and speed up) the desalination/salination processes and by employing bigger ionic diode arrays in order to increase the current flow through the process. The chamber volume could be kept small for continuous flow-through desalination processes with outlet salinity monitor. Alternatively, the chamber volume could be increased with stirring to maintain batch operation. Computer simulation could be developed for optimal reactor design and energy efficient AC-driving conditions.

Overall, ionic diode devices provide a fertile ground of fundamental study with effects based on materials, device geometry, and electrolyte media. The possibility to develop ionic circuits and a wider range of ionic devices could provide new types of interfaces between artificial electronic systems and biological ionic systems. Both experiment and theory will be important for progress in this emerging field.

9.3. Papers Published

1. B. R. Putra, B. D. B. Aaronson, E. Madrid, K. Mathwig, M. Carta, R. Malpass-Evans, N. B. McKeown, F. Marken. Ionic Diode Characteristics at a Polymer of Intrinsic Microporosity (PIM) | Nafion "Heterojunction" Deposit on a Microhole Poly(ethylene-terephthalate) Substrate. **2017**. *Electroanalysis*. 29, 10, 2217-2223.
2. B. R. Putra, M. Carta, R. Malpass-Evans, N. B. McKeown, F. Marken. Potassium Cation Induced for a Polymer of Intrinsic Microporosity | Nafion "Heterojunction" on a Microhole Substrate. **2017**. *Electrochimica Acta*. 258, 807-813.
3. W. T. Wahyuni, B. R. Putra, C. Harito, D. V. Bavykin, F. C. Wlash, T. D. James, G. Kociok-Köhn, F. Marken. Electroanalysis in 2D-TiO_2 Nanosheet Hosts: Electrolyte and Selectivity Effects in Ferroceneboronic Acid-Saccharide Binding. **2018**. *Electroanalysis*. 30, 1303-1310.
4. L. Tshwenya, O. Arotiba, B. R. Putra, E. Madrid, K. Mathwig, F. Marken. Cationic Diodes by Hot-Pressing of Fumasep FKS-30 Ionomer Film onto a Microhole in Polyethylene Terephthalate (PET). **2018**. *Journal of Electroanalytical Chemistry*. 815, 114-122.
5. B. R. Putra, K. J. Aoki, J. Chen, F. Marken. Cationic Rectifier Based on a Graphene Oxide-Covered Microhole: Theory and Experiment. **2019**. *Langmuir*. 35, 6, 2055-2065.
6. B. R. Putra, C. Harito, D. V. Bavykin, F. C. Walsh, W. T. Wahyuni, J. A. Boswell, A. M. Squires, J. M. F. Schmitt, M. A. D. Silva, K. J. Edler, A. E. Gesell, F. Marken. Processes Associated with Ionic Current Rectification at a 2D-Titanate Nanosheet Deposit on a Microhole Poly(ethyleneterephthalate) Substrate. **2019**. *Journal of Solid State Elecetrochemistry*. 23, 1237-1248.
7. W. T. Wahyuni, B. R. Putra, C. Harito, D. V. Bavykin, F. C. Walsh, P. J. Fletcher, F. Marken. Extraction of Hydrophobic Analytes from Organic Solution into a Titanate 2D-Nanosheet Host: Electroanalytical Perspectives. **2019**. *Analytica Chimica Acta X*. 1, 100001.
8. M. Konhefr, A. C. Sedgwick, T. D. James, K. Lacina, P. Skládal, B. R. Putra, C. Harito, D. V. Bavykin, F. C. Walsh, P. R. Raithby, G. Kociok-Köhn, F.

Marken. Voltammetric Characterisation of Diferrocenylborinic Acid in Organic solution and in Aqueous Media when Immobilised into a Titanate Nanosheet Film. **2019**. 48, 11200-11207.

9. B. R. Putra, K. Szot-Karpińska, P. Kudła, H. Yin, J. A. Boswell, A. M. Squires, M. A. D. Silva, K. J. Edler, P. J. Fletcher, S. C. Parker, F. Marken. Bacteriophage M13 Aggregation on a Microhole Poly(ethylene terephthalate) Substrate Produces an Anionic Current Rectifier: Sensitivity toward Anionic versus Cationic Guest. **2020**. *ACS Applied Biomaterials*. 3, 1, 512-521.
10. B. R. Putra, E. Madrid, L. Tshwenya, O. A. Arotiba, F. Marken. An AC-driven Desalination/Salination System Based on a Nafion Cationic Rectifier. **2020**. *Desalination*. 480, 114351.
11. W. T. Wahyuni, B. R. Putra, F. Marken. Voltammetric Detection of Vitamin B1 (Thiamine) in Neutral Solution at a Glassy Carbon Electrode via *in situ* pH Modulation. **2020**. *Analyst*. 145, 1903-1909.